

OPERATOR EVOLUTION IN THE SIMILARITY RENORMALIZATION GROUP

DISSERTATION

Presented in Partial Fulfillment of the Requirements for the Degree Doctor of
Philosophy in the Graduate School of The Ohio State University

By

Eric Robert Anderson, B.S., B.S., M.S.

Graduate Program in Physics

The Ohio State University

2012

Dissertation Committee:

Professor Richard J. Furnstahl, Advisor

Professor John F. Beacom

Professor Mike A. Lisa

Professor Robert J. Perry

© Copyright by
Eric Robert Anderson
2012

ABSTRACT

Short-range interactions between the constituent nucleons of atomic nuclei usually generate strong coupling between high- and low-momentum degrees of freedom in a nuclear Hamiltonian. This coupling leads to significant difficulty in computing the properties of nuclei using traditional quantum many-body techniques. The Similarity Renormalization Group (SRG) flow equations can unitarily soften these nuclear Hamiltonians by decoupling high-energy intermediate state contributions to low-energy observables. Analogous flow equations can be used to consistently evolve operators so that observables other than the binding energy can be calculated. The question in practice is whether the advantages of a softer Hamiltonian and less correlated wave functions are offset by complications in approximating and applying other operators. We begin by examining the properties of SRG-evolved operators in the deuteron, and lead into methods for few-body systems.

The nuclear Hamiltonian contains a hierarchy of many-body forces. The most significant contribution appears at the two-body level, followed by three-body forces, and with largely insignificant and diminishing strength thereafter. The SRG flow generates additional many-body forces (and contributions to other operators) while maintaining the natural hierarchy of many-body forces. Techniques to solve for the many-body Schrödinger Equation require individual treatment of the components in this hierarchy for the interaction, as well as other operators. Here we examine the many-body evolution of operators, including practical strategies for their evolution and extraction. These operators are applied in both “first” and “second quantized” many-body formalisms.

One also finds that by choosing appropriate generators for the SRG flow equations, different patterns of decoupling in a Hamiltonian can be achieved. Sharp and smooth

block-diagonal forms of phase-shift equivalent nucleon-nucleon potentials are generated as examples and compared to analogous low-momentum interactions (“ $V_{\text{low } k}$ ”). The kinetic energy has been used in the generator for most prior applications to nuclear interactions while other options have been largely unexplored. Here we show how variations of this standard choice can be used to address insufficiencies of the bases. The harmonic oscillator basis is used as an example. We also show how alternatives can allow the evolution to proceed more efficiently without losing its advantages.

Additional simplifications of some operators can be found from factorization of the unitary transformation operator. We explore how this factorization can be considered an extension of the operator product expansion for the nonrelativistic wave function. The validity of using a factorized approximation is considered, as well as how it can be used to further simplify the calculation of operator expectation values. Moreover, there has been much recent interest in electron scattering experiments, and the apparent presence of short-range correlations in the nuclear wave function (which is a reflection of coupling of high and low momentum degrees of freedom). These correlations appear to result in a nuclear scaling phenomenon at high momentum for many-body nuclear momentum distributions. This scaling has also been shown to possess a strong linear correlation with the “EMC effect”. We examine how these correlations can be understood in the context of the SRG and as an additional application of factorization.

For the quantum many-body problem enthusiast . . .

ACKNOWLEDGMENTS

I would like to express my sincerest thanks to Richard Furnstahl, my thesis advisor. He has provided me a thorough grounding in the study of nuclear physics. Thanks to him, I have been involved not only in research, but also the larger nuclear physics community since my first year of study at The Ohio State University (OSU). However, more than that, he has set an exceptional personal and professional example. He has cultivated an overwhelmingly positive atmosphere in our research group. He has an infectious energy for learning and research. He clearly loves what he does and sharing his knowledge with others. The level of care and personal attention he exhibits has been exceptional, and I am especially thankful for this.

I would also like to thank the many other outstanding teachers I have had throughout my education here at OSU, the University of Kentucky, and the school system of Campbell County, Kentucky. With their help and dedication I have gained the tools and motivation needed to continue on this path. There are too many, unfortunately, to list here all by name. However, I must thankfully acknowledge the exceptional time, support, and positive encouragement provided by my undergraduate research advisor, Prof. Susan Gardner, as well as her continued support of me.

I am also particularly grateful for the close-knit group of friends, colleagues, and collaborators who are both current and former members of the Low-Energy Nuclear Physics group at OSU including Robert Perry, Achim Schwenk, Scott Bogner, Lucas Platter, Joaquín Drut, Kai Hebeler, Heiko Hergert, Eric Jurgenson, Kyle Wendt, Weishi Li, and Brian Dainton. Their presence and support has enriched my experience at OSU both personally and professionally.

A special thanks goes to my “non-physics” friends and family. They have been a constant source of love and support through all of my work. Although not “quantum many-body enthusiasts” themselves, they have endeavored to learn about my studies and stood by, helping me whenever possible. This work would not be possible without them. And outside of work, my life has been a joy because of them. In particular, I want to thank my Mom, Dad, sister Robyn, and Amanda.

I would also like to express my sincere appreciation for the efforts of the members of my dissertation committee. They have committed their time to provide me with guidance and support as I have worked through this graduate program.

Finally, I would like to gratefully acknowledge financial support for my education and this research from OSU, as well as from the National Science foundation and the Department of Energy via the UNEDF SciDAC Collaboration. This funding has been instrumental in allowing me to conduct my day-to-day activities, as well as in providing the opportunities which have assisted me, and will continue to assist me, into the next stage of my career.

VITA

May 2006	B.S. in Physics, University of Kentucky, Lexington, Kentucky
May 2006	B.S. in Mathematics, University of Ken- tucky, Lexington, Kentucky
June 2012	M.S. in Physics, The Ohio State Univer- sity, Columbus, Ohio

Publications

Block diagonalization using similarity renormalization group flow equations

E. Anderson, S. K. Bogner, R. J. Furnstahl, E. D. Jurgenson, R. J. Perry, and A. Schwenk, Phys. Rev. C **77** (2008), arXiv:0801.1098v1 [nucl-th].

Operator evolution via the similarity renormalization group: The deuteron

E. R. Anderson, S. K. Bogner, R. J. Furnstahl, and R. J. Perry, Phys. Rev. C **82** (2010), arXiv:1008.1569v3 [nucl-th].

Similarity renormalization group with novel generators

W. Li, E. R. Anderson, and R. J. Furnstahl, Phys. Rev. C **84** (2011), arXiv:1106.2835v1 [nucl-th].

Fields of Study

Major Field: Physics

Studies in the Similarity Renormalization Group approach to the nuclear many-body problem : Professor Richard J. Furnstahl

Table of Contents

	Page
Abstract	ii
Dedication	iv
Acknowledgments	v
Vita	vii
List of Figures	xi
List of Tables	xviii
List of Abbreviations	xix
Chapters	
1 Introduction to the SRG	1
1.1 The Nuclear Many-body Problem	1
1.1.1 Nuclear Interactions	4
1.1.2 Many-body Solution Methods	11
1.2 The SRG Approach to Nuclear Physics	20
1.2.1 Resolution and Coupled Scales	20
1.2.2 SRG Formalism and Decoupling	24
1.2.3 Improved Convergence of Nuclear Few-body Calculations	30
1.2.4 Hierarchy of Many-Body Forces	32
1.3 Operators	36
1.4 Organization of Thesis and Original Contributions	39
2 Two-body Evolution of Operators	42
2.1 Decoupling and the Deuteron Momentum Distribution	43
2.1.1 Potentials and Decoupling	43
2.1.2 Momentum Distribution	45
2.1.3 General Analysis	51
2.2 Other Operators	53
2.2.1 Long-distance Operators	53
2.2.2 Deuteron form factors: G_C , G_Q , and G_M	57
2.3 Variational Calculations	60
2.4 Operator Universality	63
2.5 Chapter Summary	66
3 Many-body Evolution of Operators	68

3.1	Analysis in Second Quantization	69
3.2	Evolution, Embedding, and Extraction of Operators	71
3.2.1	Jacobi Basis Evolution Considerations	74
3.3	Ab-initio Calculations: A 1D Model	81
3.3.1	Oscillator Basis Representation: Jacobi Coordinates	83
3.3.2	Operator Evolution and Extraction in Jacobi Oscillator Basis	86
3.3.3	Oscillator Basis Representation: Single Particle Coordinates	87
3.3.4	Representative Example: Number Operator	89
3.4	Ab-initio Calculations: 3D Considerations	99
3.5	Formalism in Second Quantization	100
3.6	Chapter Summary	102
4	Alternative Generators	104
4.1	Block-Diagonalization	105
4.2	Computational Performance	113
4.2.1	Two-nucleon systems	115
4.2.2	Few-body tests in a one-dimensional model	124
4.2.3	Section Summary	130
4.3	Operators: Basis Convergence	131
4.3.1	Long-range Operators in a 1D Model Oscillator Basis	133
4.3.2	Long-range Operator in a 3D Oscillator Basis	143
4.3.3	Section Summary	145
4.4	Chapter Summary	146
5	Operator Factorization	147
5.1	Numerical Verification of Factorization	148
5.2	Connection to the Operator Product Expansion	151
5.3	Consequences of Factorization	156
5.4	Chapter Summary	158
6	Applications of Operator Evolution and Factorization	160
6.1	Nuclear Scaling	166
6.1.1	Interpreting high-momentum scaling behavior of the momentum distribution: A 1D Many-body example	168
6.2	Nuclear Matter Calculations	170
6.2.1	Overview of Calculation	171
6.2.2	Results	172
6.2.3	Next Steps	175
6.3	EMC Effect	176
6.4	Chapter Summary	178
7	Summary and Outlook	180
	Bibliography	183

Appendices

A Many-body Evolution	193
A.1 One-body operators in Jacobi coordinates	193
A.2 Separation of n -body components, 2 nd quantized analysis	195

List of Figures

Figure	Page
1.1 Degrees of freedom relevant to the nuclear many-body problem [1].	2
1.2 A map of the nuclear landscape [1].	4
1.3 Phenomenological potentials which reproduce NN elastic scattering data and bound states [2].	6
1.4 Diagrammatic contributions to Chiral EFT [3].	8
1.5 Classical system illustrating the need for three-body forces.	9
1.6 Detailed two-body internal processes (top) reduce to three-body interactions in EFT (bottom).	10
1.7 Nuclear many-body methods associated with size of system (as a function of nucleon number) to be explored [4].	11
1.8 Exponential growth of matrix size in CI methods [5].	17
1.9 High resolution image (top left) with fourier transform (bottom left) compared low resolution image (top right) generated by the application of a low pass filter in the conjugate space (bottom right) [6].	21
1.10 1S_0 partial wave of the AV18 potential in coordinate space (left) and momentum space (right).	22
1.11 Low pass filter applied to 1S_0 partial wave of AV18. The truncated potential is shown to the left. To the right is the original phase shift plot (solid line) compared to phase shifts from the truncated potential (dashed line).	24
1.12 Schematic of $V_{\text{low } k}$ transformation on the left, and SRG evolution on the right [7].	25
1.13 Evolution of 1S_0 partial wave of AV18 shown on top (at $\lambda = 20 \text{ fm}^{-1}$ the potential is effectively unevolved) to $\lambda = 2 \text{ fm}^{-1}$ as shown on bottom. The left and right images are two different perspectives of the same matrices.	27
1.14 Phase shifts in a number of AV18 partial wave momentum channels. The original phase shifts in each channel are give by the solid lines. The dashed and dotted lines are calculated from potentials whose matrix elements for which $k, k' > k_{\max} = 2.2 \text{ fm}^{-1}$ have been excluded. The dotted result from truncation of the matrix with no RG evolution. The dashed lines result from an SRG evolved potential to $\lambda = 2 \text{ fm}^{-1}$ [8].	28
1.15 Evolution of local projection for 1S_0 partial wave of AV18 (solid line) compared to original local potential (dashed line) [9]	29

1.16	Improved convergence of ^4He in NCSM calculation with respect to oscillator basis parameters for selected values of two-body SRG evolution λ of a chiral EFT potential. The top left frame is unevolved [10].	30
1.17	Ground state energy for various many-body contributions to ^3H (left) using $N_{\max} = 36$ and $\hbar\Omega = 28 \text{ MeV}$, and ^4He (right) using $N_{\max} = 28$ and $\hbar\Omega = 36 \text{ MeV}$ for the evolution and truncating to $N_{\max} = 18$ for the calculation [11].	31
1.18	Individual expectation values of contributions to the ground state energies of ^3H (left) and ^4He (right) [12]. A hierarchy of many-body force effects is apparent.	33
1.19	Convergence of ^4He and ^6Li for unevolved EFT potential versus potential after SRG evolution as a function of basis size, N_{\max} . Three-body induced forces are included [12].	34
1.20	Calculation of binding energy per particle (top), and radii (bottom) using MBPT and SRG evolved chiral EFT NN potentials, including induced three-body forces. Here, α is the same as $s = 1/\lambda^4$ [7].	35
1.21	Calculations of nuclear matter with SRG evolved NN-only potentials. The neglected three-body induced components are approximated to produce saturation. $V_{\text{low } k}$ potential calculations are also shown. See Reference [13] for details.	36
2.1	SRG evolution of the momentum-space $^3\text{S}_1$ potential starting with (a) AV18 from $\lambda = 15 \text{ fm}^{-1}$ to $\lambda = 1.5 \text{ fm}^{-1}$ [14] and (b) N ³ LO (500 MeV) from $\lambda = 6 \text{ fm}^{-1}$ to $\lambda = 1.5 \text{ fm}^{-1}$ [15].	44
2.2	The momentum distribution in the deuteron as given by the expectation value of the bare number operator $a_q^\dagger a_q$ for the (a) AV18 [14] and (b) N ³ LO (500 MeV) [15] potentials, both evolved and unevolved.	46
2.3	(a) SRG evolution of the operator $\langle k a_q^\dagger a_q k' \rangle$ for $q = 0.34 \text{ fm}^{-1}$ in the $^3\text{S}_1$ partial wave from $\lambda = 6 \text{ fm}^{-1}$ to $\lambda = 1.5 \text{ fm}^{-1}$, with the N ³ LO (500 MeV) [15] initial potential. (b) Integrand of $\langle \psi_d(s) (a_q^\dagger a_q)_s \psi_d(s) \rangle$ with linear (top) and logarithmic magnitude (bottom) scales.	47
2.4	Same as Figure 2.3 but for $q = 3.02 \text{ fm}^{-1}$	48
2.5	Decoupling in operator matrix elements is tested by calculating the momentum distribution in the deuteron after evolving the AV18 potential to several different λ and then truncating the Hamiltonian and evolved occupation operators (i.e., set them to zero above $\Lambda = 2.5 \text{ fm}^{-1}$).	49
2.6	Decoupling in operator matrix elements is tested by calculating the momentum distribution in the deuteron after evolving the N ³ LO potential to several different λ and then truncating the Hamiltonian and evolved occupation operators (i.e., set them to zero above $\Lambda = 2.0 \text{ fm}^{-1}$).	50
2.7	Operator evolution of $\langle k r^2 k' \rangle$ in the $^3\text{S}_1$ partial wave from $\lambda = 6 \text{ fm}^{-1}$ to $\lambda = 1.5 \text{ fm}^{-1}$ using the N ³ LO (500 MeV) potential.	54
2.8	Integrand given by $\langle \psi_d r^2 \psi_d \rangle$ and evolved from $\lambda = 6 \text{ fm}^{-1}$ to $\lambda = 1.5 \text{ fm}^{-1}$ using the N3LO 500 MeV potential with a linear color scale (top) and a logarithmic scale of the magnitude (bottom). Notice the difference in momentum scales.	55

2.9	Integrand of the quadrupole moment expectation value in the deuteron and evolved from $\lambda = 6 \text{ fm}^{-1}$ to $\lambda = 1.5 \text{ fm}^{-1}$ using the N3LO 500 MeV potential with a linear color scale (top) and a logarithmic scale of the magnitude (bottom). Notice the difference in momentum scales.	56
2.10	Integrand given by $\langle \psi_d r^{-1} \psi_d \rangle$ and evolved from $\lambda = 6 \text{ fm}^{-1}$ to $\lambda = 1.5 \text{ fm}^{-1}$ using the N3LO 500 MeV potential with a linear color scale (top) and a logarithmic scale of the magnitude (bottom). Notice the difference in momentum scales.	57
2.11	Deuteron form factors G_C , G_Q , and G_M using the isoscalar electric form factor parameterization from Ref. [16]. M is the nucleon mass and M_d is the mass of the deuteron. The wave function is derived from the NNLO 550/600 MeV potential and the evolution is run to $\lambda = 1.5 \text{ fm}^{-1}$ [17].	59
2.12	Integrand of G_M at $q = 6.90 \text{ fm}^{-1}$ evolved from $\lambda = 6 \text{ fm}^{-1}$ to $\lambda = 1.5 \text{ fm}^{-1}$ using the NNLO 550/600 MeV potential with a linear scale (top) and a logarithmic scale of the magnitude (bottom).	60
2.13	Integrand of G_M at $q = 0.34 \text{ fm}^{-1}$ evolved from $\lambda = 6 \text{ fm}^{-1}$ to $\lambda = 1.5 \text{ fm}^{-1}$ using the NNLO 550/600 MeV potential with a linear scale (top) and a logarithmic scale of the magnitude (bottom).	61
2.14	Deviation from E_d of the best variational energy as a function of SRG decoupling parameter for the wave function ansatz of Eq. (2.21). E_d is the deuteron binding energy for each interaction derived via a full eigenvalue calculation of the Hamiltonian.	62
2.15	The momentum distribution in the deuteron as given by the expectation value of the evolved occupation operator $U a_q^\dagger a_q U^\dagger$ using the variational wave functions derived from the Salpeter ansatz and the AV18 potential evolved to $\lambda = 6.0 \text{ fm}^{-1}$, 4.0 fm^{-1} and 1.5 fm^{-1} . The direct calculation is from a full eigenvector solution of the Hamiltonian.	63
2.16	Deuteron form factor G_M using the isoscalar electric form factor parameterization from Ref. [16]. M is the nucleon mass and M_d is the mass of the deuteron. The variational wave functions are derived from the Salpeter ansatz and the NNLO 550/600 MeV potential evolved to $\lambda = 5.0 \text{ fm}^{-1}$ and $\lambda = 1.2 \text{ fm}^{-1}$. The operators are evolved consistently. The direct calculation is from a full eigenvector solution of the Hamiltonian.	64
3.1	Operator evolution and embedding process diagram.	72
3.2	Naive implementation of the many-body evolution of number operators to calculate the momentum distribution of a one-dimensional model system. The solid lines are exact results. The starred points are the result of a naive (incorrect) implementation of the two-body only evolution to $\lambda = 2.0$	77
3.3	Revised operator evolution and embedding process diagram – care must be taken to account for a boost into the relative coordinate frame for some operators.	80
3.4	The A=2, 3, & 4 boson system momentum distributions calculated with bare operator are shown separately here at different points in the SRG evolution. First shown in [18].	91

3.5	Tests of number operator expectation value decoupling with respect to N_{cut} at $q = 15.03$ (left) and at $q = 0.51$ (right).	92
3.6	The $A=3$ boson system relative momentum distributions calculated with the inclusion of 2-body only operators, as well the fully evolved operator.	93
3.7	The $A=4$ boson system relative momentum distributions calculated with the inclusion of 2-body only operators, 2+3-body only operators, as well the fully evolved operator.	94
3.8	The $A=3$ boson system momentum distributions calculated with the inclusion of 2-body only operators, as well the fully evolved operator.	96
3.9	The $A=4$ boson system momentum distributions calculated with the inclusion of 2-body only operators, 2+3-body only operators, as well the fully evolved operator.	97
3.10	Diagrammatic representation of unevolved operator (empty square), and evolved operator (shaded square).	101
4.1	Comparison of momentum-space $V_{\text{low } k}$ (left) and SRG (right) block-diagonal potentials with $\Lambda = 2 \text{ fm}^{-1}$ evolved from an $N^3\text{LO}$ 3S_1 potential [15]. The color axis is in fm.	105
4.2	Comparison of momentum-space $V_{\text{low } k}$ (left) and SRG (right) block-diagonal potentials with $\Lambda = 2 \text{ fm}^{-1}$ evolved from an $N^3\text{LO}$ 3S_1 potential [15]. The color and z axes are in fm.	106
4.3	Evolution of the 3S_1 partial wave with a sharp block-diagonal flow equation with $\Lambda = 2 \text{ fm}^{-1}$ at $\lambda = 4, 3, 2$, and 1 fm^{-1} . The initial $N^3\text{LO}$ potential is from Ref. [15]. The axes are in units of k^2 from 0 – 11 fm^{-2} . The color scale ranges from -0.5 to $+0.5 \text{ fm}$ as in Figure 4.1.	107
4.4	Same as Figure 4.3 but for the 1P_1 partial wave.	108
4.5	Evolution of the 3S_1 partial wave with a smooth ($n = 4$) block-diagonal flow equation with $\Lambda = 2.0 \text{ fm}^{-1}$, starting with the $N^3\text{LO}$ potential from Ref. [15]. The flow parameter λ is $3, 2, 1.5$, and 1 fm^{-1} . The axes are in units of k^2 from 0 – 11 fm^{-2} . The color scale ranges from -0.5 to $+0.5 \text{ fm}$ as in Figure 4.1.	109
4.6	Evolved SRG potentials starting from Argonne v_{18} in the 1S_0 and 1P_1 partial waves to $\lambda = 1 \text{ fm}^{-1}$ using a bizarre choice for G_s (see text). The color and z axes are in fm.	110
4.7	Phase shifts for the 3S_1 partial wave from an initial $N^3\text{LO}$ potential and the evolved sharp SRG block-diagonal potential with $\Lambda = 2 \text{ fm}^{-1}$ at various λ , in each case with the potential set identically to zero above Λ	111
4.8	Same as Figure 4.7 but with Argonne v_{18} as the initial potential [14].	112
4.9	Errors in the phase shift at $E_{\text{lab}} = 100 \text{ MeV}$ for the evolved sharp SRG block-diagonal potential with $\Lambda = 2 \text{ fm}^{-1}$ for a range of λ 's and a regulator with $n = 8$	112
4.10	Computational time to evolve the Argonne v_{18} 1S_0 potential [14] as a function of the final value of λ_{eq} (see text) for several generators, with $\sigma = 2 \text{ fm}^{-1}$ for G_s^{inv} and G_s^{exp}	114

4.11 Deviation of phase shifts calculated with the Argonne v_{18} 1S_0 potential [14] evolved with $G_s = T$ and G_s^{\exp} ($\sigma = 2 \text{ fm}^{-1}$) to various λ values and then truncated at $k_{\text{cut}} = 2 \text{ fm}^{-1}$ to test decoupling. Phase shifts from untruncated potentials agree precisely with those from the initial potential.	117
4.12 Contour plots showing the evolution via Eq. (4.1) at several values of λ_{eq} starting from the momentum-space Argonne v_{18} 1S_0 potential [14] using (a) $G_s = T_{\text{rel}}$, (b) G_s^{inv} from Eq. (4.12) with $\sigma = 2 \text{ fm}^{-1}$, and (c) G_s^{\exp} from Eq. (4.13) with $\sigma = 2 \text{ fm}^{-1}$	118
4.13 Diagonal (a) and off-diagonal (b) momentum-space matrix elements for evolved Argonne v_{18} 1S_0 potential [14] with $G_s = T$ and generators G_s^{\exp} and G_s^{inv} at $\lambda = 2 \text{ fm}^{-1}$ with $\sigma = 2 \text{ fm}^{-1}$	119
4.14 Diagonal (a) and off-diagonal (b) momentum-space matrix elements for evolved Argonne v_{18} 1S_0 potential [14] with $G_s = T$ and G_s^{\exp} with different values of σ each evolved to $\lambda = 2 \text{ fm}^{-1}$. The lines with $\sigma = 3 \text{ fm}^{-1}$ are indistinguishable from the ones with $G_s = T$	120
4.15 (a) Unevolved N ³ LO 500 MeV 1S_0 potential . (b) Contour plot showing the evolved N ³ LO 1S_0 potential with different generators to $\lambda_{\text{eq}} = 2 \text{ fm}^{-1}$. For G_s^{\exp} and G_s^{inv} , $\sigma = 2 \text{ fm}^{-1}$	120
4.16 Color contour plots of the first term (excluding the factor due to V_s) on the right side of Eq. (4.15) for $G_s = T_{\text{rel}}$ (left), G_s^{inv} (middle), and G_s^{\exp} (right). The last two use $\sigma = 2 \text{ fm}^{-1}$	121
4.17 Color contour plots of the first terms (excluding the factor due to V_s) on the right side of Eq. (4.15) for G_s^{\exp} with $\sigma = 1, 2$, and 3 fm^{-1} from left to right.	121
4.18 Contour plot showing the evolution to $\lambda_{\text{eq}} = 2 \text{ fm}^{-1}$ via Eq. (4.1) starting from the momentum-space Argonne v_{18} 1S_0 potential [14] using G_s^{\exp} from Eq. (4.13) with different values of σ	122
4.19 Computational time to evolve the Argonne v_{18} 1S_0 potential [14] with $G_s = T$ and G_s^{\exp} to $\lambda_{\text{eq}} = 2 \text{ fm}^{-1}$ as a function of the value of σ	122
4.20 Decoupling using G_s^{\exp} with $\sigma = 3$ for (a) $A = 2$, (b) $A = 3$, and (c) $A = 4$. The initial two-body-only potential is evolved to each λ shown in a basis with $N_{\text{max}} = 40$. Matrix elements of the potential are set to zero if one or both states have $N > N_{\text{cut}}$ and the resulting Hamiltonian is diagonalized to obtain the ground-state energies plotted.	126
4.21 The lowest bound-state energy for a four-particle system as a function of λ evolved using the SRG G_s^{\exp} generator and an $N_{\text{max}} = 40$ basis with an initial three-body potential with strength (a) $c_E = 0.0$, (b) $c_E = -0.05$, and (c) $c_E = 0.05$. The (blue) curves with diamonds include the full evolution of the Hamiltonian while the (black) curves with circles use the two-body potential evolved in the two-particle system and the (red) curves with squares use the two- and three-body potentials evolved in the three-particle system. Evolution with G_s^{inv} is almost indistinguishable.	127
4.22 Tests of decoupling for the r^2 operator expectation value in the 3-body system at various points, λ , in the evolution using the generators (a) $G_s = T_{\text{rel}}$, (b) $G_s = H_{\text{ho}}$, and (c) $G_s = T_{\text{rel}} + r^2$	135
4.23 Decoupling of the A=3 boson system binding energy at various λ for the flow operators (a) $G_s = H_{\text{ho}}$ and (b) $G_s = T_{\text{rel}} + r^2$	137

4.24	Induced many-body contributions to the ground state binding energy of the A=4 boson system using (a) $G_s = H_{\text{ho}}$ and (b) $G_s = T_{\text{rel}} + r^2$ with an initial 2-body only interaction. Shown here are the contributions due to only 2-body matrix elements of the evolution, only 2+3-body matrix elements, and the full 4-body evolution.	138
4.25	Tests of number operator expectation value decoupling with respect to N_{cut} at $q = 15.03$ (left) and at $q = 0.51$ (right), evolved using $G_s = T_{\text{rel}}$ (top, as reproduced for comparison from Chapter 3) and $G_s = T_{\text{rel}} + r^2$ (bottom).	139
4.26	Coordinate (top) and momentum (bottom) space distributions for the 2-body wave functions evolved to $\lambda = 3$ (left) and $\lambda = 1$ (right) using the flow operators $G_s = T_{\text{rel}}$, $G_s = T_{\text{rel}} + r^2$, and $G_s = r^2$. The distribution calculated from the initial momentum space wave function is in each plot for reference.	141
4.27	Dependence of bare $\langle r^2 \rangle$ with respect to λ for different flow operators $G_s = T_{\text{rel}}$, $G_s = H_{\text{ho}}$, $G_s = T_{\text{rel}} + r^2$, and $G_s = r^2$ in a 3-body system. The evolved r^2 line indicates the initial expectation value.	142
4.28	The RMS matter radius of ${}^3\text{H}$, as derived from the SRG evolution of r^2 operator for A=3 with the flow operator $G_s = T_{\text{rel}}$. A chiral N ³ LO potential is used with and initial NN+NNN interaction [19].	144
4.29	The RMS matter radius of ${}^3\text{H}$, as derived from the SRG evolution of r^2 operator for A=3 with the flow operator $G_s = T_{\text{rel}} + \alpha r^2$. In this example, $\alpha = 10$. A chiral N ³ LO potential is used with and initial NN+NNN interaction [19].	145
5.1	Numerical tests of factorization of the unitary transformation $U_\lambda(k, q)$ by plotting the ratio in Eqs. (5.1) and (5.2) as a function of q for fixed k_0 and several values of k_i . Plateaus in q indicate factorization. The unitary transformations are generated from the Argonne v_{18} (AV18) [14] potential evolved to $\lambda = 2 \text{ fm}^{-1}$ in the (a) ${}^1\text{S}_0$ and (b) ${}^1\text{P}_1$ partial waves. The shaded region marks $q < \lambda$	148
5.2	Same as Figure 5.1 but for the ${}^3\text{S}_1$ partial wave and λ of (a) 1.5 fm^{-1} and (b) 3 fm^{-1}	149
6.1	Illustration of electron scattering experiment on atomic nucleus [20].	161
6.2	Schematic of electron scattering knockout process of correlated pair (left) [21]. An enlarged view (right) shows the naive interaction assumed by standard nuclear physics models.	161
6.3	Recall the unevolved AV18 potential on the left compared to the same potential evolved to $\lambda = 1.5 \text{ fm}^{-1}$ on the right. The evolved potential lacks the coupling of high and low momenta need to produce SRCs.	162
6.4	Inclusive electron scattering cross section ratios of various nuclei relative to ${}^3\text{He}$ as a function of x_B . For $1.5 < x_B < 2$ the plateaus indicate NN scaling, and for $x_B > 2.25$ shown here we have three-nucleon scaling [22].	166
6.5	VMC calculation of the momentum distributions for various nuclei, as well as for nuclear matter [23]. Scaling of the distributions at high momenta is evident.	167

6.6	The scaling of momentum distributions at high momenta in a 1D model is tested by using the leading-order factorized approximation to the momentum occupation number operator to predict high-momentum scaling in $A = 2, 3, 4$ (symbols). The full momentum distributions for $A = 2, 3$, and 4 are shown with solid, dot-dashed, and dashed lines, respectively.	169
6.7	Relative np -pair (lines) and pp -pair momentum distributions (for total pair momentum $P = 0$) in various nuclei, as calculated in VMC [24]. Nuclear scaling for relative momentum distribution is evident, as well as the enhancement of np pairs versus pp pairs due to tensor forces in the interaction.	171
6.8	Perturbative expansion of evolved operator, as represented by a shaded box. Both the operator and the potential, V_λ , have been evolved to λ	172
6.9	Relative np -pair momentum distribution (for total pair momentum $P = 0$) in nuclear matter at second order in perturbation theory for the AV18 potential evolved to various low-momentum values of λ [25]. The dotted lines show the result without evolving the operators. The solid lines show the result with operator evolution.	173
6.10	Ratio of relative np -pair to nn -pair momentum distributions (for total pair momentum $P = 0$) in nuclear matter at second order in perturbation theory for the AV18 potential evolved to various low-momentum values of λ [25]. On the left, the dotted lines show the result without evolving the operators; the solid lines show the result with operator evolution. On the right, the dotted lines show the result without including the tensor part of the interaction; the solid lines show the result with the tensor component. The operators have been evolved in both cases here.	174
6.11	Ratios of perturbative nuclear matter momentum distributions at densities of $k_f = 1.05 \text{ fm}^{-1}$ and $k_f = 1.35 \text{ fm}^{-1}$ for $\lambda = 1.8 \text{ fm}^{-1}$ and $\lambda = 2.0 \text{ fm}^{-1}$, as specified, over <i>ab-initio</i> calculation of the deuteron. Assuming the presence of nuclear scaling, plateaus demonstrate the reproduction of high momentum behavior in perturbative calculation of nuclear matter momentum distribution.	175
6.12	Linear correlation of the EMC effect related change in the ratio of cross sections with the nuclear scaling effect ratio given by a_2 [26].	177

List of Tables

Table	Page
2.1 Expectation value of the quadrupole moment given by the unevolved operator with the evolved deuteron wave function.	55
4.1 Speed up in model A -particle one-dimensional (1D) oscillator basis for evolution to $\lambda_{eq} \approx 3$, comparing the ratio of the time to evolve $G_s = T_{\text{rel}}$ versus G_s^{exp} . The results for G_s^{inv} are very similar.	125
5.1 Singular values of the unitary transformation $U(k, q)$ for $q > \Lambda$ and $k < \Lambda$ (see discussion in text; units in fm^{-1}) corresponding to the given potentials at $\lambda = 2 \text{ fm}^{-1}$ in the ${}^1\text{S}_0$ partial wave and ${}^3\text{S}_1 - {}^3\text{D}_1$ coupled channel.	150
5.2 Relative error of evolved operator matrix elements calculated using the SVD to factorize $U_\lambda(k, q)$ in the region where $k < \Lambda$ and $q > \Lambda$ (see discussion in text; units in fm^{-1}).	152

List of Abbreviations

AV18 Argonne v_{18} . 22

CI configuration interaction. 18

COM center-of-mass. 70

DFT density functional theory. 13

EFT effective field theory. 6

EMC Electron-Muon Collaboration. 176

FSI final-state interaction. 161

GFMC Green's function Monte Carlo. 14

HF Hartree-Fock. 20

HFB Hartree-Fock-Bogoliubov. 20

IR infrared. 128

LDA local density approximation. 176

MBPT many-body perturbation theory. 19

NCFC No Core Full Configuration. 16

NCSM No Core Shell Model. 16

NN nucleon-nucleon. 4

OPE operator-product-expansion. 148

RG renormalization group. 13

- SRCs** short-range correlations. 160
- SRG** Similarity Renormalization Group. 12
- SVD** singular value decomposition. 149
- SVM** stochastic variational method. 14
- UV** ultraviolet. 128
- VMC** variational Monte Carlo. 14

Chapter 1

INTRODUCTION TO THE SRG

A broad overview of the nuclear many-body problem and how the Similarity Renormalization Group fits into its theoretical description is presented here. The principles behind the SRG, as well as its primary results are reviewed. We also begin to explore the issues that must be addressed in order to explore nuclear observables in general via the evolution operators in the SRG.

1.1 The Nuclear Many-body Problem

The nuclear many-body problem is a broad one, encompassing the study of atomic nuclei and their constituents across several orders of magnitude in energy. This also includes the study of larger collective states (such as neutron stars) where the nuclear constituents are the relevant degrees of freedom. A hierarchy of the nuclear degrees of freedom along with their corresponding energy scales is presented in Figure 1.1. According to the standard model, nuclei are composed of quarks and gluons, whose interactions are described by quantum chromodynamics. These constituents form bound state baryons and mesons, and the lightest baryons are protons and neutrons whose interactions are most appropriately viewed at lower energies as being mediated by the exchange of light mesons such as the pion. While some aspects of nuclear physics, such as experiments (and the associated phenomenology) conducted on the quark-gluon plasma (QGP) at the Relativistic Heavy Ion Collider (RHIC) at Brookhaven and now the Large Hadron Collider (LHC) near Geneva, necessitate the consideration of the most fundamental, high energy degrees of freedom, we

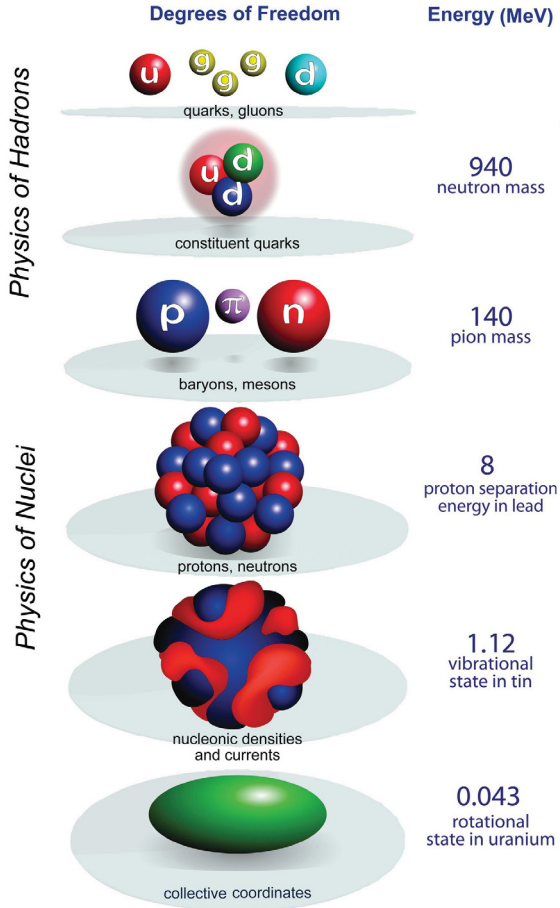


Figure 1.1: Degrees of freedom relevant to the nuclear many-body problem [1].

will be focusing here on questions that can be addressed by low-energy nuclear physics. Specifically, our “fundamental” degrees of freedom will be protons and neutrons whose interactions can be described in the framework of nonrelativistic quantum mechanics (i.e., by the Schrödinger Equation). Naturally, this picture begins to break down significantly when energies approach the neutron and proton masses.

Nevertheless, a wide range of phenomena involving the structure and reactions of atomic nuclei can be addressed in this regime. Figure 1.2 presents the landscape of atomic nuclei as given by their number of protons and neutrons. The known nuclei are shown in yellow. Those stable against spontaneous decay are shown in black. There are nearly 300 stable nuclei compared to approximately 3000 known unstable nuclei. The largest confirmed nucleus

at the time of this writing contains 118 protons and 176 neutrons, although an “island of stability” predicted by nuclear theory remains to be discovered at larger masses. There are around 7000 nuclei thought to exist in total [27]. The location of the proton and neutron drip lines (where adding more protons or neutrons to a nucleus will no longer produce a bound state under strong interactions) are shown schematically. The precise location of these drip lines, particularly on the neutron-rich side, remains an open question for theory and experiment. Also indicated here is the r-process, which is a process important for nucleosynthesis where neutron rich nuclei decay to those with more protons (toward the “stable nuclei”). Note that it runs through the “terra incognita” where experimental data is lacking. Also in relief above the landscape is a generic picture of theoretical many-body methods used to address nuclei of increasing size. This will be discussed further below.

The primary goal of low-energy nuclear physics research in this landscape is to predict properties of the structure and reactions of atomic nuclei – particularly relevant to the subject of this thesis, this includes their interactions with external probes. More broadly, this research seeks to uncover how the nuclear degrees of freedom in the hierarchy of Figure 1.1 interact to produce these properties [1]. Specifically, we would like to understand how protons and neutrons make stable and unstable nuclei, as well as the limits of formation for their isotopes (i.e., the location of the drip lines). We would like to know the equation of state for bulk nuclear matter. We would like to understand how simple patterns and collective degrees of freedom arise from the seemingly complex interactions of nucleons. Ultimately, we would like to predict properties of nuclear fission, fusion and other reactions. With such an understanding we can also better answer questions across other fields, such as how the elements formed in the early universe via nucleosynthesis. We can understand how stars ultimately explode as supernovas, and the properties of neutron stars. More fundamental questions may even be answered with the help of precision low-energy nuclear many-body methods, such as why there is more matter than antimatter in the universe, and what is the nature of neutrinos (including their interaction with atomic nuclei). Further, applications of low-energy nuclear physics can be found in the Biological and Medical Sciences, Material Sciences, Nuclear Energy, and National Security [1].

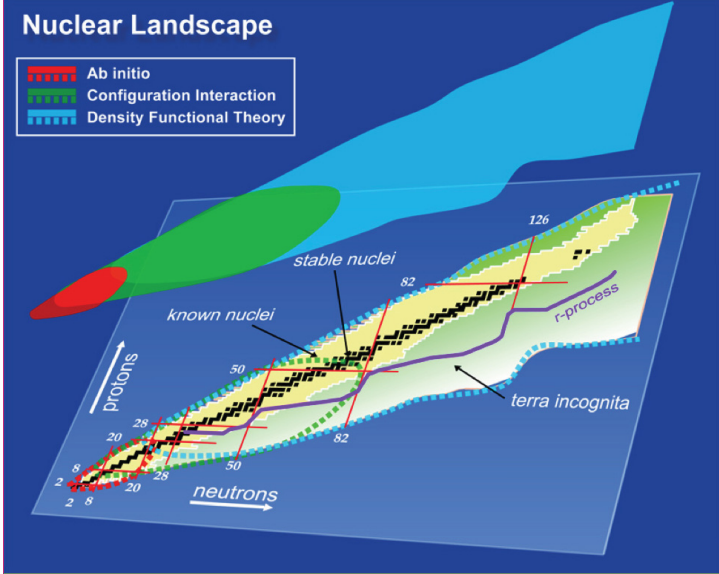


Figure 1.2: A map of the nuclear landscape [1].

1.1.1 Nuclear Interactions

A fundamental component of the nuclear many-body problem is the nuclear interaction itself, and our representation of it. As it will become clear in the next few pages, this representation is not unique. The nuclear interaction can be constructed in a variety of ways, and a majority of the interactions used for nuclear structure calculations are nucleon-nucleon (NN) only potentials – the two-body, NN component of the nuclear potential provides the dominant component to the force. Most of the interactions developed to date also rely upon the experimental description of the NN interaction in terms of phase shifts extracted from NN scattering experiments and the binding energy of the deuteron, the only bound state for two nucleons. These potentials are essentially fits to the data using as much physics as known to develop the operator structure of the interactions. Until recently, methods to produce the interaction based on quark and pion degrees of freedom were completely out of computational reach.

One of the earliest developments to have some success in the description and understanding of the nuclear interaction was due to Hideki Yukawa in the 1930’s with the introduction of meson exchange theory [28]. The idea here was that the properties observed for the

interaction between two nucleons could be described by the exchange of a heavy particle (instead of the exchange of massless photons involved in the electromagnetic force). Applying this idea with the exchange of a single pion leads to a reasonable description of the long range character of the nuclear force. To improve upon this idea and create a more detailed description of the nuclear force, more generalized combinations of meson fields including multiple meson exchanges, as well as the full range of vector, pseudoscalar, pseudovector, and scalar fields, were eventually introduced.

The culmination of this work has been the development of semi-empirical interactions known as phenomenological potentials. The operator structure of these potentials are motivated by meson exchange contributions whose coefficients are carefully fit to minimize error with experimental data (specifically NN scattering data up to about 300 MeV in the lab, where pion production becomes significant) – with as many as 40 adjustable parameters. Examples of these potentials include the work of the Bonn, Nijmegen, and Argonne groups [14, 29, 30]. A coordinate space picture of the central part of these potentials is displayed in Figure 1.3. The primary contributions due to one-pion exchange, two-pion, etc. are pointed out schematically on the plot.

Despite their success in predicting properties of light nuclei, these phenomenological potentials have a number of disadvantages. For example, there is no unambiguous way to gauge the significance of their individual meson exchange terms, or what others may be important. As a result, there are no clear theoretical error bars on the interactions, or a good understanding of the scales at which they are valid. Observing the details of the potentials in Figure 1.3, we can see that they coincide at long distances, but differ significantly at intermediate to short ranges. Nevertheless, each reproduces the NN elastic scattering data and bounds states with high precision. We will see how this flexibility in the potentials can be used to our advantage. At very short distances, where the repulsive core is located, the nucleons are no longer physical degrees of freedom (because of their internal structure). Hence, model dependent effects are introduced by the various potentials. This short-distance core, as we will also see, results in a potential that is difficult to calculate with. Moreover, there is no simple connection to the underlying QCD physics, or a clear method

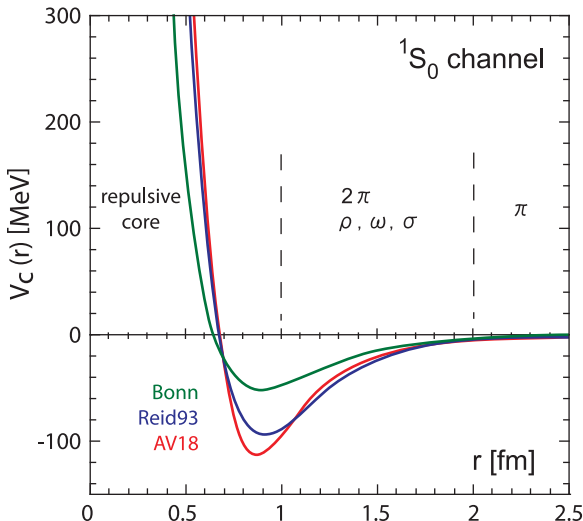


Figure 1.3: Phenomenological potentials which reproduce NN elastic scattering data and bound states [2].

for constructing operators to calculate the effects of interactions with external probes with these types of potentials.

A strategy that addresses many of these drawbacks is known as effective field theory (EFT) [31]. In this approach, all possible combinations of operators that are consistent with the symmetries of the identified low-energy degrees of freedom are written down in an expansion. Put more physically, all possible processes in which the degrees of freedom of the problem interact are accounted for in principle. However, unlike the phenomenological potentials, a “power counting” can be introduced in terms of a small parameter $(Q/\Lambda_b)^n$ for each process. Q is the momentum of the process being considered, Λ_b is the breakdown scale of the theory, and n is the order parameter of the expansion. In principle, the dimensionless coupling constants could be calculated from an underlying theory (QCD in this context) but this is not yet possible for the NN EFT. So in practice the constants in EFT are fit to data too; however, assuming the fit is constrained so that these constants are roughly the same order of magnitude, the result is a systematic and improvable expansion for the interaction with diminishing contributions at increasing values of n . At very low energies and for dilute nuclear systems, a “pionless” EFT can be formulated which simply accounts for contact

interactions between the nucleons. The breakdown scale of the theory, Λ_b , is roughly the energy at which intermediate state contributions from the appearance of the pion becomes significant to the interaction (this is around the mass of the pion, $m_\pi \simeq 140\text{MeV}$).

To reproduce the NN data to the precision of the phenomenological potentials, pion exchange interactions must be accounted for. These appear naturally from the chiral symmetry breaking of QCD, and are incorporated as such in chiral EFT. The breakdown scale of this EFT is roughly that associated with chiral symmetry breaking ($\Lambda_b \sim m_\rho$; the mass of the rho $m_\rho \simeq 770\text{MeV}$). The first several diagrams in chiral EFT for processes contributing to the NN potential and their associated power counting order are illustrated in the left column of Figure 1.4. The largest contribution comes at leading order (LO), then next-to-leading order (NLO), and so on.

Given the systematic construction of the EFT, the coupling of nucleons with external probes can also be incorporated order by order to construct operators which are consistent with the corresponding EFT potential. Thus, matrix elements of these operators can be computed with wave functions to find the electromagnetic form factors of atomic nuclei, for example, or their neutrino interaction cross sections, beta decay rates, etc. Because potentials formulated via chiral EFT have a natural cutoff scale, they have a significantly softer core compared to the phenomenological potentials. This makes them computationally more efficient. However, additional renormalization group techniques, as we will see, can be used to improve the situation further.

Expansions of interactions involving nucleons and mesons are not the only path to creating NN interactions. In principle, an interaction can be produced directly from the experimental data via inverse scattering techniques. This involves finding a direct correspondence between nucleon scattering data and binding energies for light nuclei and a given form of the potential. The J-matrix inverse scattering potential (JISP) is one such interaction that has had recent success [32]. Being a sum of separable terms and derived solely from low energy data, this is a very soft interaction, though it is unclear how to derive additional operators consistent with it. Finally, it is now becoming possible to compute properties of the nuclear interaction directly from QCD utilizing Monte Carlo techniques on the lattice.

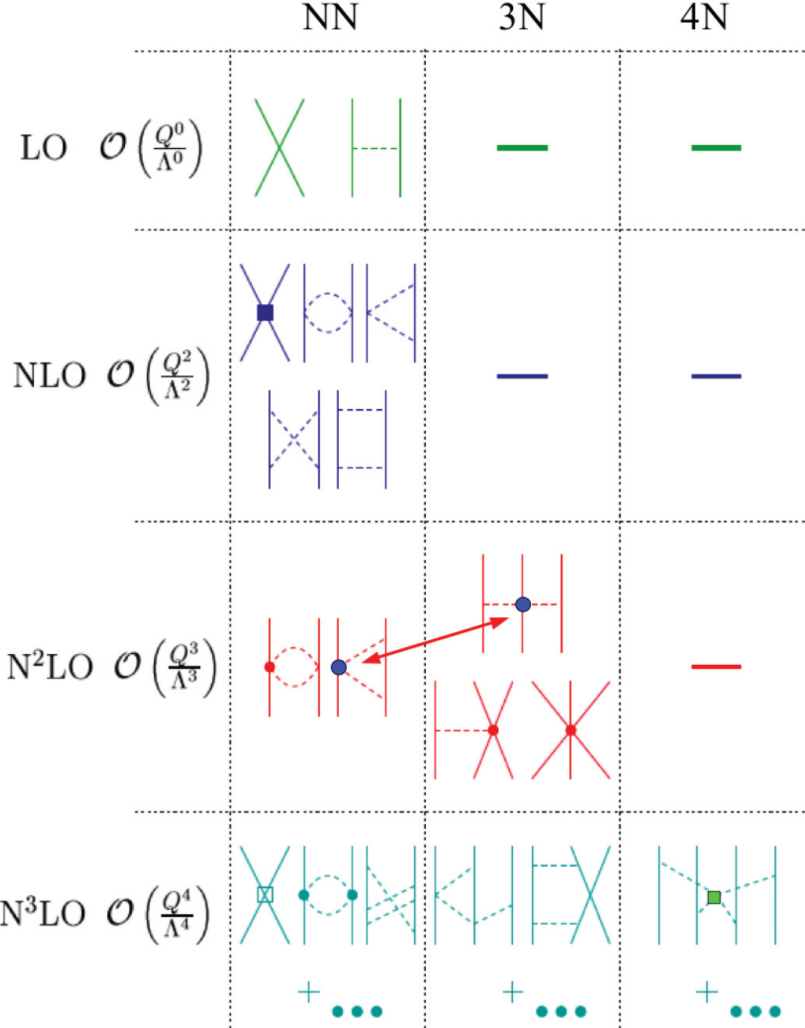


Figure 1.4: Diagrammatic contributions to Chiral EFT [3].

Two such approaches, in fact, are currently being investigated. One approach attempts to calculate the form of the nuclear interaction directly [2, 33]. However, identification of the nucleon fields and consequently the potential is not uniquely defined, which is problematic for providing quantitative guidance for practical potentials. In the other approach, one takes advantage of the framework provided by chiral EFT by calculating processes in lattice QCD that are also calculable with the EFT. These calculations can then be used to directly fix the low energy coupling constants of the EFT (in lieu of the current best fits to nuclear data) and thereby produce the nuclear potential [34, 35]. These methods are still

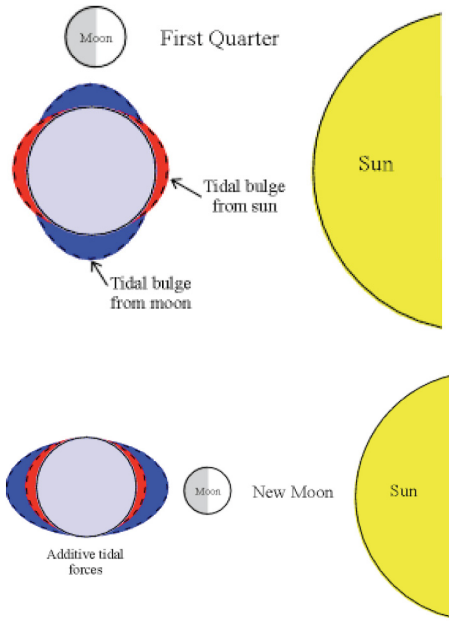


Figure 1.5: Classical system illustrating the need for three-body forces.

in their infancy, and not yet of sufficient precision to make practical calculations of larger nuclei.

Three-body Forces

Most potentials require a three-body component to reach an acceptable level of precision for even the three-particle problem. A three-body force is any force which depends in a non-trivial way on the coordinates of three particles (that is, not just a pairwise sum of two-body potentials). Classically, one might consider this in the context of the Earth-Moon-Sun system, as shown in Figure 1.5. The actual force between the earth and moon, for example, is not given simply by the well known equations of Newtonian gravity. It also depends on the position of the sun relative to them. This is because of the tidal bulge on the earth which alters its mass distribution. So, to treat it as a point particle one must introduce three-body forces. Bringing the analogy back to nuclear physics, nucleons are composite objects too, but of quarks and gluons which have distributions that are affected by the forces from other nucleons. In the context of EFT three-body forces arise from

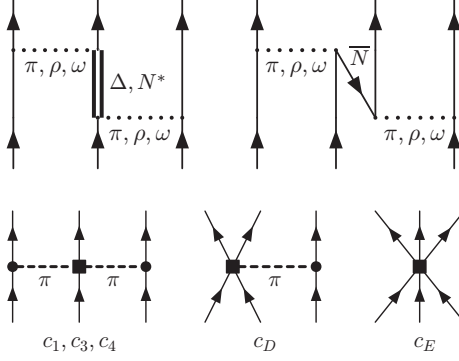


Figure 1.6: Detailed two-body internal processes (top) reduce to three-body interactions in EFT (bottom).

eliminating/decoupling degrees of freedom, excited states of nucleon, relativistic effects, and high-momentum intermediate states. As an example of this, the top row of Figure 1.6 contains diagrams of processes composed of two-body meson exchanges between nucleons. In the bottom row, we see a number of three-body force diagrams which are reduced to chiral EFT with the elimination of the detailed internal degrees of freedom.

A phenomenological implementation of the three-body force has been created for use with the NN potential of the Argonne group [36, 37]. Here the three-body force contributes a significant 1.2 MeV to the overall 8.5 MeV binding energy of the triton, and 6.5 MeV to the 28.3 MeV energy of the alpha particle, etc. In EFT, three-body forces emerge naturally as higher-order contributions to the interaction, providing a clear understanding of their lesser significance relative to the two-body force as observed phenomenologically. In Figure 1.4 we can see the emergence of two-, three-, and four-body forces in the first four orders of the EFT power counting along with a sample of the corresponding diagrams. The contribution to the triton binding energy from the three-body EFT force used in [12] at N^3LO is roughly 1.0 MeV, and around 4.3 MeV for the alpha particle. Whether or not a four-body force is necessary for a sufficiently quantitative description of much heavier nuclei, or higher orders in the EFT expansion are needed remains to be determined.

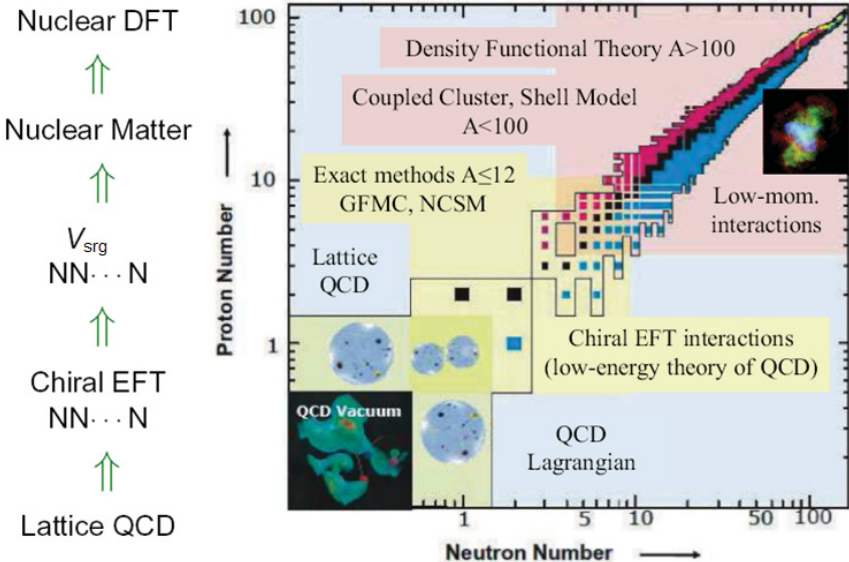


Figure 1.7: Nuclear many-body methods associated with size of system (as a function of nucleon number) to be explored [4].

1.1.2 Many-body Solution Methods

As explained earlier, the bulk of low-energy nuclear physics resides in the non-relativistic regime. At the upper end of energies relevant to the problem, relativistic corrections do begin to grow, but at the level of precision currently accessible these can be largely incorporated as perturbative corrections, if needed. The computational advantages of being able to work in a non-relativistic framework currently far outweigh the gains to be had by working in a relativistic formalism.

Thus, the equation we wish to solve is the Schrödinger Equation,

$$i\hbar \frac{\partial}{\partial t} |\Psi\rangle = \hat{H} |\Psi\rangle, \quad (1.1)$$

such that the Hamiltonian $\hat{H} = \hat{T} + \hat{V}$, where \hat{T} is the kinetic energy, \hat{V} is the potential discussed above, and Ψ is the wave function with quantum numbers corresponding to the system in question. This is the fully time-dependent version of the equation. While the quantum dynamics can be important for understanding the detailed behavior of reactions, or deriving operators to predict the outcome of interactions with a probe, many questions

of low-energy nuclear physics focus on the structure of nuclei, transitions between excited bound states, and in general, time-independent initial and final states separated by some dynamic event. Assuming the appropriate operators have been derived to probe such events, the time-independent states are all we need to calculate expectation values.

As such, our “master equation” is the time-independent Schrödinger Equation:

$$\hat{H} |\Psi\rangle = E |\Psi\rangle. \quad (1.2)$$

This is a matrix eigenvalue problem with wave function vector Ψ , eigenvalue energies E , and Hamiltonian operator \hat{H} which can be represented as a matrix in any basis. Despite the apparent simplicity of this equation, analytic solutions exist for a very limited number of model systems. In practice, the solution is most often approximated numerically and can require a tremendous amount of computational resources for nuclei. Many methods have been developed to address this problem over the years, often optimized for particular systems and properties of the potential. What follows here is short overview of these methods.

This is by no means an exhaustive list of nonrelativistic quantum many-body methods, however it does represent a strong cross section of the many-body methods in wide use and/or under active development at the time of this writing. The computational framework described and further developed in this thesis, known as the Similarity Renormalization Group (SRG)¹, can be applied to a wide variety of these methods. It acts on the representation of the operators used in the quantum formalism, and thereby facilitates the solution of the Schrödinger equation via these many-body methods. Figure 1.7 maps out the regime

¹ The SRG as originally developed by Glazek and Wilson [38] was designed to decouple high- and low-energy degrees of freedom in a Hamiltonian via similarity transformations. As specialized in the Wegner [39] flow equation formalism used in this thesis, the SRG generates a fully unitary transformation via a continuous series of infinitesimal unitary matrix operations. The “renormalization group” nomenclature refers to the fact that the initial coupling strength at high momentum for low-energy states, for example, is suppressed and the coupling at low momentum is consequently altered or “renormalized” to conserve predictions of the theory for the low-energy states. Traditional renormalization group approaches suppress all coupling at high-momentum, effectively eliminating the presence of high-energy states whereas the SRG progressively decouples all states according to a desired decoupling pattern. This is shown schematically in Figure 1.12. As used in this work, the SRG does possess the properties of a mathematical “group”, since it generates unitary transformations; however, the properties of the group structure are not otherwise used explicitly. Alternative formulations of the renormalization group do not necessarily have this property (they may only satisfy the conditions of a semi-group). See also Section 1.2.2 for more information.

with respect to proton and neutron number in which many of the methods and interactions discussed here are applied. Below the diagonal are the various nuclear interactions, and above are some of the solution methods to be discussed. On the left side of the figure is one path to realizing predictions across the length scales of low-energy nuclear physics, and understanding the connections between them. Here we begin with solutions to QCD via the lattice, which can then be used as input to fix the low energy constants of chiral EFT. The potentials derived from the EFT can be further modified by renormalization group (RG) methods, such as the SRG, to generate “low momentum interactions” which are further decoupled from high energy degrees of freedom. These interactions can then be used directly in a variety of few-body solution methods, to be discussed, as well as in the computation of nuclear matter, which offers a chance to constrain nuclear density functional theory (DFT) for predictions of the heaviest nuclei.

We will classify the methods discussed here broadly as either *ab-initio* methods, which given sufficient computational power will converge to the exact answer regardless of the potential used, or perturbative methods, which converge for sufficiently soft potentials. *Ab-initio* methods will be further subdivided into stochastic, basis-expansion, and other methods.

Stochastic Methods

We will regard stochastic methods as those which propose an ansatz for the solution of the wave function Ψ , and then find the best possible solution to Eq. 1.2 via minimization of the eigenvalue E . Essential to these methods is the Ritz variational principle, which states that for an arbitrary function Ψ of the state space the expectation value of \hat{H} in the state Ψ is such that

$$E \equiv \frac{\langle \Psi | \hat{H} | \Psi \rangle}{\langle \Psi | \Psi \rangle} \leq E_1 \quad (1.3)$$

where the equality holds only if Ψ is an eigenstate of \hat{H} with eigenvalue E_1 [40]. E_n are the discrete eigenvalues of Eq. 1.2, ordered such that $E_1 \leq E_2 \leq \dots$. Clearly, these methods are most suited to solving for the ground state of a system. However, they can be modified

to solve for excited states, with added computational cost, by projecting out the states of appropriate quantum number and enforcing the orthogonality of the excited state with the lower energy (previously calculated) states, for example.

One such method is variational Monte Carlo (VMC), which has enjoyed a great deal of success in solutions of the nuclear many-body problem when combined with Green's function Monte Carlo (GFMC) [41, 42]. For VMC, a trial wave function is first constructed with sums and products of two- and three-body correlation operators to pick up the spin, isospin, tensor, spin-orbit, etc. features of the interaction and their couplings in larger systems. The parameters in this expansion of operators are then varied to minimize the energy expectation value E of Eq. 1.3. The Monte Carlo aspect of this method is in the calculation of the multidimensional integral over all particle coordinates for the energy expectation value, which would be impractical by other means. The integration is typically performed in coordinate space via a Metropolis random walk. The minimization of the wave function in this form cannot generally be completed with the precision desired for nuclear structure, particularly for P shell or larger nuclei. To perfect these wave functions, GFMC can be applied. The idea is to project out the lowest-energy eigenstate from the VMC wave function by taking the limit

$$\Psi_1 = \lim_{\tau \rightarrow \infty} \Psi(\tau) = \lim_{\tau \rightarrow \infty} \exp[-(H - E_T)\tau]\Psi, \quad (1.4)$$

where E_T is a trial energy for the eigenstate, via small time steps, $\Delta\tau = \tau/n$, applied so that

$$\Psi(\tau) = \{\exp[-(H - E_T)\Delta\tau]\}^n\Psi \quad (1.5)$$

using Monte Carlo integration. In this way, energy eigenvalues can be reached with 1% – 2% accuracy. These methods have been applied with success up to $A = 12$ nuclei.

The stochastic variational method (SVM) is an alternative method which makes use of an expansion of correlated gaussians [40, 43, 44]. Here, each gaussian in the expansion explicitly correlates all the particles in a given system according to a fixed set of parameters. The expansion is built up by randomly choosing this set of parameters (limited by some

physical constraints) for a group of trial gaussians and then optimizing the wave function expansion by adding the gaussian which produced the most significant improvement in the bound state energy. The advantage of the method is that matrix elements of the gaussian can be calculated very precisely, and often analytically. The method is primarily limited to light nuclei at this time, but very precise results can be obtained for ${}^4\text{He}$, for example.

Other bases, in principle, can be used in attempts at the stochastic solution of nuclear wave functions. Each has its own advantages in the types of correlations that can be accounted for, and the efficiency with which it can be applied. Thus far, little use has been made of stochastic methods with SRG generated interactions due to technical limitations of the Monte Carlo methods with non-local potentials. Possible solutions to this problem, however, are being explored [45] .

Basis-expansion methods

The many-body solution techniques which have thus far enjoyed the most successful use of the SRG are basis-expansion methods. As distinguished here, basis-expansion methods are those which seek to represent the Hamiltonian in a complete and general function basis. These methods are also variational in that the energy eigenvalues derived from them are upper bounds to the true eigenvalue for a given interaction. However, here the method of solution differs in that it typically involves a direct diagonalization of the Hamiltonian matrix in the given function basis. The resulting eigenvalues and eigenfunctions are our energies and wave functions. In principle, all states can be derived in this way, but in practice, the first several bound states and corresponding wave functions are found via Lanczos, or similar algorithms for computational efficiency. Moreover, as the basis size is increased the computed eigenvalues systematically approach their true values.

One of the more popular bases to be used is the orthogonal set of harmonic oscillator potential wave function solutions to the one-particle Schrödinger equation. For systems with more than one-particle, the individual particles can be thought of having some probability for existing in various combinations of oscillator excitation states. The many-particle basis states can be built up systematically by including appropriately symmetrized products of all

possible combinations of oscillator excitations and angular momentum states (i.e., quantum numbers). In practice, the basis is then truncated according to the total number of oscillator excitations or an upper limit for single particle oscillations, and matrix elements between these basis states are calculated for the Hamiltonian to be diagonalized.

Some of the more successful incarnations of this method are known as the No Core Full Configuration (NCFC), and/or No Core Shell Model (NCSM) approaches [46, 47]. In current terminology, these methods are distinguished by the fact that NCSM used a basis dependent unitary transformation of the interaction to improve convergence of the many-body calculation, whereas the NCFC does not. However, this nomenclature is not strictly observed, and the terms are often used interchangeably. These methods can use either a single-particle basis for the system coordinates, or Jacobi coordinates. The trade off between these two sets of coordinates that the Jacobi basis can make use of a significantly smaller total basis size, and thereby require less computer memory, etc., but the procedure to symmetrize the basis functions is difficult. The single-particle basis allows one to take advantage of fast numerical Slater determinant routines to calculate matrix elements with symmetrized states, but the result is many more states. At this time, the single-particle coordinates have the edge for large systems, as they can be easily parallelized on a distributed supercomputer. But for SRG evolution, for example, the smaller matrices can be worth the added difficulty of symmetrization, and can subsequently be transformed to the single-particle basis. Advantages can be found in different choices of the angular momentum coupling scheme too. Also, we note that the truncation of the NCFC/NCSM bases ensures factorization of center-of-mass contributions to the calculation.

While these methods are conveniently systematic in their approximation to the solution, the bases built in this way grow exponentially, as plotted in Figure 1.8 for various nuclei. To give some perspective, the biggest matrix dimension that can be dealt with on today's supercomputers is limited to about 10 billion. This only results in well converged answers for lighter nuclei with about $A \lesssim 12$, depending on the interaction. This is where the SRG can be of great benefit, as we will see. A one-dimensional model in a harmonic oscillator single-particle and Jacobi coordinate basis is used in much of this thesis as a test bed for

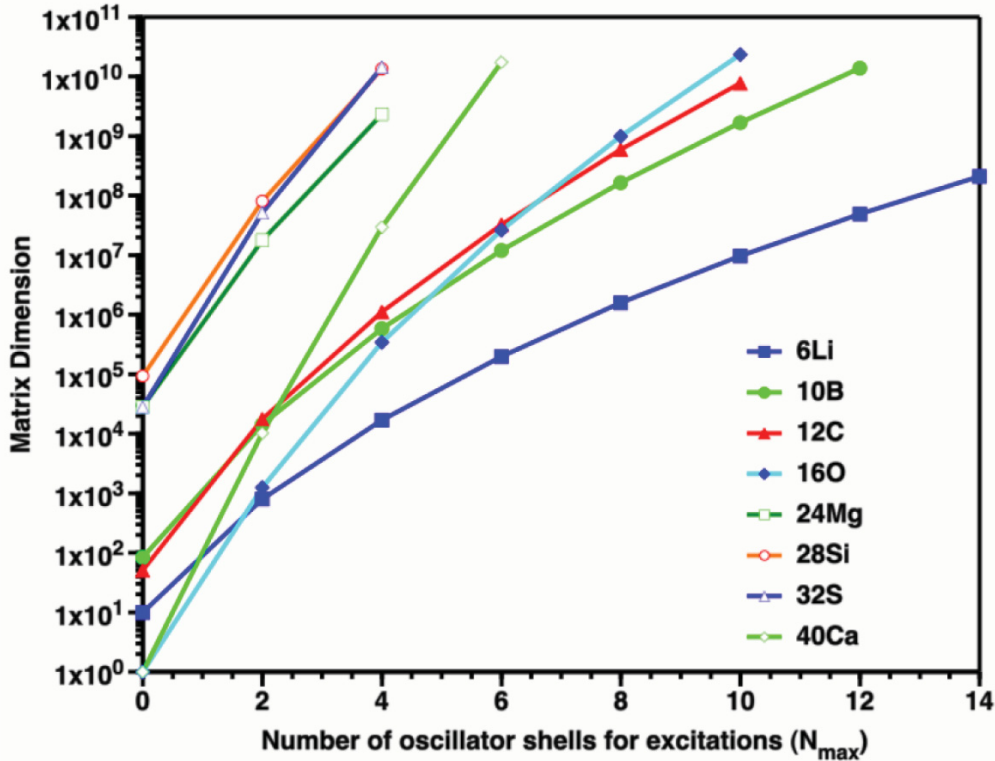


Figure 1.8: Exponential growth of matrix size in CI methods [5].

SRG results in the full three-dimensional system.

It should be pointed out that development of the nuclear shell model provided the basis for the NCFC/NCSM approach. In the nuclear shell model, nucleons are viewed as filling up “shells” of the nucleus according to their angular momentum, each with a limited number of available states. Shell model methods use strongly bound nuclei (or “closed shell” nuclei) as an additional degree of freedom in the calculation [48]. Here, an effective interaction between the nucleon and the closed shell core must be derived in a way which may not be a systematic extension of the inter-nucleon interactions. The advantage of this method is that much larger nuclei can be calculated where the closed shell core is a good approximation, as the inclusion of the core significantly reduces the degrees of freedom in the problem. While it is not strictly an *ab-initio* method, however, in the limit where the only explicit degrees of freedom are protons and neutrons, it reduces to the NCFC/NCSM approach.

In addition to harmonic oscillators, other basis expansions can be utilized in an at-

tempted to get faster convergence to the full hamiltonian. Variations making use of hyperspherical harmonics have been used with success for light nuclei [43, 49], and even nonorthogonal gaussians can be used to produce a complete basis (this is common in quantum chemistry). As elements in the basis-expansion methods can be considered to be composed of various configurations of particles, they are broadly referred to as configuration interaction (CI) methods as well.

Rather than attempting to diagonalize a typical CI matrix directly, one can also rewrite the Schrödinger equation in terms of all possible arrangements of particles into what are known as the Faddeev-Yakubovsky equations and then expand them into a discretized momentum (or coordinate) basis [50, 51]. The bound state arrangements for $A = 3, 4, \dots$ particles can be written as sets of integral equations in which the bound state poles can be solved for numerically. Using these eigenvalues, the wave functions can then be reconstructed. This formalism has been used for very precise calculations of $A \leq 4$ nuclei and is currently limited by the size of the momentum mesh needed. Recently, the SRG has been adapted to this formalism for the first three-particle momentum space SRG evolutions of an interaction [52].

Other *Ab-initio* Methods

A number of many-body methods do not fall neatly into the categories defined above. The Coupled-cluster approach to nuclear physics is one such method [53, 54]. It takes advantage of the cluster expansion of the many-body wave function into correlation operators which account for excitations of the many-body state around a reference state. The solutions found are not bounded below by the exact energy, but the expansion approaches the exact solution for an A -body system in the limit where A clusters are included. The method is limited in practice due to the truncation of the cluster expansion and the basis used for the calculation. It has been particularly successful for nuclei up to the size of calcium that are close to a closed shell nucleus.

Monte Carlo lattice methods, similar to those used in the calculation of QCD on the lattice, have recently begun to make progress in nuclear physics using proton and neutron

degrees of freedom with chiral EFT interactions [55, 56]. These calculations take advantage of the path integral formulation of quantum mechanics to sample particle configuration on a lattice which can be used to measure observables for the given system.

Finally, DFT offers a way to explore nuclei over the whole range of mass scales, particularly those at the heavy end [57]. In this formalism, nucleons are treated as independent quasi-particles. It is based on theorems which demonstrate the existence of a universal energy functional which can, in principle, be exact for a many-body system [58]. However, in practice, this universal functional has not yet been derived from explicit nuclear interactions of the type discussed above. Instead, nuclear correlations are included in a phenomenological way and the functionals are fit to sets of known nuclear data. This is then used to predict unknown properties of the nuclei. Unfortunately, while the method predicts known nuclei with high precision, the errors for extrapolations are not well understood, but work is in progress to resolve these issues.

Perturbative Approaches

Many perturbative techniques can also be utilized to approximate the solution of the Schrödinger equation, and are broadly known as many-body perturbation theory (MBPT). They enjoy a long history in the study of nuclear physics, and the literature on the subject is extensive [59–63]. Whether or not these techniques converge systematically to the exact answer at all is highly dependent on the form of the interaction (in contrast to the methods described earlier where it is only the *rate* of convergence which is affected). MBPT calculations can be performed in a first or second quantized quantum formalism. The calculation of nuclear matter, for example can be more efficient in a second quantized basis, where we are not constrained by a finite system size. Otherwise, the calculation is often performed in a finite basis, such as what would be used in the basis-expansion methods discussed above.

The strategy of the MBPT calculations is generally to perform an approximate mean-field calculation of the system in question, and then to refine the solution via the addition of perturbative corrections which involve summing over increasing numbers of intermediate

exited basis states. This first order approximation is typically Hartree-Fock (HF), which is the best possible approximation to the fully interacting state with a single slater determinant state in the given basis. This state only accounts for correlations due to symmetrization, and otherwise treats the nucleons as independent particles moving about in a “mean field” due to all of the interactions. Modifications of the initial HF approximation can be made to pick up additional correlations, such as in Hartree-Fock-Bogoliubov (HFB), which treats paired excitations of particles as quasi-particles in a new basis. It thereby incorporates the contributions due to nucleon pairing into the mean-field picture.

These methods cannot typically approach the level of precision and control found in most of the *ab-initio* methods discussed earlier. However, given the difficulty in performing those calculations with atomic nuclei, perturbative methods along with DFT, currently hold the most promise for calculating properties of very heavy nuclei.

1.2 The SRG Approach to Nuclear Physics

As we have seen, a variety of nuclear interactions have been created which can reproduce basic few-body nuclear data. And, there are many methods which have been devised to make use of these interactions in an effort to solve the nuclear many-body problem. But it is clear from Figure 1.8, for example, that these methods still require an enormous amount of computational power. The ability to calculate properties of anything but the lightest nuclei is still out of reach with present-day capabilities. One approach to mitigate this problem, which can utilize any of the interactions discussed here and be used to advantage with a wide variety of the many-body solution techniques, is known as the SRG. We now turn our attention to this approach, which is central to the research presented in this thesis.

1.2.1 Resolution and Coupled Scales

A major source of the difficulty that we face can be traced back to the form of the nuclear interaction itself. To illustrate this point, we will make a brief digression on the subject of resolution, and its relation to the nuclear potential.

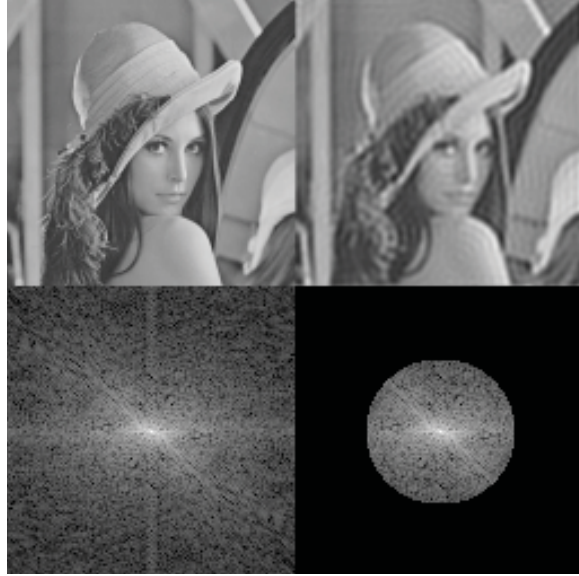


Figure 1.9: High resolution image (top left) with fourier transform (bottom left) compared low resolution image (top right) generated by the application of a low pass filter in the conjugate space (bottom right) [6].

Consider the picture in of the woman in the top left corner of Figure 1.9. This is a high resolution image which makes it possible to see short distance details such as the texture of her hair and fabric in her hat. These details are unimportant, however, to understanding the more significant pieces of information contained within the image, such as the identity of the woman and what kind of hat and hair style she is wearing. These are long distance details which have no real dependence on the fine grained textures in the image. So, there are a number of strategies we could adopt to greatly reduce the computer storage space and processing time needed for the image, without distorting the main “message.” We could, for example, adopt an algorithm whereby we average the adjacent pixels to extrapolate a lower resolution image. But for the purposes of this discussion, we will associate the resolution with the Fourier transform space of the image. From the Fourier transform space, the image can be reconstructed by a superposition of waves whose wavelength determines the finest details which can be resolved. An algorithm to lower the resolution of the image from this point of view would thus involve truncating the short wavelength modes of the Fourier transform space (simply, we need to apply a low-pass filter). This is illustrated in Figure

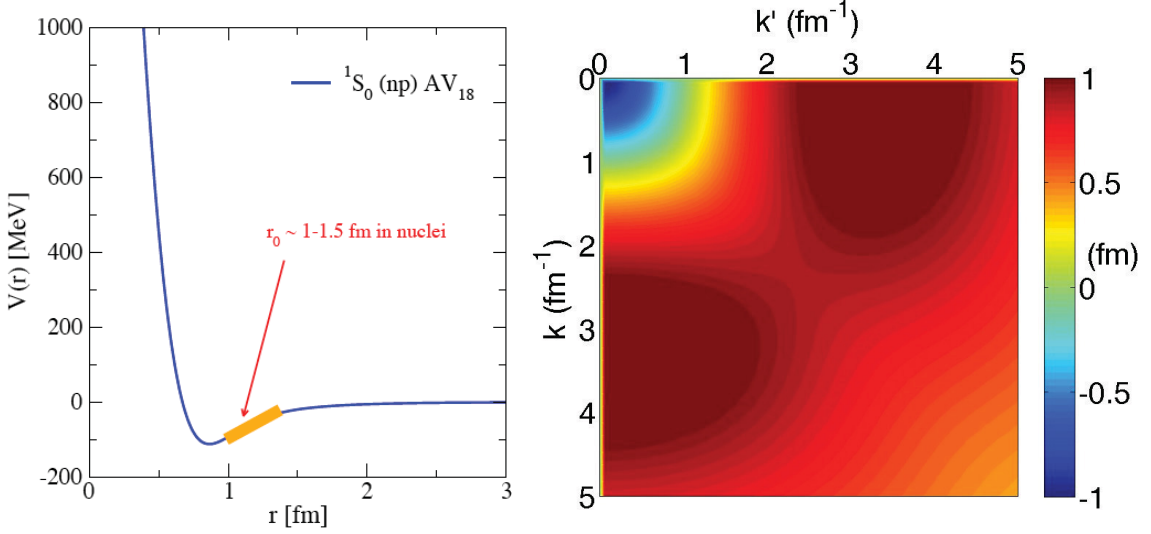


Figure 1.10: 1S_0 partial wave of the AV18 potential in coordinate space (left) and momentum space (right).

1.9. In the lower left hand corner we have a picture of the conjugate space (axis run through the center of the image). In the lower right hand corner we have truncated the outlying wavelengths, and reconstructed the image in the upper right corner. Clearly, the woman's identity, her hair style, and the hat she is wearing are still recognizable. The fine textures are no longer visible, but the long-wavelength information is preserved, and the image is easier to work with on a computer.

The resolution of the nuclear potential can be viewed in an analogous manner. Consider the coordinate space image of the 1S_0 partial wave of the Argonne v_{18} (AV18) potential (a modern phenomenological potential) on the left side of Figure 1.10 [14]. The form of the interaction at distances $\gtrsim 2 \text{ fm}$ can be attributed to one-pion exchange, and at $\approx 1 - 2 \text{ fm}$ to two-pion exchange and other mesons, as discussed earlier. But the hard core is present at resolution scale smaller than the radius of the nucleons ($\approx 1 \text{ fm}$), and thus probes what one would expect to be quark and gluon degrees of freedom. The right side of Figure 1.10 is the Fourier transformed image of the potential analogous to the lower right corner of image in Figure 1.9. This is a matrix in momentum space, and the hard core is manifested by the strong coupling between the high and low momentum modes (the short and long

wavelength modes, respectively). This potential attempts to represent the interaction at a much higher scale than the typical scale expected in a nucleus, as given by the Fermi momentum around 1 fm^{-1} , or $\approx 200\text{ MeV}$. Large non-zero matrix elements are also present at scales much greater than the data that the potential is fit to, which is up to around 300 MeV .

It is this “extra” coupling that is the source of much difficulty computing with modern nuclear interactions. Although chiral EFT typically has a lower cutoff than AV18, the issue remains. Qualitatively, the hard core leads to poor results for the mean field approaches with perturbation theory because the interaction changes drastically at different scales. Moreover, the amount of short wavelength information present in the potential requires a large basis expansion not only in momentum space, but in other bases typical of nuclear solution methods, such as harmonic oscillators. None of the nuclei in Figure 1.8 are well converged for the matrix dimensions and N_{\max} shown, for example.

As a result, our naive hope would be that we can apply low pass filter to the potential in analogy to the resolution lowering procedure illustrated for the image in Figure 1.9. So, to retain as much of the low-energy information that we might expect to need as possible, we try setting high momentum ($k \geq 2\text{ fm}^{-1}$) matrix elements to zero and observe the effect on low-energy observables.

This is illustrated in Figure 1.11. On the left side we have the truncated potential. On the right right side, we reproduce the NN phase shifts produced by the potential as representative observables (it is the phase shift scattering data to which the potentials are fit). The original, phase shifts from the original untruncated potential are shown by the solid. After applying the low pass filter, however, we have the dashed curved.

Thus, the filter appears to fail, as the original phase shift information is lost. If we look carefully, though, the problem lies in the original coupling of high and low momentum degrees of freedom. If we had a way to systematically decouple these degrees of freedom first, then the truncation could be carried out as originally intended. The SRG provides such a method.

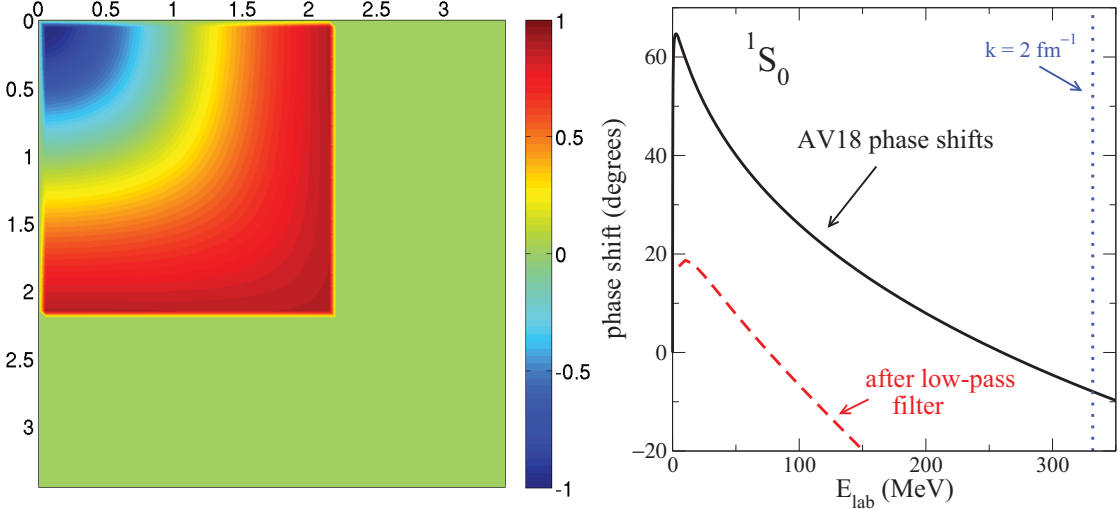


Figure 1.11: Low pass filter applied to 1S_0 partial wave of AV18. The truncated potential is shown to the left. To the right is the original phase shift plot (solid line) compared to phase shifts from the truncated potential (dashed line).

1.2.2 SRG Formalism and Decoupling

There are actually a number of RG methods which have been developed to decouple the degrees of freedom in the potential, thereby softening interactions in nuclear systems and thus extending the range of many computational methods discussed and qualitatively improving their convergence patterns. An older approach, generates what are broadly referred to as “ $V_{\text{low } k}$ ” potentials in low-energy nuclear physics [64, 65]. This approach is illustrated schematically on the left side of Figure 1.12. Here, an cutoff Λ in momentum space is lowered in small steps by requiring invariance of a quantity such as the on-shell T-matrix.

The SRG, on the other hand, provides a means to evolve any given Hamiltonian towards a diagonal form. This is illustrated on the right side of Figure 1.12. The SRG was originally developed by Glazek and Wilson, and independently by Wegner, for applications to QCD and condensed matter physics [38, 39, 66–68]. It was only recently noticed that it would be useful in the low-energy nuclear physics problem, and it has enjoyed a great deal of success since then [7, 18, 65, 69]. Here, the decoupling scale is given roughly by the width of the diagonalization, λ , in contrast to the strong momentum cutoff. The SRG is also a fully

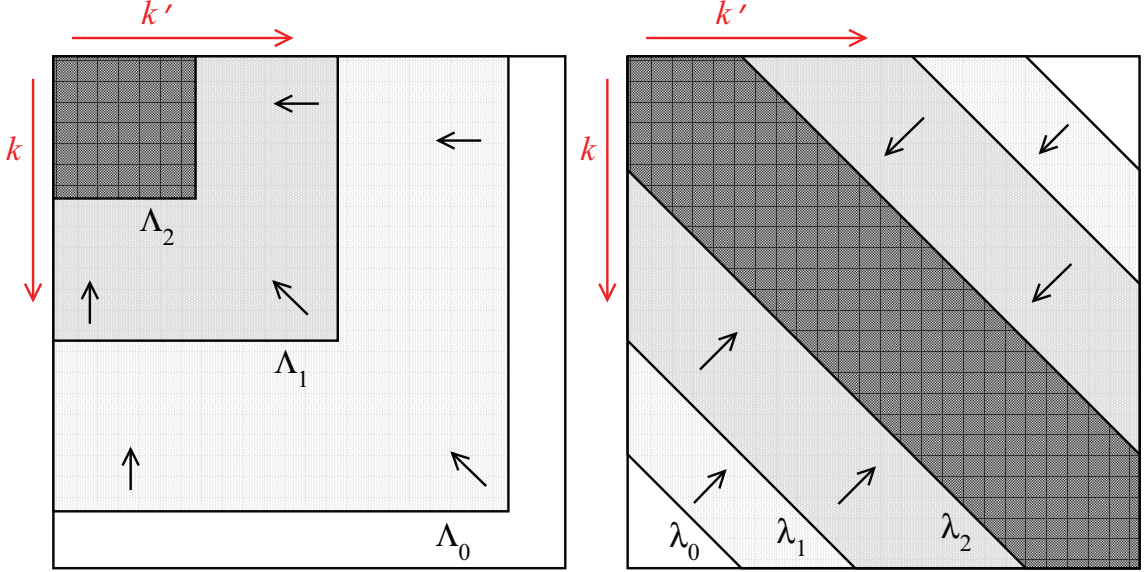


Figure 1.12: Schematic of $V_{\text{low } k}$ transformation on the left, and SRG evolution on the right [7].

unitary transformation (prior to truncation of the potential), which makes it well suited to the calculation of other operators. $V_{\text{low } k}$ potentials can also be produced via a unitary transformation; however, the technical implementation of the SRG is simpler, and critically, the SRG accounts for the many-body evolution of operators in a straightforward way, as we will see.

The SRG does this by systematically evolving Hamiltonians via a continuous series of unitary transformations chosen to decouple the high- and low-energy matrix elements of a given interaction [11, 70]. In particular, a flow equation with parameter s and generator $\eta_s \equiv [G_s, H_s]$,

$$\frac{dH_s}{ds} = [\eta_s, H_s] , \quad (1.6)$$

unitarily evolves an initial Hamiltonian $H_{s=0} \equiv H = T_{\text{rel}} + V$. Choosing the flow operator G_s specifies the SRG evolution. This equation implements the unitary transformation

$$H_s = U_s H_{s=0} U_s^\dagger = T_{\text{rel}} + V_s , \quad (1.7)$$

which defines V_s by choosing the relative kinetic energy to be invariant, and where the

generator η_s is related to U_s by

$$\eta_s = \frac{dU_s}{ds} U_s^\dagger = -\eta_s^\dagger. \quad (1.8)$$

As in most previous nuclear applications, we take $G_s = T_{\text{rel}}$ to suppress off-diagonal elements of the Hamiltonian in momentum space, unless otherwise specified (see Chapter 4 for a discussion of alternative choices). As can be seen now, one of the major technical advantages of the SRG relative to other energy-independent RG methods is that the Hamiltonian flow equation is formulated solely in terms of the evolving Hamiltonian and does not involve the T-matrix, which avoids issues with solving equations in multiple channels and allows any convenient basis to be used.

Projecting the SRG flow equation into a partial wave momentum basis with $\hbar = M = 1$ yields

$$\begin{aligned} \frac{dV_s(k, k')}{ds} &= -(k^2 - k'^2)^2 V_s(k, k') \\ &\quad + \frac{2}{\pi} \int_0^\infty q^2 dq (k^2 + k'^2 - 2q^2) V_s(k, q) V_s(q, k'), \end{aligned} \quad (1.9)$$

where a convenient evolution and decoupling parameter is given by $\lambda = 1/s^{1/4} \text{ fm}^{-1}$ (to be explained shortly). We thus evolve from $\lambda = \infty$ in principle, to some smaller value of λ . The evolution which results from this is plotted in Figure 1.13 for the AV18 1S_0 partial wave. On the left side of the figure, two-dimensional contour plots represent the potential matrix; on the right side three-dimensional surfaces plots of the corresponding matrices help emphasize the features of the evolution. On top is the potential prior to evolution; on the bottom is the potential after evolution to $\lambda = 2 \text{ fm}^{-1}$. The off-diagonal elements of the potential are clearly suppressed after evolution, with the width of the diagonal being given roughly by $\lambda = 2 \text{ fm}^{-1}$.

The decoupling seen in Figure 1.13 is readily understood from the SRG flow equations. Because of the dominance of the kinetic energy, Eq. (1.9) for sufficiently off-diagonal k and k' is given to good approximation by

$$\frac{dV_s(k, k')}{ds} \approx -(k^2 - k'^2)^2 V_s(k, k'), \quad (1.10)$$

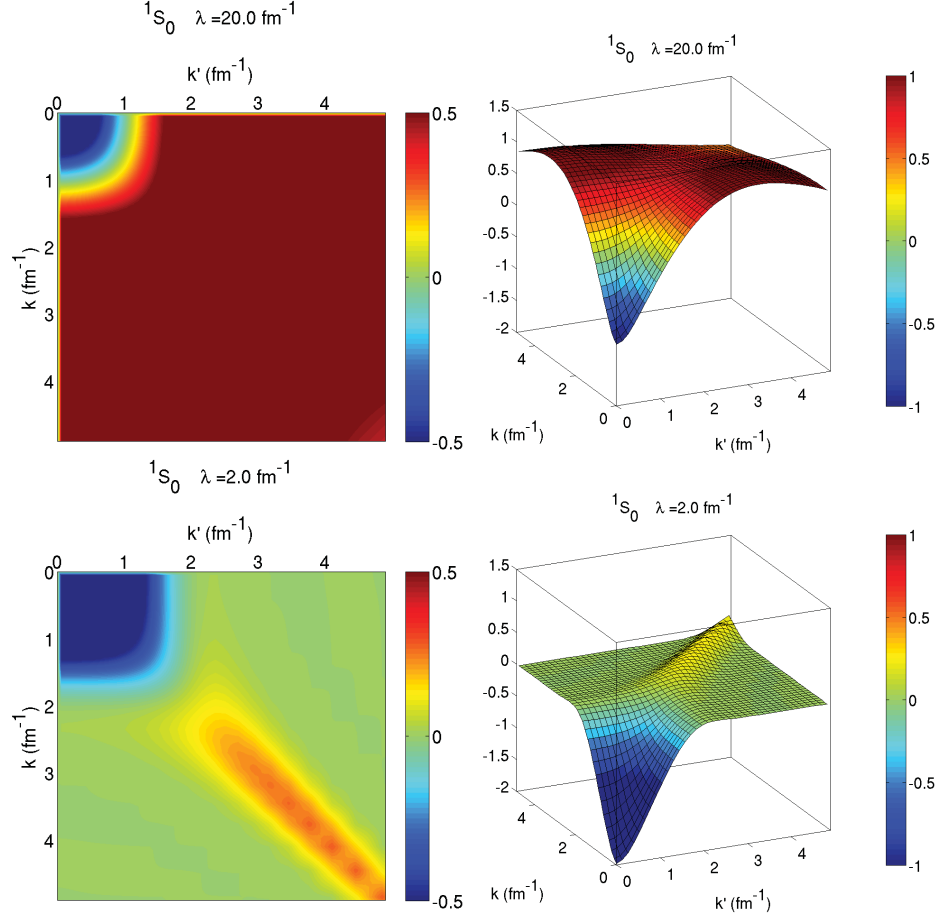


Figure 1.13: Evolution of 1S_0 partial wave of AV18 shown on top (at $\lambda = 20 \text{ fm}^{-1}$ the potential is effectively unevolved) to $\lambda = 2 \text{ fm}^{-1}$ as shown on bottom. The left and right images are two different perspectives of the same matrices.

which, when solved, predicts

$$V_s(k, k') \approx e^{-s(k^2 - k'^2)^2} V_{s=0}(k, k') = e^{-\frac{(k^2 - k'^2)^2}{\lambda^4}} V_{\lambda=\infty}(k, k') . \quad (1.11)$$

Thus, using this generator we can see that the far off-diagonal elements of the potential matrix are suppressed exponentially with an approximate width given by the flow parameter λ [69]. (If the potential is plotted as a function of k^2 , the width of the partially diagonalized potential is clearly seen to be well approximated by λ^2 [65].) While it is not obvious from the figure, the potential is also very smooth.

With the AV18 potential thus evolved, we may now return to our attempted truncation

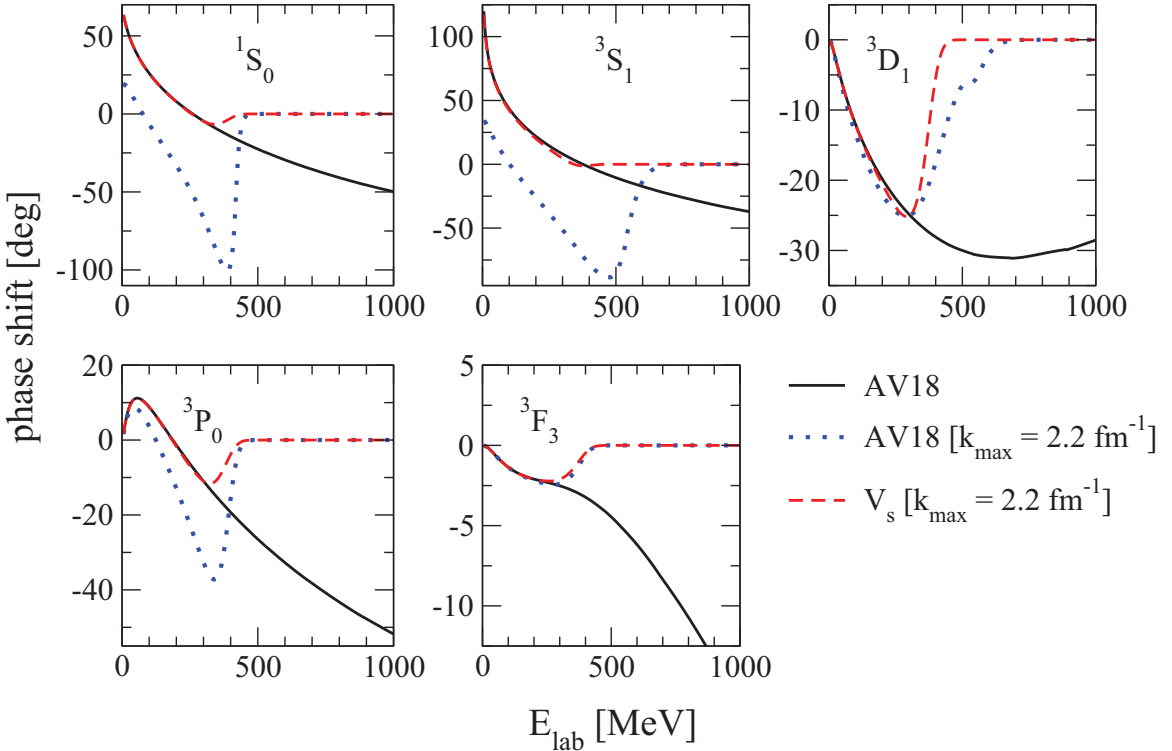


Figure 1.14: Phase shifts in a number of AV18 partial wave momentum channels. The original phase shifts in each channel are give by the solid lines. The dashed and dotted lines are calculated from potentials whose matrix elements for which $k, k' > k_{\text{max}} = 2.2 \text{ fm}^{-1}$ have been excluded. The dotted result from truncation of the matrix with no RG evolution. The dashed lines result from an SRG evolved potential to $\lambda = 2 \text{ fm}^{-1}$ [8].

of the potential and analysis of the subsequent phase shift observables. The coupling of the high- and low-energy matrix elements in the evolved potential have been significantly suppressed. So now, setting $V_s(k, k') = 0$ for $k, k' > k_{\text{max}}$ the phase shifts are very well reproduced nearly all the way up to the point of truncation at k_{max} . This is illustrated for a variety of AV18 partial waves in Figure 1.14. Here we can the effect of truncating the potential without an RG transformation (dotted lines) versus the effect of truncation with SRG evolution (dashed line). The SRG appears to be a success when used with a low-pass filter! It should be pointed out that without truncating the potential, the phase shifts of the SRG evolved potential match the original (solid) curves exactly, because it is simply a unitary transformation.

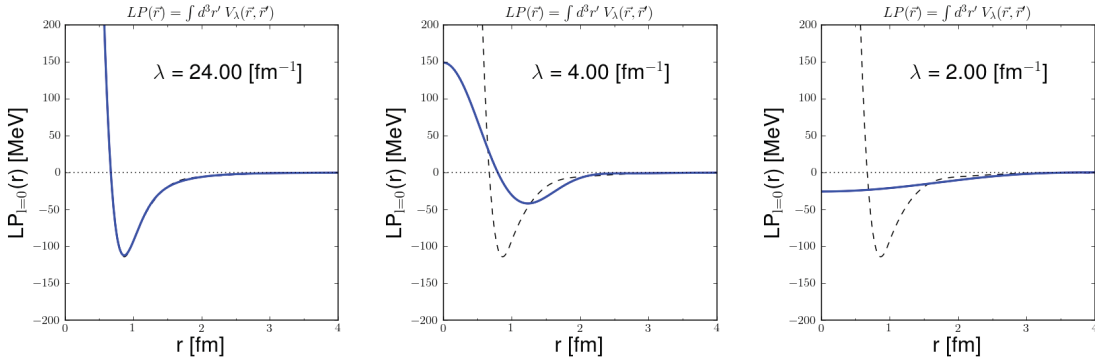


Figure 1.15: Evolution of local projection for 1S_0 partial wave of AV18 (solid line) compared to original local potential (dashed line) [9]

Before reviewing results of the SRG in calculations of light nuclei, it is worthwhile to return to the coordinate space picture of the SRG evolved potential [45]. Here we can see the effect of decoupling high- and low-energy matrix elements on the hard core of the original potential. The potentials are no longer local in coordinate space after the evolution, so we cannot simply Fourier transform the potential again. Instead, we can approximate the coordinate space evolution by taking the local projection of the potential, given by

$$LP(\mathbf{r}) = \int d\mathbf{r}' V_\lambda(\mathbf{r}, \mathbf{r}'). \quad (1.12)$$

This projection leaves the potential unchanged if it is already local. In Figure 1.15 we see the evolution of the AV18 1S_0 local projection. By $\lambda = 2 \text{ fm}^{-1}$, the effect of the suppressing the off-diagonal coupling is also to completely suppress the hard core. It is not hard to see that the resulting interaction is easier to represent, and significantly more perturbative. Now that potential is more consistent across length scales, a mean field solution can produce much better results. An explicit test of the increasing “perturbativeness” of the potential may be found in its Weinberg eigenvalues [7, 71]. The non-locality of the evolved potentials also creates a technical problem for some many-body methods, as mentioned earlier. The local projection even offers a potential way to resolve this problem by approximating the potential to a sufficient degree that the effects of the residual potential might be calculated adequately using perturbation theory.

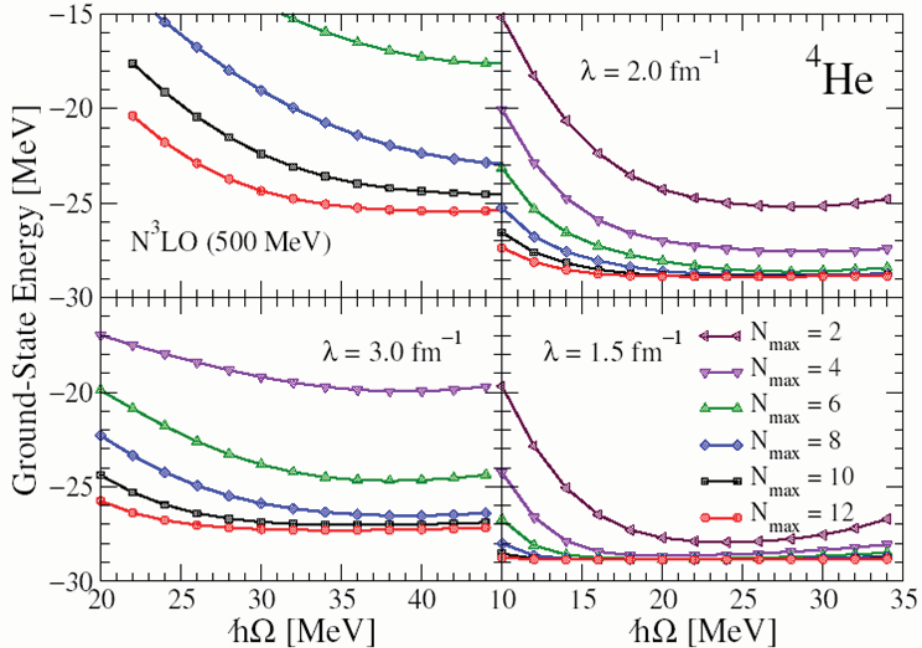


Figure 1.16: Improved convergence of ^4He in NCSM calculation with respect to oscillator basis parameters for selected values of two-body SRG evolution λ of a chiral EFT potential. The top left frame is unevolved [10].

1.2.3 Improved Convergence of Nuclear Few-body Calculations

The decoupling we have seen, and associated suppression of the hard core, leads to greatly improved convergence of the binding energy in few and many-body calculations [10, 12, 70, 72]. One strategy to make use of this is to put the original potential in a basis of sufficient size to pick up as much information as possible about the potential for the number of particles that the space represents (for example, phase shifts and binding energies for two-particle systems, three-particle systems, etc., as needed). We can then evolve this potential via the SRG to decouple the high- and low-energy degrees of freedom and subsequently truncate the basis for use in calculations of larger systems.

A simple example of this of this is shown in Figure 1.16 for evolution of the two-body only nuclear potential [10]. In this example, and many of the few-body calculations shown here, the chiral EFT 500 MeV $N^3\text{LO}$ interaction (500 MeV refers to the cutoff scale of the EFT and $N^3\text{LO}$ refers to the fourth order in the EFT expansion) has been utilized

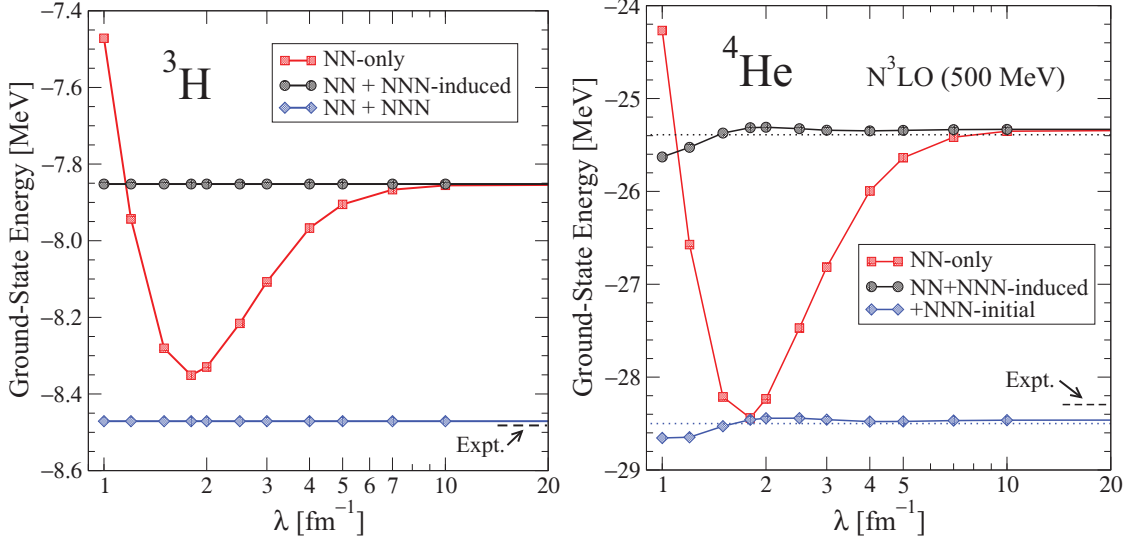


Figure 1.17: Ground state energy for various many-body contributions to ^3H (left) using $N_{\max} = 36$ and $\hbar\Omega = 28$ MeV, and ^4He (right) using $N_{\max} = 28$ and $\hbar\Omega = 36$ MeV for the evolution and truncating to $N_{\max} = 18$ for the calculation [11].

[15]. The calculations of ^4He shown here were performed with the NCSM method at a variety of different basis sizes N_{\max} (post evolution and truncation) and basis optimization parameters $\hbar\Omega$. A converged calculation is one indicated by the minima of two successive curves of increasing basis size closely matching one another within the desired tolerances of the calculated. In the top left frame of the figure we see that there is little convergence in the basis sizes used. In the other frames, however, we see that the calculation begins to approach convergence for the largest basis sizes even at $\lambda = 3$ fm $^{-1}$. By $\lambda = 1.5$ fm $^{-1}$, all but the smallest basis are sufficient to get good convergence in the binding energy (most of the curves are on top of one another).

It should be noted here that while the SRG affords better convergence of many-body calculations in a significantly smaller basis, the rapid growth of the basis for many of the solution techniques is still a problem, and can even impose limits on the SRG evolution in a few-particle basis. Solutions to this problem are being explored [73].

1.2.4 Hierarchy of Many-Body Forces

Also, before considering the improvement of convergence further, we must take note of the fact that while we see that convergence is much easier to reach in Figure 1.16, the converged value appears to change for different values of λ . This is indeed the case. Recall the discussion earlier in this chapter on the importance of many-body forces in the initial nuclear interaction. Just as many-body forces arise in the EFT formalism from the elimination of available degrees of freedom, so too does this occur when applying the SRG. Here, we have suppressed the intermediate degrees of freedom.

In addition to this rather qualitative observation, a significant advantage of the SRG is that many-body forces arise naturally in the flow equation formalism. Later, we will see how this can be taken advantage of in explicit calculations. But for now, observe the flow equation for the potential in a schematic, second-quantized representation:

$$\frac{dV_s}{ds} = \left[\left[\sum_{G_s} \underbrace{a^\dagger a}_{\text{2-body}}, \sum_{\text{2-body}} \underbrace{a^\dagger a^\dagger aa}_{\text{2-body}} \right], \sum_{\text{2-body}} \underbrace{a^\dagger a^\dagger aa}_{\text{2-body}} \right] = \cdots + \sum_{\text{3-body!}} \underbrace{a^\dagger a^\dagger a^\dagger aaa}_{\text{3-body!}} + \cdots \quad (1.13)$$

where the a 's and a^\dagger 's are annihilation and creation operators in a single particle basis with respect to some reference state (which is the vacuum in this work). The number of a 's and a^\dagger 's indicate whether the term contributes to the two-body, three-body, etc. force as shown. Thus, one can see that by expanding the commutators as shown and iterating over all the steps in the differential equation, many-body forces will be generated to all orders.

This could be a disaster for the SRG, as including all induced many-body forces in an A-body calculation (that would be all many-body forces $\leq A$) is technically difficult, and would negate the other benefits of the evolution. If there is a hierarchy of many-body forces, however, where the $(n+1)$ -body force is significantly smaller than the n -body force, then the method is saved. This, in fact, appears to be the case, although a formal justification for the hierarchy has yet to be discovered. Qualitatively, if the decoupling scale of the SRG is of natural size for the nuclear force (so that low-energy nuclear states are insensitive to the short distance details left out), then the original chiral EFT hierarchy of forces should be maintained. Thus, the hierarchy of forces simply becomes another element of the SRG

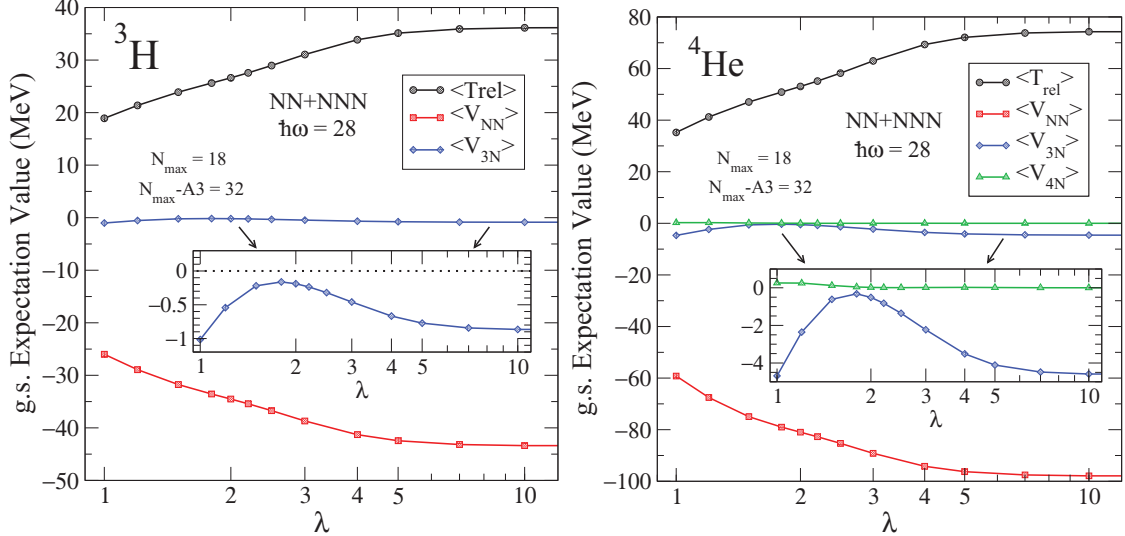


Figure 1.18: Individual expectation values of contributions to the ground state energies of ^3H (left) and ^4He (right) [12]. A hierarchy of many-body force effects is apparent.

basis truncation scheme. Most of the calculations performed to date seem to indicate that 3-body forces, or potentially 4-body forces (not yet implemented), are sufficient for the precision needed in nuclear calculations. But this is still an open topic [74].

At the very least, these many-body contributions can be probed empirically via expectation values of a given system to make the hierarchy manifest. As such, in Figure 1.17, we can analyze the effect of SRG evolution on the binding energy for the triton and ^4He . Each is plotted as a function of SRG evolution λ . The NN-only curves indicate the evolved potential was truncated at the 2-body level. NN+NNN-induced signifies that the two-body only piece of the EFT was evolved and truncated at the three-body level. Otherwise, the initial two- and three-body force were included and evolved up to the three-body level. Comparing the NN-only curves the NN+NNN-induced makes clear the changes due to the SRG. In the triton, the curves which include the induced three-body force are flat because the evolution is completely unitary in this basis. For ^4He , those curves vary somewhat due to the lack of induced four-body forces. The amount of change is much smaller than for the NN-only curves, however, thus indicating a hierarchy. The effect of the initial three-body force is to bring the predictions closer to experiment, but otherwise does not significantly

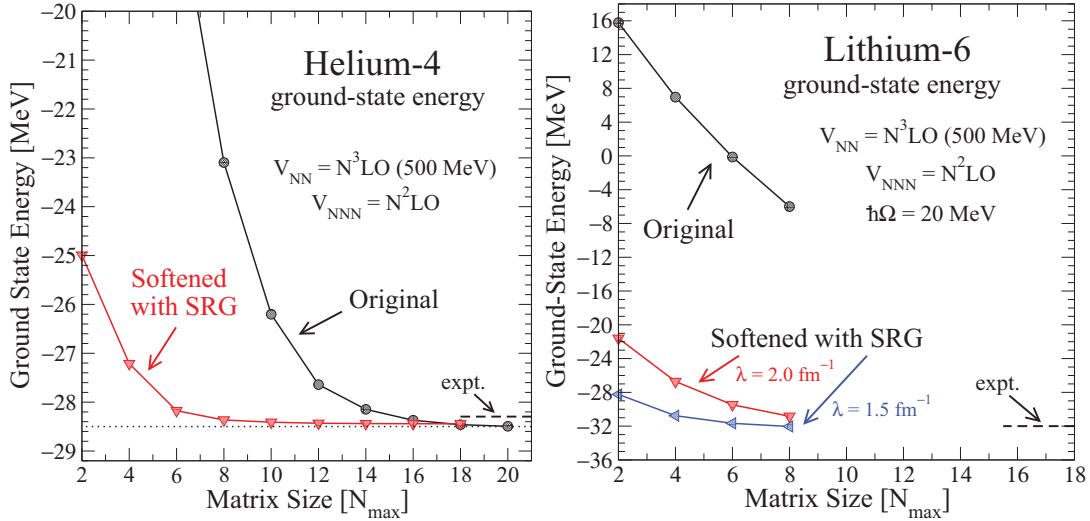


Figure 1.19: Convergence of ${}^4\text{He}$ and ${}^6\text{Li}$ for unevolved EFT potential versus potential after SRG evolution as a function of basis size, N_{\max} . Three-body induced forces are included [12].

alter the size of the induced forces. At small enough λ this pattern may break down, but most SRG evolution is not run much beyond $\lambda = 2 \text{ fm}^{-1}$. In order to analyze the hierarchy of contributions more carefully, we can also look at the individual components of the contributions to the binding energy. This is done in Figure 1.18 for the same systems. Here again, the four-body contributions are much smaller than the three-body contributions which are much smaller than the two-body pieces.

Returning now to the question of convergence, observe Figure 1.19 where the binding energy of ${}^4\text{He}$ and ${}^6\text{Li}$ are plotted with respect to the basis size. Here, and initial three-body force and the three-body induced pieces are included. For ${}^4\text{He}$ it is technically possible to reach convergence without the SRG, but with the evolution, the converged value is reached with a much smaller basis. Moreover, the evolved and unevolved answers match very closely, indicating small residual many-body induced pieces. For ${}^6\text{Li}$ the unevolved potential cannot even be extrapolated to the converged value from the largest full calculation (on the computer available) at $N_{\max} = 8$. But with the evolution we get good convergence, and the prediction is quite close to the experimental value. Some of the latest calculations have

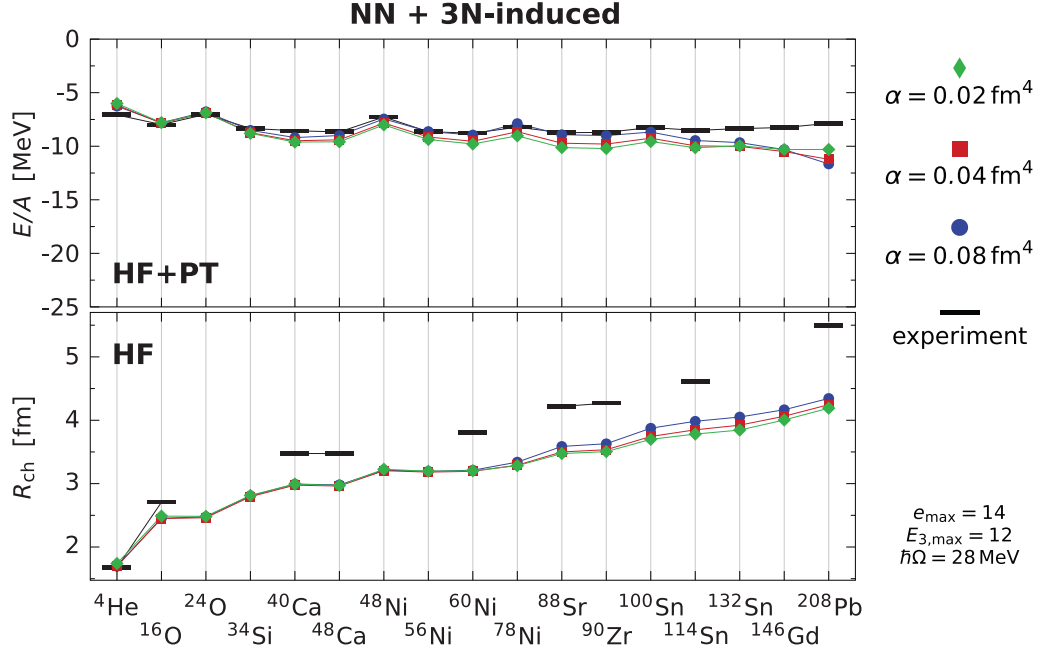


Figure 1.20: Calculation of binding energy per particle (top), and radii (bottom) using MBPT and SRG evolved chiral EFT NN potentials, including induced three-body forces. Here, α is the same as $s = 1/\lambda^4$ [7].

even used SRG-evolved interactions applied to systems as large as oxygen and calcium [74].

The SRG also holds promise for facilitating calculations that do not involve strictly basis-expansion solution methods. For example, the binding energies of particles across the periodic table from helium to lead have been calculated using Hartree-Fock with perturbative corrections with an evolved two-body initial potential and keeping the three-body induced forces. As seen in Figure 1.20, this does a very reasonable job. Improvements will come when technical problems with the inclusion of initial three-body forces are resolved [74]. We also see that SRG-evolved potentials are sufficiently soft that they can be used to calculate the binding energy in perturbative calculations of nuclear matter [13], as shown in Figure 1.21. Here, an NN-only evolved potential is used for technical reasons. By including an approximation to the induced three-body forces, saturation can be achieved. A full calculation of the nuclear matter binding energy with two- and three-body initial forces, as well as the SRG evolution up to the three-body level is in progress.

So, the SRG approach to nuclear physics provides us a way to get a lower acceptable

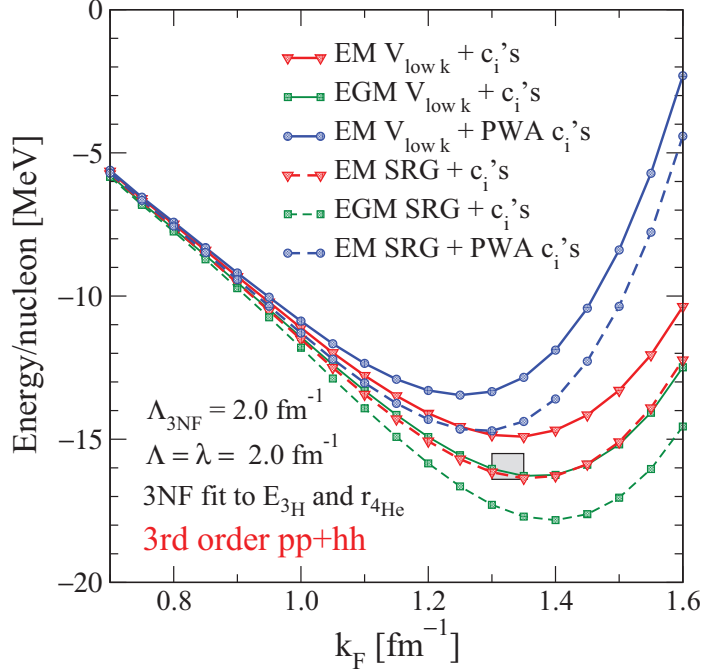


Figure 1.21: Calculations of nuclear matter with SRG evolved NN-only potentials. The neglected three-body induced components are approximated to produce saturation. $V_{\text{low } k}$ potential calculations are also shown. See Reference [13] for details.

cutoff on input Hamiltonians, thereby simplifying the short-distance physics for many-body quantum solution methods. We run the evolution, truncate the interaction, and calculate. However, thus far we have only seen calculations for many-body binding energies, and two-body phase shifts — observables which are directly related to Hamiltonian. What about other observables, such as those which result from the interaction of atomic nuclei with external probes?

1.3 Operators

For prediction of any observables not directly related to the Hamiltonian, we need to be able to include other operators in the SRG formalism. The prediction of electromagnetic form factors, neutrino-nucleus interactions, and other electroweak processes are of particular interest, for example. The methods and issues involved in doing this are the primary focus of this thesis. The bulk of this discussion will come in the following chapters, but first we

lay out the groundwork for operator evolution in the SRG.

What we find is that in order to use the wave functions produced by SRG-evolved interactions to calculate other matrix elements of interest, we cannot in general neglect the associated change in operators. The evolution of any operator $\hat{O} \equiv \hat{O}_{s=0}$ is given by the same unitary transformation used to evolve the Hamiltonian [8, 66],

$$\hat{O}_s = U_s \hat{O}_{s=0} U_s^\dagger , \quad (1.14)$$

which implies by differentiation with respect to s the general operator SRG equation is

$$\frac{d\hat{O}_s}{ds} = [\eta_s, \hat{O}_s] . \quad (1.15)$$

Although this equation can be used to find \hat{O}_s , it is computationally efficient to construct the unitary transformation directly from the eigenvectors of the evolved and unevolved Hamiltonian using

$$U_s = \sum_{\alpha} |\psi_{\alpha}(s)\rangle \langle \psi_{\alpha}(0)| , \quad (1.16)$$

where the sum on α is over all eigenvectors, and then to apply Eq. (1.14) directly. In practice we work in a discretized basis so this sum is finite and Eq. (1.14) is a simple matrix product. In cases where both methods have been used to calculate the SRG evolution, the transformations produced by Eqs. (1.15) and (1.16) agree up to numerical errors. However, it has been found that the one-step transformation produced from the eigenvectors is numerically more robust than the differential equation. The direct construction of U_s via Eq. (1.16) is used to calculate operator evolution throughout this work.

If implemented without approximation, unitary transformations preserve operator matrix elements by construction,

$$\langle \psi_{\alpha}(s) | \hat{O}_s | \psi_{\alpha'}(s) \rangle = \langle \psi_{\alpha}(0) | \hat{O}_{s=0} | \psi_{\alpha'}(0) \rangle , \quad (1.17)$$

and thus preserve the physics in the initial Hamiltonian and other operators. But do the advantages of the SRG evolution of Hamiltonians carry over to other operators and are there problems with the practical implementation of operator evolution? Equation (1.17)

implies that changes in the wave function are “compensated” by changes in the operator. This might reasonably be expected to shift around the physics while conserving the computational difficulty, so that at best we must deal with either a simple operator and complicated wave functions or a complicated operator and simplified wave functions. However, the SRG evolution of the Hamiltonian generates a much simpler interaction (smoother and decoupled), which leads to a simpler wave function (reduced short-range correlations).² What about other operators? Could there be strong and/or fine-tuned cancellations between the evolved wave functions and evolved operators? Can the hierarchy of many-body contributions be violated? We address these questions in the following chapters.

As we have seen, the evolution of three-body and higher-body interactions is critically important for the SRG and a parallel discussion is needed for other operators. To see how one-, two-, three-, and higher-body operators can be identified, it is useful to decompose the running SRG operator \hat{O}_s in second-quantized form. Schematically (suppressing indices and sums),

$$\hat{O}_s = \langle \hat{O}_s^{(1)} \rangle a^\dagger a + \langle \hat{O}_s^{(2)} \rangle a^\dagger a^\dagger aa + \langle \hat{O}_s^{(3)} \rangle a^\dagger a^\dagger a^\dagger aaa + \dots , \quad (1.18)$$

where a^\dagger and a are again creation and annihilation operators with respect to the vacuum in a single-particle basis. This *defines* $\langle \hat{O}_s^{(1)} \rangle$, $\langle \hat{O}_s^{(2)} \rangle$, $\langle \hat{O}_s^{(3)} \rangle$, . . . as the one-body, two-body, three-body, . . . operator matrix elements in that basis at each s . The SRG evolution in Eqs. (1.6) and (1.15) is dictated by commutators involving \hat{O}_s and H_s (which also has such an expansion). When they are evaluated, even if initially there are only one-body operators, higher-body terms will appear in \hat{O}_s just as in H_s with each step in s . Thus, when applied in an A -body subspace, the SRG will “induce” A -body components of any operator operator. However, we find that each $\langle \hat{O}_s^{(n)} \rangle$ is determined fully in the $A = n$ subspace, with no dependence on higher-body operators. This allows us to extract the induced many-body components of the operator as needed. Note that for Hamiltonians with no external potentials (i.e., no one-body interactions), $\langle \hat{O}_s^{(1)} \rangle$ is independent of s . It is also important to remember that input operators, $\hat{O}_{s=0}$, for low-energy effective theories

²Note that the interpretation of “simpler” can vary. For some Monte Carlo methods, the SRG Hamiltonians become more complicated in the sense of increasing non-locality in coordinate representation.

are generally never simply one- or two-body operators, although these components may dominate. The question is whether an initial many-body hierarchy (expected from chiral effective field theory formulations of the nuclear interaction) is maintained by the SRG evolution.

To avoid confusion, we note that it is also possible to normal order with respect to a finite-density reference state instead of the vacuum, which leads to the “in-medium SRG” (see Ref. [75] and references therein). This changes the definition of the matrix elements and creation and annihilation operators in Eq. (1.18) and shifts higher-body pieces to the zero-body, one-body, and two-body levels. These operators are well defined but have different properties from those considered here; for example, even one-body operators flow. The in-medium SRG shows great promise as a microscopic method of deriving effective shell model interactions for nuclei and the study of the corresponding operators is an important topic for future investigation.

1.4 Organization of Thesis and Original Contributions

This thesis is organized by chapter according to the major contributions to the field of nuclear physics. What follows here is a summary of that work.

In Chapter 2 we explore the two-body evolution of operators using the deuteron as our test system. We learn that the decoupling of the Hamiltonian is also matched, in some sense, by the operator flow, and can be utilized in operator expectation values. We examine properties of the operator flow itself for a variety of operators other than the Hamiltonian. Moreover, we perform variational calculations of the evolved binding energy and other operator expectation values which show that expectation values of SRG evolved operators are numerically robust.

In Chapter 3 we analyze the many-body evolution of SRG evolved operators explicitly in a second quantized formalism, as well as through first quantized model calculations. Here we make it clear that the n-body evolution of an operator is determined completely in an n-body basis. This provides a straightforward method for extracting the induced many-

body components of evolved operators for use in many-body solution techniques. We focus on the explicit extraction and embedding procedure in a 1D model basis expansion for its application to the many-body methods commonly used nuclear physics with the SRG today. Example model system operator calculations are performed, and the issues which must be considered when evolving one-body operators in a single-particle basis versus a Jacobi coordinate basis are explored. The hierarchy of induced many-body components is shown to be maintained. We also demonstrate the explicit structure of the unitary transformation in second quantization, providing a pathway for use of SRG evolved operators in many-body techniques where second quantized formalism plays a central role.

In Chapter 4 we digress to some extent from the main topic to explore generators other than the typical $\eta_s = [T_{\text{rel}}, H_s]$. Properties of the altered flow are explored. In particular, we first look at block-diagonal SRG evolution, which produces a potential similar in form to $V_{\text{low } k}$ potentials. General strategies for tailoring the flow to a desired pattern of decoupling are discussed. Returning to the subject of operator evolution and the calculation of other expectation values, we consider how the generator can be altered to improve convergence of operators in a given finite basis. Specifically, we address the poor convergence of long-range operators in an oscillator basis. We also, consider generators which have the potential to significantly reduce the computational requirements of the SRG, while maintaining its advantages. These generators could ultimately be used to extend the SRG evolution into larger basis spaces and additional many-body components.

In Chapter 5 the factorization of the unitary transformation operator under certain conditions is demonstrated. Of particular note, the SRG operator factorization is connected to the operator product expansion of the nonrelativistic wave function. Circumstances for which this factorization can be used in the calculation of operator expectation values are also described.

In Chapter 6 we consider applications of operator factorization to nuclear scaling and the EMC effect. These phenomena have traditionally been thought to be a consequence of short range correlations produced by the nuclear interaction. However, these short range correlations are no longer present in SRG evolved wave functions. Using factorization, we

can more clearly understand these phenomena as a consequence of low-momentum nuclear structure. As an example, a model calculation of the momentum distribution for $A \geq 2$ using the factorized form of the operator is produced. We also make use of the second quantized formalism developed Chapter 3 to calculate operator expectation values consistent with an SRG evolved potential in nuclear matter.

Finally, we conclude in Chapter 7 with a review of our current understanding of operator evolution in the SRG as well as a look to the future. We consider extensions of this work, and issues which still need to be addressed.

The appendix has been used to expand on a number of the technical details referenced in the main body of the thesis text. Here we consider the details behind the implementation of one-body operators in a Jacobi coordinate basis. We also consider, in a detailed second quantized analysis, the consequences of many-body operator evolution.

Chapter 2

TWO-BODY EVOLUTION OF OPERATORS

The SRG flow equations can be formulated to consistently evolve generic operators as well as Hamiltonians so that observables are unchanged if no approximations are made. Here we examine the properties of SRG-evolved operators, focusing in this chapter on applications to the deuteron but leading toward methods for few-body systems. We find the advantageous features of the SRG when applied to the Hamiltonian generally carry over to other operators. *

As we have seen, the SRG flow equations can be used to unitarily soften nuclear Hamiltonians by decoupling high-energy intermediate state contributions to low-energy observables while maintaining the natural hierarchy of many-body forces. Analogous flow equations can be used to consistently evolve operators so that observables are unchanged if no approximations are made. The question in practice is whether the advantages of a softer Hamiltonian and less correlated wave functions might be offset by complications in approximating and applying other operators.

In this chapter, we explore this question by restricting our attention to the deuteron, which means only one- or two-body operators are relevant. Furthermore, any running with s is due to an induced two-body part. In practice, working in the two-body system in the center-of-mass frame makes the occurrence of two-body operators uneventful; there are far more consequences for $A > 2$. We defer to Chapter 3 the discussion of evolving and extracting operator components and embedding them in larger A systems using a harmonic

*This chapter is based largely on work first presented in [76]

oscillator basis.

Nuclear SRG studies prior to this work [76] have focused primarily on the calculation of binding energies and phase shifts to analyze the characteristics of the SRG-evolved interactions. A limited analysis of the deuteron momentum distribution defined by the initial operator $a_q^\dagger a_q$ has also been made [8] and decoupling of long-distance operators for the rms radius, quadrupole moment, and r^{-1} have been examined [70], but only for the bare operators. We expand upon these studies here, emphasizing the nature of SRG-evolved operators and also include the first calculations of deuteron charge, quadrupole, and magnetic form factors. However, we use these electromagnetic operators as test cases for addressing questions about operator evolution and not yet for systematic comparison to experiment, which requires a more complete treatment of the unevolved operators.

The plan of this chapter is as follows. In Section 2.1, we explore whether decoupling of the Hamiltonian for two-body systems is mirrored in the operator flow, focusing on evolution of the momentum distribution as a characteristic example. In Section 2.2, we consider the evolution of other operators, including electromagnetic form factors in the deuteron, which are all found to flow to smooth, low-momentum forms. Variational calculations of the evolved deuteron binding energy and operator matrix elements are explored in Section 2.3. And, in Section 2.4 we discuss prospects for the universality of operators at low momenta. Our conclusions are summarized in Section 2.5.

2.1 Decoupling and the Deuteron Momentum Distribution

2.1.1 Potentials and Decoupling

In this section, we specialize the SRG evolution to a two-particle partial-wave momentum basis with flow operator $G_s = T_{\text{rel}}$. The flow equation,

$$\frac{dH_s}{ds} = [[T_{\text{rel}}, H_s], H_s] = \frac{dV_s}{ds}, \quad (2.1)$$

(recall that T_{rel} is chosen to remain constant) for nucleon-nucleon (NN) potentials is projected onto each channel using $1 = \frac{2}{\pi} \int_0^\infty q^2 dq |q\rangle \langle q|$ with $\hbar = M = 1$, yielding

$$\begin{aligned} \frac{dV_s(k, k')}{ds} &= -(k^2 - k'^2)^2 V_s(k, k') \\ &+ \frac{2}{\pi} \int_0^\infty q^2 dq (k^2 + k'^2 - 2q^2) V_s(k, q) V_s(q, k') \end{aligned} \quad (2.2)$$

just as in Eq. (1.9). This equation is implemented in a discretized Gaussian quadrature basis as a set of coupled differential equations for the matrix elements (angular momentum indices in the coupled channels have been suppressed) that are solved numerically.

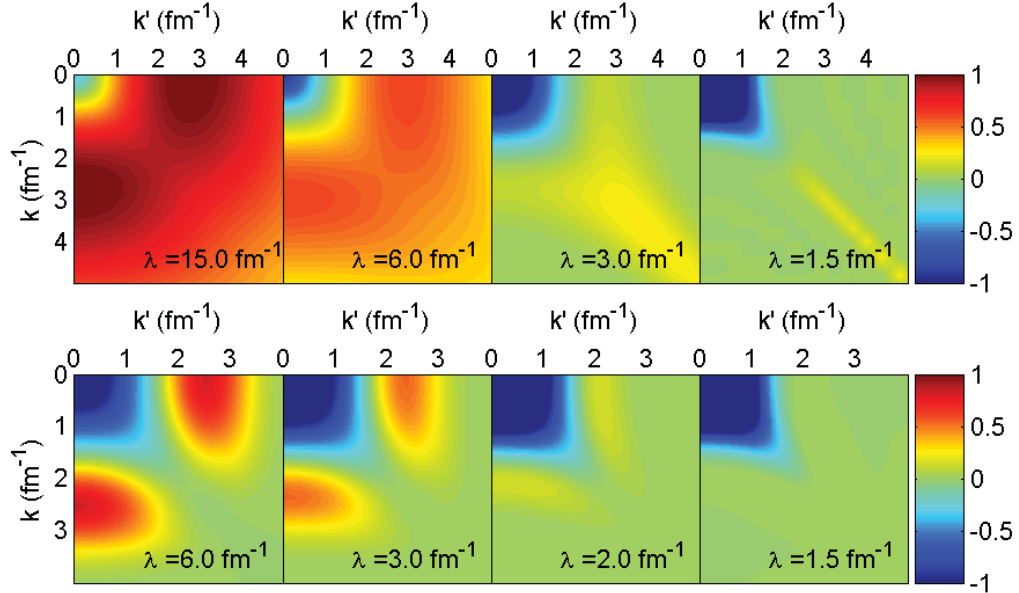


Figure 2.1: SRG evolution of the momentum-space 3S_1 potential starting with (a) AV18 from $\lambda = 15 \text{ fm}^{-1}$ to $\lambda = 1.5 \text{ fm}^{-1}$ [14] and (b) N 3 LO (500 MeV) from $\lambda = 6 \text{ fm}^{-1}$ to $\lambda = 1.5 \text{ fm}^{-1}$ [15].

The flow is visualized in Figure 2.1 for two representative initial potentials, AV18 [14] and a chiral N 3 LO (500 MeV) EFT potential from Ref. [15], which are currently the most commonly used NN interactions for microscopic nuclear structure calculations. The figures show snapshots of the potential matrix $V_s(k, k')$ in the 3S_1 partial wave at several values of λ , which is a useful alternative parameter to characterize the flow since it represents the ap-

proximate width of the off diagonal suppression, as previously explained. Again, it is related to s by $\lambda = s^{-1/4}$. The scale at the right indicates the strength of the potential (in fm); Gaussian mesh weights are not shown. One can see that the large matrix elements between low and high momentum at the initial λ 's shown (particularly for AV18) are suppressed by $\lambda = 1.5 \text{ fm}^{-1}$; that is, we see decoupling for both potentials.

It is not immediately clear, however, that this decoupling will be advantageous for the calculation of observables other than the binding energy. If we project the operator flow equation

$$\frac{d\hat{O}_s}{ds} = [[T_{\text{rel}}, H_s], \hat{O}_s] , \quad (2.3)$$

onto the partial wave momentum basis, we find

$$\frac{dO_s(k, k')}{ds} = \frac{2}{\pi} \int_0^\infty q^2 dq [(k^2 - q^2)V_s(k, q)O_s(q, k') + (k'^2 - q^2)O_s(k, q)V_s(q, k')] , \quad (2.4)$$

and decoupling is not manifest. Further, it is not clear if λ provides a measure of decoupling in the case of a general operator. So we turn to visualizations of the operator matrix elements for guidance. As noted earlier, in practice we do not solve the flow equation for operators, but apply the unitary transformation Eq. (1.14) at s by first solving the initial and final Hamiltonians for the eigenvectors and constructing the matrix

$$U_s(k_i, k_j) = \sum_\alpha \langle k_i | \psi_\alpha(s) \rangle \langle \psi_\alpha(0) | k_j \rangle , \quad (2.5)$$

where $\{k_i\}$ is the discrete momentum mesh.

2.1.2 Momentum Distribution

We begin our examination of operator evolution with perhaps the simplest nontrivial example: the momentum occupation operator $a_q^\dagger a_q$ in the center-of-mass frame (in this frame — for the A=2 particle space — q is the magnitude of both the relative momentum and the single-particle momentum). By varying the momentum q we can gain insight into how the SRG evolution behaves for initial operators dominated by either high or low momenta. In Figure 2.2 the plot of the momentum distribution is reproduced from the expectation

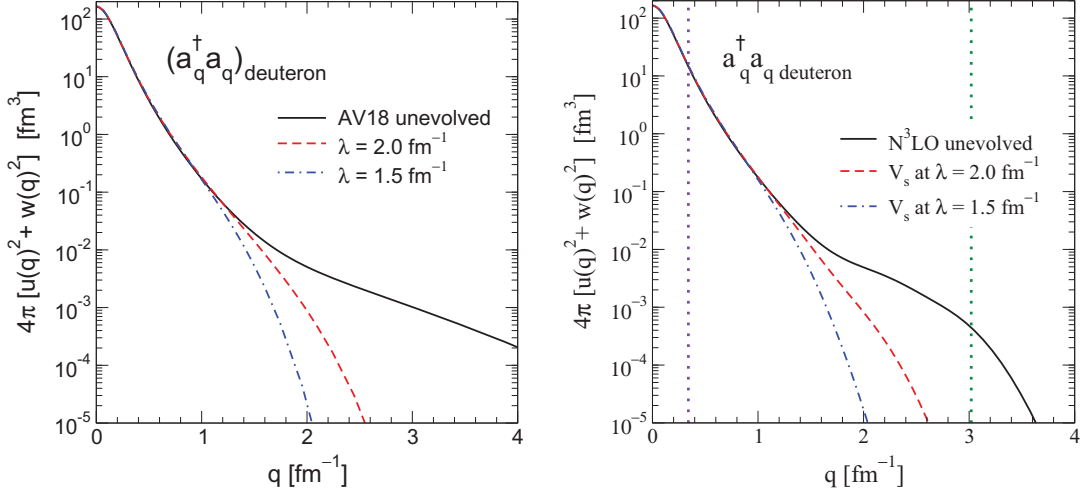


Figure 2.2: The momentum distribution in the deuteron as given by the expectation value of the bare number operator $a_q^\dagger a_q$ for the (a) AV18 [14] and (b) N^3LO (500 MeV) [15] potentials, both evolved and unevolved.

value $\langle \psi_d | a_q^\dagger a_q | \psi_d \rangle$ in the deuteron for the two initial potentials of Figure 2.1. The solid line is the result when the unevolved wave function (i.e., the wave function derived from the unevolved potential) is used with the unevolved $a_q^\dagger a_q$ operator. This sets the baseline for evaluating the effects of the SRG for each potential. When one uses the evolved wave function with the evolved operator, $U_s a_q^\dagger a_q U_s^\dagger$, the lines are indistinguishable. The dashed and dot-dashed lines are calculated using the *unevolved* operator with the *evolved* wave function at $\lambda = 2.0 \text{ fm}^{-1}$ and $\lambda = 1.5 \text{ fm}^{-1}$, respectively. These curves quantify the effect of not consistently evolving operators and also give the momentum dependence of the evolved wave functions. As can be seen, the high momentum components of the wave functions are significantly suppressed, as is consistent with the decoupling seen in the potential.

An analogous visual representation to that used for the potential allows us to analyze the RG flow and properties of these objects. Figures 2.3 and 2.4 illustrate the flow of the momentum occupation operator consistent with the renormalization of the N^3LO 500 MeV potential. We present the SRG results using only one potential, but qualitatively similar results will be obtained using any nuclear potential of interest. Each of the figures shows three sequences: the initial operator matrix elements $\langle k | a_q^\dagger a_q | k' \rangle$ evolved to four

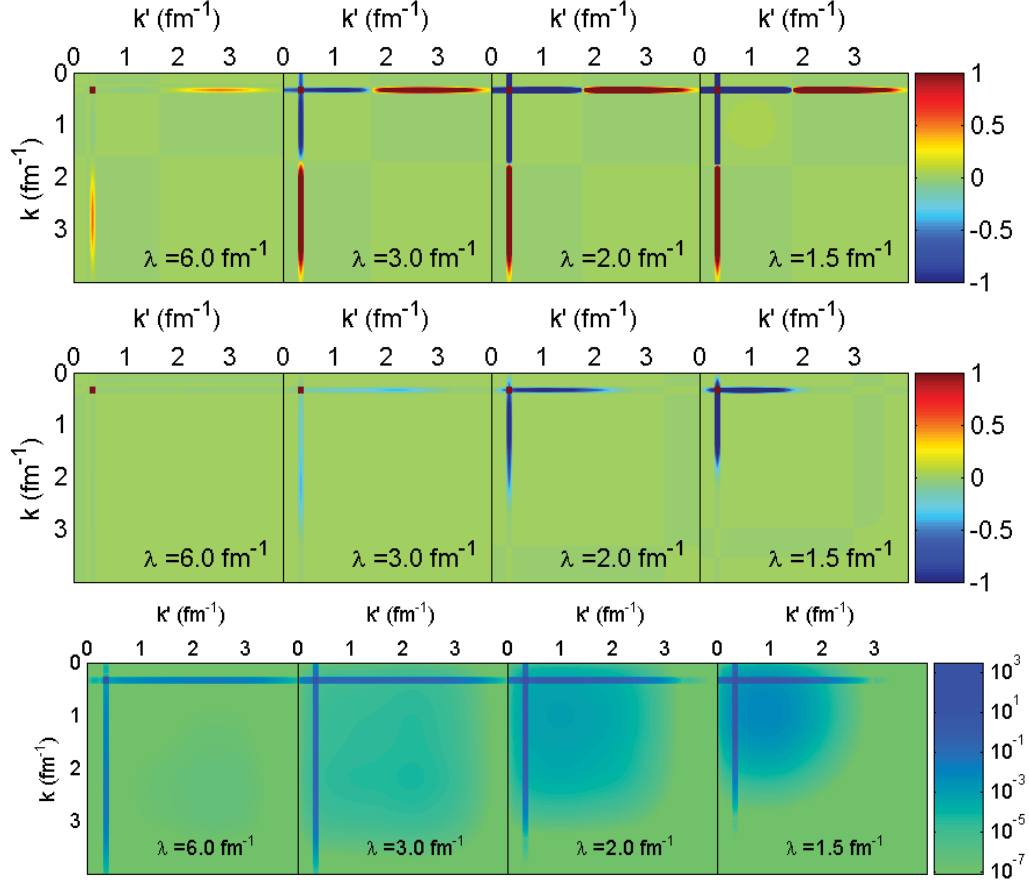


Figure 2.3: (a) SRG evolution of the operator $\langle k | a_q^\dagger a_q | k' \rangle$ for $q = 0.34 \text{ fm}^{-1}$ in the 3S_1 partial wave from $\lambda = 6 \text{ fm}^{-1}$ to $\lambda = 1.5 \text{ fm}^{-1}$, with the N³LO (500 MeV) [15] initial potential. (b) Integrand of $\langle \psi_d(s) | (a_q^\dagger a_q)_s | \psi_d(s) \rangle$ with linear (top) and logarithmic magnitude (bottom) scales.

different $\lambda = s^{-1/4}$ values and the integrand of $\langle \psi_d(s) | (a_q^\dagger a_q)_s | \psi_d(s) \rangle$ with first linear and then logarithmic scales. The operators shown correspond to those used to calculate the momentum distribution at $q = 0.34 \text{ fm}^{-1}$ and $q = 3.02 \text{ fm}^{-1}$ (marked by the dotted lines in Figure 2.2(b)). It is apparent that the unevolved operator is simply a delta function in momentum space (some minor evolution can already be seen at $\lambda = 6 \text{ fm}^{-1}$ because the scale must be magnified to view the evolution at lower values of λ).

Consider the operator (top row) sequences first. For both q values, the evolution begins along the momentum axes around the delta function where we see strength developing that was not present in the original operator. This behavior can be understood from the

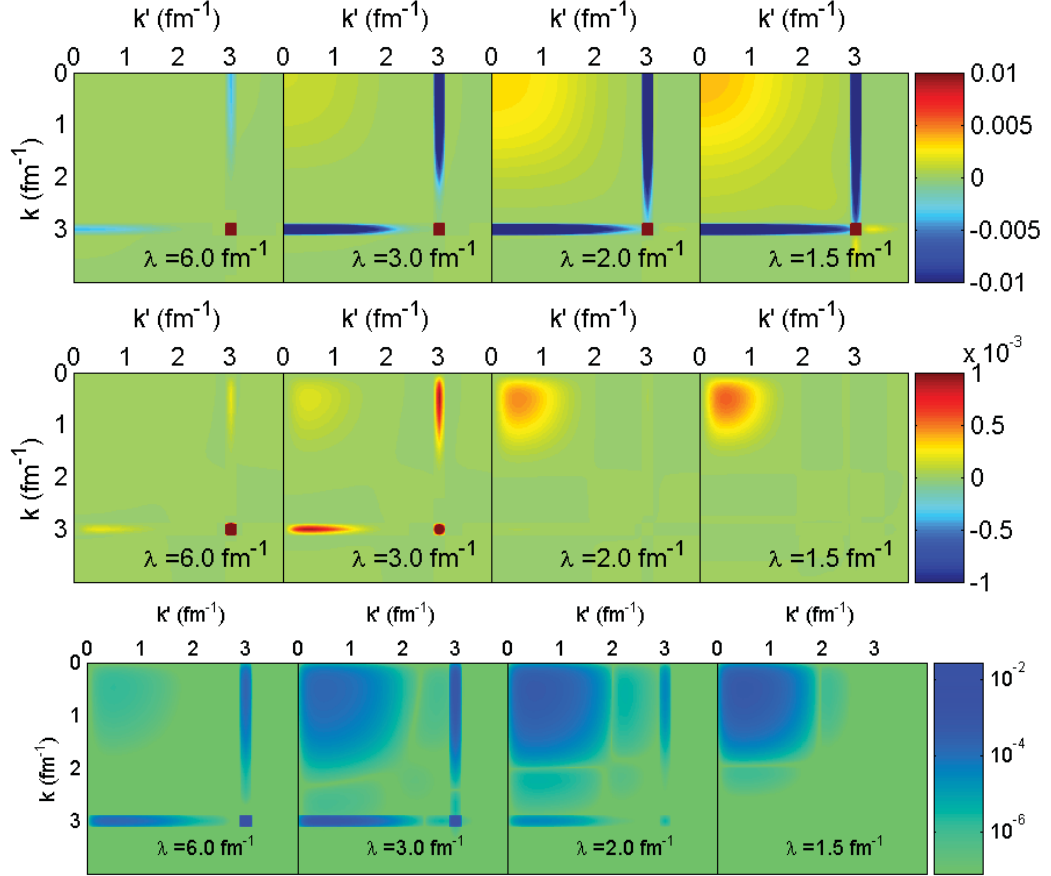


Figure 2.4: Same as Figure 2.3 but for $q = 3.02 \text{ fm}^{-1}$.

momentum basis SRG [Eq. (2.4)] and the features of the corresponding potential evolution. Holding k fixed, one can see that only the second term in the integral initially picks up strength along the axis that passes through the delta function, because the operator is zero everywhere else, and vice versa holding k' fixed. For the operator at high q we see that it develops more and more strength at low momentum as it evolves. The need for this additional strength is particularly evident because of the decoupling via evolution of the potential and the consequent suppression of high-momentum components in the deuteron wave function, as seen in Figure 2.2(b). As a result, the operator must pick up additional strength for the expectation values to remain unchanged. This strength can appear in two ways: (i) It can come in at low momentum, as we see here; or, (ii) the operator can gain strength only at high momenta, where the operator would have to become pathologically

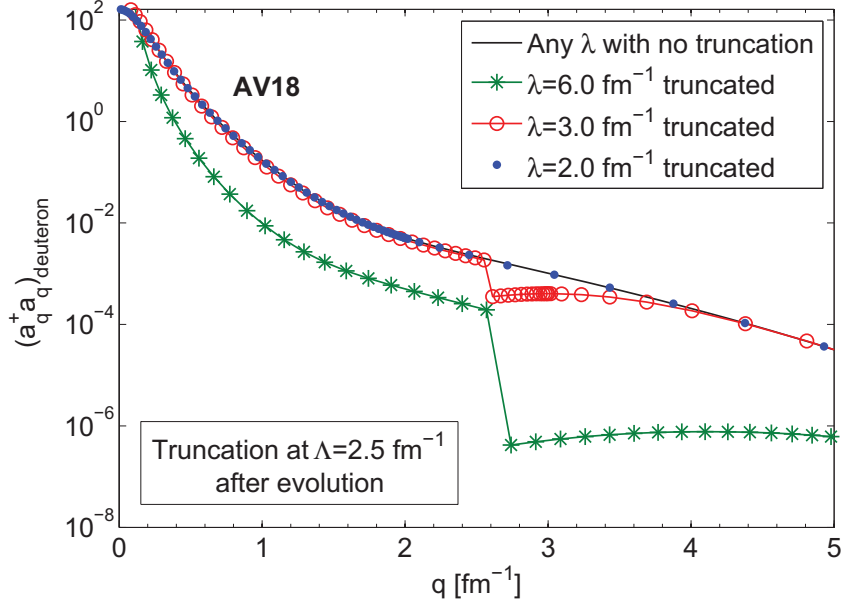


Figure 2.5: Decoupling in operator matrix elements is tested by calculating the momentum distribution in the deuteron after evolving the AV18 potential to several different λ and then truncating the Hamiltonian and evolved occupation operators (i.e., set them to zero above $\Lambda = 2.5 \text{ fm}^{-1}$).

large. If the second case were to occur, practical calculations with the SRG in a reduced basis would probably not be possible. This is found empirically to not be the case, and we can be confident such pathologies will not occur based on more general arguments discussed in what follows.

The operator at low q , however, picks up some strength at larger values of momentum than present in the initial operator. This is also needed to compensate for the suppression of low momentum dependence in high-energy eigenstates to maintain their expectation values. One should note that the operator display scale used here can be a bit deceptive, in that it has been amplified to make the qualitative features of the evolution more apparent. Most of the evolution does, in fact, remain at low momentum for deuteron expectation values.

We show the occupation operator as an integrand given by $\langle \psi_d | a_q^\dagger a_q | \psi_d \rangle$ in Figures 2.3(b) and 2.4(b). The expectation value filters the general operator by weighting its matrix elements with the deuteron wave function. Now we can see a clean RG flow in

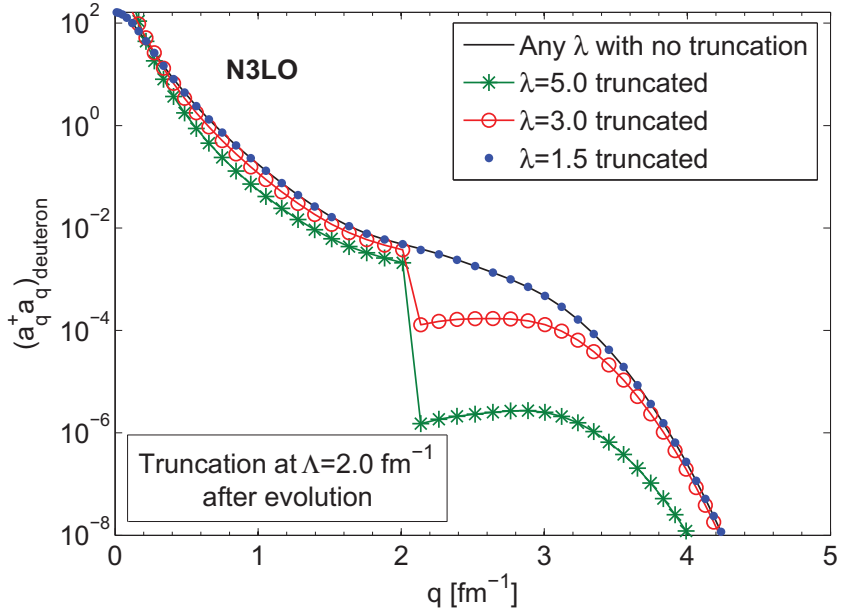


Figure 2.6: Decoupling in operator matrix elements is tested by calculating the momentum distribution in the deuteron after evolving the N^3LO potential to several different λ and then truncating the Hamiltonian and evolved occupation operators (i.e., set them to zero above $\Lambda = 2.0 \text{ fm}^{-1}$).

the strength for both operators. The integrand of the operator at $q = 3.02 \text{ fm}^{-1}$ begins as a sharp spike, corresponding to the original operator, but then flows out along the momentum axes to lower momentum. By the time the integrand reaches lower values of λ in the evolution nearly all of the strength in the expectation value is in the low-momentum region. The original spike disappears as the wave function dependence at high momentum falls off.

As for the operator at $q = 0.34 \text{ fm}^{-1}$, the strength does begin to flow out to some extent but remains almost entirely in the low-momentum region. Once again, the display scale has overemphasized the extent of the evolution in the values of the integrand. The spike that remains at $\lambda = 1.5 \text{ fm}^{-1}$ actually contains $\approx 96\%$ of the full expectation value. Owing to the possibility of misinterpreting these plots on a linear display scale, we also include the same plots with a logarithmic display scale. These pictures show only the magnitude of the integrands, but display nearly the full range of their values. Now it is conclusive that

the strength of the high momentum operator flows to low momentum, and the strength of the low-momentum operator remains at low momentum for a low-energy state. We see this pattern repeat in the calculation of other operators in the next section.

Despite the apparent changes in the integrands as they evolve, it is important to note that the sum of all the points (the expectation value) remains unchanged because of the unitarity of the SRG transformation. The momentum distribution calculations shown in Figure 2.2 were performed in the full momentum space of the original potential. Decoupling of the potential allows us to truncate the model space, thereby making numerical simulations more feasible, while at the same time allowing us to calculate the correct binding energies. If the calculation of other expectation values must be performed in the full model space, then the benefits of the SRG would be lost. However, the redistribution of strength implies that we have a form of decoupling for the operator. A critical test is to verify that decoupling is maintained in the calculation of operator expectation values.

This check is shown in Figures 2.5 and 2.6 for the momentum distributions of AV18 and N³LO potentials. To perform the check, we evolved the original Hamiltonians and operators in the full momentum space to various λ then truncated the model space to Λ . The deuteron wave function derived in this truncated space is used to calculate the expectation value of the evolved number operators to produce the momentum distributions shown here. The figures show that when the SRG evolution $\lambda > \Lambda$, the curves deviate significantly from that produced in the full space (because the wave function is distorted). However, once the operators are evolved to λ below the truncation at Λ , the expectation values are reproduced for all values of momenta, even in the region outside of the new model space. Thus decoupling is successful and λ provides a rough guide as to where this decoupling occurs. We see that this is also the case for other operator matrix elements of interest, as well as understand further how this comes about, in what follows.

2.1.3 General Analysis

The plots of the deuteron integrands show that no pathologies appear at high momentum in the evolved operators and verify that decoupling can be successful when calculating

expectation values of this operator. The plots even indicate where the model space can be truncated — this is simply where the integrand strength becomes negligible in the logarithmic plot. Here we develop a more general understanding of operator evolution to build confidence that pathologies will not occur in other operators.

Consider the representation of a generic operator in terms of the energy eigenstates,

$$\hat{O}_s = \sum_{ij} O_{ij} |\psi_i(s)\rangle \langle \psi_j(s)| , \quad (2.6)$$

where

$$O_{ij} = \langle \psi_i(s) | \hat{O}_s | \psi_j(s) \rangle . \quad (2.7)$$

It is important to remember that these matrix elements are invariant under SRG transformations, so O_{ij} does not depend on s . Thus, the momentum space behavior of evolved operators is given, in turn, by the momentum space behavior of the evolved eigenstates — specifically the sum of their outer products weighted by O_{ij} ,

$$O_s(k, k') = \sum_{ij} O_{ij} \langle k | \psi_i(s) \rangle \langle \psi_j(s) | k' \rangle . \quad (2.8)$$

The behavior of these eigenstates is well under control. As we have seen from the momentum distribution of the deuteron, low-energy bound-state wave functions are suppressed at high momentum. The rest of the (positive) eigenstates are effectively smeared out delta functions (normalized in a finite basis), which because of decoupling in the Hamiltonian become increasingly narrow peaks with the evolution in s . So, the evolution will not become pathological unless the unevolved operator is already pathological (i.e., only if some O_{ij} are unnaturally large).

If we now consider this operator in the deuteron eigenstate $|\psi_d(s)\rangle = |\psi_1(s)\rangle$, we find that only the O_{11} matrix element of the operator is projected out and the momentum dependence is given by the outer product of the deuteron wave function. Specifically, the only nonzero part of the operator will be formally given by

$$O_s(k, k') \rightarrow O_{11} \langle k | \psi_1(s) \rangle \langle \psi_1(s) | k' \rangle . \quad (2.9)$$

However, if we would like to reconsider the issue of decoupling and a finite model space truncation, we find that we are restricted by the potential breaking of eigenstate orthogonality in the truncated space; that is, the extent to which

$$\frac{2}{\pi} \int_0^\Lambda k^2 dk \langle \psi_i(s) | k \rangle \langle k | \psi_j(s) \rangle \neq 0 , \quad \text{for } i \neq j . \quad (2.10)$$

The logarithmic integrand plots show us that this problem is negligible if one of the states is the deuteron. Furthermore, SRG-driven decoupling of states well separated in energy will make them increasingly orthogonal in the truncated space. Thus, the momentum-space evolution of operators in a specific basis can be brought under control; we will consider the case of induced many-body components of the operators in the following chapter.

2.2 Other Operators

2.2.1 Long-distance Operators

We begin our presentation of additional operators with the evolution of operators for three paradigmatic expectation values in the deuteron: the rms radius, the quadrupole moment, and r^{-1} . These operators all act on relatively long distance scales. At leading order they are naturally defined in coordinate space so that deuteron expectation values can be written as [77]

$$\langle r_d \rangle = \frac{1}{2} \left[\int_0^\infty dr r^2 (u(r)^2 + w(r)^2) \right]^{1/2} , \quad (2.11)$$

$$\langle Q_d \rangle = \frac{1}{20} \int_0^\infty dr r^2 w(r) \left(\sqrt{8} u(r) - w(r) \right) , \quad (2.12)$$

and

$$\left\langle \frac{1}{r} \right\rangle = \int_0^\infty dr \left(\frac{1}{r} \right) (u(r)^2 + w(r)^2) , \quad (2.13)$$

where u and w are the 3S_1 and 3D_1 deuteron radial wave functions. However, we will continue to analyze the operators in momentum space. To avoid numerical instabilities associated with putting the derivatives in the momentum-space expressions on a mesh (see Ref. [77]), we extract the coordinate-space operators from Eqs. (2.11)–(2.13) and transform

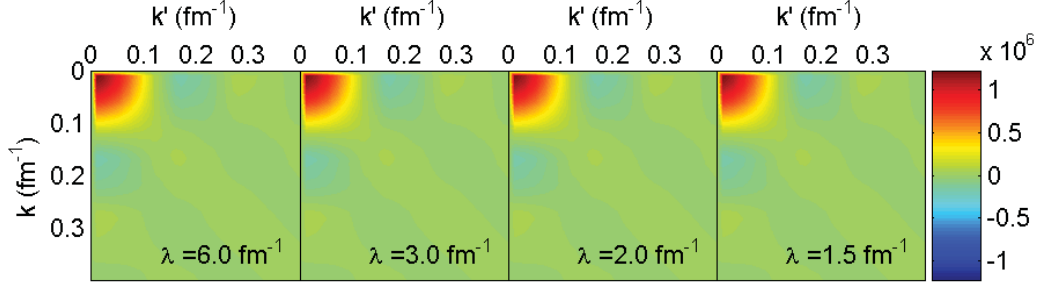


Figure 2.7: Operator evolution of $\langle k | r^2 | k' \rangle$ in the 3S_1 partial wave from $\lambda = 6 \text{ fm}^{-1}$ to $\lambda = 1.5 \text{ fm}^{-1}$ using the N³LO (500 MeV) potential.

to the partial wave momentum basis. For example, from Eq. (2.11) we can see that the r^2 operator is given by the diagonal matrix (discretized in coordinate space)

$$\langle r | r^2 | r' \rangle = r^2 \delta(r - r') \quad (2.14)$$

in the 3S_1 and 3D_1 channels. The only transformations needed are given by

$$\langle r | k; {}^3S_1 \rangle = \sqrt{\frac{2}{\pi}} r k^2 j_0(kr) \quad (2.15)$$

and

$$\langle r | k; {}^3D_1 \rangle = \sqrt{\frac{2}{\pi}} r k^2 j_2(kr), \quad (2.16)$$

where the j_l 's are spherical Bessel functions (additional partial waves are needed for states other than the deuteron, of course). The transformations are represented as $n \times m$ matrices (where n and m are the sizes of the coordinate and momentum space meshes, respectively) and applied to both sides of the $n \times n$ coordinate-space operator matrix to produce an $m \times m$ matrix in momentum space for each partial wave. Then, to evolve the operator in momentum space, we apply the unitary transformation $\hat{O}_s = U_s \hat{O} U_s^\dagger$.

The SRG evolution sequence for r^2 shown in Figure 2.7 is again a picture of just the operator in the momentum basis. Note the restricted momentum scale of the plot, as well as the magnitude of the operator display scale. As a long distance operator, the strength is highly concentrated at low momentum. It is evident that very little renormalization occurs at the lowest values of momentum, which is consistent with the findings for the number

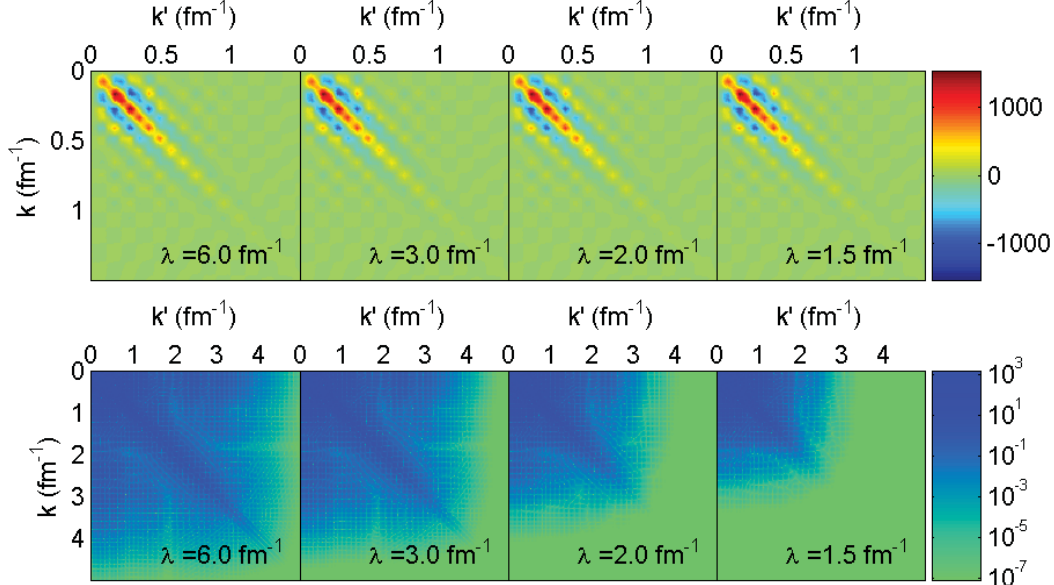


Figure 2.8: Integrand given by $\langle \psi_d | r^2 | \psi_d \rangle$ and evolved from $\lambda = 6 \text{ fm}^{-1}$ to $\lambda = 1.5 \text{ fm}^{-1}$ using the N3LO 500 MeV potential with a linear color scale (top) and a logarithmic scale of the magnitude (bottom). Notice the difference in momentum scales.

λ	6.0 fm^{-1}	3.0 fm^{-1}	2.0 fm^{-1}	1.5 fm^{-1}
Q_d	0.275 fm^2	0.274 fm^2	0.269 fm^2	0.260 fm^2

Table 2.1: Expectation value of the quadrupole moment given by the unevolved operator with the evolved deuteron wave function.

operator. Looking at the deuteron integrand of the r^2 operator in Figure 2.8, the linear display scale plot shows the same behavior. The log-scale shows the entirety of the contributions to the integral. At low momentum, the strength is orders of magnitude greater than elsewhere. While the pattern of the contribution changes very little with λ in the linearly scaled plot, the log-scale plot clearly shows the characteristic exponential suppression with decreasing λ due to the decoupling of the potential and consequent reduction of high-momentum components in the deuteron wave function.

The quadrupole moment operator is also a long-distance operator and we find its evolution shares most of the same characteristics found for the evolution of the r^2 operator (note that it also picks up strength in the ${}^3S_1 - {}^3D_1$ channel). The deuteron integrand is shown

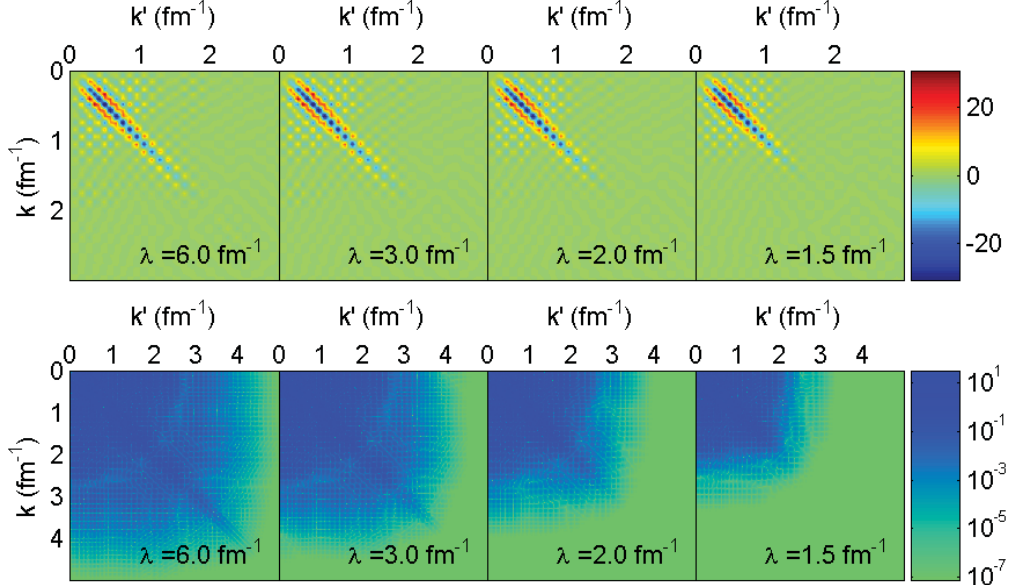


Figure 2.9: Integrand of the quadrupole moment expectation value in the deuteron and evolved from $\lambda = 6 \text{ fm}^{-1}$ to $\lambda = 1.5 \text{ fm}^{-1}$ using the N3LO 500 MeV potential with a linear color scale (top) and a logarithmic scale of the magnitude (bottom). Notice the difference in momentum scales.

in Figure 2.9. There is little change in the actual evolution of the operator, while high-momentum contributions become exponentially suppressed. The lack of evolution can be quantified by calculating the expectation value of the unevolved operator with the evolved wave function. Results for various λ are given in Table 2.1. Note that we are using the basic, one-body quadrupole moment operator without two-body or other higher order renormalized corrections. The “true” value for this potential and operator is $Q_d \approx 0.275 \text{ fm}^2$ while the experimental value of this quantity is $Q_{\text{expt.}} \approx 0.285 \text{ fm}^2$. Thus the induced two-body contribution is the same order as omitted two-body contributions to the initial operator. As such, the SRG has not led to any changes larger than one would expect from including the fully renormalized operator from the EFT.

Finally, in Figure 2.10 we show the evolution in the deuteron of the r^{-1} operator, which has larger contributions at short range than the previous examples. Consequently, this operator is more spread out in momentum space. Yet, we see the same general behavior with respect to renormalization and the suppression at large momenta without, as usual,

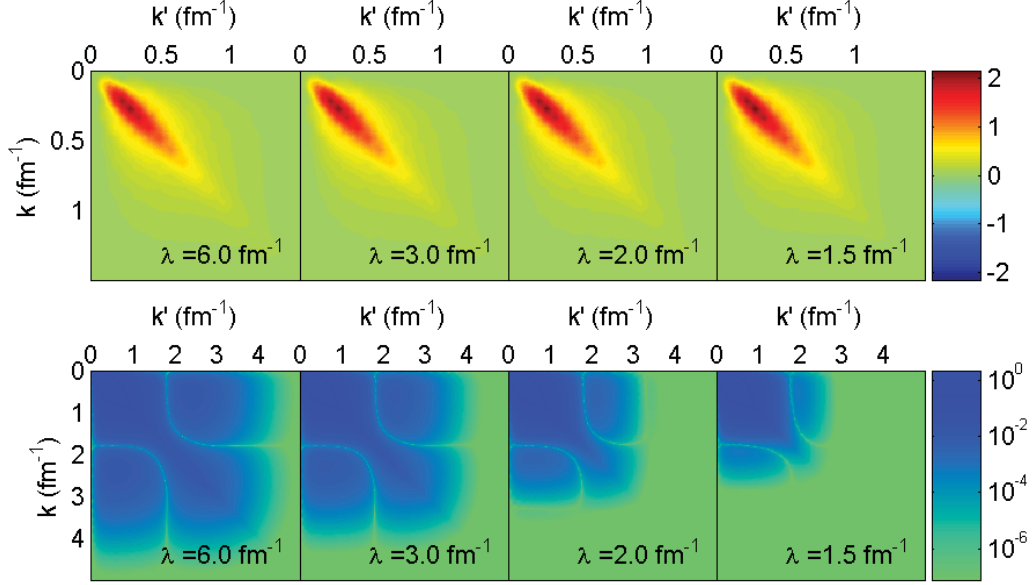


Figure 2.10: Integrand given by $\langle \psi_d | r^{-1} | \psi_d \rangle$ and evolved from $\lambda = 6 \text{ fm}^{-1}$ to $\lambda = 1.5 \text{ fm}^{-1}$ using the N3LO 500 MeV potential with a linear color scale (top) and a logarithmic scale of the magnitude (bottom). Notice the difference in momentum scales.

any changes in the expectation value.

2.2.2 Deuteron form factors: G_C , G_Q , and G_M .

We now turn to the SRG evolution of electromagnetic operators that determine the deuteron charge, quadrupole, and magnetic form factors (i.e., G_C , G_Q , and G_M respectively) [78–82]. We restrict our discussion to deuteron expectation values that have been derived consistently with chiral EFT at leading order in coordinate space [82]. These are given by

$$G_C(Q^2) = G_E^{(s)}(Q^2) \int dr [u^2(r) + w^2(r)] j_0(|\mathbf{q}|r/2) , \quad (2.17)$$

$$G_Q(Q^2) = G_E^{(s)}(Q^2) \frac{6\sqrt{2}}{Q^2} \int dr \left[u(r)w(r) + w^2(r)/\sqrt{8} \right] j_2(|\mathbf{q}|r/2) , \quad (2.18)$$

$$\begin{aligned}
G_M(Q^2) = & G_E^{(s)}(Q^2) \frac{3}{2} \int dr w^2(r) [j_0(|\mathbf{q}|r/2) + j_2(|\mathbf{q}|r/2)] \\
& + G_M^{(s)}(Q^2) 2 \int dr u^2(r) j_0(|\mathbf{q}|r/2) \\
& + G_M^{(s)}(Q^2) \{ \sqrt{2} \int dr u(r) w(r) j_2(|\mathbf{q}|r/2) \\
& - \int dr w^2(r) [j_0(|\mathbf{q}|r/2) - j_2(|\mathbf{q}|r/2)] \}, \quad (2.19)
\end{aligned}$$

where $Q^2 = |\mathbf{q}|^2$, and $G_E^{(s)}(Q^2)$ and $G_M^{(s)}(Q^2)$ are the single-nucleon isoscalar electric and magnetic form factors obtained from the parameterization given in Reference [16]. From these coordinate-space expressions, we can apply the same procedure used earlier to extract the operators, then use Eqs. (2.15) and (2.16) to convert to momentum space and transform via the SRG unitary transformation. One should note that starting from a coordinate-space operator is by no means essential; it is simply a numerical convenience in this case.

The expectation values as functions of $q = \sqrt{Q^2}$ for each of these operators is presented in Figure 2.11. The solid line has been calculated using the unevolved potential with the unevolved operator, which again serves as our reference value. The starred points are calculated using the evolved wave function with the evolved operator (both at $\lambda = 1.5 \text{ fm}^{-1}$). As advertised, they lie precisely on top of the solid line for all values of q , up to small numerical errors. The dot-dashed line is calculated using the *unevolved* operator with the *evolved* wave function as an indication of the effect of renormalization on the expectation value. We see noticeable deviation above $q \sim \lambda$; however, from the magnitude of the suppression seen in the wave function at high momentum one might have expected the curve to drop much faster with respect to q . But at the same time, the form factor operators probe momenta in the deuteron center-of-mass frame whereas q is specified in the laboratory frame. Thus, the operators are probing the wave function largely at $\frac{1}{2}q$, which again brings the calculations in line with our SRG expectations.

The basic features of the SRG evolution of all three operators are qualitatively very similar, so we present the visual matrix representation of the magnetic form factor at high and low q as a representative example in Figures 2.12 and 2.13. This form factor picks up strength in all deuteron channels. The high-momentum form factor has a much greater

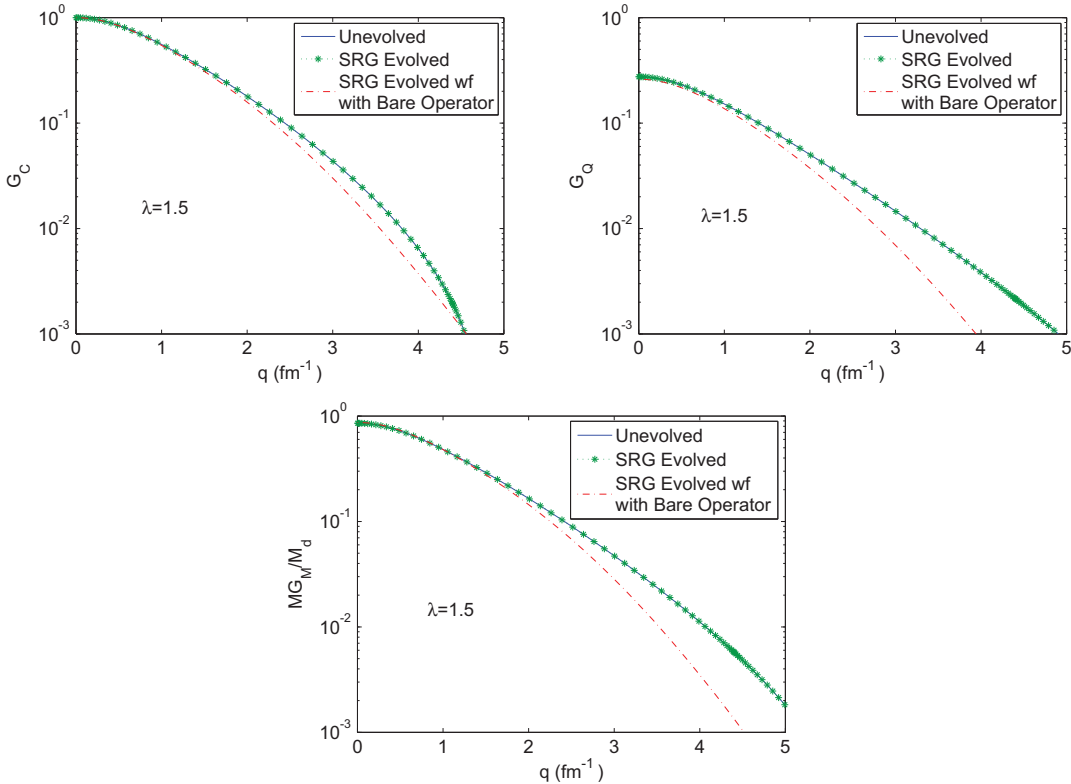


Figure 2.11: Deuteron form factors G_C , G_Q , and G_M using the isoscalar electric form factor parameterization from Ref. [16]. M is the nucleon mass and M_d is the mass of the deuteron. The wave function is derived from the NNLO 550/600 MeV potential and the evolution is run to $\lambda = 1.5 \text{ fm}^{-1}$ [17].

diffusion of strength at high momentum than seen in any of the static properties explored earlier. Yet it is apparent that the strength in the operator flows to low momentum in this case also. In contrast, the low-momentum operator exhibits very little renormalization, as we have come to expect. For both cases, we can see from the logarithmic display scale plots that the momentum dependence of the form factors is virtually eliminated at large momenta without affecting the outcome of the computation.

This lack of dependence on high momenta in evaluating expectation values is particularly significant for the practical application of the SRG in calculations of low-energy few- or many-body systems. Had this renormalization led to singular behavior in the operators at high momentum, the effects due to the suppression of the wave function would have been negated and led to wildly erroneous results in the evaluation of observables in a reduced

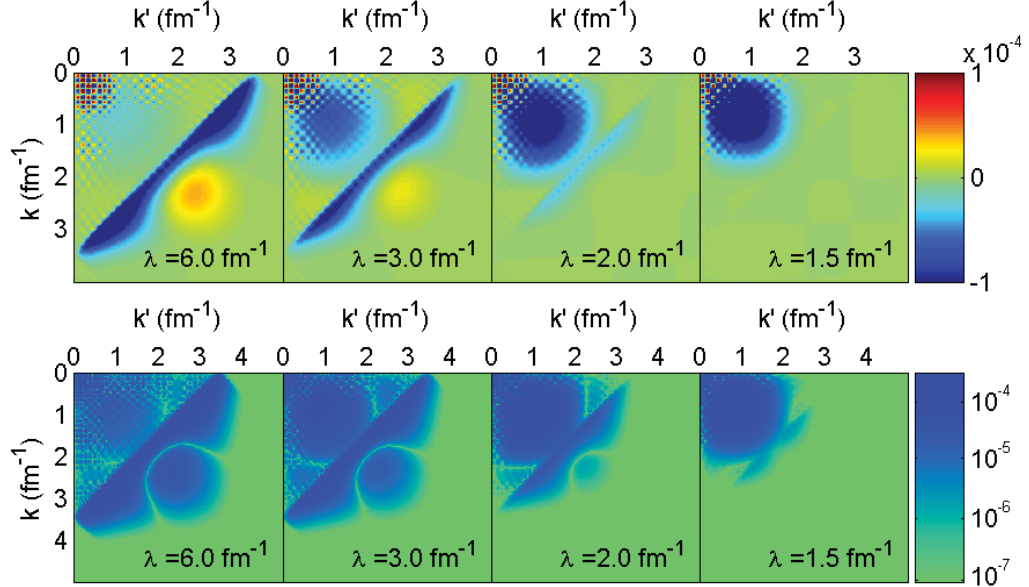


Figure 2.12: Integrand of G_M at $q = 6.90 \text{ fm}^{-1}$ evolved from $\lambda = 6 \text{ fm}^{-1}$ to $\lambda = 1.5 \text{ fm}^{-1}$ using the NNLO 550/600 MeV potential with a linear scale (top) and a logarithmic scale of the magnitude (bottom).

model space. The arguments in Section 2.1.3 explain why this will generally be the case.

2.3 Variational Calculations

We have argued previously that SRG-evolved interactions and the resulting wave functions become “simpler.” Variational calculations of the ground-state wave function can provide a test (and additional meaning) of the extent to which this is true in practical applications. The decoupling of high- and low-momentum states caused by SRG evolution means that the resulting wave functions are much less correlated than the original wave functions. Consequently, one expects that variational calculations of the evolved wave functions should be effective with a much simpler ansatz than one would normally require for the corresponding unevolved interaction. In conjunction with this, one might be concerned that a delicate interplay of the evolved operators and wave functions would be necessary to preserve matrix elements. However, it turns out that the evolved operators are not only equally good, but actually superior to the original operators in this respect. Rather than high-momentum

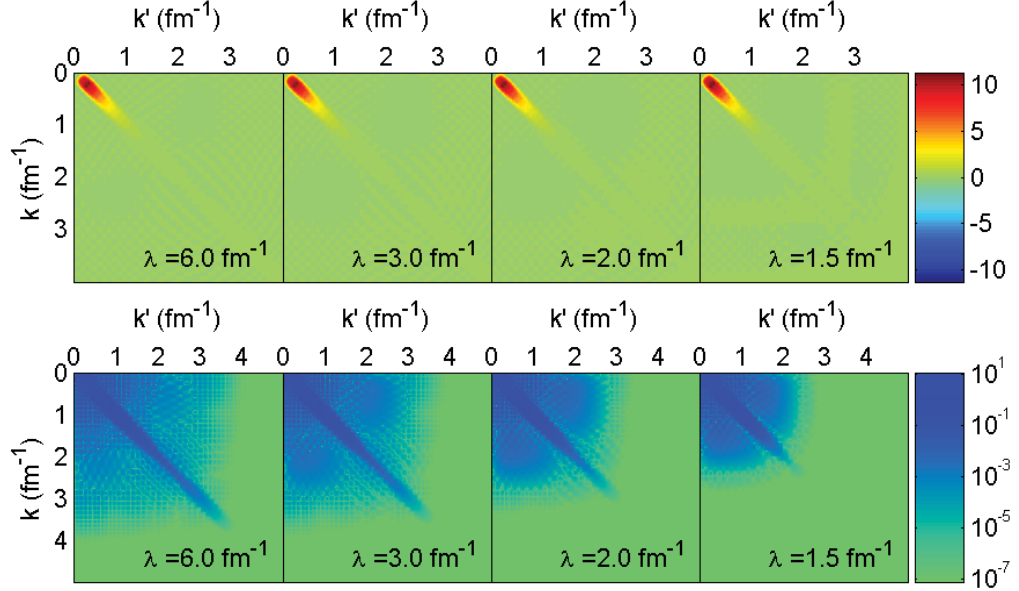


Figure 2.13: Integrand of G_M at $q = 0.34 \text{ fm}^{-1}$ evolved from $\lambda = 6 \text{ fm}^{-1}$ to $\lambda = 1.5 \text{ fm}^{-1}$ using the NNLO 550/600 MeV potential with a linear scale (top) and a logarithmic scale of the magnitude (bottom).

operators picking up small pieces of the wave function (which could never be reproduced by a simple variational calculation), we get a smooth sum over where the wave function is large and easily approximated. We illustrate these points here by choosing a simple variational ansatz and looking at how convergence improves for SRG-evolved operator expectation values.

Variational calculations have been performed on low-momentum potentials (specifically “ $V_{\text{low } k}$,” derived using an alternative RG formulation) in the past to demonstrate a significantly improved convergence of the binding energies [83, 84]. We choose to adapt a simple ansatz for the deuteron used in those calculations to make our point for the SRG. In particular, we take the (unnormalized) 3S_1 and 3D_1 partial waves to be

$$u(k) = \frac{1}{(k^2 + \gamma^2)(k^2 + \mu^2)} e^{-\left(\frac{k^2}{\lambda^2}\right)^2}, \quad (2.20)$$

$$w(k) = \frac{ak^2}{(k^2 + \gamma^2)(k^2 + \nu^2)^2} e^{-\left(\frac{k^2}{\lambda^2}\right)^2}, \quad (2.21)$$

where γ, μ, ν , and a are variational parameters. The exponential factors are chosen to

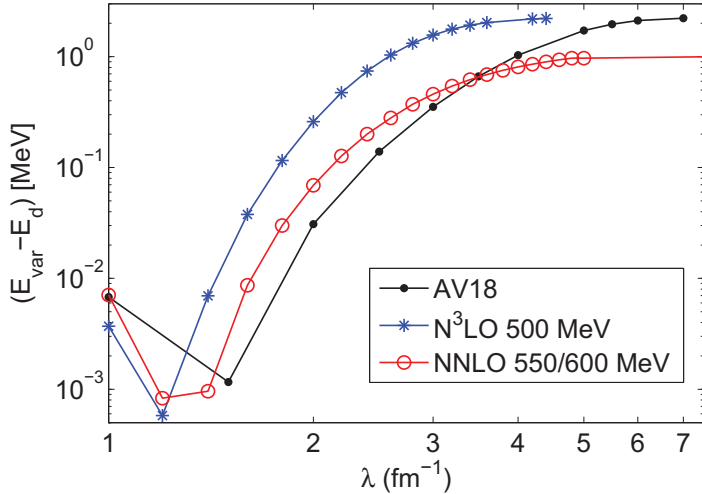


Figure 2.14: Deviation from E_d of the best variational energy as a function of SRG decoupling parameter for the wave function ansatz of Eq. (2.21). E_d is the deuteron binding energy for each interaction derived via a full eigenvalue calculation of the Hamiltonian.

match the asymptotic suppression of the wave function resulting from the decoupling of the interaction according to Eq. (1.11). The energy is minimized with respect to the variational parameters at various λ for the three different potentials used in this article. The binding-energy results are shown in Figure 2.14. Without evolution, the AV18 and N³LO trial wave functions are not even bound, and the NNLO wave function accounts for less than half the binding energy. With evolution, the AV18 and N3LO wave functions begin to bind at $\lambda \approx 7 \text{ fm}^{-1}$ and $\lambda \approx 4.5 \text{ fm}^{-1}$ respectively and when the evolution is taken further, the trial wave function is able to reproduce the exact binding energies to within $\approx 1 \text{ keV}$.

Examining the matrix elements of operators which initially have strength concentrated over a range of different momenta — such as the occupation operators with respect to momenta q — provides a stricter test of the variational solution to the evolved wave functions and the sensitivity of evolved operators to them. The initial AV18 potential has particularly strong correlations at high momenta. If we look at the evolved occupation operators in Figure 2.15, we see three curves: one with a wave function near the binding threshold, one at about half the binding energy, and one that is well converged with respect to the binding energy (evolved to $\lambda = 6.0 \text{ fm}^{-1}$, 4.0 fm^{-1} and 1.5 fm^{-1} respectively). Near the

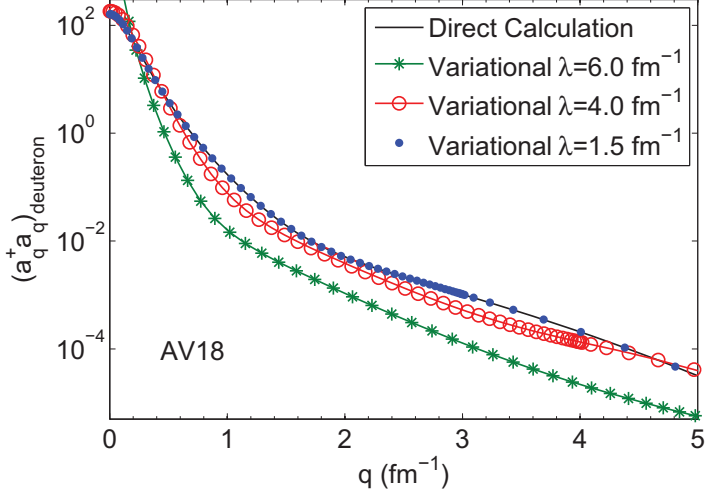


Figure 2.15: The momentum distribution in the deuteron as given by the expectation value of the evolved occupation operator $U a_q^\dagger a_q U^\dagger$ using the variational wave functions derived from the Salpeter ansatz and the AV18 potential evolved to $\lambda = 6.0 \text{ fm}^{-1}$, 4.0 fm^{-1} and 1.5 fm^{-1} . The direct calculation is from a full eigenvector solution of the Hamiltonian.

binding threshold, the momentum distribution is reproduced rather poorly, but at smaller λ the curve improves, and once the binding energies are converged the operator expectation values are also converged to approximately 1% or better.

The same pattern holds for other operators and interactions; that is, the operator matrix elements are not sensitive to the fine details of the evolved wave function. The magnetic form factor of the deuteron using the NNLO potential, for example, is shown in Figure 2.16. Not only does this operator pick up strength in both partial wave states of the deuteron, but also their coupling. Again, for a variational wave function at half binding energy ($\lambda = 5.0 \text{ fm}^{-1}$) the matrix elements deviate significantly from the direct, non-variational calculation, but when the binding energy is converged (at $\lambda = 1.2 \text{ fm}^{-1}$), the form factor expectation values are reproduced to better than 1%.

2.4 Operator Universality

The tendency for phase shift equivalent NN potentials to flow toward a universal low-momentum form via the SRG is evident (visually, at least) in Figure 2.1 when we compare

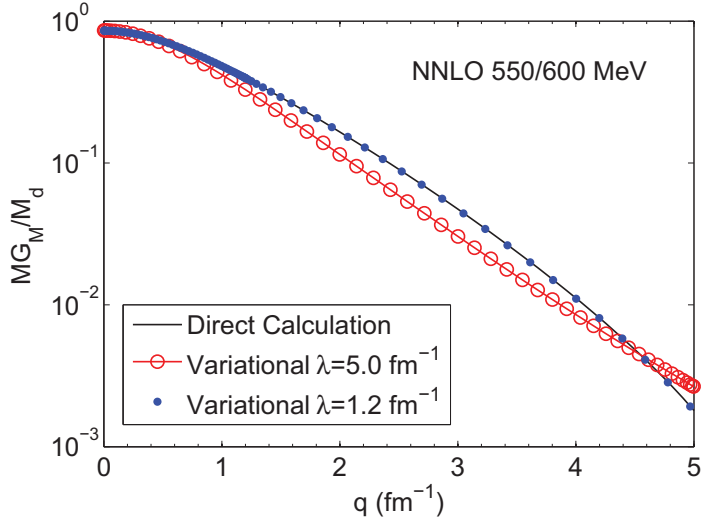


Figure 2.16: Deuteron form factor G_M using the isoscalar electric form factor parameterization from Ref. [16]. M is the nucleon mass and M_d is the mass of the deuteron. The variational wave functions are derived from the Salpeter ansatz and the NNLO 550/600 MeV potential evolved to $\lambda = 5.0 \text{ fm}^{-1}$ and $\lambda = 1.2 \text{ fm}^{-1}$. The operators are evolved consistently. The direct calculation is from a full eigenvector solution of the Hamiltonian.

the evolved AV18 potential to N³LO (500 MeV) at low momenta. Initially, these potentials have a very different form. This phenomenon was observed early in applications of the SRG to nuclear physics for the evolution of different EFT potentials, as well as with $V_{\text{low } k}$ transformed potentials [7, 65, 69], and recently in coordinate space local projections of the evolved potentials [45]. More detailed studies are forthcoming [85].

This naturally raises the question of universality for other operators. Such questions can only be addressed directly for operators constructed to reproduce the same experimental data (such as phase shifts for the NN interaction), which is not the case for the “bare” operators considered here. In the future, when consistent electroweak operators are available for different Hamiltonians at high order in EFT, the universality of operators can be reconsidered in detailed calculations. However, even without operators sufficiently refined to test for universality directly, an explicit demonstration of universality in SRG evolved potentials would provide strong support for universality in other operators.

This is apparent when we consider the spectral representation of an operator, as in

Eq. (2.8) ,

$$O_s(k, k') = \sum_{ij} O_{ij} \langle k | \psi_i(s) \rangle \langle \psi_j(s) | k' \rangle .$$

To understand how this implies universality for operators, recall that the Hamiltonian in momentum space can also be rewritten as

$$H_s(k, k') = \sum_i E_i \langle k | \psi_i(s) \rangle \langle \psi_i(s) | k' \rangle . \quad (2.22)$$

If, after sufficient evolution in s , two Hamiltonians $H_s^{(1)}$ and $H_s^{(2)}$ show universality at low momenta it must be true that the low energy eigenstates also approach a universal form — particularly in light of the increasingly decoupled nature of the interaction. In other words, the extent to which

$$\langle \psi_i^{(1)}(s) | \psi_j^{(2)}(s) \rangle \approx 1 \quad \text{for } i = j \quad (2.23)$$

and

$$\langle \psi_i^{(1)}(s) | \psi_j^{(2)}(s) \rangle \approx 0 \quad \text{for } i \neq j \quad (2.24)$$

for evolved states corresponding to E_i provides a basis independent measure of universality. The energies up to which one might expect this to be true would naively correspond to the maximum range of the experimental data to which the potentials are matched (around 300 MeV), but this requires further study.

Nevertheless, assuming a universal form of the energy eigenstates, we now see that operators must also approach a universal form in general. For operators $O_s^{(1)}$ and $O_s^{(2)}$ corresponding to the Hamiltonians $H_s^{(1)}$ and $H_s^{(2)}$ to reproduce the same predictions for experimental data at low momenta, the matrix elements $O_{ij}^{(1)}$ and $O_{ij}^{(2)}$ must clearly also match for sufficiently small i and j . One should note that, due to the nature of the outer product expansion, the universal form of the operators may not be visually apparent in momentum space without limiting the summation in Eq. (2.8) to the universal regime.

It is also interesting to note that, given sufficiently detailed experimental data or (more likely) the results from a lattice calculation, one could construct the operators for a given probe consistent with a universal evolved potential directly from the matrix elements O_{ij}

in the eigenbasis of the Hamiltonian.

2.5 Chapter Summary

In this chapter, we have examined the evolution of operators via the SRG with restricted application to the deuteron. We considered only the most commonly used generator $G_s = [T_{\text{rel}}, H_s]$ with normal ordering in the vacuum. At this two-particle level it is easy to ensure that the transformations are unitary to high accuracy, so the invariance of matrix elements is assured. Thus our focus is instead on the nature of the evolved operators: Does a form of decoupling apply? Do operators become increasingly complicated as the wave functions become increasingly less correlated? How large are induced two-body contributions to various one-body operators?

By considering the operator matrix elements in momentum representation both with and without deuteron wave functions included, we are able to follow the flow of strength. Because the transformations are unitary, the integrated value does not change with λ , but the nature of the operator does. There is little evolution in long distance operators, whereas high-momentum operators must evolve significantly to compensate for suppression of high momenta in low-energy wave functions. In the end, one can see that the movement of the strength in the operator expectation values is given by the evolution of the eigenstates of the Hamiltonian itself. Moreover, we find that decoupling succeeds for operator expectation values in general, not just for the binding energies.

The momentum distribution is particularly interesting because the evolution of high-momentum operators leads to their strength flowing completely to low momentum. Thus while the deuteron wave function has rapidly decreasing support at the high momentum, its matrix elements are preserved without pathologies in the transformed operators. Indeed, operator matrix elements are less sensitive to details, as evidenced by the improved effectiveness of estimates using variational wave functions. Decoupling for operators follows as the contributions from higher energy/momentum basis states become unimportant, allowing truncation. This was explicitly illustrated in Figures 2.5 and 2.6. The generality of

these conclusions is evident by considering the eigenvector expansion of the SRG unitary transformations, which dictates the flow of strength. Moreover, there is good reason to believe that operators evolve to a universal form independent of the potential for which they are constructed.

For low-momentum operators, which also includes the low-momentum part of one-body electromagnetic form factors, there is relatively little running and therefore only small induced two-body parts (which for $A = 2$ is simply the difference between the initial and the evolved result). In general, if the initial operator matrix elements pick up their strength predominantly at long distance, the operators will evolve only slightly until λ is small. For electroweak operators, the real interest is in few- and many-body systems, where the simpler SRG-evolved wave functions are most advantageous. The implication of evolution in many-body systems will be considered in the next chapter.

In closing, we reiterate that the favorable consequences of the SRG reflect a specific realization of the more general observation that the RG allows one to focus on the most relevant degrees of freedom in a physical problem [86]. Thus, an evolution to low momentum for nuclear systems can be win-win not only for the Hamiltonian and wave functions but for operators as well. The SRG has some special advantages in practice because it uses operator flow equations that can be applied in any convenient basis with a variety of options for tailoring the flow. Furthermore, residual dependence on the flow parameter s or λ becomes a powerful tool for assessing approximations. These advantages will become increasingly apparent as we explore the many-body evolution of operators, and their applications.

Chapter 3

MANY-BODY EVOLUTION OF OPERATORS

To maintain the advantages of SRG evolution in nuclear calculations for systems of $A > 2$ we must account for the many-body induced evolution of the Hamiltonian as well as other operators . Here we demonstrate that the many-body evolution of operators is fully defined in each subspace of specific particle number. This feature is used to develop operator evolution and embedding procedures for use in many-body calculations. A model one-dimensional system is used as a lab for testing these methods in preparation for realistic calculation. Operator evolution techniques for solution methods which utilize second quantized formalism are also developed.

Until now, the study of operator evolution and its fundamental properties via the SRG has been confined to the two-body sector and smaller. However, as learned in Chapter 1, additional many-body forces are critical for reproducing experimental data (with most interactions) for systems with more than two particles. Moreover, the SRG induces its own many-body forces as high- and low-momentum degrees of freedom are decoupled in the interactions. These must be accounted for up to at least the three-body level, and possibly the four-body level. Consequently, the associated evolution of other operators is necessary for a consistent and convergent calculation of other expectation values in a given state.

The challenge now is to confirm that the advantages of the operator flow properties found in the previous chapter carry over into larger many-particle spaces, and that a hierarchy of many-body operator contributions exists so that reasonable truncations can be made in those spaces. In conjunction with this, and sometimes as a necessary prerequisite, it is

important to develop practical methods to embed operators in many-particle space, evolve those operators, and extract their many-body components. Ideally, these methods need to be useful for a wide variety of quantum many-body solution techniques. As such, the discussion in this chapter will be kept general at first, then applied to a specific technique as an example.

In Section 3.1 we develop the foundation for understanding many-body operator evolution through a second-quantized analysis of operator evolution in the many-body sector. Based on this, we present the basic strategies in Section 3.2 that one may employ to evolved operators in a many-particle space and extract the many-body components needed for application to realistic nuclear solution techniques. We then test these methods extensively in Section 3.3 using a 1D model system of bosons, and discuss how the methods can be implemented in a basis-expansion type many-body solution technique. Important considerations for applying the results of this chapter to realistic, three-dimensional calculations are discussed in Section 3.4. Finally, we develop the technology in Section 3.5 to include many-body evolved operators in solution techniques which rely on the formalism of second quantization.

3.1 Analysis in Second Quantization

The SRG production and evolution of induced many-body operators can be most clearly understood by considering the evolution equations in second-quantized form. In this work, we define the second-quantized states relative to the vacuum. As such, recall that we can write any single-particle state with the particle creation and annihilation operators as $|i\rangle = a_i^\dagger |0\rangle$ where $[a_i, a_j^\dagger] = \delta_{ij}$. Thus, many-particle basis states are given by

$$|i, j, k, \dots\rangle = a_i^\dagger a_j^\dagger a_k^\dagger \cdots |0\rangle \quad (3.1)$$

where i, j, k, \dots here label the quantum numbers of different single-particle states in any given basis. A one-body operator is given by

$$\sum_{ik} a_i^\dagger \langle i | \hat{O}^{(1)} | k \rangle a_k, \quad (3.2)$$

a two-body operator by

$$\left(\frac{1}{2!}\right) \sum_{ijkl} a_i^\dagger a_j^\dagger \langle ij | \hat{O}^{(2)} | kl \rangle a_k a_l, \quad (3.3)$$

etc. The SRG flow equation of Eq. (2.3),

$$\frac{d\hat{O}_s}{ds} = [[T_{\text{rel}}, H_s], \hat{O}_s]$$

can thus be written in second-quantized form (e.g., using a two-body interaction) as

$$\frac{d\hat{O}_s}{ds} = \left[\left[\sum_{ij} T_{ij} a_i^\dagger a_j, \sum_{i'j'} T_{i'j'} a_{i'}^\dagger a_{j'} + \frac{1}{2} \sum_{pqkl} V_{pqkl|s} a_p^\dagger a_q^\dagger a_l a_k \right], \hat{O}_s \right] \quad (3.4)$$

where $V_{pqkl|s} = \langle pq | V_s^{(2)} | kl \rangle$ and – since we are otherwise generally working in relative coordinates – the second-quantized expression here is equivalent to our standard formulation because the center-of-mass (COM) motion commutes with the relative interaction. So, it is clear that at each step in the solution of the SRG differential equation the commutators produce terms with additional creation and annihilation operators.

In order to demonstrate this explicitly, and to better understand the many-body dependence of evolved operator components, it is sufficient to expand the commutators in this expression for a single (infinitesimal) step in the SRG evolution. We can then take advantage of the fact that the only non-vanishing contraction in the vacuum is given by $\overline{a_i a_j^\dagger} = \delta_{ij}$ to normal order the expansion. In this form, it is clear which matrix elements contribute to many-body induced operators, and how they contribute. Upon iterating the differential equation, the dependence found here for generic operator matrix elements remains the same, even though additional many-body components are generated to all orders. The details of this analysis are left to Appendix A.2. Here, we summarize the main results.

After expanding this expression and making contractions to get a normal ordered form, etc., one finds that the end result, for our purposes, is that the SRG evolved operator

$$\hat{O}_s = \hat{O}_s^{(1)} + \hat{O}_s^{(2)} + \cdots + \hat{O}_s^{(n)} + \cdots \quad (3.5)$$

will indeed have additional contributions at all levels of n so that $\hat{O}^{(n)} \neq \hat{O}_s^{(n)}$. Critically, we find that any \hat{O}_s (including the interaction) is completely determined up to its $\hat{O}^{(n)}$

contribution by its n -body matrix elements. More specifically, this means that if we evolve an operator \hat{O} in a one-particle space to \hat{O}_s , this determines $\hat{O}_s^{(1)}$ for all $n \geq 1$. If we evolve an operator \hat{O} in a two-particle space to \hat{O}_s , this determines $\hat{O}_s^{(2)}$ for all $n \geq 2$. If we evolve an operator \hat{O} in a three-particle space to \hat{O}_s , this determines $\hat{O}_s^{(3)}$ for all $n \geq 3$, and so on. This is a key result of the second-quantized analysis, which permits us to develop an algorithm for the evolution and extraction of many-body operators, as described in the following section.

We should also point out that $\hat{O}_s^{(1)} = \hat{O}^{(1)}$ using the conventional choice of generator $G_s = T_{\text{rel}}$ because, considering the second quantized form of the equations, we see that the commutators in the SRG flow equation will not produce any additional one-body components with this generator. This is a consequence of the fact that the one-body operators involved here commute. In general, this may not be the case.

3.2 Evolution, Embedding, and Extraction of Operators

If we wish to calculate the expectation value of an operator for a system in a manner consistent with the SRG-evolved Hamiltonian used to determine the wave function of that system, we need to retain the same number of many-body components for the operator as for the Hamiltonian in question. In principle, for the evolution of an A -body system to remain unitary, we need to evolve the Hamiltonian and operators in the A -body space (so that all 1-, 2-, ..., A -body operators are included). However, this may not be necessary in order to achieve sufficiently accurate results, as found in previous calculations of the binding energy, as discussed in Chapter 1. The hierarchy of many-body forces provides a means to truncate the evolution in the many-particle sector once a sufficient level of convergence has been reached (if this were not true, calculations would quickly become impractical). A similar hierarchy for many operators (which possess a hierarchy prior to evolution) allows us to do the same for those operators in general.

The calculation of evolved operator expectation values proceeds in the same way in the

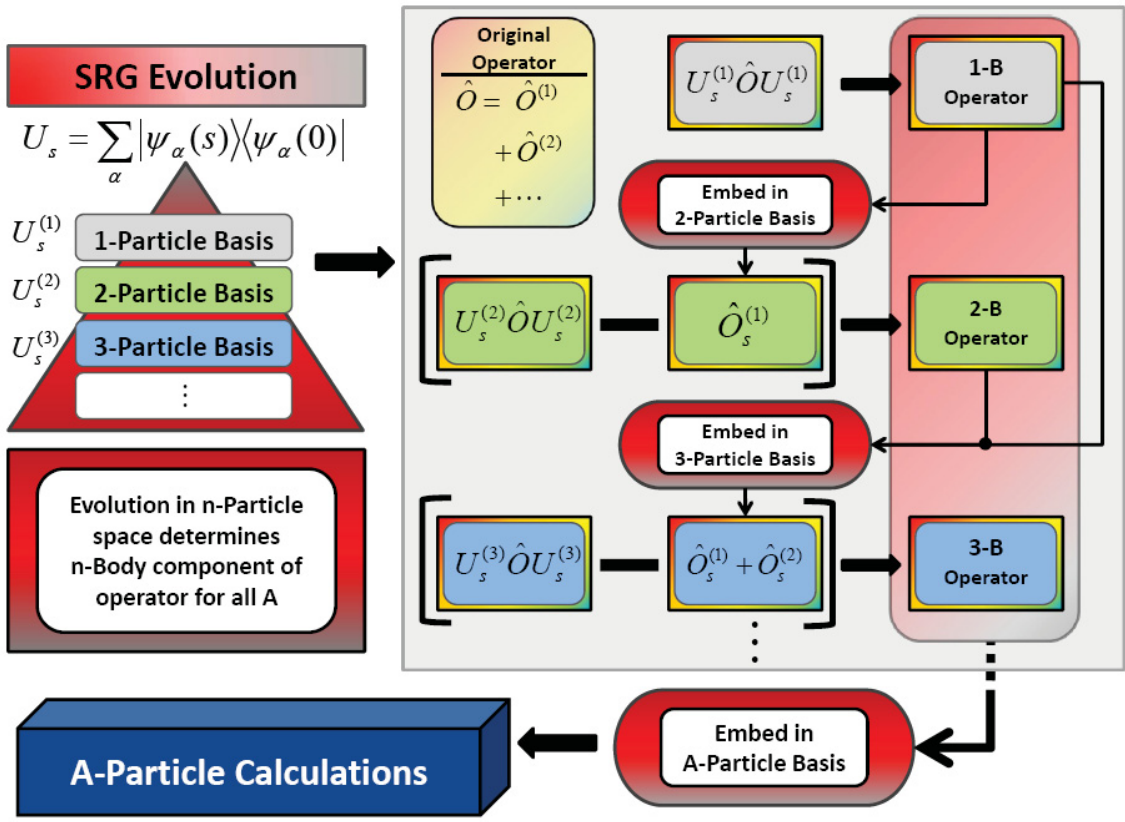


Figure 3.1: Operator evolution and embedding process diagram.

many-particle space as for two particles via

$$\langle \hat{O}_s \rangle = \langle \psi_{\alpha}(s) | \hat{O}_s | \psi_{\alpha'}(s) \rangle,$$

as is well known. The challenge now is that \hat{O} has many-body components, and it, as well as the wave functions $\psi_{\alpha}(s)$, are embedded in a many-particle space. The size of the space is naturally determined by the size of the system being calculated: for an A -particle system we need an effective (depending on the solution technique being used) A -particle space.

Our findings in the previous section permit us to deal with the many-body evolved components of operators in practice. What we can develop from those findings is, in principle, a straightforward algorithm for the evolution, extraction, and embedding of operators. However, as we will see, some special considerations must be addressed under certain cir-

cumstances. This algorithm is summarized in the process diagram of Figure 3.1. The flow of the process is indicated by the arrows.

In the upper left corner of the diagram we indicate that SRG evolution (i.e., solving of the SRG differential equation) must be carried out in the one-particle, two-particle, etc., basis . . . as many as are needed for good convergence of the expectation values to be calculated. As usual, a sufficiently large basis must be used to capture the initial details of the Hamiltonian and other operators. The evolution can be carried out iteratively as indicated by the final results; the number of many-body operators does not have to be known beforehand. In each basis, the unitary transformation can then constructed. If it is easier to evolve the operators individually using the flow equations for technical reasons, this must be done wherever the transformation is applied.

So, moving on into the upper right box of the diagram, we may begin with any many-body operator as defined in the same scheme as the Hamiltonian (by chiral EFT, for example). Evolution is first carried out in the one-particle basis using the unitary transformation. This then defines the one-body operator completely, as discovered in the previous section. We then embed this evolved result into a two-particle basis. Concurrently, we evolve the initial operator in the same two-particle basis. This completely evolves the one-body and two-body parts of the initial operator. In order to disentangle these components, we can simply subtract the one-body only evolved and embedded operator from the operator evolved completely in the two-particle space. The result is the two-body evolved component of the operator. This includes evolution of the initial operator in the two-body sector, as well as induced two-body components from the initial one-body part of the operator (if it was present initially). This process is repeated to extract the three-body evolved operator, only now we must embed both the one-body and two-body evolved operators in the basis to subtract from the fully evolved operator including one-, two-, and three-body components. This operator includes the induced three-body components from the fewer-body operators, as well as evolution from any initial three-body operator. As stated already, the process is repeated until sufficient convergence is reached in the final calculation.

The final two segments in the process diagram indicate this calculation. Prior to this

stage, any truncation of the basis which can be achieved thanks SRG decoupling must be performed. The level of truncation here is also dictated by the final results. The evolved and extracted operators can then be embedded in any A -particle basis to calculate properties as desired in an A -particle system.

The ability to evolve and extract the individual components of these many-body operators is critical to successful many-body calculations. This is because for use in the solution techniques discussed in Chapter 1, the various one-body, two-body, etc., components must be treated differently (when embedding in larger spaces, for example). It is especially clear that the process proposed here can be carried out when working in a single-particle, first-quantized basis, since this corresponds to the single-particle basis underlying the arguments in second quantization outlined above. Indeed, these are basis independent results. However, if we are working in a relative coordinate Jacobi basis, for example, special care must be taken.

3.2.1 Jacobi Basis Evolution Considerations

In a single-particle basis all of the many-body components of operators can be expressed simply in terms of single particle coordinates. This is a coordinate system where the position or momentum of a single particle is identified by a single coordinate variable. As a result, the evolution, embedding, and extraction procedure for operators discussed above can be carried out directly. Often it is advantageous to use an alternative set of coordinates, however, which can allow for a significantly smaller basis size when performing many-particle calculations.

The Jacobi basis is particularly useful for analyzing systems which are independent of their COM motion. More specifically, this is true if the interactions within the system can be expressed in terms of the relative distance between particles. These coordinates are used in a number of the solution techniques discussed in Chapter 1. The Jacobi coordinates are a particular parameterization of these distances as a new set of coordinates. In this parameterization, each additional particle coordinate is defined relative to the COM of the previous coordinates. For the purposes of this chapter we consider a system of identical particles of mass $m = 1$. This will be true of the model system described below, and can be

used as a reasonable approximation to particles in an atomic nucleus due to approximate isospin symmetry. So, the Jacobi coordinates of an A -particle system can be written

$$p_j = \sqrt{\frac{j}{j+1}} \left[\left(\frac{1}{j} \sum_i^j k_i \right) - k_{j+1} \right], \quad (3.6)$$

for $j < A$ and

$$p_A = \frac{1}{A} \sum_i^A k_i \quad (3.7)$$

which is the COM coordinate of the system, and may be neglected for translationally invariant interactions (hence the advantage of these coordinates). We use the notation where k_i refers to the absolute coordinates and p_i to the relative coordinates. In systems of unequal mass particles, the Jacobi coordinates must be redefined appropriately.

In the Jacobi basis the same procedure as used in the single-particle basis can be followed for the evolution and embedding of initial two-body, three-body, and greater n -body operators. These operators can be expressed in terms of the same Jacobi coordinates in any A -particle basis (restricted by the necessary requirement that $n \geq A$). So, they are necessarily defined in the same way for any size system. Some well known operators which fall into this category include the translationally invariant Hamiltonian, the r^2 operator, and the operator for the relative momentum distribution. However, special consideration must be taken for one-body operator evolution and embedding. Operators which fall into this category include the number operator for the single particle momentum distribution, and the operators for electromagnetic form factors at leading order.

Here, as worked out in Appendix A.1, we see that a special “trick” must be employed to identify a Jacobi coordinate in the rest frame of the system with a single particle coordinate. Specifically, we find that

$$p_{A-1} = -\sqrt{\frac{A}{A-1}} k_A, \quad (3.8)$$

which is a consequence of the fact that we may take the COM motion to be zero with a translationally invariant interaction. In a symmetrized basis, it is thus sufficient to use the second to last Jacobi coordinate to define a one-body operator (which is most naturally associated with single-particle coordinates).

The difficulty arises then – when one wishes to use the same operator in different A -particle bases – that the operator is defined differently depending on the A -particle space. It must be effectively “boosted” to a different frame of reference. As a result, one must be particularly careful in naively applying the evolution and extraction procedure defined above for one-body operators. See, for example, the calculation of the momentum distributions in Figure 3.2 for various A -particle bosons systems in a one-dimensional model (described below) with the number operator implemented as the process described by Figure 3.1 in the previous section would naively suggest. The two-particle calculation is fine, since all operators are initially defined in this basis and evolution is unitary. But in the larger spaces, the calculation either fails completely, or we have unusually large neglected many-body contributions. We now explore this issue more carefully.

Since we confined ourselves to the Jacobi coordinates in this solution technique, the smallest basis we had access to for our evolution is the two-particle basis. There is no evolution in the one-body sector using our standard SRG generator and an interaction which contains no one-body components, so this shouldn’t be an issue. However, the one-body operator can no longer be defined once and for all in the smallest available basis and then embedded into larger bases for evolution, even if we scale the final results according to Eq. (3.8).

It turns out there are a number of issues to consider for dealing with the problem at hand. For later reference, we’ll number these issues, as each results in a different method for dealing with the operator evolution and extraction problem.

1. Physically, the source of this problem is due to the fact that a one-body operator which probes a specific momentum for a single particle in the rest frame of a two-particle system will probe a different momentum when embedded into the rest frame of a three-particle system, and so on. The single particle momenta in the three-particle rest frame, for example, will contain a momentum component relative one of the particles, as well as a component from the COM motion of that two-particle subsystem. We can use this picture to explicitly write a corrected n -body induced operator from the corresponding $(n - 1)$ -body operator coordinates.

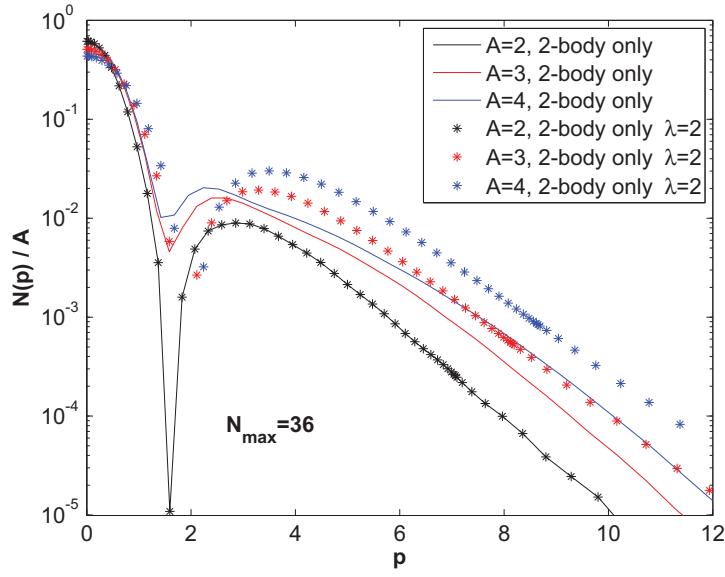


Figure 3.2: Naive implementation of the many-body evolution of number operators to calculate the momentum distribution of a one-dimensional model system. The solid lines are exact results. The starred points are the result of a naive (incorrect) implementation of the two-body only evolution to $\lambda = 2.0$.

Given an initial one-body operator $\hat{O}(q) = \hat{O}^{(1)}(q)$ which probes a function of momentum q , we embed the operator in a two-particle Jacobi basis, using the $q \propto p_{2-1}$ coordinate with the appropriate factor. After applying the unitary transformation in this basis we have

$$\hat{O}_\lambda(q_2) = \hat{O}_\lambda^{(1)}(q_2) + \hat{O}_\lambda^{(2)}(q_2) \quad (3.9)$$

where q_i corresponds to our momentum probe in the i^{th} -body rest frame. Note: higher body forces are produced in principle, but only two components are written here because working in a two-particle basis effectively truncates the hierarchy – hence the recursive procedure to find these operators. Subtracting the one-body (evolved) operator in this basis, we are left with $\hat{O}_\lambda^{(2)}(q_2)$.

But now suppose we need embed this induced two-body operator properly in the three-particle basis. First, one must in principle actually generate the evolved $\hat{O}_\lambda^{(2)}(q_2)$ for all values of q_2 which are not suppressed by the wave function in order to account

for all pieces of the two-body operator in the three-particle space. We then use the standard procedure to embed all of the evolved two-body operators into the three-particle basis. Using our picture of the neglected total two-particle COM motion, we can write

$$\widehat{O}_\lambda^{(2)}(q_3) = \int dq_2 \int dQ_2 \quad \widehat{O}_\lambda^{(2)}(q_2)\delta(q_3 - (q_2 + Q_2)) \quad (3.10)$$

where Q_i corresponds to the COM momentum of the i^{th} -body subsystem. Q_i can also be conveniently identified as proportional to the single-particle coordinate / $(i-1)$ Jacobi coordinate because we are in the COM frame of the i -particle system. At this point we can evolve the one-body operator in the three-particle basis to generate

$$\widehat{O}_\lambda(q_3) = \widehat{O}_\lambda^{(1)}(q_3) + \widehat{O}_\lambda^{(2)}(q_3) + \widehat{O}_\lambda^{(3)}(q_3) \quad (3.11)$$

and we can use our expression for $\widehat{O}_\lambda^{(1)}(q_3)$ and $\widehat{O}_\lambda^{(2)}(q_3)$ to isolate $\widehat{O}_\lambda^{(3)}(q_3)$. The cycle repeats for embedding in the four-particle space. Now we must carry out

$$\widehat{O}_\lambda^{(2)}(q_4) = \int dq_3 \int dQ_3 \quad \widehat{O}_\lambda^{(2)}(q_3)\delta(q_4 - (q_3 + Q_3)) \quad (3.12)$$

and

$$\widehat{O}_\lambda^{(3)}(q_4) = \int dq_3 \int dQ_3 \quad \widehat{O}_\lambda^{(3)}(q_3)\delta(q_4 - (q_3 + Q_3)) \quad (3.13)$$

before using these operators, and so on. In the one-dimensional model used throughout much of this thesis, this procedure is computationally feasible. However, as one might suspect, the full three-dimensional integrals to realize this procedure numerically for calculations of atomic nuclei could become prohibitive. Moreover, we have only considered an initial operator which depends on a simple one-coordinate momentum probe for simplicity. Generalizing this procedure for operators defined by non-local components in momentum space, given by $\widehat{O}^{(1)}(q, q')$ in general, would be even more difficult. Luckily, one may employ other methods to realize the same effect.

2. Certainly, one can perform the evolution and extraction procedure in a single-particle basis as described in the previous section, and then transform the induced operators into the Jacobi basis if needed for use in the the desired many-particle solution

technique. This has the advantage of being conceptually straightforward. However, generating a sufficiently complete basis for greater and greater induced many-body forces can also quickly become prohibitive. Moreover, one may not be able to use this technique to easily utilize the existing SRG code infrastructure for solutions to the quantum many-body problem.

3. As it turns out, it is not nearly as difficult as the previous two methods might suggest to evolve and extract operators. At the same time we can reduce the size of the bases needed to that of the Jacobi coordinates, as originally desired. One must simply define the one-body operator carefully and correctly in each few-particle basis according to Eq. (3.8). In this way equivalent operators will be evolved in each basis. It will not do to simply define the operator in the smallest (two-particle) basis and scale the results accordingly after SRG evolution is applied. Even though the actual matrix elements of the initial operator would be the same in each basis, the operators will no longer be the same with respect to SRG evolution.

It can be demonstrated in *ab-initio* calculations that this is, in fact, equivalent to Method 1 although it may not be obvious at first glance. The i -body operators given by the integrals in Method 1 have been defined so that the $(i - 1)$ -body rest frame contributions to the operators are different for each “slice” of the operator in the $(i - 1)$ -body COM coordinates. In this method, the same rest frame $(i - 1)$ -body operator is defined for all values of the $(i - 1)$ -body COM momentum. Ultimately the equivalence of these methods stems from the translational invariance of the interaction and generator used. Had this not been the case, then Method 1 or Method 2 would have to be employed, although it is unlikely we would be working in the Jacobi basis in the first place. Since the interactions depend only on the relative coordinates, the sum of expectation values over $(i - 1)$ -body COM momentum probes for specific rest frame coordinates was equivalent to simply probing an individual rest frame momentum coordinate (independent of the $(i - 1)$ -body COM) once and for all for induced operators. We emphasize, however, that the lack of translational invariance

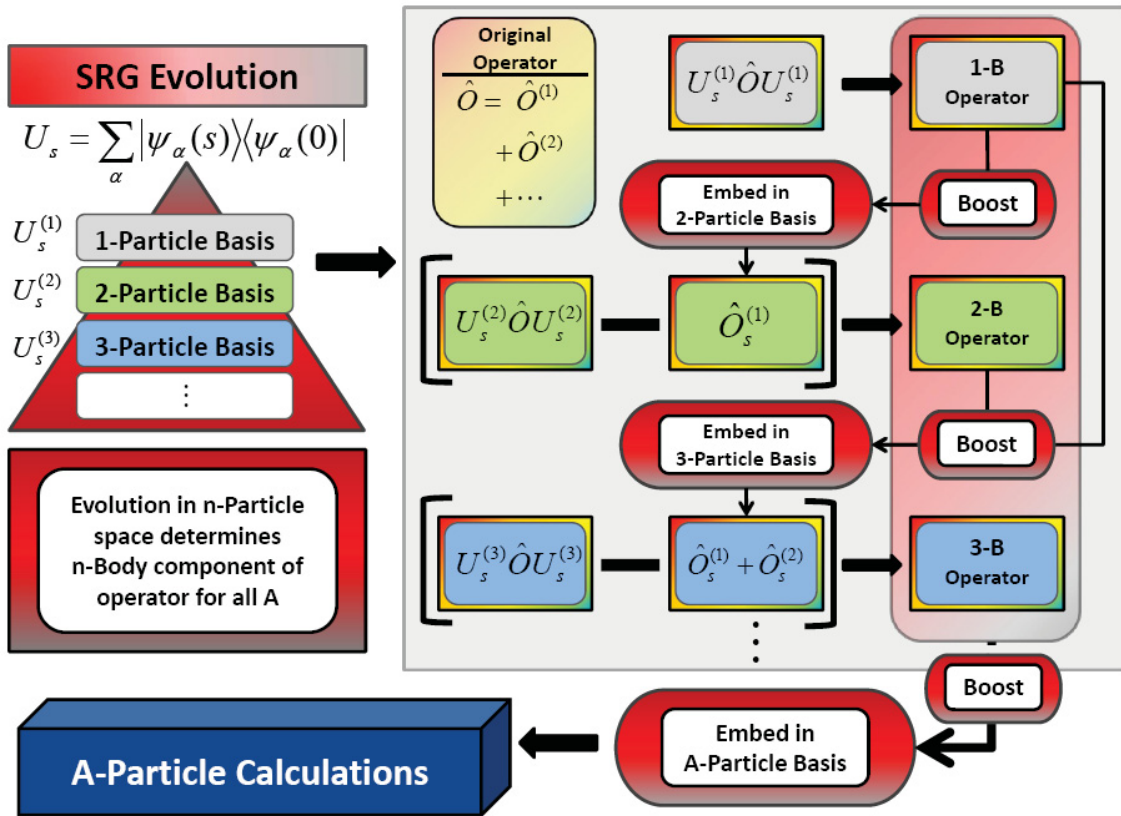


Figure 3.3: Revised operator evolution and embedding process diagram – care must be taken to account for a boost into the relative coordinate frame for some operators.

for the initial operator must still be accounted for as described.

Although not incorrect per se, the process described by the diagram in Figure 3.1 can be misleading for certain operators. As such we have revised original embedding process diagram in Figure 3.3 to emphasize the need to account for proper “boosting” of non-translationally invariant operators prior to SRG evolution. As possibly the simplest non-trivial example which can be used to probe a wide range of momenta, we continue to consider the number operator to the explore these issues and methods, in a simple one-dimensional model.

3.3 Ab-initio Calculations: A 1D Model

The full SRG has, in fact, already been implemented to calculate wave functions and binding energies in a model one-dimensional (1D) system, as well as in realistic three-dimensional (3D) systems [11, 72]. Using the 1D code described in [72], we can take the first steps here in demonstrating that operators can be implemented and transformed using the methods described above to evaluate expectation values in few-body systems. Moreover, we can show that much of the behavior demonstrated for the two-body system translates directly to the few-body system. However, as we will see, we must carefully account for the lack of Galilean invariance for certain operators, as described above. Some additional complications will also be introduced due to intrinsic properties of the harmonic oscillator basis itself. But first, let us briefly review the model system used in [72] and the specific instantiation of the interaction for that system used here.

This model is a 1D system of A bosons with equal mass $m \equiv 1$ and a Hamiltonian in single-particle coordinates k_i given by

$$H = \sum_{i=1}^A \frac{k_i^2}{2m} + \sum_{i < j=1}^A V(k_i, k_j). \quad (3.14)$$

In practice, the system is initially defined on the relative momentum Jacobi basis of Eq. (3.6)

$$p_j = \sqrt{\frac{j}{j+1}} \left[\left(\frac{1}{j} \sum_i^j k_i \right) - k_{j+1} \right],$$

and the interaction, originally introduced in Ref. [87], is chosen to resemble the radial features of typical NN potentials,

$$V(p, p') = \frac{V_1}{2\pi\sqrt{2}} e^{-(p-p')\sigma_1^2/8} + \frac{V_2}{2\pi\sqrt{2}} e^{-(p-p')\sigma_2^2/8}, \quad (3.15)$$

where $V_1 = 12$, $\sigma_1 = 0.2$, $V_2 = -12$, and $\sigma_2 = 0.8$. We only look at two-body initial interactions here, but keep in mind that the SRG induces up to A -body interactions in $A > 2$ -body spaces. Also, thanks to the symmetry of the system, the sum over interacting pairs in Eq. (3.14) can be accomplished by calculating a single pair and multiplying by the appropriate factor of two-body combinations, $C[A, 2] = \frac{1}{2}A(A-1)$, in the few-body system;

one need not rotate the interaction into all possible permutations of Jacobi momenta pairs. The kinetic energy term, although typically defined by a one-body operator, can also be described by a two-body operator in a translationally invariant system, as discussed in Appendix A.1. Thus, our Hamiltonian for use with properly symmetrized states is given by

$$H = C[A, 2] \left[\frac{p_1^2}{2m} + (V(p_1, p'_1)) \right] \prod_{j>1}^{A-1} \delta_{p_j p'_j}, \quad (3.16)$$

where a delta function over the other Jacobi coordinates is shown explicitly. The system is then solved by calculating matrix elements of the Hamiltonian in the symmetrized basis states of the harmonic oscillator, and finding its eigenvectors and eigenvalues.

These symmetrized basis states are labeled by $|N_A i_A\rangle$, where N_A signifies the maximum number of total oscillator excitations the system may have in that state, and i_A labels the degeneracies for each state of a given N_A (there are multiple configurations of particles which may result in a state of total oscillator number N_A). The states run from $N_A=0$ to N_{\max} , where a larger N_{\max} implies a more accurate representation and a greater computational cost. The actual process of embedding our momentum space Hamiltonian into the symmetric oscillator basis involves first introducing a set of harmonic oscillator states $|n_j\rangle$ which correspond to the Jacobi coordinates of Eq. (3.6) with $n_j = 0, \dots, N_{\max}$ for each j . These are simply eigenstates in order of increasing energy of the harmonic oscillator Hamiltonian,

$$H = \frac{p^2}{2m} + \frac{1}{2}m\omega^2 r^2 \quad (3.17)$$

where ω is used as a variational parameter in this method, and r is the coordinate space Jacobi coordinate . A general transformation from one basis to the other has the form

$$\prod_{j=1}^{A-1} \langle p_j | n_j \rangle, \quad (3.18)$$

and these states can be projected into the symmetric oscillator basis via a sequence of matrices of the form

$$\langle n_1 | N_2 i_2 \rangle \quad (3.19)$$

and

$$\langle N_{A-1}i_{A-1}; n_{A-1} \| N_A i_A \rangle, \quad (3.20)$$

also known as coefficients of fractional parentage. For details on the construction of these matrices, please see [72]. Thus, for example, the two-body momentum space Hamiltonian can be embedded into the symmetric harmonic oscillator basis via the matrix expression

$$\langle N_2 i_2 \| n_1 \rangle \langle n_1 | p_1 \rangle \langle p_1 | H | p'_1 \rangle \langle p'_1 | n'_1 \rangle \langle n'_1 \| N'_2 i'_2 \rangle. \quad (3.21)$$

This expression can be implemented in any numerical software package or code, as done with the coordinate transformations of the deuteron operators described above. It is then a “simple” matter to diagonalize this matrix (it is not so simple in that the matrix size, along with the time to calculate the matrix, is one of the major limitations of the method – it is here that the SRG may prove to be a valuable tool) in order to solve for the eigenvalues and eigenstates of the system. The SRG evolution is also applied in this basis.

This few-body solution method is formally, and technically (though much simpler in 1D), similar to the *ab initio* no-core shell model method of calculating properties of atomic nuclei. Moreover, results found in this 1D system with respect to the SRG have had direct analogues in full 3D calculations completed thus far [11, 72]. As such, we again expect that results found here for operator evolution will carry over in the same manner.

3.3.1 Oscillator Basis Representation: Jacobi Coordinates

Given this discussion, it is relatively straightforward to embed operators into the few-body harmonic oscillator basis. The same methods used to embed the Hamiltonian can be used to embed any operator, which has been projected into relative momentum Jacobi coordinates, into the harmonic oscillator basis. A general transformation can thus be built up via the

following expression:

$$\begin{aligned} & \left[\prod_{k=3}^A \langle N_k i_k \| N_{k-1} i_{k-1}; n_{k-1} \rangle \right] \langle N_2 i_2 \| n_1 \rangle \left[\prod_{j=1}^{A-1} \langle n_j | p_j \rangle \right] \langle p_1 \dots p_{A-1} | \hat{O} | p'_1 \dots p'_{A-1} \rangle \\ & \times \left[\prod_{j=1}^{A-1} \langle p'_j | n'_j \rangle \right] \langle n'_1 \| N'_2 i'_2 \rangle \left[\prod_{k=3}^A \langle N'_{k-1} i'_{k-1}; n'_{k-1} \| N'_k i'_k \rangle \right]. \end{aligned} \quad (3.22)$$

This is for a generic A -body operator. However, to be more clear, let's consider the case of a two-body operator with the matrix elements $\hat{O}^{(2)}$. Just as in Eq. (3.21), we can write

$$\langle N_2 i_2 | \hat{O}^{(2)} | N'_2 i'_2 \rangle = \langle N_2 i_2 \| n_1 \rangle \langle n_1 | p_1 \rangle \langle p_1 | \hat{O}^{(2)} | p'_1 \rangle \langle p'_1 | n'_1 \rangle \langle n'_1 \| N'_2 i'_2 \rangle. \quad (3.23)$$

To embed this in the three-particle space, we must effectively include a delta function on the second Jacobi coordinate in the product basis space (since there is no dependence on this coordinate for two-body relative momentum operators) before applying the matrix of coefficients of fractional parentage to transform into the symmetrized space. As such,

$$\begin{aligned} \langle N_3 i_3 | \hat{O}^{(2)} | N'_3 i'_3 \rangle &= \langle N_3 i_3 \| N_2 i_2; n_2 \rangle \langle n_2 | \langle N_2 i_2 | \hat{O}^{(2)} \delta_{n_2, n'_2} | N'_2 i'_2 \rangle | n'_2 \rangle \\ &\times \langle N'_{k-1} i'_{k-1}; n'_{k-1} \| N'_3 i'_3 \rangle. \end{aligned} \quad (3.24)$$

In the same way, this two-body operator can be iteratively embedded in larger A -particle spaces.

Care must also be taken to treat the many-body components of the operator individually in the correct way. A general operator \hat{O} for an A -body system can be written as

$$\hat{O} = \hat{O}^{(1)} + \hat{O}^{(2)} + \hat{O}^{(3)} + \dots + \hat{O}^{(A)}, \quad (3.25)$$

where the $\hat{O}^{(n)}$ label the $n = 1, 2, 3, \dots, A$ -body components of the operator. Here, each component must also be embedded in the A -body symmetrized space with the appropriate combinatorial factor $C[A, n] = \frac{A!}{n!(A-n)!}$. When embedding iteratively as we have described, the combinatorial factor must also be divided out when embedding into the next space, to be consistent (i.e., at each new level in the operator embedding we must multiply the symmetrized n -body operator matrix elements by $C[A, n]/C[A - 1, n]$). In general, the

details of this embedding can be somewhat more involved, depending on the basis and operator used.

For example, when embedding a one-body operator we have seen that we must use the last Jacobi coordinate with an appropriate scaling factor in momentum space, as given by Eq. (3.8). To isolate this last coordinate, we can simply skip to the last step of the embedding procedure just described, including, effectively, an identity matrix for the 1-body through ($A - 1$)-body embedded operators in the partially symmetrized ($A - 1$) product space so that

$$\begin{aligned} \langle N_A i_A | \hat{O}^{(1)} | N'_A i'_A \rangle &= \langle N_3 i_3 | N_{A-1} i_{A-1}; n_{A-1} \rangle \langle N_{A-1} i_{A-1} | n_{A-1} | p_{A-1} \rangle \\ &\times \langle p_{A-1} | \hat{O}^{(1)} | p'_{A-1} \rangle \langle p'_{A-1} | n'_{A-1} \rangle | N'_{A-1} i'_{A-1} \rangle \langle N'_{k-1} i'_{k-1}; n'_{k-1} | N'_3 i'_3 \rangle. \end{aligned} \quad (3.26)$$

It should also be noted that to actually implement the momentum-space representation of the operator prior to oscillator space embedding, a different momentum-space mesh may be needed to adequately account for the scaling factor for different A -particle bases. Otherwise, an interpolation routine can also be used successfully for simple operators so that the momentum to oscillator basis matrices don't need to be recalculated. We will address in the following section some of the the additional specifics involved in applying the operator evolution and extraction methods described in Section 3.2.

At this stage, what we have are matrix elements of any given operator in our basis, written here as

$$\langle N'_A i'_A | \hat{O} | N_A i_A \rangle. \quad (3.27)$$

In this matrix form, the operator can then be evolved as done earlier in momentum space. Specifically, after evolving the initial Hamiltonian to H_s , we can construct the unitary transformation, U , via Eq. (1.16) to find $\hat{O}_s = U_s \hat{O} U_s^\dagger$ in every many-particle subspace up to where it is truncated. This is also the point where we can begin to follow the procedures outlined in Sec. 3.2 regarding the separation and use of many-body operator components.

3.3.2 Operator Evolution and Extraction in Jacobi Oscillator Basis

Implementing the operator evolution and extraction Methods 2 and 3 are relatively straight forward. Method 2 requires the use of a single-particle basis. This method will not be checked explicitly because to do so would simply be a matter of reproducing results found completely in a single-particle basis. These single-particle basis calculations have been performed as an external check on the Jacobi basis operator methods, and are described in the following subsection. Method 3 can be implemented by simply using the machinery described in the previous subsection. Method 1, however, requires a little bit of care to confirm that the integrals over all of the evolved operators and internal COM momenta match the other two evolution and extraction methods.

Given a one-body operator $\hat{O}^{(1)}(q)$ which probes a function of single-particle momentum q , according to Method 1 we must first embed this operator into the two-particle space for all q in a sufficiently fine the momentum mesh which is also adequate in range to pick up all significant contributions in a particular state. These implementation details must be determined case-by-case. All of these operators must then be evolved to a desired λ , and the two-body induced components extracted by subtracting the original embedded operators (since there is likely no one-body evolution if this method is applied) and then stored. So we have a set of matrices $\langle N_2 i_2 | \hat{O}_\lambda^{(2)}(q_2) | N'_2 i'_2 \rangle$ over a range of q_2 (defined in the Method 1 description).

In order to perform the integral over momentum as written in Eq. (3.10) to embed the induced two-body operators into the three-particle space with operators in the oscillator basis, sums over the evolved operator matrices must then be performed with the appropriate factors, etc., which is no problem. The non-trivial issue, however, is to account for the delta function on the two-particle COM momentum for each operator. Fortunately, we may here again make use of the $(A - 1)$ Jacobi coordinate which we found earlier to be equivalent to a single-particle coordinate with the appropriate factor when the COM momentum of the entire system can be taken to be zero. Since we are in a system of total momentum effectively equal to zero this single particle coordinate k_A must have a momentum equal and

opposite to that of the total momentum of the remaining ($A - 1$) particles; i.e., $k_3 = 2 \cdot Q_2$ or $\frac{1}{2}\sqrt{\frac{2}{3}}p_2 = Q_2$ for embedding into the three-particle space, for example. The associated delta function $\delta(q_3 - (q_2 + Q_2))$ of Eq. (3.10) can thus be expressed as a matrix in the final Jacobi coordinate in much the same way as a one-body operator, but with different factors involved. For a simple product of $\langle n_2 | \delta(q_3 - (q_2 + Q_2)) | n'_2 \rangle$ and $\langle N_2 i_2 | \hat{O}_\lambda^{(2)}(q_2) | N'_2 i'_2 \rangle$ to be valid in the calculation of the integral, the numerical sum must be taken in the product space $|N'_2 i'_2\rangle |n'_2\rangle$ before symmetrizing the matrices in the three-particle basis with the appropriate transformation. In this way, the oscillator bases corresponding to the first and second Jacobi coordinates remain independent of each other, instead of mixed up in a symmetrized basis, and the evolved operator matrix, and COM delta function matrix can commute. Once we have $\langle n_2 | \langle N_2 i_2 | \hat{O}_\lambda^{(2)}(q_3) | N'_2 i'_2 \rangle | n'_2 \rangle$, however, the final transformation can be applied to create $\langle N_3 i_3 | \hat{O}_\lambda^{(2)}(q_3) | N'_3 i'_3 \rangle$, the symmetrized oscillator basis matrix for the induced two-body operator embedded in the three-particle space. The same trick for calculating COM delta function scales up into larger systems so that we may iteratively calculate whatever operators are needed and limited by computing power.

3.3.3 Oscillator Basis Representation: Single Particle Coordinates

To test the many-body operator methods developed in Chapter 3, a code utilizing a single-particle coordinate basis was developed as an external check on results found in the Jacobi basis code. We briefly discuss some of the details of this implementation in this subsection.

Not only does the single-particle basis provide a convenient check on the Jacobi implementation, it is considerably more straightforward to develop, in principle. We simply need to be able to calculate matrix elements of an n -body operator in an unsymmetrized n -particle space of single-particle functions. We can then use this to get the matrix element in a symmetrized space via simple expressions. As mentioned in Chapter 1, the limitation we face here is the large basis involved; however, the procedure has the advantage of being easier to compute in a distributed fashion. Moreover, as described above, extracting the induced many-body operators at each order is a simple matter of subtracting the evolved results in smaller spaces for all n -body operators, including $n = 1$.

To begin, the available basis elements we use must be enumerated. The unsymmetrized basis states are given by

$$|\phi_{\alpha_1}(1), \phi_{\alpha_2}(2), \dots, \phi_{\alpha_A}(A)\rangle \quad (3.28)$$

where $\phi_\alpha(n)$ is the chosen single-particle basis (here the single particle oscillator eigenbasis), α is the order of the element in the basis expansion, and n is the particle coordinate. To form a complete basis, we must include all possible combinations of the basis elements, with the restriction that we do not repeat set of elements upon rearrangement and, for fermions, we do not have any particles in the same state. The basis expansion must also be restricted in some way. For harmonic oscillators, we restrict it to N_{\max} , which is simply the sum over α_i . The properly symmetrized states can then be written via the slater determinant

$$\Psi = \frac{1}{\sqrt{A!}} \begin{vmatrix} \phi_{\alpha_1}(1) & \phi_{\alpha_1}(2) & \cdots & \phi_{\alpha_1}(A) \\ \phi_{\alpha_2}(1) & \phi_{\alpha_2}(2) & \cdots & \phi_{\alpha_2}(A) \\ \vdots & \vdots & & \vdots \\ \phi_{\alpha_A}(1) & \phi_{\alpha_A}(2) & \cdots & \phi_{\alpha_A}(A) \end{vmatrix} \quad (3.29)$$

for fermions or the corresponding permanent for bosons.

At this point, a number of relations can be derived which relate the overlaps and matrix elements between the symmetrized basis states [88]. In general, for fermions, one can write

$$\langle \Psi(\phi_{\alpha_1}(1), \dots, \phi_{\alpha_A}(A)) | \Psi'(\phi'_{\alpha'_1}(1), \dots, \phi'_{\alpha'_A}(A)) \rangle = \det\{B\} \quad (3.30)$$

where

$$B_{ij} = \langle \phi_{\alpha_i}(n_i) | \phi_{\alpha_j}(n_j) \rangle \quad (3.31)$$

are the single particle overlaps. For the embedding of one-body operators $\hat{O}^{(1)}$, we may write

$$\langle \Psi | \hat{O}^{(1)} | \Psi' \rangle = \sum_{i=1}^N \sum_{j=1}^N \left\langle \phi_{\alpha_i}(n_i) | \hat{O}^{(1)} | \phi_{\alpha_j}(n_j) \right\rangle (-1)^{i+j} \det\{B^{ij}\} \quad (3.32)$$

with B as defined above, and where B^{ij} is obtained by omitting the i^{th} row and j^{th} column

of the matrix B . For the embedding of two-body matrix elements we have

$$\langle \Psi | \hat{O}^{(2)} | \Psi' \rangle = \sum_{i<1}^N \sum_{k,l=1}^N \langle \phi_{\alpha_i}(n_j) \phi_{\alpha_j}(n_j) | \hat{O}^{(2)} | \phi_{\alpha_k}(n_k) \phi_{\alpha_l}(n_l) \rangle (-1)^{i+j+k+l} \det\{B^{ijkl}\} \quad (3.33)$$

where B^{ijkl} is defined like B^{ij} . The symmetrized matrix elements of larger n -body operators can be defined in the same manner. For the case of bosons, all explicit (-1) factors vanish, and the determinant functions become permanents. The same formalism can, in fact, be used in three-dimensional realistic calculations; however, additional indices will appear on the single-particle states to account for angular momentum and other quantum numbers. Special care must also be taken to isolate states of particular quantum numbers in these calculations.

Given these matrix elements, we can construct the matrix of any operator, including the Hamiltonian, and eigenvector solutions of the Hamiltonian consequently provide us with the means to calculate operator expectation values. One particular technical issue, however, which must be dealt with here (and not the Jacobi basis) is presence of contamination from excited COM states which naturally exist in the single-particle basis. We can deal with this by explicitly calculating the ground COM state from the COM Hamiltonian, and using this to project out the sought after wave function. Alternatively, we employ a trick that adds a large COM contribution to the original Hamiltonian, thereby pushing states with non-zero COM contributions higher in the spectrum, and thus isolating the desired ground state [18].

Operator calculations in this basis have indeed provided a successful check on calculations in the Jacobi basis. A number of these calculations will be discussed in the following section.

3.3.4 Representative Example: Number Operator

It is not possible in this 1D system to explore analogs to every 3D operator due to a lack of angular momentum dependence, etc. However, the number operator is not only rather simple to define, it is representative of operators over a range of length scales, and thus can demonstrate the effects of the SRG over these scales, as we saw in the previous chapter.

Calculations of the r^2 operator in this model, as well as in a realistic 3D potential are presented in Chapter 4 in the context of basis convergence issues which we notice first here.

The number operator is given by the matrix elements

$$\langle N_A i_A | a_{\mathbf{q}}^\dagger a_{\mathbf{q}} | N_A i_A \rangle, \quad (3.34)$$

where we start with the delta function in relative momentum Jacobi coordinates and embed into the symmetrized A -body oscillator space as described above. This is a one-body operator, so a factor of A must be included in the embedding of the operator in the larger space. By calculating this expectation value at \mathbf{q} taken over a range of momenta we produce the momentum distribution of the system, as shown earlier by the solid lines in Figure 3.2 for the ground state of the model two-, three-, and four-boson system. The binding energies of these systems are -0.920 , -2.628 , and -4.695 respectively [72]. The distributions show that there is an elevated probability per particle of having higher momentum components with increasing system size, consistent with the increase in binding energy per particle. The curves shown were calculated using the bare, unevolved operators with the unevolved wave function. When the calculation is done using evolved operators with evolved wave functions, the solid curves are reproduced exactly (up to numerical errors).

Again in Figure 3.4 we see the momentum distribution for the two-, three-, and four-boson system; but this time each distribution is in a separate pane and the additional curves indicate the momentum dependence of the few-body, SRG evolved, wave functions at a number of different λ . These additional curves were calculated using the SRG evolved wave functions with the unevolved operators. As found for the deuteron, these wave functions are suppressed by orders of magnitude for high-momentum (short-distance) components $k \gtrsim \lambda$. This was to be expected, as the fundamental properties of the SRG flow should be independent of basis for any given generator and Hamiltonian.

In order to analyze the decoupling properties of expectation values calculated using few-body operators evolved in the harmonic oscillator basis, we depart from our use of the two dimensional matrix plots of the expectation value integrand in the ground state which were presented in Chapter 2. In momentum space, it was straightforward to interpret

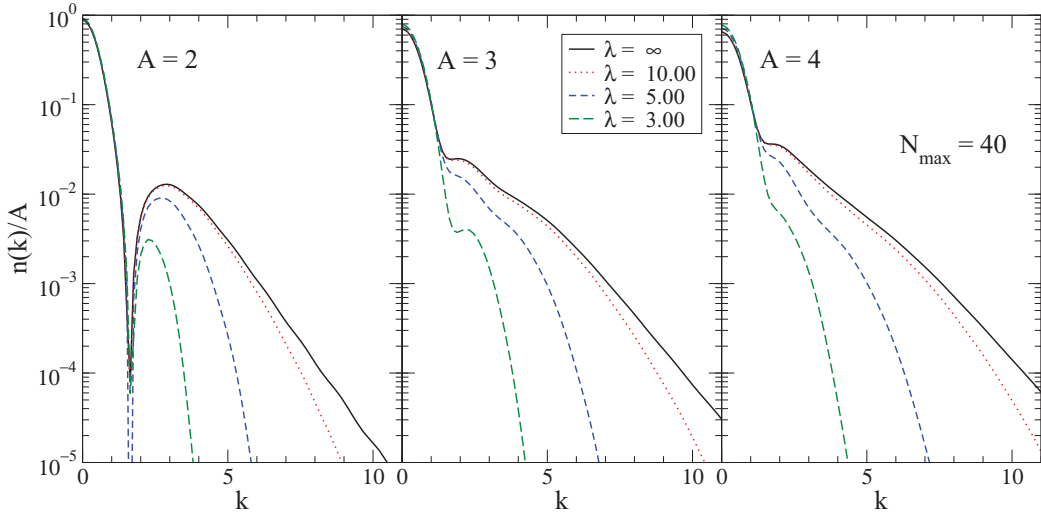


Figure 3.4: The $A=2, 3, \& 4$ boson system momentum distributions calculated with bare operator are shown separately here at different points in the SRG evolution. First shown in [18].

the onset of decoupling in these plots by the suppression of matrix elements at large k ; however, while the oscillator basis states are ordered with respect to N_A , the ordering of states at each level N_A is arbitrary. Thus, it is unclear how to interpret decoupling in a similar two-dimensional oscillator basis plot. So, following the analysis in [72] for decoupling of the ground state energy, we truncate the SRG evolved Hamiltonian for states less than and including $N_{\text{cut}} = 1$ to N_A , solve for the resulting eigenstates, and take the expectation value of the corresponding truncated (and SRG evolved) operator with the new ground state. Values for which the operator expectation values are roughly independent of N_{cut} indicate the regions of truncation in which we have decoupling.

The two panes in Figure 3.5 are N_{cut} plots for the $A=3$ boson system calculated with a high momentum number operator at $q = 15.03$ (on the left) and a low momentum number operator at $q = 0.51$ on the right. For the high momentum operator we clearly see decoupling to some extent. The unevolved expectation value (neither the operator or the wave functions are evolved) drops off sharply around $N_{\text{cut}} = 25$, whereas the evolved values (from fully evolved operators with evolved wave functions) remain relatively stable over a wide range

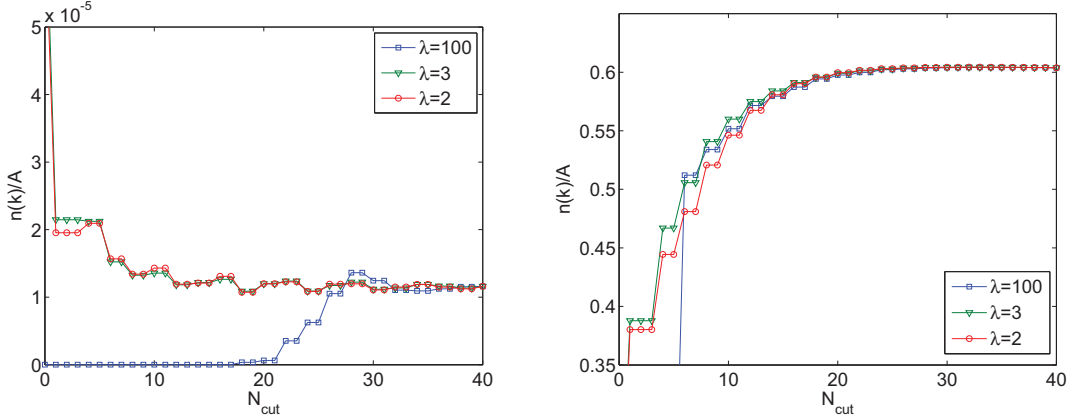


Figure 3.5: Tests of number operator expectation value decoupling with respect to N_{cut} at $q = 15.03$ (left) and at $q = 0.51$ (right).

of values. The lack of smoothness in this plot can be attributed to the fact that even at larger N_{cut} there exist harmonic oscillator basis configurations which mix particles in high- and low- momentum states, combined with the fact that as a high-momentum operator is evolved, it picks up strength at low momentum (as we learned in the previous chapter). For the low-momentum / long-distance operator decoupling is not, in fact, evident. There is little difference between the evolved and unevolved operators — it actually appears as though the differences at lower N_{cut} even start to get worse for lower λ ! As it turns out, this is also consistent with our findings in the previous chapter; i.e., that little renormalization occurs for low momentum, long distance operators. The fall off behavior that we do see is a function of the harmonic oscillator basis itself. Recall that the single oscillator basis states in coordinate space are an expansion of Hermite polynomials attenuated by a gaussian function of the coordinates. Thus, there is an infrared (in addition to an ultraviolet) cutoff imposed by the size of the oscillator basis N_A used in any calculation. It is at least somewhat reassuring that the deviation in the expectation value does not appear to become significant (on visual inspection) until the N_{cut} value above which the binding energy was found to decouple in [72]. This is also true if one looks at the N_{cut} plots for intermediate values of number operator momenta q . But, one might worry that this issue will cause problems for other operators, such as the long distance r^2 operator often calculated for nuclear systems.

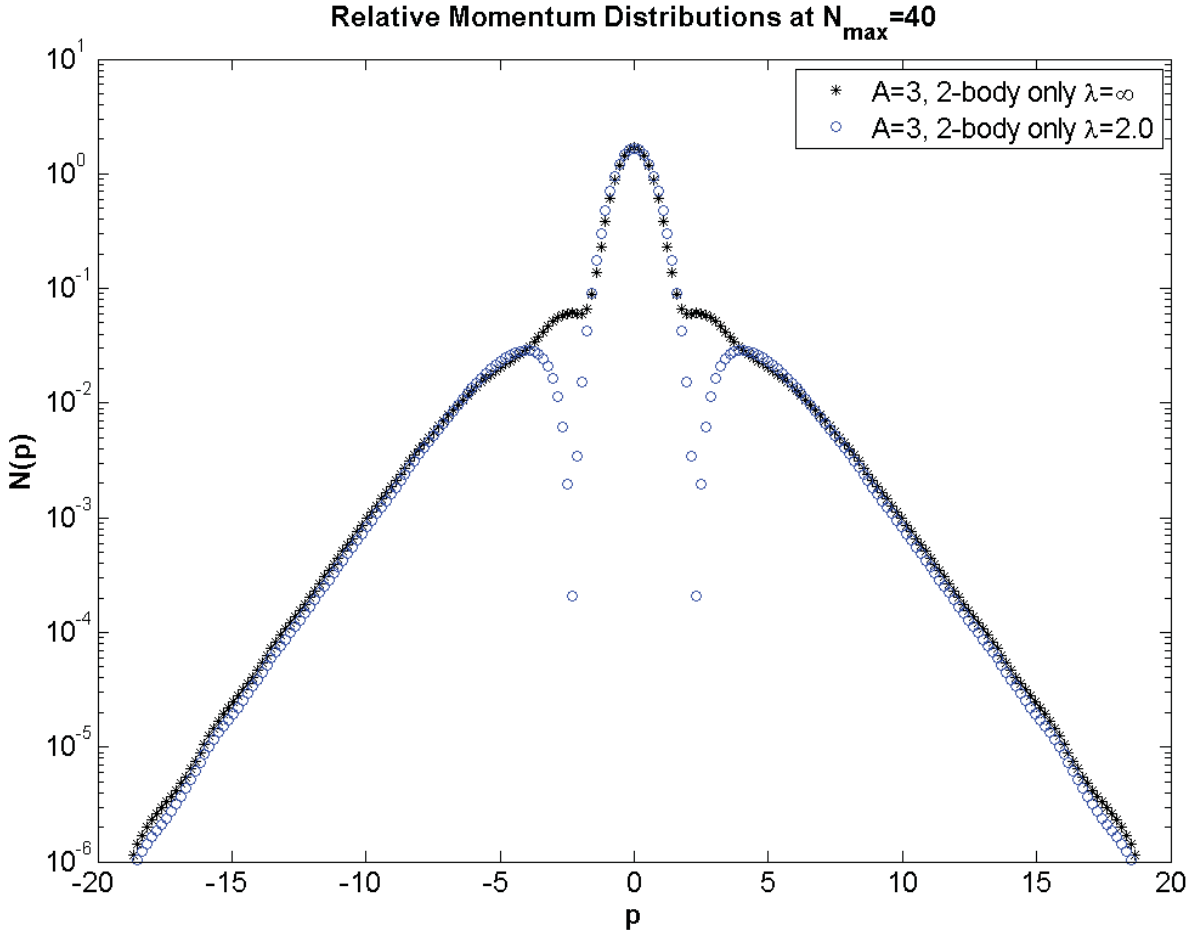


Figure 3.6: The $A=3$ boson system relative momentum distributions calculated with the inclusion of 2-body only operators, as well the fully evolved operator.

We will return to this issue, and a possible way to address it in Chapter 4.

Many-Body Contributions

As one of the major subjects this chapter, we highlight here the results of applying the many-body operator evolution and extraction methods to the number operator for both the single-particle momentum distribution, and the relative particle momentum distribution. These calculations have been performed for the model systems with $A=3$ and $A=4$ bosons.

The relative momentum distribution is different from the single particle momentum distributions that we have so far considered. Although its initial numerical representation is

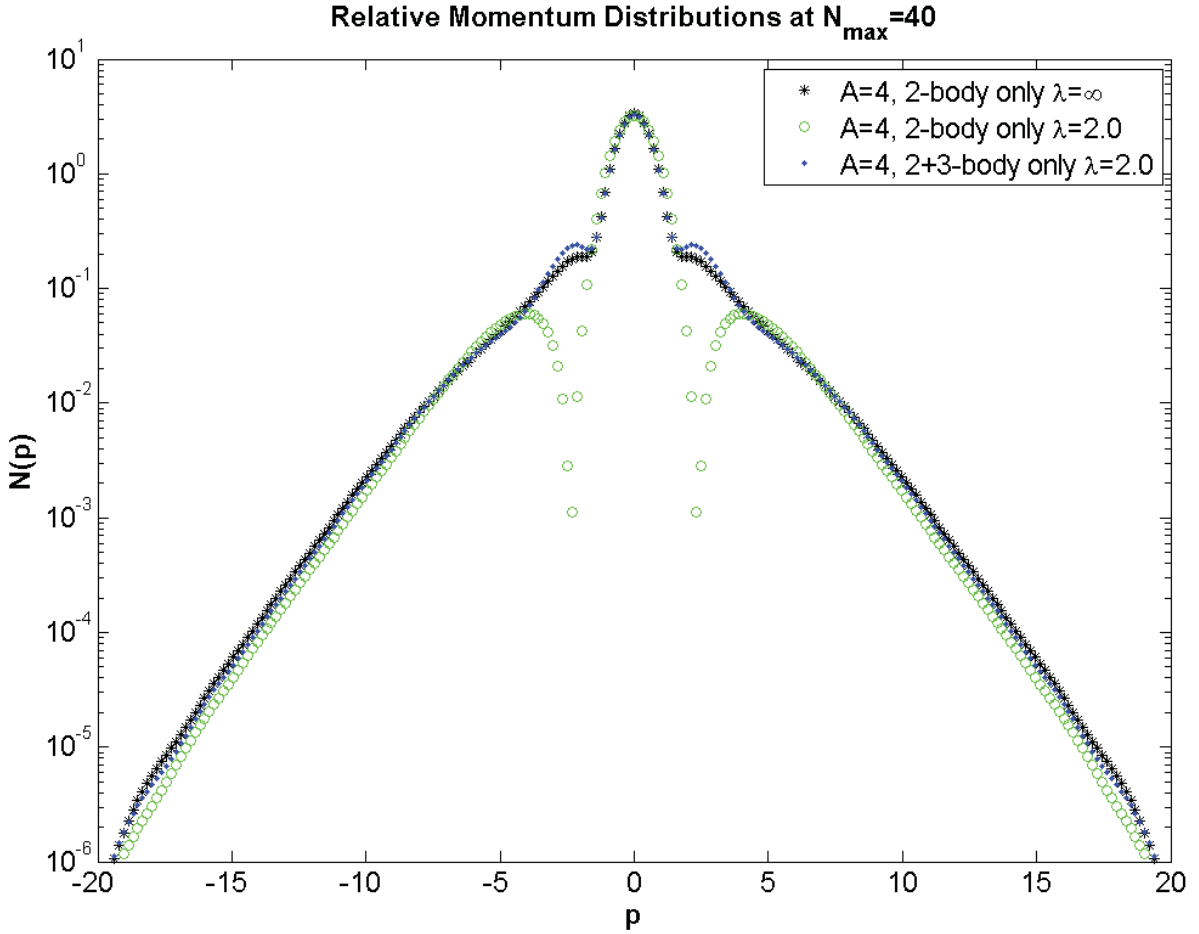


Figure 3.7: The $A=4$ boson system relative momentum distributions calculated with the inclusion of 2-body only operators, 2+3-body only operators, as well the fully evolved operator.

very similar, it must be embedded differently. Instead of being defined by delta functions on single-particle coordinates, its individual operators are defined by a delta function, $\delta(p_1 - q)$, on the first Jacobi coordinate p_1 so that they probe the relative pair momentum distribution as a function of q . As such, they are two-body translationally invariant operators instead of one-body operators, and can be evolved in a straightforward manner as described in Figure 3.1, just like the two-body Hamiltonian.

In Figures 3.6 and 3.7 we have calculations of the relative pair momentum distribution using SRG-evolved operators and wave functions to $\lambda = 2.0$, as an example. For reference,

the unevolved “exact” result is also displayed. In Figure 3.6 we can see the effect of neglecting the three-body induced operator components in the three-particle system. If we include the three-body components too, the exact result is reproduced up to numerical errors, and so this is not displayed. Although a large portion of the distribution is reproduced by the two-body operator a significant amount of strength is still missing at large values of momenta. Since the SRG progressively suppresses high-momentum matrix elements of low-energy states, it is expected that this is where the neglect of many-body induced pieces would show up. For the binding energy, it has also been shown that there is a significant level of missing many-body forces at $\lambda = 2.0$; but it was not clear where that strength was from because the binding energy has contributions at all values of momenta [72]. There is also a region of large apparent deviation at mid-to-high values of momenta characterized by a dip in the plot. This area of deviation cannot be interpreted as a significant SRG related effect because the two-body ground state wave function passes through a node in this region which affects the two-body unitary transformation. At low momentum, there is very little difference, just as expected from the earlier analysis of the deuteron momentum distributions. Since there is not much evolution in this region, the induced many-body forces are insignificant.

In Figure 3.7 we see the same overall pattern. Here we have an exact result for reference, along with calculations including only two-body operators, as well as calculations with two-body and three-body components included. Again, if all induced components are included, the initial exact result is reproduced. Here, we also see that neglecting induced many-body components has a greater effect at large momentum, than at low. Critically, in this plot we see that a hierarchy of many-body components exists for operators over the whole range of momentum space. The difference between the exact curve and the 2+3-body only curve is much smaller than the difference between the exact curve and the 2-body only curve. This is an essential demonstration of the effectiveness of the SRG as applied to other operators. Not shown in these two plots are other values of λ ; but it is found that the effect of the many-body induced components gets smaller as λ increases until all curves are effectively the same.

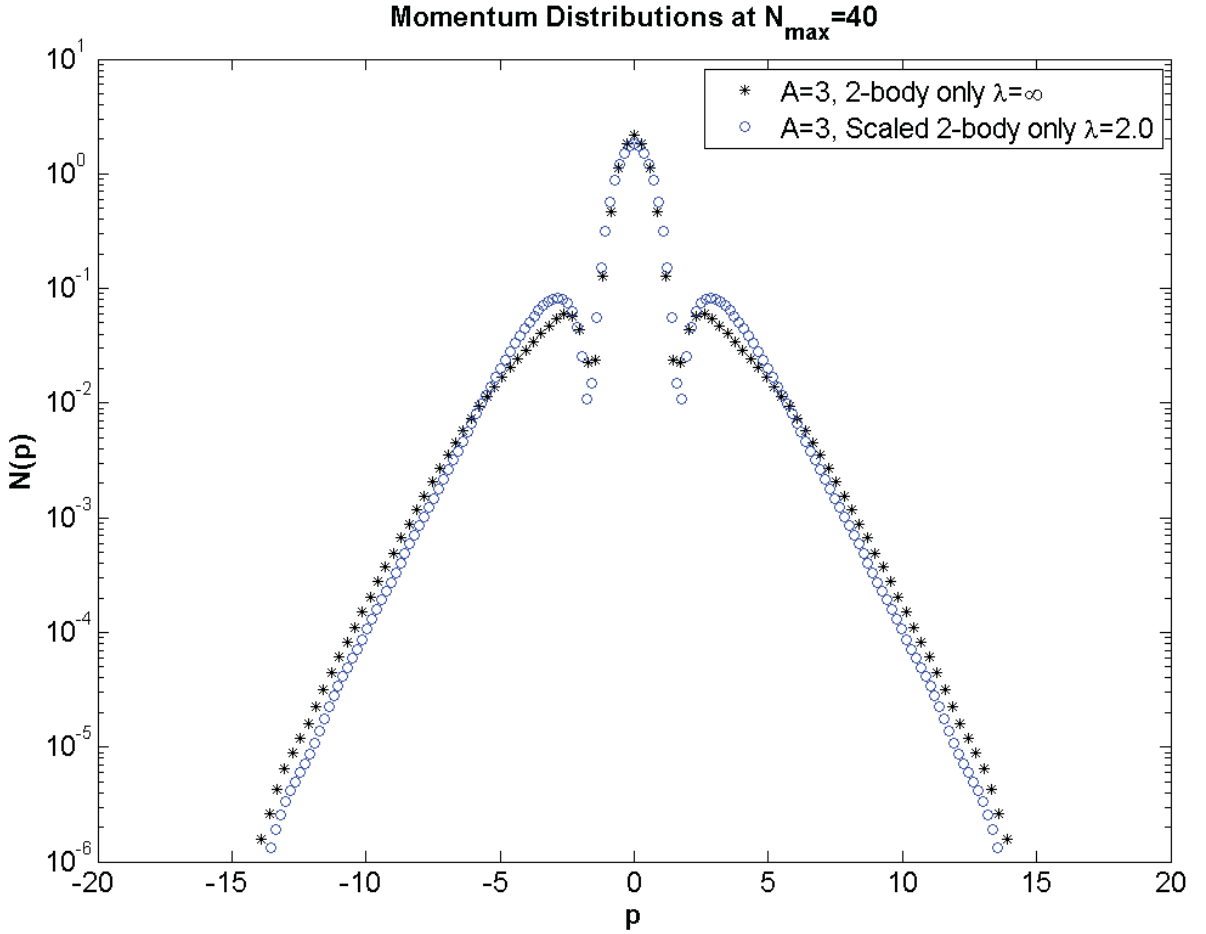


Figure 3.8: The $A=3$ boson system momentum distributions calculated with the inclusion of 2-body only operators, as well the fully evolved operator.

In Figures 3.8 and 3.9 we return to calculations of the single-particle momentum distributions. We find that properties found in evolution of the relative momentum distributions are also reflected here, but with some differences. A key check on the many-body operator evolution and extraction procedures for non-translationally invariant operators is also represented by these calculations, since the single-particle distributions are defined initially by one-body operators which probe specific single-particle momenta q . To confirm that these methods are consistent the evolution and extraction procedure described by Methods 1 and 3 were performed to create the same plots. As an outside check, which includes part of the procedure in Method 2, these calculations were performed completely in the single-particle

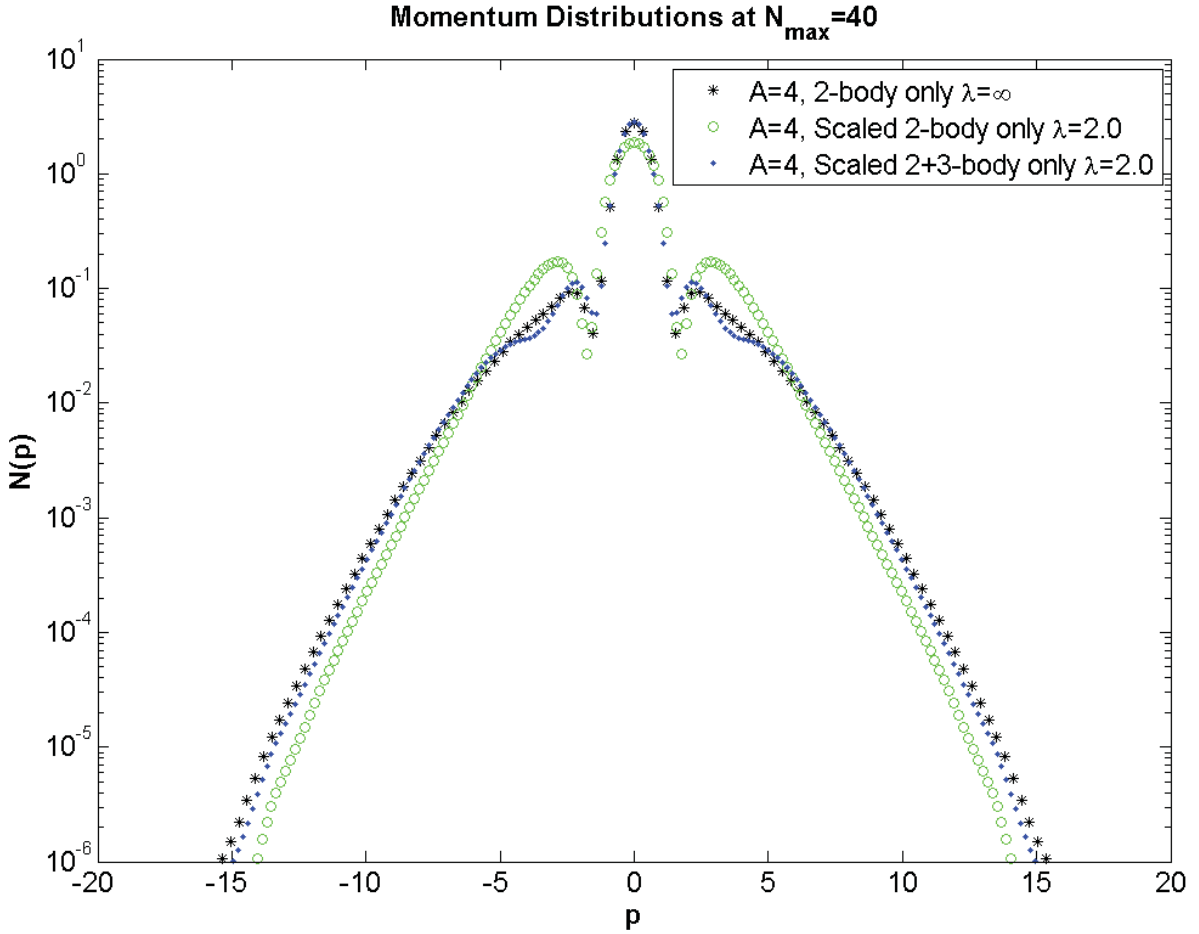


Figure 3.9: The $A=4$ boson system momentum distributions calculated with the inclusion of 2-body only operators, 2+3-body only operators, as well the fully evolved operator.

basis described above. All three of these procedures produced the same plots, up to reasonable numerical errors. As such, we have chosen to only present the plots produced by Method 3, as this is likely subject to the least numerical error, given its simplicity.

Returning our attention to the actual plots, in Figure 3.8 we have the distribution in the three-boson ground state for evolution to $\lambda = 2.0$. In this plot, as in the relative momentum distribution, the two-body only results largely reproduce the unevolved reference curve; but there is still a significant induced many-body component which must be included, as expected. In contrast to the other distributions, however, there is deviation at low momentum, as well as high momentum. This would not appear to follow the pattern

that we have established for SRG evolution. In the context of Method 1, however, we can interpret this as a result of the fact that the two-body SRG-induced components of one-body operators which are embedded in the three-particle space can be equivalently expressed as a sum of induced operators over all values of momentum. Thus, induced operators which only appear at high momentum in the two-particle sector contribute to the operators at all values of momentum when embedded in the three-particle space. So, neglecting additional many-body induced components produces deviations even at low momentum. We can look at this issue in another way via Method 3, where we see that there is a “boosted” difference between the one-body operator in the three-particle system and that used for evolution in the two-particle space. This results in a distortion in what we would expect to see at low momenta after removing the induced three-body component.

This break with the standard pattern of SRG evolution for non-translationally invariant operators could be troubling. In Figure 3.9, however, we see that the hierarchy of many body induced components is maintained for all values of momentum. We have plotted here the single-particle distributions evolved to $\lambda = 2.0$ again, and show the results using two-body induced operators (with the initial one-body operator too, of course), as well as result where only the four-body induced operator has been neglected. An exact curve for reference is also included. Clearly, the four-body induced contributions are much smaller than the three-body contributions, and by adding increasing orders of many-body induced contributions to the one-body operator we approach the exact result. As such, there is good reason to believe that with just a few of the induced many-body components, convergence can be reached for operator expectation values in larger systems.

It should also be pointed out that by increasing λ the many-body induced contributions systematically decrease, and all the curves begin to converge in the $A=3$ and $A=4$ single-particle momentum distribution calculations. One will also note that in all of these figures, the high momentum dependence of the distributions is largely reproduced by just the two-body induced components, up to a scaling factor. This might represent a systematic induced many-body operator effect (potentially related to factorization discussed in Chapter 5). Approximation methods to account for this part of the induced many-body operators are

currently being explored, which could prove useful for some problems where producing additional many-body components is prohibitive.

3.4 Ab-initio Calculations: 3D Considerations

Calculations of many-body evolution in a realistic 3D system have actually been performed already in Chapter 2 of this thesis, although it was obvious in the context in which it was presented. Note that in Figure 2.11, we have evolved leading-order electromagnetic form factor operators in expectation values with evolved wave functions to demonstrate the unitarity of the transformation. Along with these curves, we also have the bare, unevolved operator in expectations values with the evolved wave functions for comparison. Not only does this demonstrate the high-momentum dependence of the induced two-body operators, but we can also see the relative differences between a one-body operator and its SRG-induced two-body components. As we learned earlier in this chapter, one-body operators do not evolve in the one-body sector with relative coordinate interactions and our standard choice of generator, so by comparing the initial electromagnetic operator to the evolved, we are actually comparing the effects of the different many-body evolved contributions.

Otherwise, the purpose of this chapter has been to lay the foundation for many-body operator calculations in larger, realistic 3D systems. The framework for operator evolution and embedding has been laid out in a general way so that any many-body solution technique can be utilized. In principle, the same embedding and extraction procedures used here in 1D can also be used straightforwardly in 3D. One must use caution, however, in attempting to implement our Method 1 evolution scheme for non-translationally invariant operators. While similar tricks could be used to implement the integral in a harmonic oscillator basis, one would then have to integrate over all angles and distances in 3D. This would likely be prohibitive with current computing power. Luckily Methods 2 or 3 can also be used. For problems where one must account for non-translationally invariant interactions as well as other operators (such as for nucleons in a trap), a safe policy would be to perform all SRG-related calculations in a single-particle basis, for conceptual simplicity.

Harmonic oscillator basis methods appear to be a promising initial avenue for calculating expectation values of few-body operators (such as electromagnetic interactions) in realistic systems. As such, the 1D harmonic oscillator basis was chosen for the examples shown here. Calculations using this 1D model in particular, have proven to be a useful test bed for 3D NCSM calculations in the past. Hopefully, the success found here for other operators will also carry over into 3D. Initial few-body evolved operator calculations are already under way.

3.5 Formalism in Second Quantization

A number of many-body solution techniques take advantage of the technology provided by a second quantized basis. In order to provide a framework for SRG-evolved operators when using these techniques, we have reformulated the expression for our SRG unitary transformation in second quantization.

For evolution of a given translationally invariant Hamiltonian to λ the second quantized expression is given by

$$\begin{aligned}\widehat{U}_\lambda = & 1 + \frac{1}{2} \left[U_\lambda \left(\frac{k_1-k_2}{2}, \frac{k_3-k_4}{2} \right) - \delta \left(\frac{k_1-k_2}{2}, \frac{k_3-k_4}{2} \right) \right] \\ & \times \delta(k_1+k_2, k_3+k_4) a_{k_1}^\dagger a_{k_2}^\dagger a_{k_4} a_{k_3} + \dots\end{aligned}\quad (3.35)$$

where a_i and a_i^\dagger are the usual creation and annihilation operators for plain-wave momentum states in a many body space labeled by k_i . A particular advantage of this expression is that it makes use of the corresponding unitary transformation which is easily calculated in a first-quantized basis, given by the matrix elements $U_\lambda \left(\frac{k_1-k_2}{2}, \frac{k_3-k_4}{2} \right)$. The $\delta(k_1+k_2, k_3+k_4)$ function enforces independence of the COM motion, and $-\delta \left(\frac{k_1-k_2}{2}, \frac{k_3-k_4}{2} \right)$ removes the identity in the two-particle sector so as not to conflict with the identity in the many-body space. The factor of 1/2 on the two-body term was simply deduced by enforcing

$$\widehat{U}_\lambda^\dagger \widehat{U}_\lambda = 1 \quad (3.36)$$

from the definition of the unitary transformation. The expression here is valid up to two-

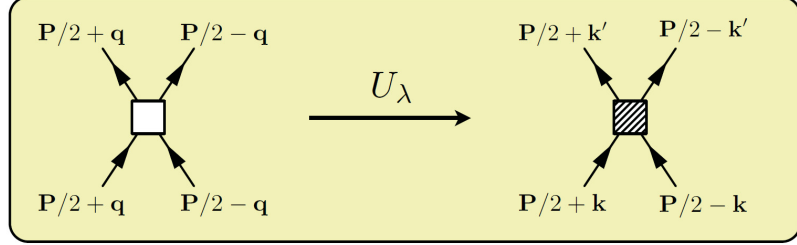


Figure 3.10: Diagrammatic representation of unevolved operator (empty square), and evolved operator (shaded square).

body induced components. In order to extend it to the three-body sector, we must first have the first-quantized unitary transformation matrix elements in the three-particle space. We can then deduce the rest of the three body terms in the expression by again enforcing unitarity out to the three-body level

It has been shown that this transformation is equivalent to simply evolving in a first-quantized two-particle space. As an example of applying this expression to operators in second quantization, truncated at second order, we first apply it to the familiar one-body operator for momentum distributions $\hat{O} = a_q^\dagger a_q$. The result is

$$\hat{U}_\lambda \hat{O} \hat{U}_\lambda^\dagger \rightarrow a_q^\dagger a_q - a_q^\dagger a_i^\dagger a_i a_q + U_\lambda \left(\frac{k_1 - k_2}{2}, \frac{i - q}{2} \right) a_{k_1}^\dagger a_{k_2}^\dagger a_{k_4} a_{k_3} U_\lambda^\dagger \left(\frac{i - q}{2}, \frac{k_3 - k_4}{2} \right) + \dots \quad (3.37)$$

where we see that the one-body component is unchanged, as expected, and there are induced two-body pieces. If we apply this to the two-body relative pair momentum distribution operator, $\hat{O} = a_{P/2+q}^\dagger a_{P/2-q}^\dagger a_{P/2-q} a_{P/2+q}$, we get

$$\hat{U}_\lambda \hat{O} \hat{U}_\lambda^\dagger = U_\lambda \left(\frac{k_1 - k_2}{2}, 2q \right) a_{k_1}^\dagger a_{k_2}^\dagger a_{k_4} a_{k_3} U_\lambda^\dagger \left(2q, \frac{k_3 - k_4}{2} \right) + \dots \quad (3.38)$$

which is exactly of the form we would expect. There are no one-body components, and the usual first-quantized form of an operator sandwiched between unitary transformations is reproduced if we project into a first-quantized basis. As a side note, a transformed operator such as this could be represented diagrammatically as in Figure 3.10 to assist in some many-body calculations.

3.6 Chapter Summary

In this chapter we explore the characteristics of many-body operator evolution and provide a proof of principle that operators can be evolved and used in A -particle calculations. As is well documented, the decoupling which results in the Hamiltonian is our initial motivation for the evolution. We also begin to explore how this decoupling carries over into the calculation of few-body observables. To the extent that it carries over (which we have shown that it does – other than the basis related complication encountered for long-range operators), the fact that the operator expectation values decouple in few-body systems will allow us to truncate the operator matrices in few-particle bases after evolution, and then embed the resulting Hamiltonians and operators (up to the A -body contributions) in the full A -body space, thereby making calculations for larger systems tractable. Other typical SRG evolution related properties, such as the suppression of the high-momentum components in the few-body wave functions, are also evident.

One of the practical pathways to few-body operator expectation values and applications to $A > 2$ is at present through the (Jacobi) harmonic-oscillator basis. The successful SRG evolution of three-body forces (and higher in model systems) in this basis is detailed in Refs. [11, 72]. The corresponding challenge has been to evolve operators for $A = 2$ and $A = 3$ and then embed them (including induced contributions) in higher- A spaces. Here, we have taken the steps to do just that, and provided examples. A key result which allows us to do this is that an evolved operator \hat{O}_s is completely determined up to its $\hat{O}^{(n)}$ contribution by its n -body matrix elements,. As a consequence, we have been able to develop procedures for carrying out the necessary many-body operator evolution, extraction, and embedding, even in second quantized form. Careful implementation of these procedures is especially important so that one can keep track of the n -body components of the operators separately. Using these components, their embedding into larger A -particle spaces can be accomplished consistently. A major success of these procedures in model calculations performed here has

been to show that the hierarchy of SRG induced many-body contributions exists for generic many-body operators, not just the Hamiltonian. These model calculations will be expanded upon in future work for realistic 3D systems.

Chapter 4

ALTERNATIVE GENERATORS

By choosing appropriate generators for the Similarity Renormalization Group (SRG) flow equations, different patterns of evolution and decoupling in a Hamiltonian can be achieved. The kinetic energy has been used in the generator for most prior applications to nuclear interactions, while other options have been largely unexplored in nuclear physics. Here, sharp and smooth block-diagonal forms of phase-shift equivalent nucleon-nucleon potentials in momentum space are generated as alternative examples and compared to analogous low-momentum interactions (“ $V_{\text{low } k}$ ”).* We also show how variations of the standard choice can allow the evolution to proceed more efficiently without losing its advantages.[†] Finally we explore how the choice of generator can alter the convergence properties of other operators.

We digress in this chapter briefly from the generic evolution of operators to consider alternatives to the standard choice of SRG flow. The SRG applied to inter-nucleon interactions, as we have become familiar with it, uses a continuous series of unitary transformations implemented via the flow equation, Eq. (1.6), for evolving an input Hamiltonian H_s :

$$\frac{dH_s}{ds} = [\eta_s, H_s] = [[G_s, H_s], H_s]. \quad (4.1)$$

Again, s is a flow parameter and the generator η_s is specified by the flow operator G_s . Decoupling between low-energy and high-energy matrix elements is naturally achieved in a momentum basis by choosing a momentum-diagonal flow operator such as the kinetic energy T_{rel} or the diagonal of H_s ; either drives the Hamiltonian toward *band-diagonal* form.

*This is based largely on work first presented in [89]

[†]This is based largely on work first presented in [90]

This particular pattern of decoupling leads to dramatically improved variational convergence in few-body nuclear systems compared to unevolved phenomenological or chiral EFT potentials, as we have seen.

Other choices for the flow operator can be made, however. In Section 4.1 we explore a simple method for choosing a desired pattern of decoupling in the Hamiltonian, using a pattern analogous to that found in $V_{\text{low } k}$ as an example. In Section 4.2 we examine choices of the flow operator which largely maintain the pattern of decoupling and advantages found for $G_s = T_{\text{rel}}$, but instead have the ability to significantly reduce the computational requirements of the SRG evolution. Finally, we return in Section 4.3 to the subject of more generic operator evolution. Here, we study how alternative choices of the generator can be used to address the convergence issues of other operators.

4.1 Block-Diagonalization

RG methods that evolve NN interactions with a sharp or smooth cutoff in relative momentum, known generically as $V_{\text{low } k}$, rely on the invariance of the two-nucleon T matrix [64, 77]. These approaches achieve a *block-diagonal* form characterized by a cutoff Λ (see left plots in Figures 4.1 and 4.2). As usually implemented they set the high-momentum matrix elements

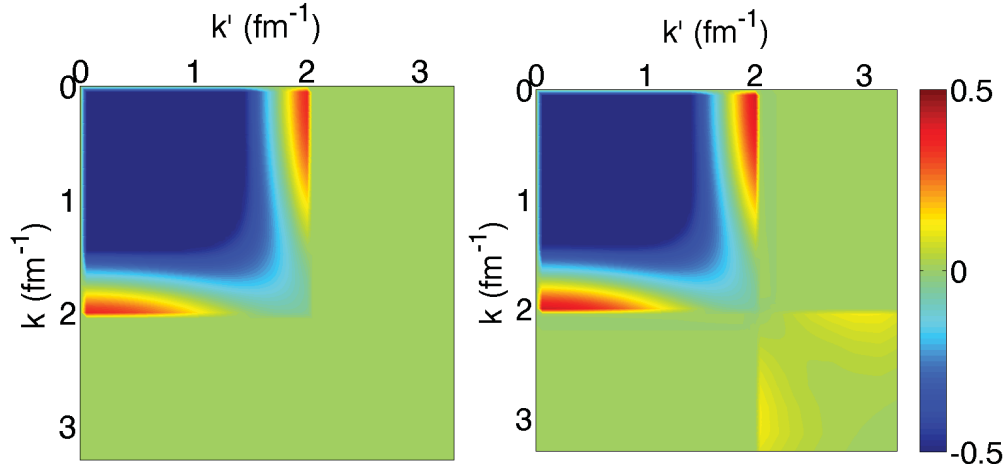


Figure 4.1: Comparison of momentum-space $V_{\text{low } k}$ (left) and SRG (right) block-diagonal potentials with $\Lambda = 2 \text{ fm}^{-1}$ evolved from an N³LO $^3\text{S}_1$ potential [15]. The color axis is in fm.

to zero but this is not required.

Block-diagonal decoupling of the sharp $V_{\text{low } k}$ form can be generated using SRG flow equations by choosing a block-diagonal flow operator [91, 92],

$$G_s = \begin{pmatrix} PH_s P & 0 \\ 0 & QH_s Q \end{pmatrix} \equiv H_s^{\text{bd}} , \quad (4.2)$$

with projection operators P and $Q = 1 - P$. In a partial-wave momentum representation, P and Q are step functions defined by a sharp cutoff Λ on relative momenta. This choice for G_s , which means that η_s is non-zero only where G_s is zero, suppresses off-diagonal matrix elements such that the Hamiltonian approaches a block-diagonal form as s increases. If one considers a measure of the off-diagonal coupling of the Hamiltonian,

$$\text{Tr}[(QH_s P)^\dagger (QH_s P)] = \text{Tr}[PH_s QH_s P] \geq 0 , \quad (4.3)$$

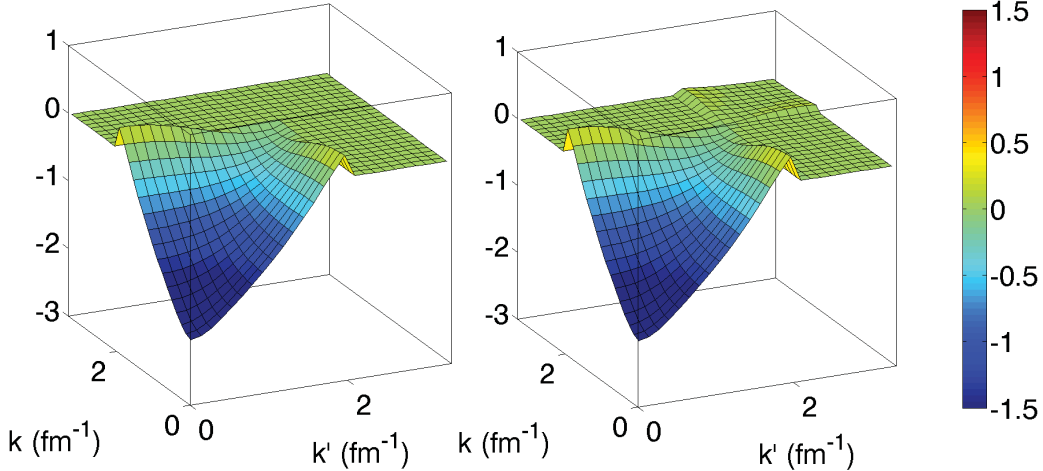


Figure 4.2: Comparison of momentum-space $V_{\text{low } k}$ (left) and SRG (right) block-diagonal potentials with $\Lambda = 2 \text{ fm}^{-1}$ evolved from an $N^3\text{LO } {}^3S_1$ potential [15]. The color and z axes are in fm.

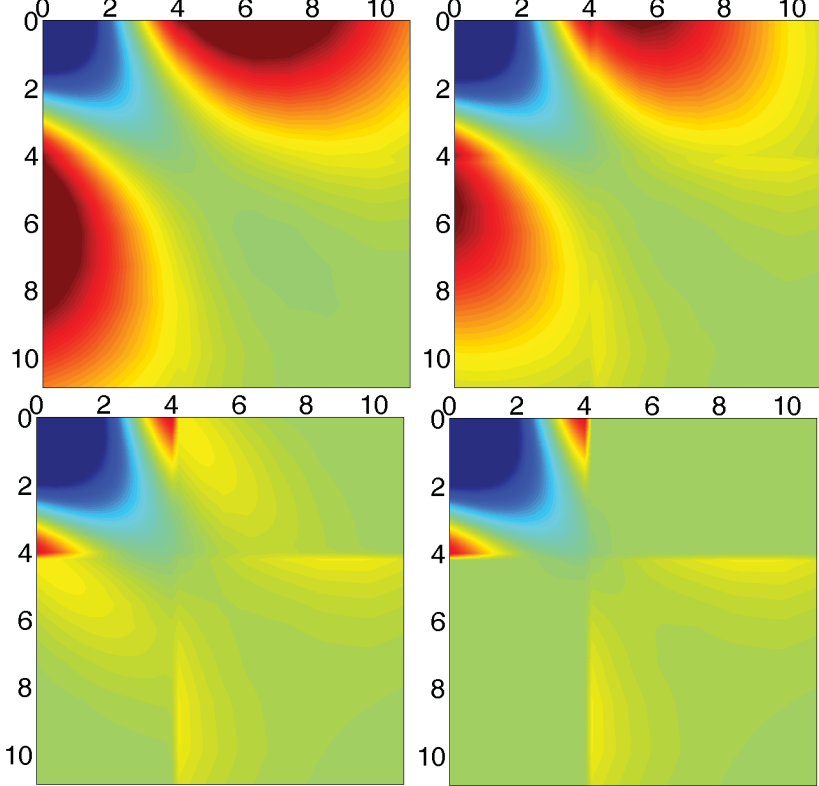


Figure 4.3: Evolution of the 3S_1 partial wave with a sharp block-diagonal flow equation with $\Lambda = 2 \text{ fm}^{-1}$ at $\lambda = 4, 3, 2$, and 1 fm^{-1} . The initial $N^3\text{LO}$ potential is from Ref. [15]. The axes are in units of k^2 from $0\text{--}11 \text{ fm}^{-2}$. The color scale ranges from -0.5 to $+0.5 \text{ fm}$ as in Figure 4.1.

then its derivative is easily evaluated by applying the SRG equation, Eq. (4.1):

$$\begin{aligned}
 & \frac{d}{ds} \text{Tr}[PH_sQH_sP] \\
 &= \text{Tr}[P\eta_sQ(QH_sQH_sP - QH_sPH_sP)] + \text{Tr}[(PH_sPH_sQ - PH_sQH_sQ)Q\eta_sP] \\
 &= -2\text{Tr}[(Q\eta_sP)^\dagger(Q\eta_sP)] \leqslant 0.
 \end{aligned} \tag{4.4}$$

Thus, the off-diagonal QH_sP block will decrease in general as s increases [91, 92].

The right plots in Figures 4.1 and 4.2 result from evolving the $N^3\text{LO}$ potential from Ref. [15] using the block-diagonal G_s of Eq. (4.2) with $\Lambda = 2 \text{ fm}^{-1}$ until $\lambda \equiv 1/s^{1/4} = 0.5 \text{ fm}^{-1}$. The agreement between $V_{\text{low } k}$ and SRG potentials for momenta below Λ is striking. A similar degree of universality is found in the other partial waves. However, an explicit connection between these approaches has yet to be derived.

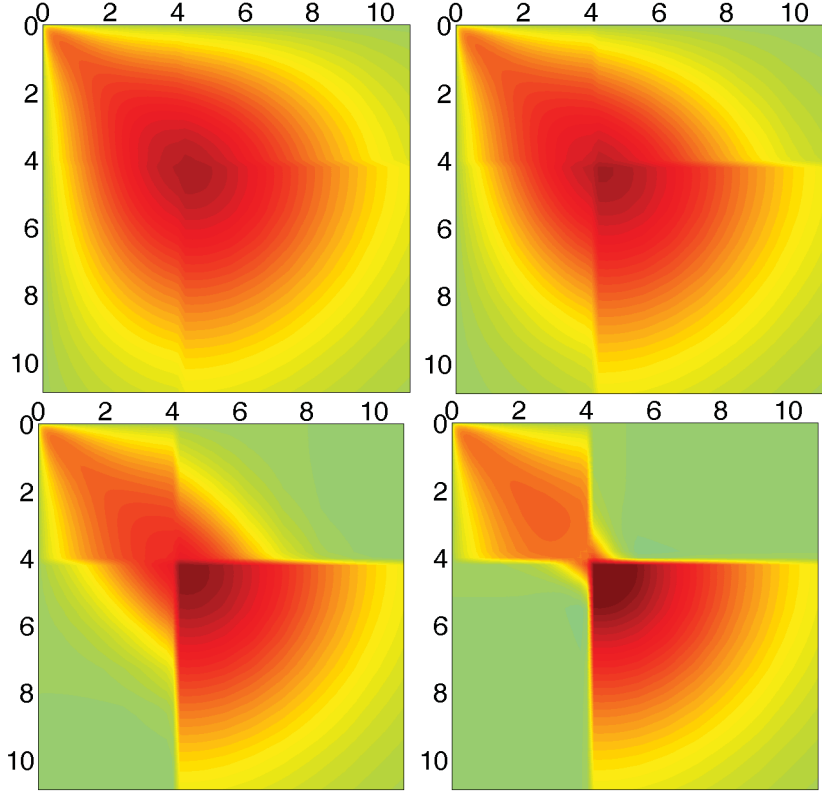


Figure 4.4: Same as Figure 4.3 but for the $^1\text{P}_1$ partial wave.

The evolution with λ of two representative partial waves ($^3\text{S}_1$ and $^1\text{P}_1$) are shown in Figures 4.3 and 4.4. The evolution of the “off-diagonal” matrix elements (meaning those outside the PH_sP and QH_sQ blocks) can be roughly understood from the dominance of the kinetic energy on the diagonal. Let the indices p and q run over indices of the momentum states in the P and Q spaces, respectively. To good approximation we can replace PH_sP and QH_sQ by their eigenvalues E_p and E_q in the SRG equations, yielding [91, 92]

$$\frac{d}{ds} h_{pq} \approx \eta_{pq} E_q - E_p \eta_{pq} = -(E_p - E_q) \eta_{pq} \quad (4.5)$$

and

$$\eta_{pq} \approx E_p h_{pq} - h_{pq} E_q = (E_p - E_q) h_{pq} . \quad (4.6)$$

Combining these two results, we have the evolution of any off-diagonal matrix element:

$$\frac{d}{ds} h_{pq} \approx -(E_p - E_q)^2 h_{pq} . \quad (4.7)$$

In the NN case we can replace the eigenvalues by those for the relative kinetic energy, giving an explicit solution

$$h_{pq}(s) \approx h_{pq}(0) e^{-s(\epsilon_p - \epsilon_q)^2} \quad (4.8)$$

with $\epsilon_p \equiv p^2/M$. Thus the off-diagonal elements go to zero with the energy differences just like with the SRG with T_{rel} ; one can see the width of order $1/\sqrt{s} = \lambda^2$ in the k^2 plots of the evolving potential in Figures 4.3 and 4.4.

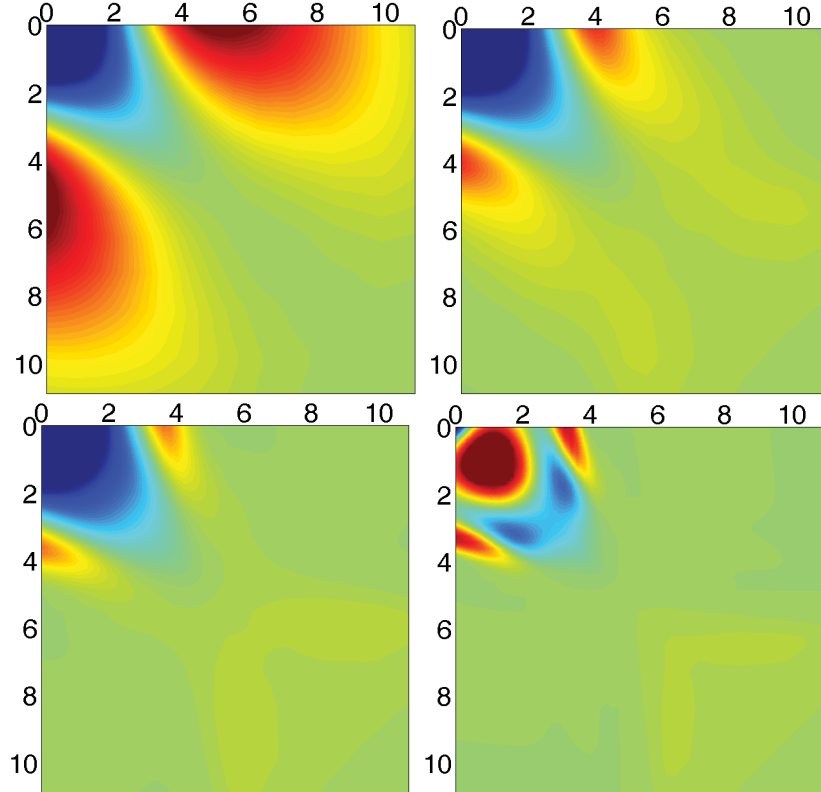


Figure 4.5: Evolution of the 3S_1 partial wave with a smooth ($n = 4$) block-diagonal flow equation with $\Lambda = 2.0 \text{ fm}^{-1}$, starting with the N 3 LO potential from Ref. [15]. The flow parameter λ is 3, 2, 1.5, and 1 fm^{-1} . The axes are in units of k^2 from 0–11 fm^{-2} . The color scale ranges from -0.5 to $+0.5 \text{ fm}$ as in Figure 4.1.

While in principle the evolution to a sharp block-diagonal form means going to $s = \infty$ ($\lambda = 0$), in practice we need only take s as large as needed to quantitatively achieve the decoupling implied by Eq. (4.8). Furthermore, it should hold for more general definitions

of P and Q . To smooth out the cutoff, we can introduce a smooth regulator f_Λ , which we take here to be an exponential form:

$$f_\Lambda(k) = e^{-(k^2/\Lambda^2)^n}, \quad (4.9)$$

with n an integer. For $V_{\text{low } k}$ potentials, typical values used are $n = 4$ and $n = 8$ (the latter is considerably sharper but still numerically robust). By replacing H_s^{bd} with

$$G_s = f_\Lambda H_s f_\Lambda + (1 - f_\Lambda) H_s (1 - f_\Lambda), \quad (4.10)$$

we get a smooth block-diagonal potential.

A representative example with $\Lambda = 2 \text{ fm}^{-1}$ and $n = 4$ is shown in Figure 4.5. We can evolve to $\lambda = 1.5 \text{ fm}^{-1}$ without a problem. For smaller λ the overlap of the P and Q spaces becomes significant and the potential becomes distorted. This distortion indicates that there is no further benefit to evolving in λ very far below Λ ; in fact the decoupling worsens for $\lambda < \Lambda$ with a smooth regulator.

Another type of SRG that is second-order exact and yields similar block diagonalization

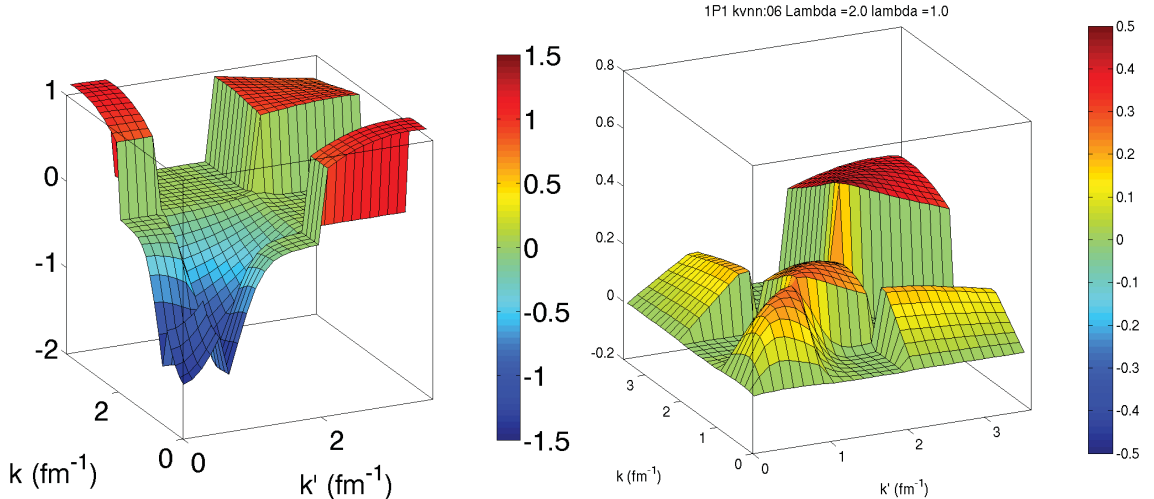


Figure 4.6: Evolved SRG potentials starting from Argonne v_{18} in the 1S_0 and 1P_1 partial waves to $\lambda = 1 \text{ fm}^{-1}$ using a bizarre choice for G_s (see text). The color and z axes are in fm.

is defined by

$$\eta_s = [T, PV_s Q + QV_s P] , \quad (4.11)$$

which can be implemented with $P \rightarrow f_\Lambda$ and $Q \rightarrow (1 - f_\Lambda)$, with f_Λ either sharp or smooth. We can also consider bizarre choices for f_Λ in Eq. (4.10), such as defining it to be zero out to Λ_{lower} , then unity out to Λ , and then zero above that. This means that $1 - f_\Lambda$ defines both low and high-momentum blocks and the region that is driven to zero consists of several rectangles. Results for two partial waves starting from the Argonne v_{18} potential [14] are shown in Figure 4.6. Despite the strange appearance, these remain unitary transformations of the original potential, with phase shifts and other NN observables the same as with the original potential. These choices provide a proof-of-principle that the decoupled regions can be tailored to the physics problem at hand.

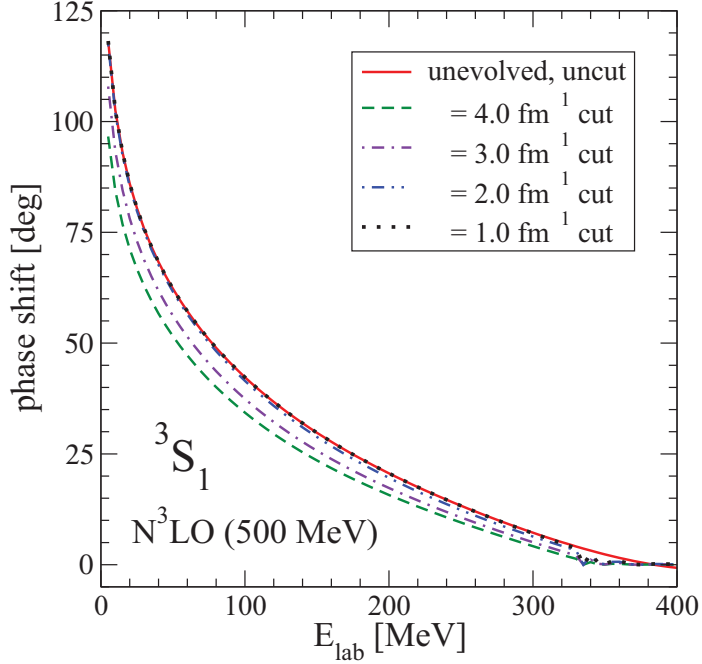


Figure 4.7: Phase shifts for the 3S_1 partial wave from an initial N^3LO potential and the evolved sharp SRG block-diagonal potential with $\Lambda = 2 \text{ fm}^{-1}$ at various λ , in each case with the potential set identically to zero above Λ .

Definitive tests of decoupling for NN observables are again possible for $V_{\text{low } k}$ -like po-

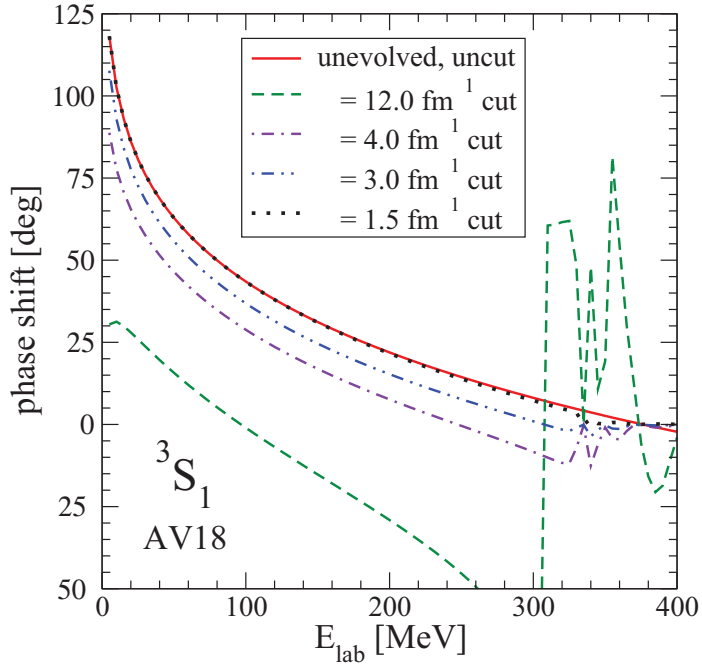


Figure 4.8: Same as Figure 4.7 but with Argonne v_{18} as the initial potential [14].

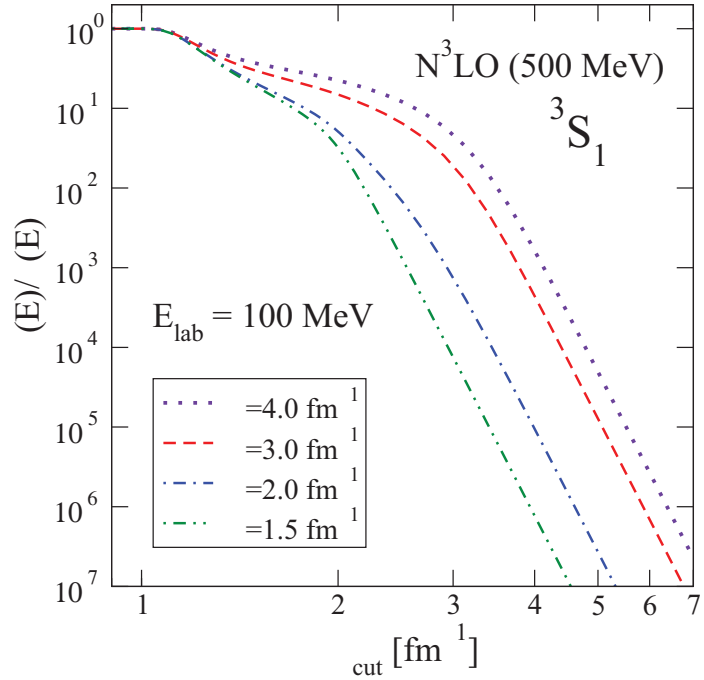


Figure 4.9: Errors in the phase shift at $E_{\text{lab}} = 100$ MeV for the evolved sharp SRG block-diagonal potential with $\Lambda = 2 \text{ fm}^{-1}$ for a range of λ 's and a regulator with $n = 8$.

tentials since the unitary transformation of the SRG guarantees that no physics is lost. For example, in Figures 4.7 and 4.8 we show 3S_1 phase shifts from an SRG sharp block diagonalization with $\Lambda = 2 \text{ fm}^{-1}$ for two different potentials. The phase shifts are calculated with the potentials cut sharply at Λ . That is, the matrix elements of the potential are set to zero above that point. The improved decoupling as λ decreases is evident in each case. By $\lambda = 1 \text{ fm}^{-1}$ in Figure 4.7, the unevolved and evolved curves are indistinguishable to the width of the line up to about 300 MeV.

In Figure 4.9 we show a quantitative analysis of the decoupling as in Ref. [70]. The figure shows the relative error of the phase shift at 100 MeV calculated with a potential that is cut off by a smooth regulator as in Eq. (4.9) at a series of values Λ_{cut} . We observe the same universal decoupling behavior seen in Ref. [70]: a shoulder indicating the perturbative decoupling region, where the slope matches the power $2n$ fixed by the smooth regulator. The onset of the shoulder in Λ_{cut} decreases with λ until it saturates for λ somewhat below Λ , leaving the shoulder at $\Lambda_{\text{cut}} \approx \Lambda$. Thus, as $\lambda \rightarrow 0$ the decoupling scale is set by the cutoff Λ .

In the more conventional SRG, where we use $\eta_s = [T, H_s] = [T, V_s]$, it is easy to see that the evolution of the two-body potential in the two-particle system can be carried over directly to the three-particle system. In particular, it follows that the three-body potential does not depend on disconnected two-body parts [69, 93]. If we implemented η_s as proposed here with analogous properties, we would have a tractable method for generating $V_{\text{low } k}$ three-body forces. While it seems possible to define Fock-space operators with projectors P and Q that will not have problems with disconnected parts, it is not yet clear whether full decoupling in the few-body space can be realized. Work on this problem is in progress.

4.2 Computational Performance

Thus far, we have seen how the choice of G_s can give rise to different patterns of evolution and decoupling. In this section, we continue to explore the advantages which may be gained by that choice. Specifically, two alternatives to T_{rel} are evaluated for their effectiveness in

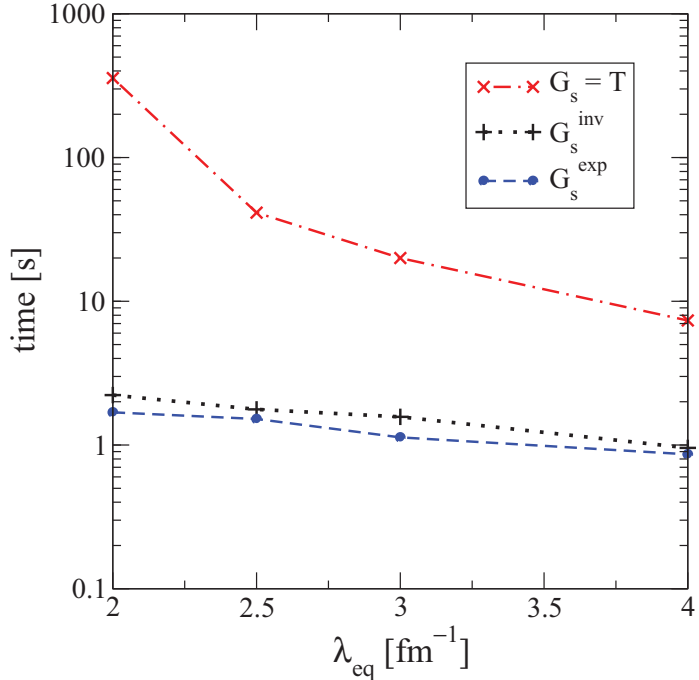


Figure 4.10: Computational time to evolve the Argonne v_{18} 1S_0 potential [14] as a function of the final value of λ_{eq} (see text) for several generators, with $\sigma = 2 \text{ fm}^{-1}$ for G_s^{inv} and G_s^{exp} .

decoupling and, in particular, for improvements in computing speed (see Figure 4.10 for a representative example). Our tests are for realistic nucleon-nucleon (NN) interactions in two-body systems and for a one-dimensional model Hamiltonian applied to few-body bound states.

We focus on novel generators that have G_s as functions of T_{rel} . (Note: we can just as well consider the full kinetic energy T in our discussion, because the center-of-mass part commutes with the running Hamiltonian H_s , so we will use T for convenience.) In particular, we explore the “inverse” G_s operator

$$G_s = -\frac{\sigma^2}{1 + T_{\text{rel}}/\sigma^2} \equiv G_s^{\text{inv}} , \quad (4.12)$$

and the “exponential” G_s given by

$$G_s = -\sigma^2 e^{-T_{\text{rel}}/\sigma^2} \equiv G_s^{\text{exp}} . \quad (4.13)$$

Each has a Taylor series that reduces to T_{rel} (up to a constant, which drops out from the

commutator) at low momentum or when σ is large. As such, the independent parameter σ controls the separation of a low-energy region where G_s behaves as T and the potential is driven toward the diagonal, and a high-energy region where evolution is suppressed. This suppression can result in a significant computational speedup of the SRG evolution when compared to calculations with $G_s = T_{\text{rel}}$, while not impacting the advantageous properties of the evolution for low-momentum applications.

The generators' suppression of running in unneeded parts of the Hamiltonian could mitigate the difficulties of evolving very large matrices for calculations of light atomic nuclei [12], opening the door to more tailored SRG generators and more effective evolution of three- and eventually four-body interactions. Even at the two-body level there are problems when trying to evolve to large values of the flow parameter s . A recent example is a study of SRG decoupling with large-cutoff effective field theory (EFT) potentials, which require evolution beyond the range usually considered [94]. In doing so, the SRG differential equations can become extremely stiff and take a prohibitively long time (weeks on a single processor) to evolve. This problem has hindered exploratory studies into issues such as what happens when a chiral EFT is evolved to the regime of pionless EFT.

In Section 4.2.1, we give representative results for applications to two-body systems, including an analysis of the flow pattern. These results are extended to few-body systems in Section 4.2.2 using the model one-dimensional Hamiltonian of Chapter 3 that has proved useful in past applications [72, 76]. We summarize and outline future studies in Section 4.2.3.

4.2.1 Two-nucleon systems

In this section we give representative results for evolving realistic nucleon-nucleon potentials using the novel generators from Eqs. (4.12) and (4.13) in comparison to the usual choice of $G_s = T_{\text{rel}}$.

Performance

The key advantage of the generators that we highlight here is the improvement in computational performance. For example, the time needed to evolve the Argonne v_{18} $^1\text{S}_0$ poten-

tial [14] to equivalent levels of decoupling with several generators is plotted in Figure 4.10. The parameter $\lambda \equiv 1/s^{1/4}$, which has dimensions of a momentum, has been used to identify the momentum decoupling scale. However, different generators will evolve a given potential at different rates, so comparing results with the same definition of λ can be misleading. Therefore, we identify an “equivalent” λ_{eq} for each generator that equalizes the degree of decoupling compared to $G_s = T$ (for which $\lambda_{\text{eq}} = \lambda$ by definition); the details are described below.

The value of σ will also have an impact, as discussed below; in Figure 4.10 we use the intermediate value $\sigma = 2 \text{ fm}^{-1}$. With this choice, there is nearly an order of magnitude difference in the time to evolve the Argonne v_{18} potential with G_s^{exp} and G_s^{inv} compared to $G_s = T_{\text{rel}}$ at $\lambda_{\text{eq}} = 4 \text{ fm}^{-1}$ and two orders of magnitude by $\lambda_{\text{eq}} = 2 \text{ fm}^{-1}$. Note that nuclear interactions typically have been evolved for nuclear structure studies in the range $\lambda = 1.5\text{--}2.2 \text{ fm}^{-1}$. The speed gains will depend on the initial potential and can be much less for the evolution of softer initial potentials; e.g., for the N³LO 500 MeV chiral EFT potential of Ref. [15], evolving with G_s^{exp} to $\lambda_{\text{eq}} = 2 \text{ fm}^{-1}$ is about 1.5 times as fast as with $G_s = T_{\text{rel}}$ and about 3 times as fast to $\lambda_{\text{eq}} = 1.5 \text{ fm}^{-1}$.

The numerical solution of the SRG evolution equations requires repeated dense matrix-matrix multiplications. As a consequence, the evolution has been carried out on shared-memory computer architectures. Recent calculations using the SRG with many-body forces are approaching the limits of what is practical to evolve in memory on a single node because of the size of the model space needed [12]. A distributed scheme to solve the equations would permit larger model spaces to be utilized; however, the dense matrix multiplication would then be limited by internode communication times. The reduced number of operations required by novel generators might help make such a scheme possible.

Decoupling and λ_{eq}

To validate the apparent computational advantages of these generators, one must confirm that the decoupling characteristics of the $G_s = T$ generator are also reproduced, so that calculations of physical observables also become more convergent. However, if we evolve

to the same λ , the degree of decoupling for identical initial potentials differs for G_s^{exp} and G_s^{inv} compared to $G_s = T$. These differences are evident in the deviations of ${}^1\text{S}_0$ phase shifts calculated from the evolved potentials using G_s^{exp} and $G_s = T$ from the unevolved potential shown in Figure 4.11 for several different λ values (only G_s^{exp} is shown; G_s^{inv} behaves similarly). If the full potentials were used, the phase shifts would agree – up to numerical precision – with those from the initial potential, because the evolution in all cases is unitary. However, the degree of decoupling for a given value of λ can be made manifest by first cutting off the potential (that is, setting its matrix elements to zero) above some value of k and then calculating the phase shifts. In Figure 4.11, for illustration, we choose the cutoff value k_{cut} to be 2 fm^{-1} . The signature of decoupling is that the phase shifts agree at lower energies and only deviate close to and above the cutoff. This is typically observed when the potential is evolved so that λ is less than the cut momentum [8, 70].

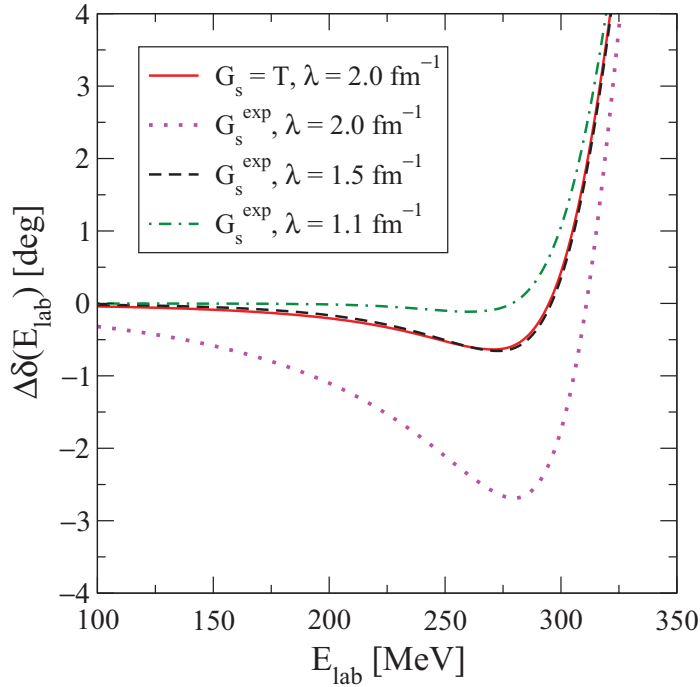


Figure 4.11: Deviation of phase shifts calculated with the Argonne v_{18} ${}^1\text{S}_0$ potential [14] evolved with $G_s = T$ and G_s^{exp} ($\sigma = 2 \text{ fm}^{-1}$) to various λ values and then truncated at $k_{\text{cut}} = 2 \text{ fm}^{-1}$ to test decoupling. Phase shifts from untruncated potentials agree precisely with those from the initial potential.

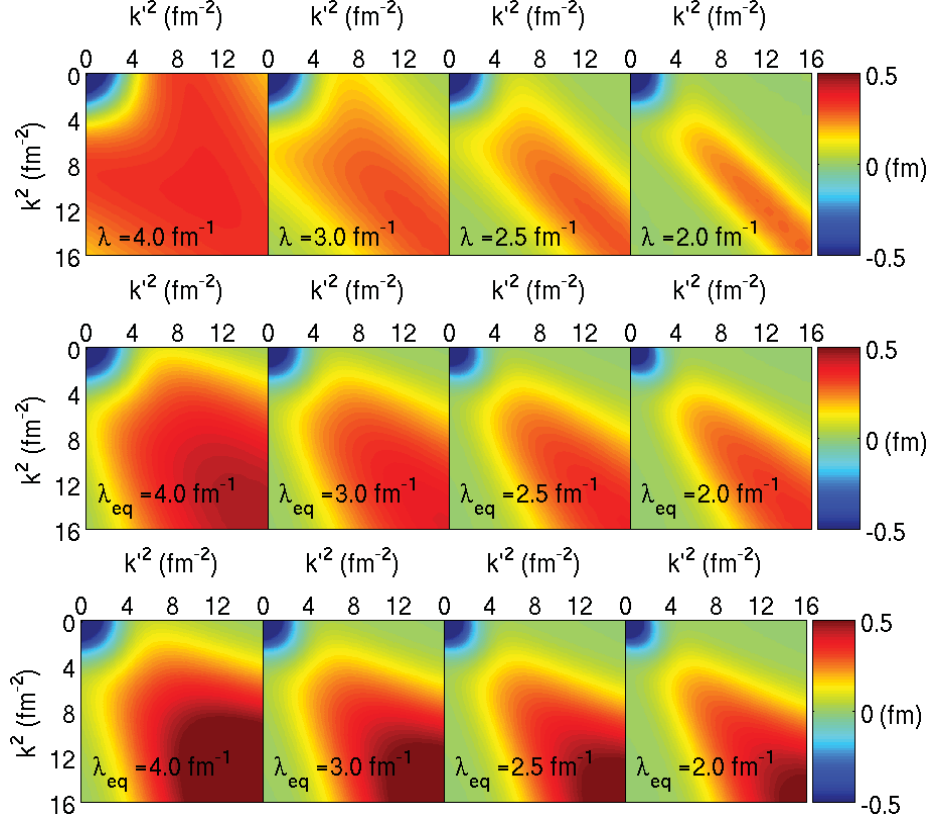


Figure 4.12: Contour plots showing the evolution via Eq. (4.1) at several values of λ_{eq} starting from the momentum-space Argonne v_{18} 1S_0 potential [14] using (a) $G_s = T_{\text{rel}}$, (b) G_s^{inv} from Eq. (4.12) with $\sigma = 2 \text{ fm}^{-1}$, and (c) G_s^{exp} from Eq. (4.13) with $\sigma = 2 \text{ fm}^{-1}$.

This behavior provides us with a pragmatic way to define λ_{eq} : identifying it with the decoupling behavior that is found for $G_s = T$ for a given λ . We use the results in Figure 4.11 to illustrate the procedure. The continuous curve shows the deviation of phase shifts for the potential evolved with $G_s = T$ to $\lambda = 2 \text{ fm}^{-1}$ and cut at $k = 2 \text{ fm}^{-1}$. As expected from decoupling, the deviation is small up to roughly k_{cut} . We use this level of agreement as the criterion for identifying equivalent λ 's for other generators. That is, a potential is evolved to a series of λ values with a different G_s and then cut at k_{cut} after evolution. The phase shifts are then compared to the level of decoupling observed for $G_s = T$ at $k_{\text{cut}} = \lambda$. The approximate point in the novel G_s evolution for which the cut phase shifts agree is equated with λ_{eq} . Consider the phase shifts for the potential evolved with G_s^{exp} to several values of λ and cut at $k = 2 \text{ fm}^{-1}$, as shown in Figure 4.11. For G_s^{exp} , λ evolved to 1.5 fm^{-1} gives

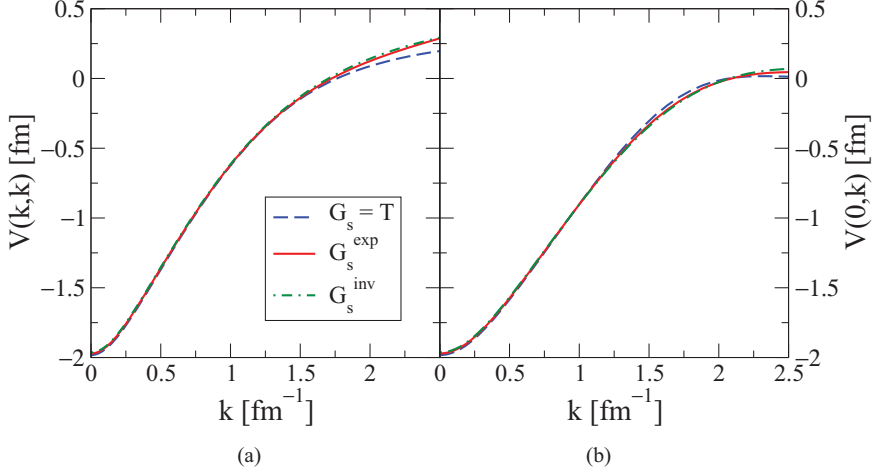


Figure 4.13: Diagonal (a) and off-diagonal (b) momentum-space matrix elements for evolved Argonne v_{18} 1S_0 potential [14] with $G_s = T$ and generators G_s^{exp} and G_s^{inv} at $\lambda = 2 \text{ fm}^{-1}$ with $\sigma = 2 \text{ fm}^{-1}$.

a similar degree of decoupling as λ evolved to 2 fm^{-1} with $G_s = T$. As a result, we define $\lambda = 1.5 \text{ fm}^{-1}$ to be the $\lambda_{\text{eq}} = 2 \text{ fm}^{-1}$ for G_s^{exp} . We use λ_{eq} for most comparisons in the following discussion.

Flow Analysis

Having chosen a working definition for the decoupling scale of evolution with our novel generators, we take a closer look at the properties of the evolved potentials. In particular, we would like to see how a potential flows with evolution using these generators compared to $G_s = T_{\text{rel}}$ and to understand how the choice of σ affects this flow.

In Figure 4.12 we compare the evolution pattern of the two-body potential in the 1S_0 channel with different generators. Each frame is a representation of the potential matrices in momentum space; where the matrix is zero, there is no coupling between momentum components. The initial potential in all cases is Argonne v_{18} [14] and the value of σ is taken to be 2 fm^{-1} . Note that at $\lambda = 4 \text{ fm}^{-1}$, the first matrix plotted here, there is already significant evolution. As the potential is evolved, its high and low momentum components become increasingly decoupled, as expected. It is evident that the evolved potentials are similar (but not identical) in the region where $k^2, k'^2 < \sigma^2$. When $\lambda < \sigma$ we find that σ

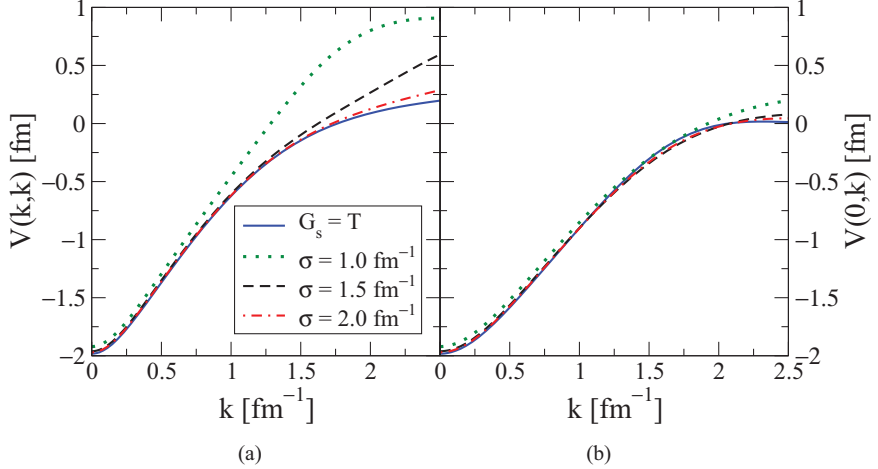


Figure 4.14: Diagonal (a) and off-diagonal (b) momentum-space matrix elements for evolved Argonne v_{18} $^1\text{S}_0$ potential [14] with $G_s = T$ and G_s^{exp} with different values of σ each evolved to $\lambda = 2 \text{ fm}^{-1}$. The lines with $\sigma = 3 \text{ fm}^{-1}$ are indistinguishable from the ones with $G_s = T$.

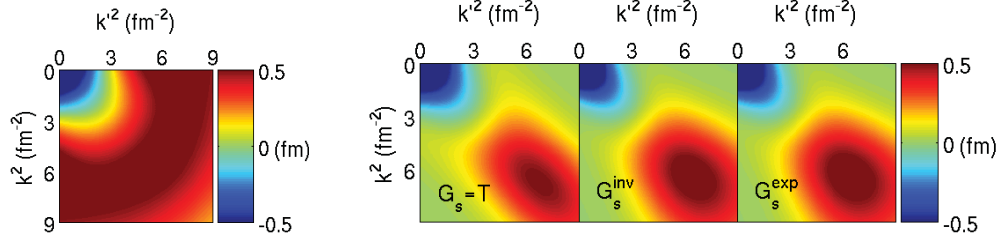


Figure 4.15: (a) Unevolved $N^3\text{LO}$ 500 MeV $^1\text{S}_0$ potential . (b) Contour plot showing the evolved $N^3\text{LO}$ $^1\text{S}_0$ potential with different generators to $\lambda_{\text{eq}} = 2 \text{ fm}^{-1}$. For G_s^{exp} and G_s^{inv} , $\sigma = 2 \text{ fm}^{-1}$.

roughly defines the low-momentum region where these generators behave as $G_s = T_{\text{rel}}$. The minor differences in this low-momentum region can be attributed to the fact that the point in evolution, λ , needed for these generators to reach the corresponding λ_{eq} occurs when $\lambda < \lambda_{\text{eq}}$. At higher momenta, novel generator evolution is suppressed relative to $G_s = T_{\text{rel}}$. The patterns here are characteristic of the particular generator and are similar for other potentials and in other channels.

This nature of the evolution is further illustrated by the plots in Figures 4.13 and 4.14, which show a detailed view of the diagonal and off-diagonal values of the matrices at low

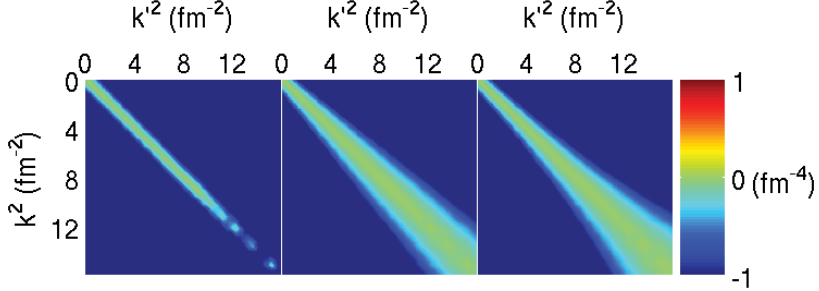


Figure 4.16: Color contour plots of the first term (excluding the factor due to V_s) on the right side of Eq. (4.15) for $G_s = T_{\text{rel}}$ (left), G_s^{inv} (middle), and G_s^{exp} (right). The last two use $\sigma = 2 \text{ fm}^{-1}$.

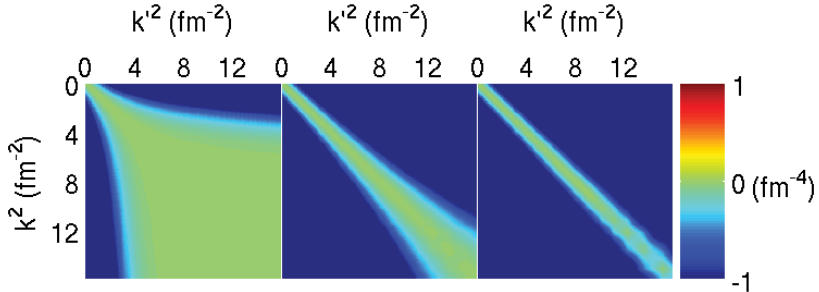


Figure 4.17: Color contour plots of the first terms (excluding the factor due to V_s) on the right side of Eq. (4.15) for G_s^{exp} with $\sigma = 1, 2$, and 3 fm^{-1} from left to right.

momentum for each generator applied to the Argonne v_{18} 1S_0 potential. The flow parameter was run to $\lambda = 2 \text{ fm}^{-1}$ with the generators here to distinguish between ambiguities caused by using λ_{eq} . In Figure 4.13, the values from different generators agree quite well for $k < \sigma$, where $\sigma \approx \lambda$. Moreover, we see that the minor ‘‘pincushion’’ effect seen in Figure 4.12 for these generators relative to $G_s = T$ is indeed an artifact of using λ_{eq} , as each curve falls to zero at approximately the same time. In Figure 4.14 we focus on G_s^{exp} versus $G_s = T$ and the fact that they differ for $\sigma \leq \lambda$. However, as $\sigma \rightarrow \lambda$ it is evident that the evolution of the novel generator becomes increasingly similar to $G_s = T$ in the low-momentum region $k < \lambda$. For larger values of σ , these generators become indistinguishable from $G_s = T$.

As a demonstration of similar behavior for different NN potentials, an evolved potential with different generators in the 1S_0 channel of the N³LO 500 MeV potential [15] is shown in

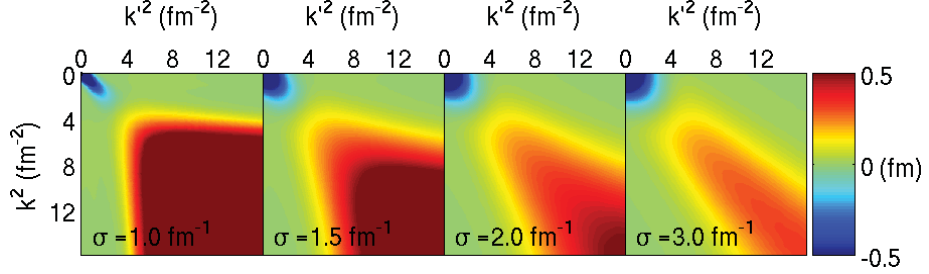


Figure 4.18: Contour plot showing the evolution to $\lambda_{\text{eq}} = 2 \text{ fm}^{-1}$ via Eq. (4.1) starting from the momentum-space Argonne v_{18} ${}^1\text{S}_0$ potential [14] using G_s^{exp} from Eq. (4.13) with different values of σ .

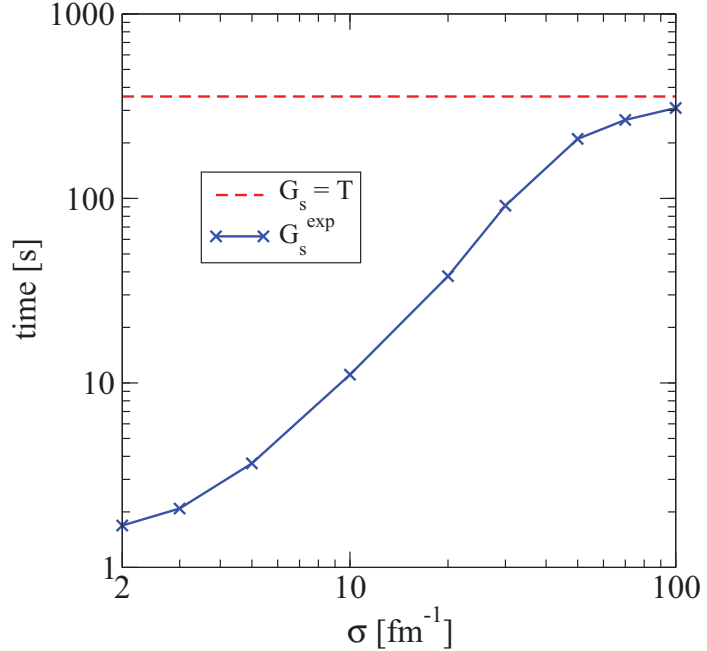


Figure 4.19: Computational time to evolve the Argonne v_{18} ${}^1\text{S}_0$ potential [14] with $G_s = T$ and G_s^{exp} to $\lambda_{\text{eq}} = 2 \text{ fm}^{-1}$ as a function of the value of σ .

Figure 4.15. Note that the initial potential has significantly less coupling at high momentum compared to Argonne v_{18} [65]. As a result, there is correspondingly less improvement in evolution speed. However, the general features of the evolution patterns with different generators seen with Argonne v_{18} are also seen for the N³LO potential.

To better understand the evolution process, we need to look further into the flow equa-

tion itself. Recall that evaluating Eq. (4.1) in a two-body partial-wave momentum space basis with $G_s = T$ yields

$$\begin{aligned}\frac{dV_s(k, k')}{ds} &= -(k^2 - k'^2)^2 V_s(k, k') \\ &+ \frac{2}{\pi} \int_0^\infty q^2 dq (k^2 + k'^2 - 2q^2) V_s(k, q) V_s(q, k') .\end{aligned}$$

In the far off-diagonal region, the first term dominates (this is true for the ordinary range of λ but is modified when λ is comparable with the binding momentum of a bound state). Again, this implies that each off-diagonal matrix element is driven to zero as

$$V_s(k, k') \xrightarrow{k \neq k'} V_{s=0}(k, k') e^{-s(k^2 - k'^2)^2} . \quad (4.14)$$

For $G_s = f(T)$, these results are modified to

$$\begin{aligned}\frac{dV_s(k, k')}{ds} &= -(k^2 - k'^2)(f(k^2) - f(k'^2)) V_s(k, k') \\ &+ \frac{2}{\pi} \int_0^\infty q^2 dq (f(k^2) + f(k'^2) - 2f(q^2)) \\ &\times V_s(k, q) V_s(q, k')\end{aligned} \quad (4.15)$$

and

$$V_s(k, k') \xrightarrow{k \neq k'} V_{s=0}(k, k') e^{-s(k^2 - k'^2)(f(k^2) - f(k'^2))} . \quad (4.16)$$

The difference in the exponents of Eqs. (4.14) and (4.16) for $k \sim \lambda$ leads to $\lambda_{\text{eq}} < \lambda$.

The first term of the flow equation (excluding the factor due to the potential) for each of our generators is shown as a contour plot in Figures 4.16 and 4.17. In Figure 4.16 we see that T works uniformly (in k^2) on the entire region of the potential. With G_s^{inv} , there is much less evolution close to the diagonal. The plot for G_s^{exp} is similar, but exhibits even less evolution in the middle region.

It is evident here that the novel generators will result in less evolution at high momenta, as we have seen, and that this should be a generic result for other partial waves and for higher-body evolution, because it depends on only kinetic energy differences. We also see how the value of σ controls the degree to which the operator G_s is similar to T . This is illustrated in Figure 4.17. If $\sigma = 1 \text{ fm}^{-1}$, only the edges of the potential are modified; the

shape is completely different from T . For $\sigma = 3 \text{ fm}^{-1}$, there is the thinnest band on the diagonal, which is closest to T . At very large σ , there is a transition to T . In the plots of Figure 4.18 we see how the final evolved flow is affected by differing choices of σ .

The limited evolution at high momenta seen in these generators suggests that the time to evolve to a given decoupling parameter λ_{eq} should be less for G_s^{inv} or G_s^{exp} than for $G_s = T$. The dramatic drop in evolution time seen in Figure 4.10 for the generators makes it apparent that they are more efficient. However, we can also look at how the choice of σ affects their performance. This is shown in Figure 4.19 for G_s^{exp} , where we see that the time spent evolving to $\lambda_{\text{eq}} = 2 \text{ fm}^{-1}$ decreases as σ decreases. As σ becomes smaller, the evolution at high momentum is increasingly limited, which we correlate with improvement in computation time; as σ increases, the evolution time approaches that of T_{rel} (as does the flow). Note that for the Argonne v_{18} potential a large σ is needed before G_s is effectively equal to T .

In practical applications, one might optimize the trade-off between decoupling and computational speedup by choosing σ to be approximately equal to, or slightly greater than the λ corresponding to λ_{eq} . Then the decoupling properties of $G_s = T_{\text{rel}}$ are preserved in the low momentum region of interest while still enhancing the computational performance of the evolution by limiting the evolution at high momentum. However, this prescription has not yet been tested in detail.

4.2.2 Few-body tests in a one-dimensional model

The effects on matrices in a momentum basis demonstrated in the last section are generic and so should carry over to alternative bases and to higher-body forces. Calculations for realistic three-dimensional few-body systems are not yet available, but we can test the generators in the one-dimensional model of bosons used in Chapter 3 that has proven to accurately predict the evolution of three-dimensional few-body forces [72]. For completeness, we reiterate here that the potential is written in momentum space as

$$V^{(2)}(p, p') = \frac{V_1}{2\pi\sqrt{2}} e^{-(p-p')^2\sigma_1^2/8} + \frac{V_2}{2\pi\sqrt{2}} e^{-(p-p')^2\sigma_2^2/8}, \quad (4.17)$$

Basis System	Momentum	Oscillator		
	$A = 2$	$A = 2$	$A = 3$	$A = 4$
$\sigma = 2$	3.3	3.3	3.8	4.1
$\sigma = 3$	2.6	2.6	2.7	2.8

Table 4.1: Speed up in model A -particle one-dimensional (1D) oscillator basis for evolution to $\lambda_{eq} \approx 3$, comparing the ratio of the time to evolve $G_s = T_{\text{rel}}$ versus G_s^{exp} . The results for G_s^{inv} are very similar.

where $V_1 = 12$, $\sigma_1 = 0.2$, $V_2 = -12$, and $\sigma_2 = 0.8$ (see Ref. [87] for discussion of units). Also, in calculations with an initial three-body potential, a regulated contact interaction is used. This is written as

$$V^{(3)}(p, q, p', q') = c_E f_\Lambda(p, q) f_\Lambda(p', q'), \quad (4.18)$$

where c_E corresponds to the strength of the interaction and

$$f_\Lambda(p, q) = e^{-((p^2+q^2)/\Lambda^2)^n}. \quad (4.19)$$

The regulator cutoff $\Lambda = 2$, and the sharpness of the fall off is set to $n = 4$. We have chosen these parameters for comparison with Ref. [72].

Performance

Our first test is to confirm that the enhanced computational performance characteristics of these generators are maintained in the few-body basis. Table 4.1 shows the speedup obtained using the G_s^{exp} generator with the model potential described previously. The performance of the G_s^{inv} generator is very similar to the G_s^{exp} results quoted here. Results are reported at an optimal λ_{eq} ; we do not use a range of λ values here because of the particularities of the oscillator basis convergence properties, which is discussed in more detail in what follows.

We find that the evolution of the two-body force in two-, three-, and four-particle systems with novel generators are all 2.5–4 times faster than the evolution with $G_s = T_{\text{rel}}$ (to the same degree of decoupling). The performance enhancement is relatively basis independent, with the speedup for the momentum and oscillator bases roughly equivalent. While the

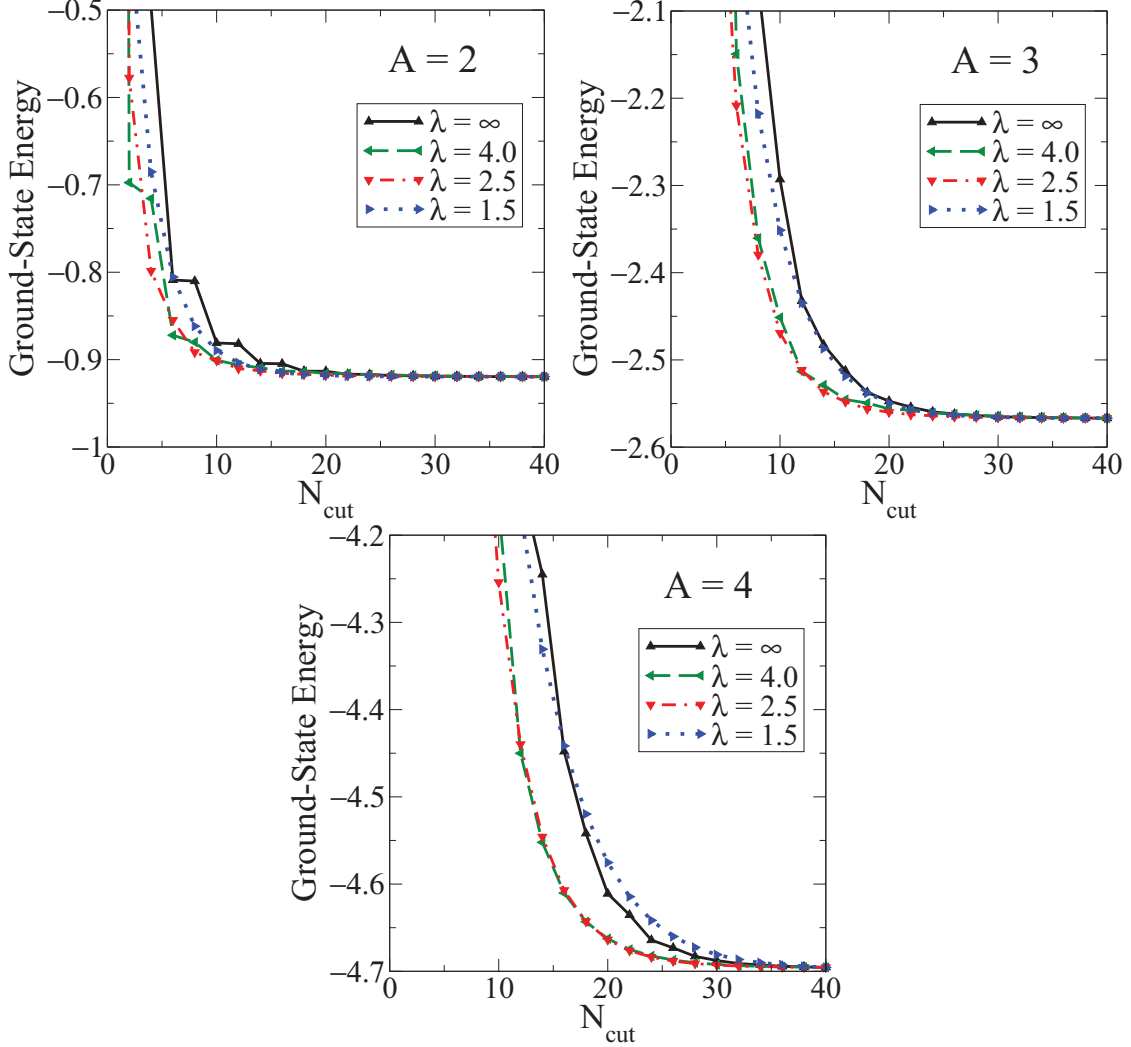


Figure 4.20: Decoupling using G_s^{exp} with $\sigma = 3$ for (a) $A = 2$, (b) $A = 3$, and (c) $A = 4$. The initial two-body-only potential is evolved to each λ shown in a basis with $N_{\text{max}} = 40$. Matrix elements of the potential are set to zero if one or both states have $N > N_{\text{cut}}$ and the resulting Hamiltonian is diagonalized to obtain the ground-state energies plotted.

speedup improvement is much smaller than that found for Argonne v_{18} , we do not expect a direct correspondence. The important point is that the speedup in the $A=2$ particle system serves as a good predictor of the speedup in the $A=3$ and $A=4$ systems. Thus, one might expect a similar improvement in few-body oscillator basis calculations with Argonne v_{18} as found previously for Argonne v_{18} in the two-particle partial-wave momentum basis. This will be significant as we move to novel generator calculations in realistic three-dimensional

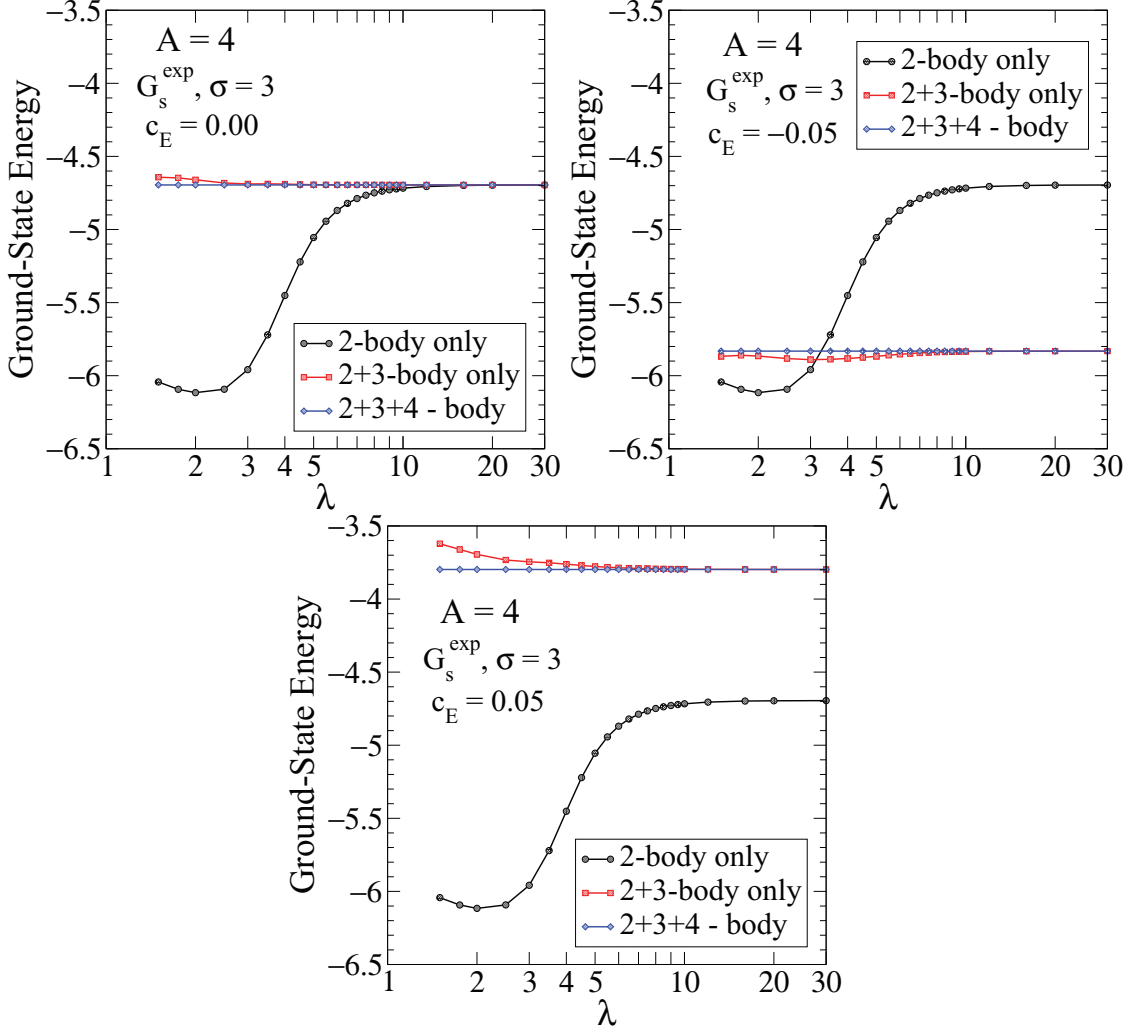


Figure 4.21: The lowest bound-state energy for a four-particle system as a function of λ evolved using the SRG G_s^{exp} generator and an $N_{\max} = 40$ basis with an initial three-body potential with strength (a) $c_E = 0.0$, (b) $c_E = -0.05$, and (c) $c_E = 0.05$. The (blue) curves with diamonds include the full evolution of the Hamiltonian while the (black) curves with circles use the two-body potential evolved in the two-particle system and the (red) curves with squares use the two- and three-body potentials evolved in the three-particle system. Evolution with G_s^{inv} is almost indistinguishable.

systems.

Decoupling

The measure of performance using these generators depends explicitly on their decoupling properties in the few-body harmonic oscillator basis relative to $G_s = T_{\text{rel}}$. Ultimately, we

find the level of decoupling obtained with $G_s = T_{\text{rel}}$ to be matched by these generators.

However, the convergence properties of the oscillator basis with respect to SRG evolution, and consequently the issue of selecting an appropriate λ_{eq} in this basis, is more complicated than for the momentum basis. The convergence of observables depends on a balance of the ultraviolet (UV) and infrared (IR) cutoffs intrinsic to the choice of a particular oscillator basis. These cutoffs are given by [12]

$$\Lambda_{\text{UV}} \sim \sqrt{mN_{\max}\hbar\Omega} \quad (4.20)$$

and

$$\Lambda_{\text{IR}} \sim \sqrt{\frac{m\hbar\Omega}{N_{\max}}}, \quad (4.21)$$

where Ω is the oscillator frequency and N_{\max} is the maximum number of total oscillator excitations in the basis. Thus, a cutoff in oscillator basis states results in two approximate cutoffs in momentum space. However, the SRG, using the generators considered here, provides only a means to effectively lower the UV cutoff (by decoupling high- and low-momentum degrees of freedom in the Hamiltonian). As such, convergence is not monotonically improved with respect to evolution in λ .

As a measure of the decoupling, we plot the binding energy of the lowest energy state for an A -particle system with respect to N_{cut} for evolutions of the initial Hamiltonian to various λ (this procedure was carried out for $G_s = T_{\text{rel}}$ using this model in [72]). The actual calculation is carried out by evolving the model interaction to λ in an initial basis large enough so that the binding energy is well converged. The Hamiltonian is then truncated at N_{cut} and the binding energies are calculated in the reduced basis. The value of N_{cut} refers to the number of oscillator excitations in the basis and is the oscillator basis equivalent of the k_{cut} parameter in momentum space, as used in Sec. 4.2.1. Again, each N_{cut} here corresponds to a rough Λ_{UV} and Λ_{IR} truncation in momentum space.

Results are shown in Figure 4.20 for the $A = 2$, $A = 3$, and $A = 4$ particle systems using G_s^{exp} with $\sigma = 3$ for selected values of λ . The signature of decoupling is the improved convergence of the binding energy at smaller N_{cut} with respect to SRG evolution. As the

interaction is evolved, the degree of decoupling gets better. This is true only up to some value of λ , however, at which point the degree of decoupling starts to get worse. It is the latter behavior, introduced by the IR cutoff of the oscillator basis, that complicates our efforts to choose a λ_{eq} because a one-to-one correspondence with λ is no longer clear.

Nevertheless, a practical choice can be made by equating λ with λ_{eq} when decoupling is found to be optimal in the $G_s = T_{\text{rel}}$ and novel generator evolutions. The optimal levels of evolution happen to coincide at $\lambda \approx 3$ for $G_s = T_{\text{rel}}$ and these generators. Thus, the speedup results in Table 4.1 were reported at $\lambda_{\text{eq}} = 3$. Moreover, given these values for λ and λ_{eq} , we have chosen $\sigma = 3$ for most of the model space calculations in this section.

One may note that differences do exist between the $G_s = T_{\text{rel}}$ and novel generator decoupling results, particularly at low N_{cut} [72]. However, the level at which any of the generators become well converged to the exact results with respect to N_{cut} are effectively the same. Thus, it is reasonable to make the comparisons we have done here to determine λ_{eq} .

Induced Many-Body Forces

In general, we know the evolution of an interaction via the SRG leads to induced many-body forces. As observed earlier, this is evident if we examine the second quantized form of the Hamiltonian

$$H = T_{ij}a_i^\dagger a_j + V_{ijkl}a_i^\dagger a_j^\dagger a_l a_k + \dots \quad (4.22)$$

where the dots indicate that higher-body forces may also be present in the initial interaction. When the SRG commutators in Eq. (4.1) are performed, one can see that many-body forces will be induced for the novel generators just as for T_{rel} . These induced forces could pose a serious problem for few-body calculations because at some point we must truncate the model space in numerical calculations, which will alter the predicted value of observables. Recall that these can be controlled, however, if there is a hierarchy of many-body forces so that successively larger many-body components are suppressed, and one can include at most one or two induced pieces to obtain well converged results. This has been found to be

the case for $G_s = T_{\text{rel}}$ and needs to hold for any practical alternative generators.

A measure of the induced many-body forces (mentioned in Chapter 1, which has been used in previous studies [11, 12, 72]) is to calculate the ground-state energies of the $A = 3$ and $A=4$ particle systems starting with a two-body interaction and to examine how this energy changes with and without the induced three- and four-body components, as a function of the evolution parameter λ . We do this in Figure 4.21 with a plot of the ground-state energy for the four-particle system with the initial two-body interaction embedded and evolved in the $A = 2$, $A=3$, and $A=4$ body bases with the G_s^{exp} generator. The results for G_s^{inv} are virtually indistinguishable. The curves show that the hierarchy of induced many-body forces is preserved for these generators just as with $G_s = T_{\text{rel}}$ [72] (see, however, Ref. [95]). This hierarchy also holds for calculations with an initial three-body force and in the $A = 3$ particle system.

In summary, the model results suggest that the advantageous features of SRG evolution with $G_s = T_{\text{rel}}$ can be maintained with the added computational performance of these generators when applied to realistic three-dimensional few-body calculations.

4.2.3 Section Summary

In this section, novel generators for the SRG that are functions of the kinetic energy operator T with an adjustable scale parameter σ were tested. We found that functions that reduce to T for basis states with kinetic energy less than σ preserved the good features of T , such as decoupling, but efficiently suppressed evolution for higher kinetic energies and thereby took much less time to evolve. Specific examples were considered, but other choices with a Taylor expansion starting with T should give comparable results. Their action was understood using a simple analysis of how the generators directly affect regions of high and low momentum. If σ is large enough, the generators become equivalent to T . It is important to note that not only the two-body properties of T_{rel} were preserved by these generators, but so were its characteristics in a few-body model space. This includes decoupling and the hierarchy of induced many-body forces, which is critical for applications to larger systems of particles.

The generators allow us to evolve potentials to much smaller values of λ than previously feasible. This should enable us to explore the transition between pionful and pionless regions of EFT potentials and further test the observations of Glazek and Perry about evolving past a bound state [96]. The original choice for G_s advocated by Wegner and collaborators [39, 68] and applied extensively in condensed matter is the diagonal component of the interaction, $G_s = H_{\text{diag}}(s)$,

$$\langle i | H_{\text{diag}}(s) | j \rangle \equiv \begin{cases} \langle i | H(s) | j \rangle & \text{if } i = j , \\ 0 & \text{otherwise.} \end{cases} \quad (4.23)$$

In Ref. [96], it was observed that when evolving a simple model past a bound state the Wegner evolution with H_{diag} will decouple the bound state by leaving it as a δ function on the diagonal of the Hamiltonian. In contrast, with $G_s = T_{\text{rel}}$ the bound states remained coupled to low momentum and were pushed to the lowest momentum part of the matrix. This behavior was explored in Ref. [94] for leading-order, large-cutoff EFT potentials featuring deeply bound spurious states. However, it has not been studied for the physical deuteron state, which requires evolving well below $\lambda = 1 \text{ fm}^{-1}$. This is now easily possible with the replacement of H_{diag} for T in Eqs. (4.12) and (4.13), although there are as-yet-unsolved complications from the discretization of the momentum basis.

The most important next step for these novel generators is to apply them to evolve realistic few-body potentials, where speeding up the evolution is desirable because of the large sizes of the matrices involved. The generators can be applied directly to few-particle bases using the method described in Refs. [11, 12, 72]. Calculations in a one-dimensional model performed here imply that the speed up carries over to three-body forces and could have a significant impact in making realistic calculations with additional induced many-body forces feasible.

4.3 Operators: Basis Convergence

Thus far, we have seen how alternative generators can be utilized to tailor the flow of the SRG evolution to nearly any desired pattern of decoupling, as well as to speed up the

evolution and thereby surpass the technical limits inherent in our conventional choice of flow operator. So, building on the flexibility and potential advantages offered by alternative generators in the evolution of Hamiltonians, we now consider their applicability to other operators.

First, it is important to note that the operator evolution and embedding techniques described in Chapter 3 work equally well regardless of the generator being used. In general, a generator in a many-particle basis can be represented schematically in second quantized form as

$$\eta_s = \langle \eta_s^{(1)} \rangle a^\dagger a + \langle \eta_s^{(2)} \rangle a^\dagger a^\dagger aa + \langle \eta_s^{(3)} \rangle a^\dagger a^\dagger a^\dagger aaa + \dots , . \quad (4.24)$$

where a^\dagger and a are creation and annihilation operators with respect to the vacuum in a single-particle basis as usual, and $\langle \eta_s^{(n)} \rangle$ are matrix elements of η_s in the corresponding n -particle basis. As a result, our analysis of SRG evolution in second quantization, and the conclusion that operator evolution is defined completely in each many-particle subspace, follows through equally well for alternative generators. Hence, so too do the rest of the techniques discussed that chapter.

One must use some care, however, in our conventional construction of the generator via the commutator $\eta_s = [G_s, H_s]$. If the flow operator G_s contains a one-body component that does not commute with T_{rel} , the generator will also contain a one-body component even if the potential itself has only two-body or larger pieces. Following the arguments laid out in Chapter 3, the effect of this is to generate evolution in the one-particle subspace in addition to all higher-body subspaces. The evolution in this subspace cannot simply be ignored as it was for $G_s = T_{\text{rel}}$ if this is the case.

Given the simplicity with which one can make use of the formalism and techniques in the previous chapter, there is little more to do in order to use the generators we have already considered (and others) in this chapter with evolved operators. So in this section we instead look at one way how the choice of generator can be used to improve the convergence of specific operator expectation value calculations. Although SRG evolution as we have seen it used thus far is particularly successful in isolating and decoupling parts of the Hamiltonian

to allow the use of a smaller, or simpler basis, the basis that we work in also has significant effects on other operators. While the components of an SRG-evolved Hamiltonian most relevant to predicting the binding energy can be reproduced well in one basis, the same may not be true of all operators evolved in a consistent manner.

This is particularly true for long-range operators in a harmonic oscillator basis, which is commonly used nuclear many-body calculations. We analyze the problem and a potential solution here initially in a 1D model space, and then examine how these results carry over into a realistic calculation.

4.3.1 Long-range Operators in a 1D Model Oscillator Basis

Recall the decoupling analysis of the low-momentum number operator in Figure 3.5. We saw that for an increasingly truncated oscillator basis, SRG evolution of the initial operator in a full basis had little effect on its convergence. For number operators at high momentum (and throughout much of the momentum space), however, SRG evolution significantly improved the convergence in a truncated basis as usual. We would like to understand this problem and how to resolve it. Without a good solution the calculation of some expectation values may remain intractable, despite our newfound ability to calculate the binding energy of increasingly larger nuclear systems.

In an effort address this issue here with a more prototypical long-range operator of interest, we consider the r^2 operator associated with the calculation of the RMS radius of a system. The model calculations performed in this subsection use the same Jacobi oscillator basis code and model Hamiltonian as described in Chapter 3.

RMS Radius and the r^2 Operator

The embedding of the r^2 operator in the few-body 1D boson space, however, involves a little more subtlety than the number operator. It appears at first glance to be an A -body operator defined by

$$r^2 = \frac{1}{A} \sum_{i=1}^A (r_i - x_{CM})^2, \quad (4.25)$$

where r_i are the single particle coordinates and x_{CM} is the center of mass of the system. Accordingly, it may not be immediately apparent how to calculate this in a relative momentum Jacobi few-body space and embed into the harmonic oscillator basis as usual. However, it can be shown that

$$\sum_{i=1}^A (r_i - x_{CM})^2 = \frac{1}{A} \sum_{j>i}^A (r_i - r_j)^2 \quad (4.26)$$

when the masses of the particles are all the same [40]. The 2-body relative Jacobi coordinate x is given by

$$x = \frac{1}{\sqrt{2}}(r_1 - r_2), \quad (4.27)$$

which when combined with Eqns (4.25) and (4.26) implies

$$r^2 = \frac{1}{A} \frac{1}{A} \sum_{j>i}^A (r_i - r_j)^2 = C[A, 2] \frac{1}{A^2} (r_1 - r_2)^2 = C[A, 2] \frac{2}{A^2} x^2 \quad (4.28)$$

for an A -particle symmetric system of identical particles where $C[n, r]$ is the function for combinations defined by $n!/(r!(n - r)!)$. This 2-body operator is analogous to that used with the deuteron, but in order to transform to the 1D relative momentum Jacobi basis we must use the 1D Fourier transform given by

$$\langle x | k \rangle = \frac{1}{\sqrt{2\pi}} e^{ikx}. \quad (4.29)$$

Then, we can embed this into the 1D oscillator space as usual. Thus, the A -body r^2 operator expectation value calculation, as originally defined, is equivalent to a calculation with a 2-body x^2 operator and the standard embedding factor, along with an additional factor of $\frac{2}{A^2}$ in our system.

Figure 4.22a is an N_{cut} plot of the r^2 expectation value for the $A=3$ boson system. The expected value (based on an SVM [40] calculation) is reproduced at large values of N_{cut} . At most points in the evolution, the qualitative behavior seen here is very similar to that found for the low-momentum number operator. The SRG has little effect on the decoupling of the r^2 expectation value for most values of λ . This time, however, the deviation in the expectation value *does* appear to become significant even at N_{cut} for which the binding energy is decoupled (as we were worried it may). The last curve, at $\lambda = 1$, is included to

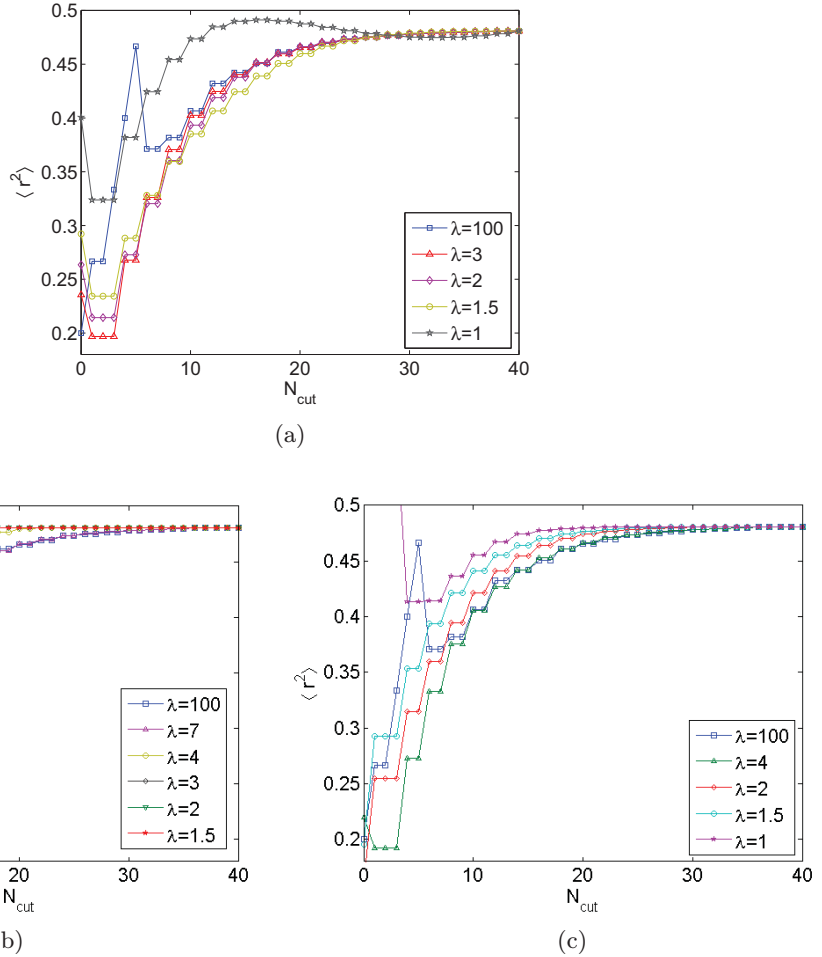


Figure 4.22: Tests of decoupling for the r^2 operator expectation value in the 3-body system at various points, λ , in the evolution using the generators (a) $G_s = T_{\text{rel}}$, (b) $G_s = H_{\text{ho}}$, and (c) $G_s = T_{\text{rel}} + r^2$.

show that even when running the evolution to an extreme, the results ultimately become much worse rather than better. Apparently, while the SRG suppresses high-momentum / short-distance components of the potential at first, if it is run far enough it can produce enough non-locality in coordinate space to begin affecting long range observables as well. The behavior of the expectation value at most values of λ is also very much like that found in calculations of the radii of atomic nuclei using the NCSM [97].

As we discussed for the low-momentum number operator in Chapter 3, this is due to the

limits imposed by the IR cutoff of the harmonic oscillator basis with respect to the size of the basis. The IR and UV cutoffs in the oscillator basis are thanks to the gaussian attenuation of the polynomial expansion (according to the definition of the basis) in coordinate and momentum space respectively. The UV cutoff is given roughly by Eq. (4.20),

$$\Lambda_{\text{UV}} \sim \sqrt{mN_{\max}\hbar\Omega},$$

in momentum space where Ω is the oscillator frequency and N_{\max} is the maximum number of total oscillator excitations in the basis. The standard choice of generator decouples high- and low-momentum components of the Hamiltonian, thereby suppressing the UV component of low-energy states. In doing so, a much lower Λ_{UV} , and consequently N_{\max} , is needed. This is a major advantage of the SRG. The IR cutoff, however, is given by Eq. (4.21),

$$\Lambda_{\text{IR}} \sim \sqrt{\frac{m\hbar\Omega}{N_{\max}}}.$$

By reducing N_{\max} we increase Λ_{IR} for the basis and thereby limit its ability to reproduce the long-range behavior of states and operators. The conventional SRG has little effect in this regime, which is typically a feature of the method. At high enough energies non-nucleonic degrees of freedom become significant and the standard potentials are thus increasingly unphysical. But at low energy, point-like nucleon interactions are appropriate and thus important to maintain. Moreover, many properties can be analyzed with minimal effects due to the IR cutoff.

Although this problem may ultimately limit the usefulness of the harmonic oscillator basis in few-body calculations, there may still be ways to get around the issue. By considering the SRG evolution with a flow operator, G_s , diagonal in the oscillator basis, for example, we can renormalize both the IR and UV components of the wave function. This results in improved convergence of the few-body system binding energies with respect to λ , while also maintaining both long- and short-distance operator expectation values to much smaller values of N_{cut} . Thus, the simplifications afforded by decoupling in the Hamiltonian can also be applied in calculations to a much wider range of expectation values. However,

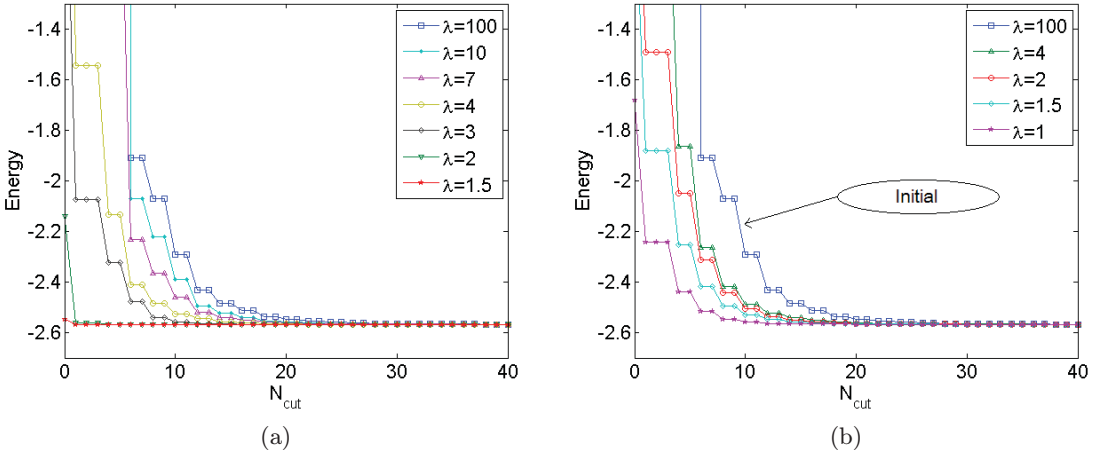


Figure 4.23: Decoupling of the $A=3$ boson system binding energy at various λ for the flow operators (a) $G_s = H_{ho}$ and (b) $G_s = T_{rel} + r^2$.

complications do arise from the artificial renormalization in the IR, as discussed below.

Alternative Generators for Oscillator Basis: 1D Model

Using the SRG, one can ask if there is an alternative generator such as those considered earlier in this chapter, which will produce a pattern of decoupling that would take care of the long-range operator problems we have encountered. Naively, one might consider a flow operator G_s diagonal in the working basis in order to decouple small and large components in that basis, as T_{rel} did in the momentum basis. One such flow operator in the harmonic oscillator basis is the harmonic oscillator Hamiltonian, H_{ho} . This is simply a diagonal matrix of the oscillator excitation energy with respect to the basis states $|N_A i_A\rangle$. Using this parameter in the SRG flow equation generator, running the new evolution on H and r^2 , and making the N_{cut} plot of the expectation value results in Figure 4.22b. This appears to work surprisingly well. The expectation value becomes increasingly independent of N_{cut} as it is evolved down in λ . Moreover, there is also an improvement in the decoupling of the binding energy, as shown in Figure 4.23a.

However, running through an analysis with this flow operator as performed for the evolution equations with $G_s = T_{rel}$ in [72], we find that there is a serious cost for such

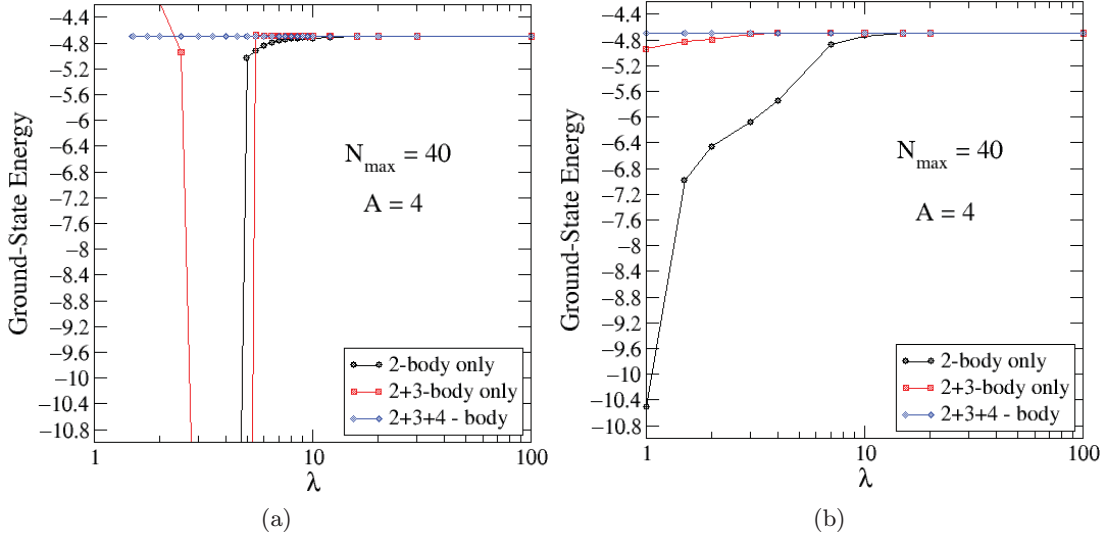


Figure 4.24: Induced many-body contributions to the ground state binding energy of the $A=4$ boson system using (a) $G_s = H_{\text{ho}}$ and (b) $G_s = T_{\text{rel}} + r^2$ with an initial 2-body only interaction. Shown here are the contributions due to only 2-body matrix elements of the evolution, only 2+3-body matrix elements, and the full 4-body evolution.

dramatic improvement in the decoupling. Specifically, the SRG induced many-body forces appear to grow uncontrollably. The left pane of Figure 4.24 is an explicit demonstration of this fact. Here, we show a plot of the ground state energy of the $A=4$ boson system with respect to the evolution λ . The various curves show the behavior of the ground state energy when calculated with the inclusion of a limited number of n -body induced interactions. The curve with no change in the ground state energy is that calculated when all n -body contributions are included (the transformation is unitary here). We see from these curves that no apparent hierarchy in the contributions to the binding energy with the inclusion of successively higher n -body induced interactions is maintained (as was found with $G_s = T_{\text{rel}}$). In fact, the overall behaviour seems rather pathological. Moreover, additional spurious bound states appear. If one ultimately wishes to truncate the many-body contributions at some n -body level smaller than the system size in order to make few-body calculations more tractable, as described above, this generator will thus not be suitable.

Instead of choosing a flow operator diagonal in the harmonic oscillator basis, one might

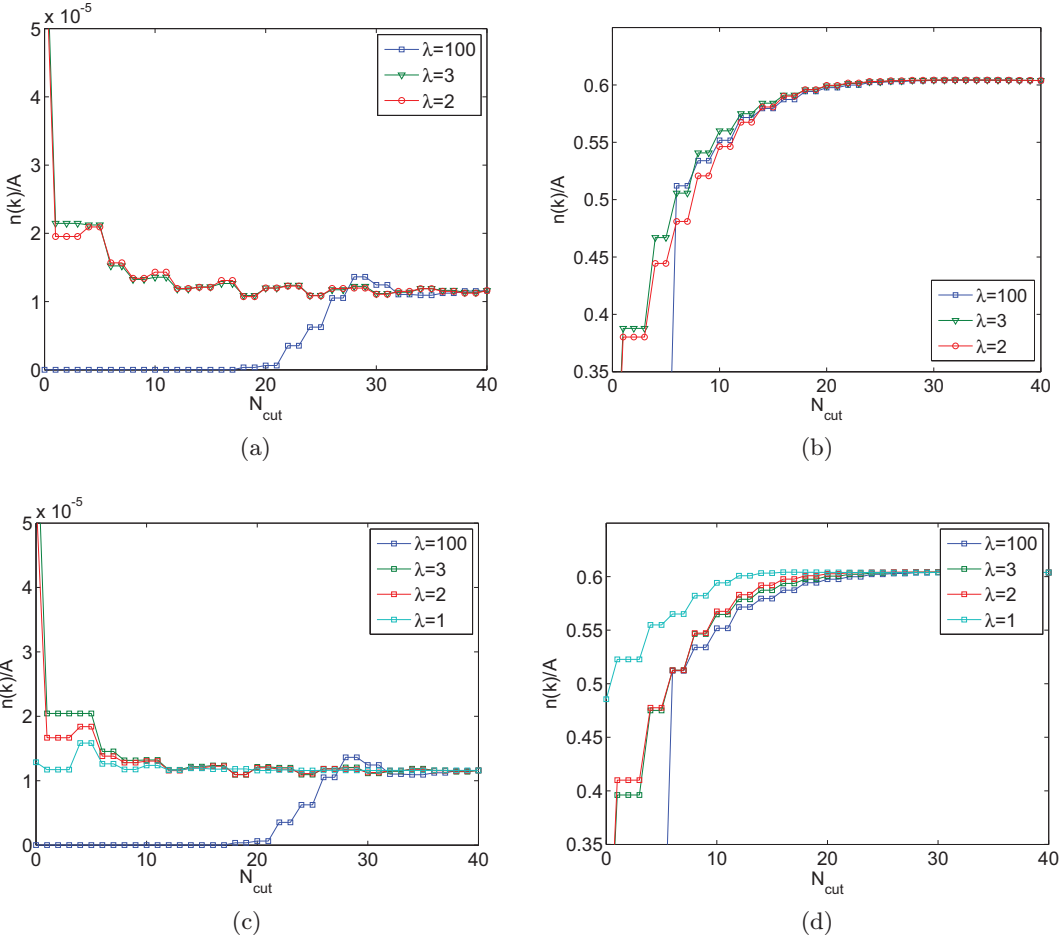


Figure 4.25: Tests of number operator expectation value decoupling with respect to N_{cut} at $q = 15.03$ (left) and at $q = 0.51$ (right), evolved using $G_s = T_{\text{rel}}$ (top, as reproduced for comparison from Chapter 3) and $G_s = T_{\text{rel}} + r^2$ (bottom).

try an alternative approach. We have seen that our inability to achieve satisfactory decoupling with long-range operators stems from the long-range / IR cutoff imposed by the limited size of the harmonic oscillator basis. As such, one would like a flow operator which would cause some renormalization of the long-range components of the interaction, as well as the short range part. In analogy with $T_{\text{rel}} \sim k^2$, which reduces off-diagonal coupling in the momentum space Hamiltonian and thereby suppress the large momentum dependence of the ground state wave function, we could also use r^2 in the flow operator to reduce off-diagonal coupling in the corresponding coordinate space Hamiltonian and thereby suppress

long-range dependence in ground state wave function. Thus, we will use the flow operator $G_s = T_{\text{rel}} + \alpha r^2$ with the idea of renormalizing down from the ultraviolet and up from the infrared. The coefficient $\alpha = 1$ here, but is kept explicit to allow adjustment in future work as a control on the level of IR renormalization for the evolution in λ . Running the SRG evolution with this flow operator and doing the r^2 operator calculations results in the N_{cut} plot of the expectation value in Figure 4.22c. Here, we see that the decoupling of the r^2 expectation value improves substantially as it is evolved down in λ . Moreover, Figure 4.23 shows that the binding energy also improves monotonically with decreasing λ (recall from [72] that there is a point of maximal improvement with respect to λ when using $G_s = T_{\text{rel}}$). In addition, the bottom two panes of Figure 4.25 indicate that this generator has resolved our problems with the number operator as well. And critically, as we can see from the plot in the right pane of Figure 4.24, a hierarchy of many-body induced forces is maintained, and they are not uncontrollably large if we truncate the model space at a point where both the binding energy and r^2 achieve good convergence. As one might expect, the induced forces are somewhat larger than those produced by T_{rel} in the flow operator alone, but it seems plausible that a truncation of induced many-body forces for use in the calculation of larger systems will be realistic.

In order to confirm that our new generator behaves as expected with respect to the renormalization of the ground state wave function, consider Figure 4.26. Here we have the $A=2$ boson system momentum and coordinate space distributions evolved to $\lambda = 3$ and $\lambda = 1$ with the new generator. Also included on the plots are the original wave functions for reference, as well as the wave functions evolved with only the T_{rel} and r^2 parts of the flow operator to better understand their individual contributions. Indeed, the $G_s = T_{\text{rel}} + r^2$ curves show that the wave function is suppressed at both high momenta and long range. It is thus much better able to “fit” in the harmonic oscillator basis. The T_{rel} only curve shows that it is responsible for the suppression of high momentum components of the wave function, as we have already found out. In addition, if it is evolved far enough, it will eventually contribute to long-range components of the wave function. Similarly, the r^2 -only curve shows that it is responsible for not only the suppression of long-range components of

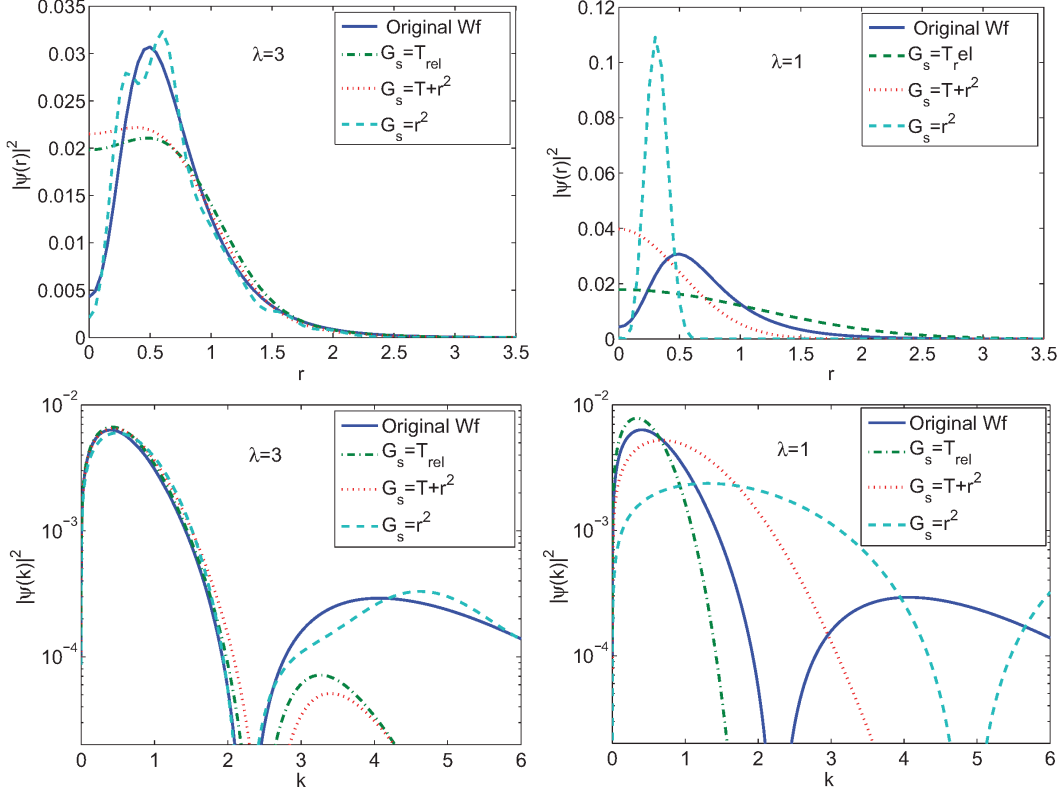


Figure 4.26: Coordinate (top) and momentum (bottom) space distributions for the 2-body wave functions evolved to $\lambda = 3$ (left) and $\lambda = 1$ (right) using the flow operators $G_s = T_{\text{rel}}$, $G_s = T_{\text{rel}} + r^2$, and $G_s = r^2$. The distribution calculated from the initial momentum space wave function is in each plot for reference.

the wave function, but also an increase in high momentum components of the wave function if evolved far enough. Thus, a balance of these effects through adjustment of λ and α must be found as needed (and is likely dependent on the system in question).

To further highlight the long-range effects due to the various generators considered here, Figure 4.27 has been included. This is a plot of the expectation value of the bare, unevolved r^2 operator with evolved ground state wave function with a variety of generators. As one would expect, the average radius of the wave function is “pulled in” by varying amounts by the evolution using the H_{ho} , $T_{\text{rel}} + r^2$, and r^2 flow operators, whereas the radius eventually expands when using the T_{rel} -only parameter.

One will also note that our new flow operator, $G_s = T_{\text{rel}} + r^2$, is essentially H_{ho} with a

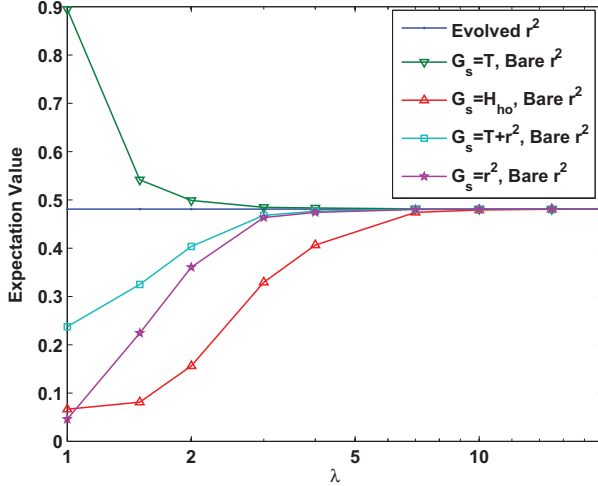


Figure 4.27: Dependence of bare $\langle r^2 \rangle$ with respect to λ for different flow operators $G_s = T_{\text{rel}}$, $G_s = H_{\text{ho}}$, $G_s = T_{\text{rel}} + r^2$, and $G_s = r^2$ in a 3-body system. The evolved r^2 line indicates the initial expectation value.

factor of $\alpha = 1$ instead of $\alpha = \frac{1}{2}m\Omega^2$. As such, we now have a way of understanding, to some extent, the behavior seen in the evolution using H_{ho} as the flow operator. Besides being diagonal in the harmonic oscillator basis, H_{ho} works by renormalizing the long- and short-distance components of the interaction. With a larger factor of α in H_{ho} , this generator led to an emphasis (or “speed up”) of the long range suppression of the wave function, and the associated coupling in the Hamiltonian. This interpretation is supported by the fast drop of the H_{ho} curve in Figure 4.27. Thus, all things considered, it would appear that the IR renormalization of the interaction can lead to the generation of very large induced many-body forces if taken too far. With the flow operator set to $T_{\text{rel}} + r^2$ we were able to achieve a more controlled renormalization at both length scales.

Qualitatively, one might have expected an even greater effect on induced many-body forces, given that at long-range more and more particles will be exposed to changes in the interaction. But this effect is suppressed by the initial lack of strength in the interaction at very large range. Since our tests only ran for up to $A = 4$ particles, it is not known if this will ultimately have a significant effect in a large many-particle space.

Nevertheless, from this initial work, use of the SRG in few-body harmonic oscillator

basis calculations with a generator of the form $G_s = T_{\text{rel}} + \alpha r^2$ appears very promising. There is clearly a balance in the values of α and λ that have the potential to work. However, a more careful study of the extent to which it works and how to control it, as well as its ramifications in 3D no-core shell model calculations, is needed. An important part of this, which should also be mentioned, is how our measure of the decoupling scale (previously given by λ) can now be expressed in the UV and IR. We begin to answer some of these questions below.

4.3.2 Long-range Operator in a 3D Oscillator Basis

The major question we would like to address now is whether or not the use of the flow operator, $G_s = T_{\text{rel}} + \alpha r^2$, just proposed and showing great promise in our one-dimensional model test laboratory, can have the same effect in an oscillator basis calculation of a realistic nuclear system. In doing so, we also perform the first full evolution of an operator in three-dimensions up to the three-body level. The computational framework we take advantage of here is that of the NCFC, as utilized in [12], with the chiral EFT N³LO potential.

In Figure 4.28 we repeat the decoupling analysis of the r^2 in the three-particle space by presenting the RMS matter radius of ³H as a function of the N_{max} truncation after evolution using our conventional choice of generator. A variety of curves are shown, from effectively no evolution all the way down to $\lambda = 1.00 \text{ fm}^{-1}$. Clearly, the realistic oscillator basis calculations suffer from the IR cutoff of the basis to the same degree as seen in the one-dimensional model of bosons. So, we have also performed the same analysis with the alternative generator for a range of α . The results for $\alpha = 10$ are presented in Figure 4.29. As it turns out, the model calculations were an excellent prediction of the effectiveness of a generator with $G_s = T_{\text{rel}} + \alpha r^2$ for the convergence of a long-range operator with respect to a truncated oscillator basis. As the evolution proceeds from $\lambda = \infty$ to $\lambda = 1.00 \text{ fm}^{-1}$, the value of the radius becomes well converged at smaller and smaller values of the N_{max} truncation. Unfortunately, as α is increased and λ decreased to the point where both the binding energy and r^2 are well converged in the three-particle space for an N_{max} truncation that is feasible for use in larger systems, many-body forces and spurious bound states

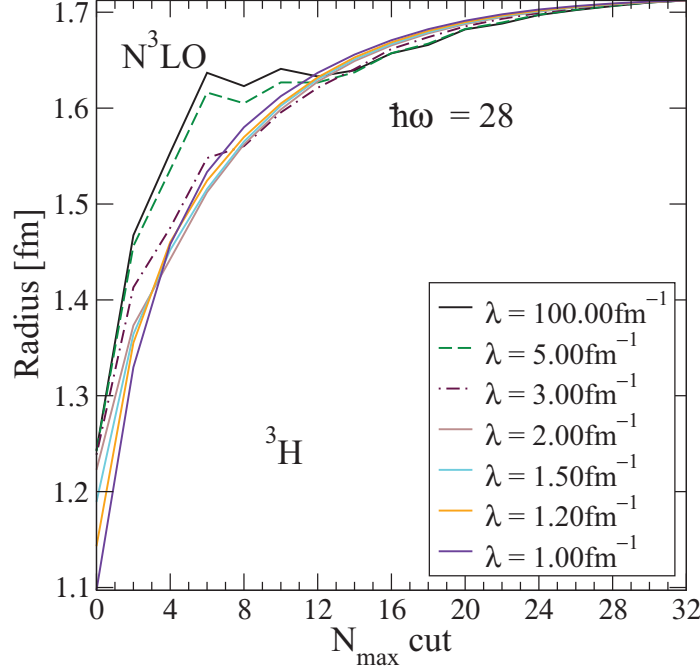


Figure 4.28: The RMS matter radius of ${}^3\text{H}$, as derived from the SRG evolution of r^2 operator for $A=3$ with the flow operator $G_s = T_{\text{rel}}$. A chiral N^3LO potential is used with and initial NN+NNN interaction [19].

appear. This is evident in calculations of the ${}^4\text{He}$ binding energy (not shown) with the associated two- and three-body evolved and truncated Hamiltonian for the various α and λ . The behavior is again very similar to the one-dimensional model, except that for the realistic system it proves difficult, if not impossible, to find an advantageous zone of α and λ which does not result in extremely deep bound states and an associated disruption of the many-body forces. This may simply be a result of the increased importance of longer-range components in the nuclear force, such as from higher partial waves, not present in the simple one-dimensional model.

A complete exploration of N_{max} , $\hbar\omega$, λ , and α parameter space has not been completed, and so it remains possible that an optimal point where calculations can be effectively performed will be found. However, a sufficient number of calculations have been done to cast a great deal of doubt on how well operators evolved via this generator will scale in the many-body space. Any realistic use of this strategy will involve system-dependent fine tuning.

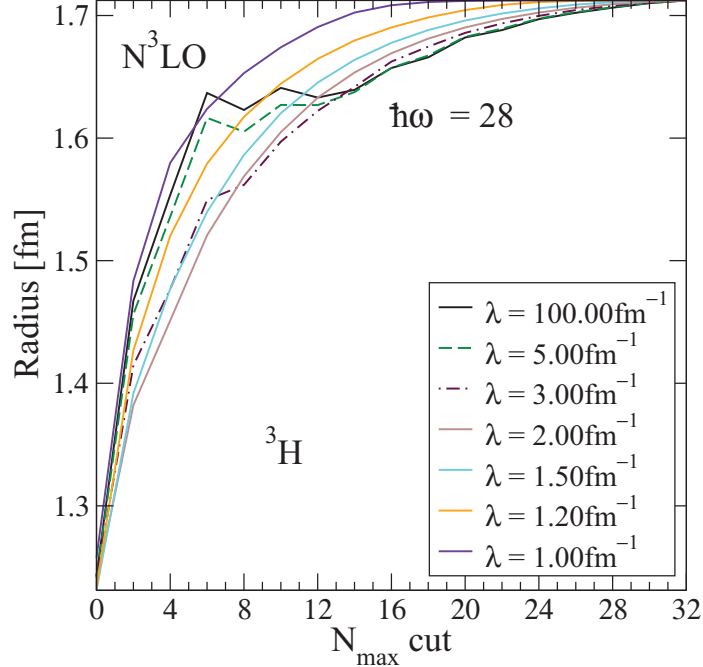


Figure 4.29: The RMS matter radius of ${}^3\text{H}$, as derived from the SRG evolution of r^2 operator for $A=3$ with the flow operator $G_s = T_{\text{rel}} + \alpha r^2$. In this example, $\alpha = 10$. A chiral $N^3\text{LO}$ potential is used with initial NN+NNN interaction [19].

Nevertheless, it may remain a viable option if careful consistency checks are performed with expectation values such as the binding energy which do not have long range dependence for $\alpha = 0$ and $\alpha > 0$ evolutions.

4.3.3 Section Summary

Despite the fact that SRG operators are evolved consistently with the Hamiltonian, taking advantage of the decoupling for calculations of binding energies and wave functions can still present a problem for long-range operators in some commonly used bases. The fault lies not in pathologies or technical issues associated with the SRG, but rather in the inability of some bases to effectively reproduce the asymptotic behavior of the coordinate-space wave function, and similarly, the lowest momentum matrix elements of operators.

The alternative generator considered here held some promise of resolving these particular basis issues. However, in doing so, the many-body forces generated by the evolution were

altered in a fundamental and particularly problematic way for realistic nuclear systems. As a result, this method, in its current form, does not appear to be a sufficient resolution to the problem. On the other hand, this investigation has helped to bring into focus the advantages and possible limitations of SRG operator evolution in the solution of the quantum many-body problem.

Many questions can be answered in these bases with the help of the SRG, as we have seen, but other methods must be developed which can address the problems considered here which do have a significant dependence on the asymptotic behavior of the system. The choice may simply be to use an alternative basis, such as the more flexible gaussian bases used quantum chemistry, or a Woods-Saxon basis for the standard basis-expansion codes. Also, solution techniques which can selectively (either stochastically, or via a systematic criterion) probe a larger sample of the basis space, particularly in the context of a solution of specific operators, may be able to help resolve these issues. Recently, work has also been undertaken to find consistent methods for extrapolating the solution to long-range operator expectation values, using the solutions from more limited bases [98]. Variations of the alternative generator considered here may offer a strategy that can be used in conjunction with this work for a more general set of operators, while avoiding the level of evolution which leads to spurious bound states. This idea is currently being pursued.

4.4 Chapter Summary

The results and open problems still left to address for the alternative generators discussed in this chapter have been summarized in their respective sections. It is worth emphasizing, however, that many more possibilities exist in choosing the evolution pattern of the SRG. Many of the shortcomings of particular Hamiltonians, and possibly even other operators, in the computational solution of the nuclear many-body problem can potentially be resolved by a judicious choice of generator. The possibilities discussed here and other variations on the approach to selecting the flow operator deserve to remain a part of the consideration as the SRG continues to be applied to the solution of the quantum many-body problem.

Chapter 5

OPERATOR FACTORIZATION

We find that factorization of the SRG unitary transformation operator results in the factorization, in some cases, of other SRG evolved operators. Numerical calculations confirm the factorization of the transformation, and we provide a theoretical foundation for this factorization via the operator product expansion (OPE). We also explore the conditions under which additional simplifications result for other operators. *

A number of processes that are of interest in the study of nuclear physics involve large momentum transfers in the interaction of a nucleus with an external probe. Predictions for such processes are made in conjunction with traditional nuclear interactions using operators that have strength largely at high momentum. We explore examples of such processes in the following chapter. But first, in this chapter, we consider in more detail the generic expectation value in a low-energy bound state of operators that initially have strength only at high momentum.

The momentum distribution of the deuteron at large q , which we have already encountered, is a simple example of such an expectation value. The momentum distribution for the initial potentials in Figure 2.2 show structure at high momenta because of the short-range repulsion in the potential (particularly for AV18). When evolved to low momentum, this structure disappears and the deuteron wave function will select only the low-momentum part of the evolved operator. But this evolved operator must still reflect the external high-momentum scale. We can anticipate simplifications by exploiting this separation of

*This chapter is based largely on work first presented in [76]

scales provided by the SRG; in particular, we expect a factorization of the evolved operator based on operator-product-expansion (OPE) arguments applied to nonrelativistic effective theories [99, 100].

5.1 Numerical Verification of Factorization

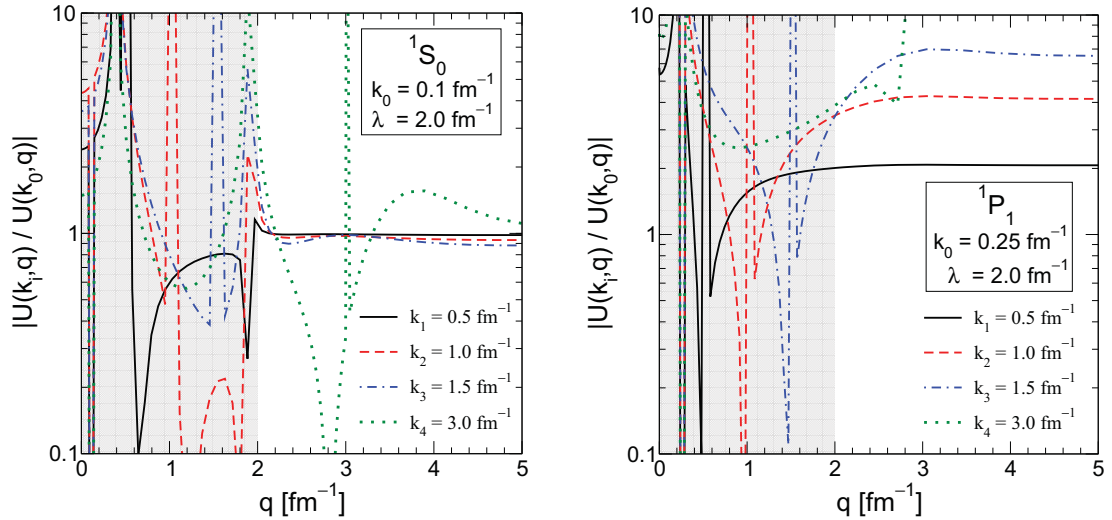


Figure 5.1: Numerical tests of factorization of the unitary transformation $U_\lambda(k, q)$ by plotting the ratio in Eqs. (5.1) and (5.2) as a function of q for fixed k_0 and several values of k_i . Plateaus in q indicate factorization. The unitary transformations are generated from the Argonne v_{18} (AV18) [14] potential evolved to $\lambda = 2 \text{ fm}^{-1}$ in the (a) $^1\text{S}_0$ and (b) $^1\text{P}_1$ partial waves. The shaded region marks $q < \lambda$.

Calculations of the deuteron momentum distribution prior to this work suggested that the unitary evolution operator, $U_\lambda(k, q)$,³ factorizes into a function of k times a function of q , $U_\lambda(k, q) \rightarrow K_\lambda(k)Q_\lambda(q)$, for $k < \lambda$ and $q \gg \lambda$ [8]. To numerically test for factorization in the SRG unitary transformation, we use the transformations generated via Eq. (2.5) and the evolution of NN potentials, and consider the ratio

$$\frac{U_\lambda(k_i, q)}{U_\lambda(k_0, q)} \xrightarrow{?} \frac{K_\lambda(k_i)Q_\lambda(q)}{K_\lambda(k_0)Q_\lambda(q)}, \quad (5.1)$$

³Because λ is an important momentum scale in our factorization discussion, we use the notation U_λ with $\lambda = s^{-1/4}$ rather than U_s in this section.

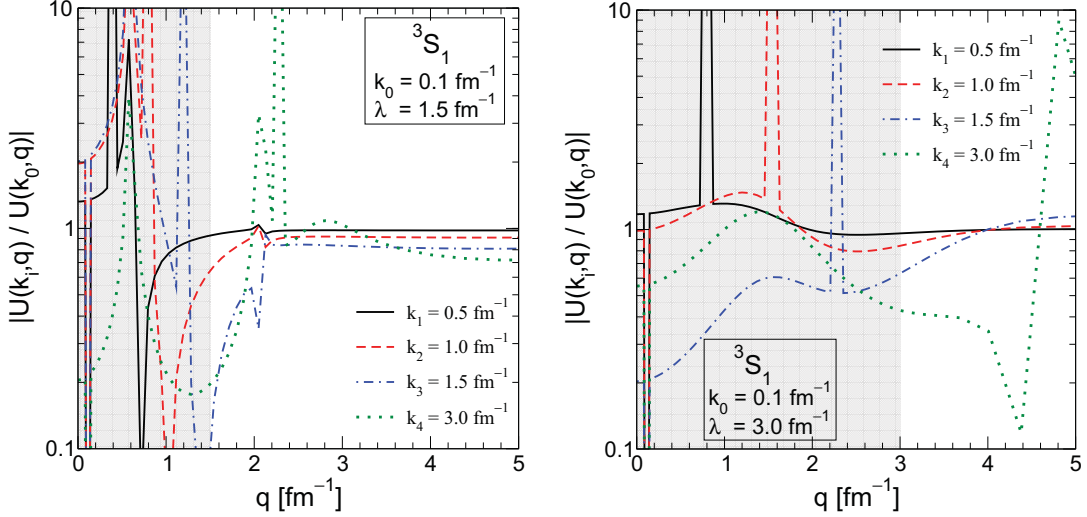


Figure 5.2: Same as Figure 5.1 but for the 3S_1 partial wave and λ of (a) 1.5 fm^{-1} and (b) 3 fm^{-1} .

holding k_i and k_0 constant with $k_0 \ll \lambda$. If there is factorization, the q dependence should cancel; that is, for $k < \lambda$ and $q \gg \lambda$ we should find

$$\frac{U_\lambda(k_i, q)}{U_\lambda(k_0, q)} \approx \frac{K_\lambda(k_i)}{K_\lambda(k_0)}. \quad (5.2)$$

In Figures 5.1 and 5.2 we plot the ratio in Eq. (5.1) versus q for representative cases. The signature of factorization is a plateau in q . The shaded regions are where $q \leq \lambda$. In all cases, there is no factorization in this region, consistent with the requirement that $q \gg \lambda$. In the unshaded region we see definite plateaus for $q > \lambda$ as long as $k_i < \lambda$, with diminishing prominence as k_i increases (they disappear for $k_i > \lambda$). Thus we have at least a qualitative verification of factorization. Note that Figure 5.2(b) shows that for larger λ the clean factorization breaks down (as well as restricting the applicable domain).

The singular value decomposition (SVD) can be used as a tool to quantitatively analyze the extent to which U_λ factorizes. The SVD of a matrix M can be expressed in general as an outer product expansion

$$M = \sum_{i=1}^r d_i \mathbf{u}_i \mathbf{v}_i^t, \quad (5.3)$$

where r is the rank of the matrix and the d_i are the singular values (in order of decreasing

Potential	$^1\text{S}_0$			$^3\text{S}_1 - ^3\text{D}_1$		
	d_1	d_2	d_3	d_1	d_2	d_3
AV18	0.763	0.033	0.007	0.671	0.015	0.008
N3LO 500 MeV	1.423	0.221	0.015	1.873	0.225	0.044
N3LO 550/600 MeV	3.074	0.380	0.061	4.195	0.587	0.089

Table 5.1: Singular values of the unitary transformation $U(k, q)$ for $q > \Lambda$ and $k < \Lambda$ (see discussion in text; units in fm^{-1}) corresponding to the given potentials at $\lambda = 2 \text{ fm}^{-1}$ in the $^1\text{S}_0$ partial wave and $^3\text{S}_1 - ^3\text{D}_1$ coupled channel.

value). The idea is that if the first singular value, d_1 , is sufficiently large compared to the others, the first term dominates and we have a factorized approximation. We can apply this to U_λ in the region where high and low momentum couple. Thus, the vector \mathbf{u}_1 would correspond to the low momentum function $K_\lambda(k)$ from Eq. (5.1) and \mathbf{v}_1 to $Q_\lambda(q)$. If valid, one can calculate the factorized operator using the unitary transformation obtained directly from the SVD. Moreover, the expansion provided by the SVD allows us to make systematic corrections to the factorized unitary transformation and the operators evolved with it.

To test if such an expansion can be used, the first few singular values have been calculated in Table 5.1 for the $q > \lambda$ and $k < \lambda$ region of the SRG unitary transformations for several different potentials, each evolved to $\lambda = 2 \text{ fm}^{-1}$. That is, the SVD is applied to the matrix obtained when elements of $U_\lambda(k, q)$ with $k > \Lambda$ and $q < \Lambda$ are set to zero; in practice a cutoff $\Lambda \approx 2.5 \text{ fm}^{-1}$ is used to ensure that we are in the region where off-diagonal coupling is strongly suppressed everywhere in the Hamiltonian. The dominance of d_1 in each case is promising.

To test if a truncated outer product sum is a good approximation to the contribution from $k < \Lambda$, $q > \Lambda$, we consider the errors in some representative expectation values (calculated without factorization in Chapter 2) in Table 5.2 for several levels of truncation. The “zeroth-order” contribution is from the matrix where $k > \Lambda$ and $q > \Lambda$ is set to zero (this is denoted by SVD=0 in the table). The first-order (SVD=1 in the table) contribution uses the same matrix plus the approximation of $U_\lambda(k, q)$ for $k < \Lambda$ and $q > \Lambda$ given by the first outer product in the SVD expansion. The second-order approximation uses two outer

products, etc. The occupation and charge form factor operators shown here are chosen to illustrate the effects of the factorized approximation at various momenta. Additionally, the initial occupation operator has no off-diagonal strength, whereas the initial charge form-factor operators have relatively substantial off-diagonal contributions at large values of q ; this is significant for the applicability of factorization to an operator, as we see below. So, what we find at low momentum for the occupation operator is that it is essentially exact, up to errors resulting from decoupling and truncation of the wave function, and it is the same with or without the SVD approximation. This error increases, as expected, for larger λ . Because G_C is more diffuse initially, we see a small improvement even at small momenta when using the SVD approximations.

For the occupation operator at high momenta (well above the cutoff), the error is 100% without an approximation to $U_\lambda(k, q)$ because there is a hard cutoff and the initial operator is localized in the upper region of momentum space. However, with just one term in the SVD expansion we recover that expectation value for $\lambda = 1.5 \text{ fm}^{-1}$ to better than 1%, and the situation improves with additional terms in the expansion. At $\lambda = 3.0 \text{ fm}^{-1}$ decoupling is evidently not sufficient for this approximation to work well. At very large values of momenta (e.g., $q \approx 6.9 \text{ fm}^{-1}$) the charge form factor shows improvement with the SVD approximation, but because this operator has significant off-diagonal strength, the improvement is not as pronounced. At a value of $q \approx 3.0 \text{ fm}^{-1}$ it is evident that the SVD still improves the relative error. However, recall from the definition of the operators in Chapter 2 that the strength in the form factor matrix elements is larger around $\approx \frac{1}{2}q$, since we are in the two-body center-of-mass frame. As a result, this value for the form factor is fairly well reproduced to begin with.

5.2 Connection to the Operator Product Expansion

The OPE was developed for the evaluation of singular products of local field operators at small separation. In our case, where such operators are treated as matrices and we typically work in momentum representation, the focus becomes low-momentum matrix elements of

SRG $\lambda = 1.5 \text{ fm}^{-1}$				
Operator	SVD	$q = 0.34$	$q = 3.01$	$q = 6.90$
$\langle a_q^\dagger a_q \rangle$	0	7.61×10^{-7}	1.00	
with N ³ LO	1	7.61×10^{-7}	4.28×10^{-3}	
	2	7.61×10^{-7}	4.79×10^{-4}	
$G_C(q)$	0	6.90×10^{-4}	5.01×10^{-3}	8.93×10^{-1}
with NNLO	1	1.28×10^{-7}	8.90×10^{-5}	4.06×10^{-2}
	2	1.04×10^{-6}	2.10×10^{-5}	4.18×10^{-2}
SRG $\lambda = 3.0 \text{ fm}^{-1}$				
Operator	SVD	$q = 0.34$	$q = 3.01$	$q = 6.90$
$\langle a_q^\dagger a_q \rangle$	0	1.06×10^{-3}	1.00	
with N ³ LO	1	1.06×10^{-3}	6.36×10^{-1}	
	2	1.06×10^{-3}	6.35×10^{-1}	
$G_C(q)$	0	4.10×10^{-4}	3.36×10^{-3}	8.92×10^{-1}
with NNLO	1	1.63×10^{-4}	2.66×10^{-4}	4.00×10^{-1}
	2	1.63×10^{-4}	3.04×10^{-4}	4.09×10^{-1}

Table 5.2: Relative error of evolved operator matrix elements calculated using the SVD to factorize $U_\lambda(k, q)$ in the region where $k < \Lambda$ and $q > \Lambda$ (see discussion in text; units in fm^{-1}).

a product in which high-momentum states dominate the intermediate sum. This leads us directly to consider low- to high-momentum matrix elements of SRG-evolved operators, and a generic analysis is then based on the study of $U_\lambda(k, q)$ for $k < \lambda$ and $q \gg \lambda$.

The utility of the OPE rests on factorization; short-distance details decouple from long-distance dynamics. Factorization enables one, for example, to separate the momentum and distance scales in hard-scattering processes in terms of perturbative QCD and parton distribution functions. In our case, factorization is the direct result of decoupling. It provides tools that let us parameterize the high-momentum components of operators that would normally require degrees of freedom we do not retain. We can, for example, build effective few-body operators containing state-independent functions of high momenta that can be measured directly in few-body experiments. These operators can then be employed to make predictions for A -body systems, as we will see in the following chapter.

Consider a generic operator, $\hat{O}_\lambda = U_\lambda \hat{O} U_\lambda^\dagger$, and employ the spectral representation for

U_λ :

$$U_\lambda(k, q) = \sum_{\alpha} \langle k | \psi_{\alpha}(\lambda) \rangle \langle \psi_{\alpha}(\infty) | q \rangle. \quad (5.4)$$

The OPE deals with cases in which the unevolved operator is dominated by high momenta (e.g., $a_q^\dagger a_q$ with large q is the simplest paradigm) and we focus on $k < \lambda$ and $q \gg \lambda$. For $k < \lambda$ we exploit the fact that low-momentum components of high-energy eigenstates of H_λ are exponentially suppressed because of decoupling. As a result the sum is dominated by low-energy states,

$$U_\lambda(k, q) \approx \sum_{E_{\alpha} \ll \lambda^2} \langle k | \psi_{\alpha}(\lambda) \rangle \langle \psi_{\alpha}(\infty) | q \rangle. \quad (5.5)$$

Once the sum is restricted we can turn our focus to approximating the high-momentum components of the unevolved low-energy states. This analysis is closely related to Lepage's discussion of the OPE analysis of wave functions, which leads him to write for S-waves in position representation [99]:

$$\Psi_{\text{true}}(r) = \bar{\gamma}(r) \int d^3 r \Psi_{\text{eff}} \delta_a^3(\mathbf{r}) + \bar{\eta}(r) a^2 \int d^3 r \Psi_{\text{eff}} \nabla^2 \delta_a^3(\mathbf{r}) + \mathcal{O}(a^4), \quad (5.6)$$

where the coefficient functions $\bar{\gamma}(r)$ and $\bar{\eta}(r)$ are state-independent parameterizations of the short-distance physics, and a is approximately the distance of the ultraviolet cutoff. In this section, we outline how SRG factorization can be understood more generally (and analytically) in the context of the OPE for nonrelativistic Schrödinger problems by deriving an analogous equation in momentum space for the SRG-evolved wave function.

To do so, we first define the projection operators

$$\mathcal{P}_{\Lambda} = \int_0^{\Lambda} d\tilde{p} |p\rangle\langle p| \quad (5.7)$$

and

$$\mathcal{Q}_{\Lambda} = \int_{\Lambda}^{\infty} d\tilde{q} |q\rangle\langle q|, \quad (5.8)$$

where Λ divides momentum space and $d\tilde{p} \equiv \frac{2}{\pi} p^2 dp$ in the partial-wave momentum basis. This Λ is to be distinguished from λ , which is the SRG evolution parameter and an approximate measure of decoupling in the evolved potential. We use ψ_{α}^{λ} to denote the eigenstates of the Hamiltonian ordered according to increasing energy E_{α} and evolved to λ via the

SRG. H_λ and V_λ represent the corresponding SRG evolved Hamiltonian and potential. The initial, unevolved operators correspond to $\lambda = \infty$.

From the unevolved Schrödinger equation

$$H_\infty |\psi_\alpha^\infty\rangle = E_\alpha |\psi_\alpha^\infty\rangle , \quad (5.9)$$

we can write

$$\begin{pmatrix} \mathcal{P}_\Lambda H_\infty \mathcal{P}_\Lambda & \mathcal{P}_\Lambda H_\infty \mathcal{Q}_\Lambda \\ \mathcal{Q}_\Lambda H_\infty \mathcal{P}_\Lambda & \mathcal{Q}_\Lambda H_\infty \mathcal{Q}_\Lambda \end{pmatrix} \begin{pmatrix} \mathcal{P}_\Lambda \psi_\alpha^\infty \\ \mathcal{Q}_\Lambda \psi_\alpha^\infty \end{pmatrix} = E_\alpha \begin{pmatrix} \mathcal{P}_\Lambda \psi_\alpha^\infty \\ \mathcal{Q}_\Lambda \psi_\alpha^\infty \end{pmatrix} , \quad (5.10)$$

and thus for the “ \mathcal{Q} ” space we have

$$\begin{aligned} \mathcal{Q}_\Lambda |\psi_\alpha^\infty\rangle &= (E_\alpha - \mathcal{Q}_\Lambda H_\infty \mathcal{Q}_\Lambda)^{-1} \mathcal{Q}_\Lambda H_\infty \mathcal{P}_\Lambda \mathcal{P}_\Lambda |\psi_\alpha^\infty\rangle \\ &= (E_\alpha - \mathcal{Q}_\Lambda H_\infty \mathcal{Q}_\Lambda)^{-1} \mathcal{Q}_\Lambda V_\infty \mathcal{P}_\Lambda |\psi_\alpha^\infty\rangle , \end{aligned} \quad (5.11)$$

where we have used $(\mathcal{P}_\Lambda)^2 = \mathcal{P}_\Lambda$, $H_\infty = T + V_\infty$, and $\mathcal{Q}_\Lambda T \mathcal{P}_\Lambda = 0$. For low-energy states ψ_α^∞ such that $|E_\alpha| \ll \text{Min}[|E_{QHQ}|]$ (where E_{QHQ} are the eigenvalues of $\mathcal{Q}HQ$), we can neglect the E_α dependence. Also, assuming that the potential $V_\infty(q', p)$ is slowly varying with respect to p compared to $\psi_\alpha^\infty(p)$ in the region $p < \Lambda$ and $q' \gg \Lambda$, we can use the expansion for S-waves

$$\begin{aligned} \int_0^\Lambda d\tilde{p} V_\infty(q', p) \psi_\alpha^\infty(p) &\approx V_\infty(q', p')|_{p'=0} \times \int_0^\Lambda d\tilde{p} \psi_\alpha^\infty(p) \\ &\quad + \frac{d^2}{dp'^2} V_\infty(q', p') \Big|_{p'=0} \times \int_0^\Lambda d\tilde{p} p^2 \psi_\alpha^\infty(p) + \dots \end{aligned} \quad (5.12)$$

to first order, combined with the fact that the low-energy states will have momentum components peaked at small p , to write

$$\langle q | \psi_\alpha^\infty \rangle \approx - \int_\Lambda^\infty d\tilde{q}' \int_0^\Lambda d\tilde{p} \langle q | \frac{1}{\mathcal{Q}_\Lambda H_\infty \mathcal{Q}_\Lambda} | q' \rangle V_\infty(q', 0) \psi_\alpha^\infty(p) . \quad (5.13)$$

Tests indicate that these assumptions are valid for realistic NN potentials.

Further, we see empirically via Figure 2.2 that $\mathcal{P}_\Lambda |\psi_\alpha^\infty\rangle \approx Z(\lambda) |\psi_\alpha^\lambda\rangle$ when $\lambda \gtrsim \Lambda$ (this is consistent with our understanding that the SRG with $G_s = T_{\text{rel}}$ renormalizes/suppresses only the short-distance components of the wave function for values of λ considered here).

Thus, setting $\Lambda = \lambda$ and defining

$$\gamma^\lambda(q) \equiv - \int_\lambda^\infty d\tilde{q}' \langle q | \frac{1}{\mathcal{Q}_\lambda H_\infty \mathcal{Q}_\lambda} | q' \rangle V_\infty(q', 0), \quad (5.14)$$

we have

$$\psi_\alpha^\infty(q) \approx \gamma^\lambda(q) \int_0^\lambda d\tilde{p} Z(\lambda) \psi_\alpha^\lambda(p). \quad (5.15)$$

So we see that the high-momentum components of low-energy eigenstates can be factorized into a state-independent function $\gamma^\lambda(q)$, which summarizes the short distance behavior of the wave function, and a coefficient (given by an integral over the renormalized wave function) that gives the contribution due to the long-distance structure of the state. Moreover, if we include higher-order corrections resulting from the expansion of $\int_0^\lambda d\tilde{p} V_\infty(q', p) \psi_\alpha^\infty(p)$ about $p = 0$, we recover the analog to Lepage's OPE, Eq. (5.6), in momentum space for the short-distance structure of a wave function. It is given by

$$\psi_\alpha^\infty(q) \approx \gamma^\lambda(q) \int_0^\lambda d\tilde{p} Z(\lambda) \psi_\alpha^\lambda(p) + \eta^\lambda(q) \int_0^\lambda d\tilde{p} p^2 Z(\lambda) \psi_\alpha^\lambda(p) + \dots \quad (5.16)$$

where $\gamma^\lambda(q)$ is given previously and

$$\eta^\lambda(q) \equiv - \int_\lambda^\infty d\tilde{q}' \langle q | \frac{1}{\mathcal{Q}_\lambda H_\infty \mathcal{Q}_\lambda} | q' \rangle \left. \frac{\partial^2}{\partial p^2} V_\infty(q', p) \right|_{p=0}. \quad (5.17)$$

Now, from the definition of the SRG unitary evolution operator in Eq. (2.5), in the region $k < \lambda$ and $q \gg \lambda$ we can use the leading-order term of our OPE to write

$$\begin{aligned} U_\lambda(k, q) &= \sum_\alpha^\infty \langle k | \psi_\alpha^\lambda \rangle \langle \psi_\alpha^\infty | q \rangle \\ &\approx \left[\sum_\alpha^{|E_\alpha| \ll |E_{\mathcal{Q}_H \mathcal{Q}}|} \langle k | \psi_\alpha^\lambda \rangle \int_0^\lambda d\tilde{p} Z(\lambda) \psi_\alpha^{\lambda\dagger}(p) \right] \gamma^\lambda(q) \\ &\equiv K_\lambda(k) Q_\lambda(q), \end{aligned} \quad (5.18)$$

where the sum is only over states in the “ \mathcal{P} ” space thanks to decoupling. Thus, we can understand the factorization of U_λ as a general consequence of our ability to factorize the high-momentum components of low-energy nuclear wave functions via an OPE plus decoupling in the SRG-evolved Hamiltonian. Moreover, because $\psi_\alpha^\lambda(k)$ to good approximation

has no support when $k < \lambda$ for α in the “ \mathcal{Q} ” space, we can extend the α sum in Eq. (5.18) to the full space and apply closure to find

$$U_\lambda(k, q) \approx \left[Z(\lambda) \int_0^\lambda d\tilde{p} \sum_{\alpha}^{\infty} \langle k | \psi_{\alpha}^{\lambda} \rangle \langle \psi_{\alpha}^{\lambda} | p \rangle \right] \gamma^{\lambda}(q) \approx Z(\lambda) \gamma^{\lambda}(q) . \quad (5.19)$$

Thus, to a first approximation, $K_\lambda(k)$ is a constant factor.

This approximate constancy implies that the ratios for the $L = 0$ channels in Figures 5.1(a) and 5.2(a) and (b) should tend to one in the factorization region, which is realized at the 10–20% level for sufficiently low λ . For $L > 0$, the generalization of Eq. (5.19) follows from modifying the Taylor series in Eq. (5.12) to account for $V_\infty(q', p) \propto p^L$ for small p . Then Eqs. (5.14) and (5.15) are changed to

$$\gamma^{\lambda}(q) \equiv - \int_{\lambda}^{\infty} d\tilde{q}' \langle q | \frac{1}{\mathcal{Q}_{\lambda} H_{\infty} \mathcal{Q}_{\lambda}} | q' \rangle \left. \frac{d^L}{dp^L} V_{\infty}(q', p) \right|_{p=0} , \quad (5.20)$$

and

$$\psi_{\alpha}^{\infty}(q) \approx \gamma^{\lambda}(q) \int_0^{\lambda} d\tilde{p} Z(\lambda) p^L \psi_{\alpha}^{\lambda}(p) . \quad (5.21)$$

With these changes, Eq. (5.19) for the factorization at leading approximation becomes

$$U_\lambda(k, q) \approx \left[Z(\lambda) \int_0^{\lambda} p^L d\tilde{p} \sum_{\alpha}^{\infty} \langle k | \psi_{\alpha}^{\lambda} \rangle \langle \psi_{\alpha}^{\lambda} | p \rangle \right] \gamma^{\lambda}(q) \approx k^L Z(\lambda) \gamma^{\lambda}(q) . \quad (5.22)$$

This approximation implies that the ratios in the factorization region should tend for $L > 0$ to $(k_i/k_0)^L$, which is seen at the same 10–20% level in Figure 5.1(b).

5.3 Consequences of Factorization

To gain insight into the implications of this factorization, we consider the expectation value of $a_q^\dagger a_q$ in a low-energy state, the deuteron. Because we know that strength in the evolved number operator expectation value decouples from high-momentum contributions in the

deuteron, we can write

$$\begin{aligned}
\left\langle \psi_d^\lambda \left| \left(a_q^\dagger a_q \right)_\lambda \right| \psi_d^\lambda \right\rangle &= \left\langle \psi_d^\lambda \left| U_\lambda \left(a_q^\dagger a_q \right) U_\lambda^\dagger \right| \psi_d^\lambda \right\rangle \\
&\approx \int_0^\lambda d\tilde{k}' \int_0^\infty d\tilde{q}' \int_0^\infty d\tilde{q}'' \int_0^\lambda d\tilde{k} \psi_d^{\lambda\dagger}(k') U_\lambda(k', q') \delta(q' - q) \\
&\quad \times \delta(q'' - q') U_\lambda(q'', k) \psi_d^\lambda(k) \\
&= \int_0^\lambda d\tilde{k}' \int_0^\lambda d\tilde{k} \psi_d^{\lambda\dagger}(k') U_\lambda(k', q) U_\lambda(q, k) \psi_d^\lambda(k).
\end{aligned} \tag{5.23}$$

For a low-momentum operator, one with $q < \lambda$, the expectation value thus depends only on the low-momentum details of the wave function (original and evolved). For $q \gg \lambda$, however, we can make use of factorization and set $U(k, q) \rightarrow K_\lambda(k)Q_\lambda(q)$ to write

$$\int_0^\lambda d\tilde{k}' \int_0^\lambda d\tilde{k} \psi_d^{\lambda\dagger}(k') K_\lambda(k') [Q_\lambda(q) Q_\lambda(q)] K_\lambda(k) \psi_d^\lambda(k) \tag{5.24}$$

from Eq. (5.23). Here we see that the expectation value of a high-momentum number operator is independent of the long-distance structure of the wave function. This is consistent with earlier calculations of the deuteron momentum distribution [8]. Again, as with decoupling in the potential, we appear to have a means by which long- and short-distance details can be separated for an operator evolved via the SRG.

The generalization of this result is straightforward. Consider the expectation value of an arbitrary operator, $O(q', q)$, in a low-energy state, $\psi_{\text{low}}^\lambda$. Because decoupling is valid for operator expectation values in a momentum basis (as we have seen via the expectation value integrand plots in Secs. 2.1 and 2.2), we can write

$$\begin{aligned}
\left\langle \psi_{\text{low}}^\lambda \left| U_\lambda \hat{O} U_\lambda^\dagger \right| \psi_{\text{low}}^\lambda \right\rangle &\approx \int_0^\lambda d\tilde{k}' \int_0^\infty d\tilde{q}' \int_0^\infty d\tilde{q} \int_0^\lambda d\tilde{k} \\
&\quad \times [\psi_{\text{low}}^\lambda(k')]^\dagger U_\lambda(k', q') O(q', q) U_\lambda(q, k) \psi_{\text{low}}^\lambda(k).
\end{aligned} \tag{5.25}$$

We separate the integrals over the operator in the expectation value and apply factorization to set $U(k, q) \rightarrow K_\lambda(k)Q_\lambda(q)$ in the region where $k < \lambda$ and $q \gg \lambda$. If the *unevolved* operator has coupling between high and low momentum above the the factorization cut, then there is no great simplification. However, if the *unevolved* operator *does not* have coupling of high and low momentum above the factorization cut, factorization will allow us to separate

out the high- and low-momentum structure of an operator into two contributions:

$$\int_0^\lambda d\tilde{k}' \int_0^\lambda d\tilde{q}' \int_0^\lambda d\tilde{q} \int_0^\lambda d\tilde{k} [\psi_{\text{low}}^\lambda(k')]^\dagger U_\lambda(k', q') O(q', q) U_\lambda(q, k) \psi_{\text{low}}^\lambda(k) \quad (5.26)$$

and

$$\int_0^\lambda d\tilde{k}' \int_\lambda^\infty d\tilde{q}' \int_\lambda^\infty d\tilde{q} \int_0^\lambda d\tilde{k} [\psi_{\text{low}}^\lambda(k')]^\dagger K_\lambda(k') [Q_\lambda(q') O(q', q) Q_\lambda(q)] K_\lambda(k) \psi_{\text{low}}^\lambda(k) . \quad (5.27)$$

This is analogous to what was found for the number operator.

Thus, we see that the breakdown of contributions to the expectation value of a general operator is consistent with our interpretation of the SRG flow equations as a means by which one can achieve a separation of scales in the evaluation of nuclear few- and many-body problems. We see explicitly here that the effects of a low-momentum probe of the ground state wave function depends (almost entirely) on the low-momentum details of the renormalized wave function. Likewise, the effect of a high-momentum probe is largely independent of the low-momentum structure. It is only for operators which probe the coupling of high and low momentum (long and short distance) details of the wave function that we must consider the full momentum space evolution of the operator. For the operators that have been considered in this work, the latter is only true of the electromagnetic form factors at relatively high momenta (beyond the typical regime of interest for nuclear structure); for any operators which weakly couple high and low momentum, these terms can be neglected.

5.4 Chapter Summary

We have seen that SRG operator factorization occurs when there is a scale separation between the initial (unevolved) operator and the wave function momentum scale, which is limited by λ . This factorization was shown to be a natural consequence of applying the OPE to the unitary transformation. To summarize the consequences of factorization in the study of external probes, we can write the expectation value of an operator that has weak

coupling between high and low momentum as

$$\begin{aligned} \left\langle \psi_{\text{low}}^{\lambda} \left| U_{\lambda} \hat{O} U_{\lambda}^{\dagger} \right| \psi_{\text{low}}^{\lambda} \right\rangle &\approx \int_0^{\lambda} dk' \int_0^{\lambda} dk [\psi_{\text{low}}^{\lambda}(k')]^{\dagger} \left[\int_0^{\lambda} dq' \int_0^{\lambda} d\tilde{q} \right. \\ &\quad \times U_{\lambda}(k', q') O(q', q) U_{\lambda}(q, k) + I_{QOQ} K_{\lambda}(k') K_{\lambda}(k) \left. \right] \psi_{\text{low}}^{\lambda}(k), \end{aligned} \quad (5.28)$$

where

$$I_{QOQ} = \int_{\lambda}^{\infty} dq' \int_{\lambda}^{\infty} d\tilde{q} Q_{\lambda}(q') O(q', q) Q_{\lambda}(q). \quad (5.29)$$

Thus, by using factorization we see that such an expectation value breaks into a sum of two components: one which describes low-momentum structure, and a high-momentum component that factorizes into a piece depending on the low-momentum structure, and another piece that is a universal function of high momentum q .

Extensions of calculations performed here to systems of $A > 2$ will be previewed in the following chapter, with an application of factorization to momentum distributions of low-energy bound states, for example. Here we will see how Eqs. (5.29) and (5.29) provide an alternative interpretation to the commonly invoked role of short-range correlations.

Chapter 6

APPLICATIONS OF OPERATOR EVOLUTION AND FACTORIZATION

Here we apply the evolved operator methods and simplifications developed in previous chapters to a sample of relevant nuclear many-body techniques and problems. Preliminary calculations in nuclear matter, as well as Hartree-Fock-Bogoliubov are presented. The question of nuclear scaling and the relevance of short-range correlations in atomic nuclei are addressed, particularly in the context of factorization. We also see how this is connected to the EMC effect. Finally, we explore an extension of this work to reactions via deuteron breakup calculation.

There has been a great deal of recent interest in the study of electron scattering experiments on atomic nuclei, particularly at the Continuous Electron Beam Facility at Jefferson Lab. An illustration of one such experiment is shown in Figure 6.1. Here, an electron scatters off a nucleus, transferring momentum via photon exchange. A correlated pair of nucleons is ejected as a result, and some of the final constituents can be detected to reproduce the event. One of the primary goals of these experiments are to probe the high momentum components of the nuclear interaction, and in particular, to isolate the effects of short-range correlations (SRCs) within the atomic nucleus.

Some of the pairs which are produced in experiments like that shown in Figure 6.1 are thought to have high relative momentum within the nucleus, assuming a one photon exchange approximation for the interaction with the nucleus and the plane-wave impulse approximation for the ejected nucleons (i.e., the photon interacts with only one nucleon and

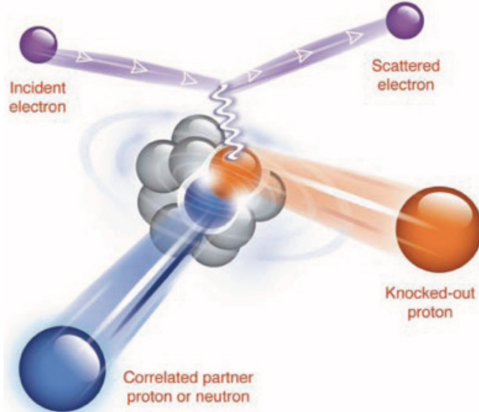


Figure 6.1: Illustration of electron scattering experiment on atomic nucleus [20].

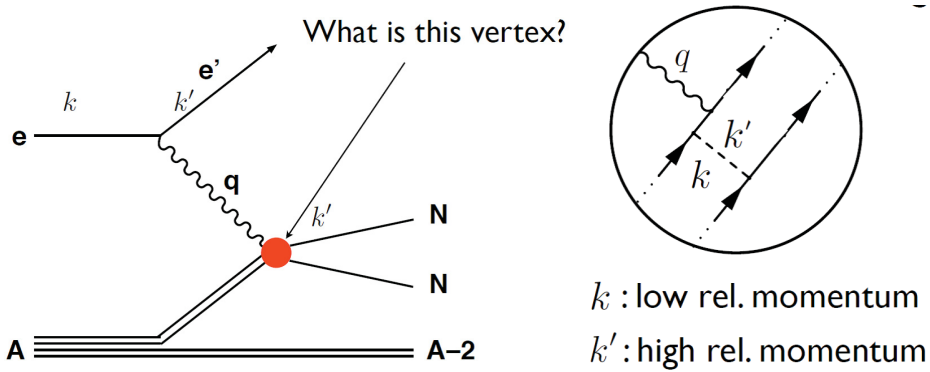


Figure 6.2: Schematic of electron scattering knockout process of correlated pair (left). An enlarged view (right) shows the naive interaction assumed by standard nuclear physics models.

the final-state interaction (FSI) of the nucleons between themselves and the original nucleus can be sufficiently neglected because of the energy at which they are ejected). The detection of these pairs is believed to signify the importance of SRCs in the nuclear interaction. A more detailed schematic of this scattering process is shown in Figure 6.2. The interaction of the photon with the nucleus is represented by a vertex “blob” signifying the short-distance physics which is occurring there. It is the nature of this vertex that these experiments wish to explore. In the conventional nuclear physics picture, this interaction would look like the enlarged view of the blob on the righthand side of the figure, consisting

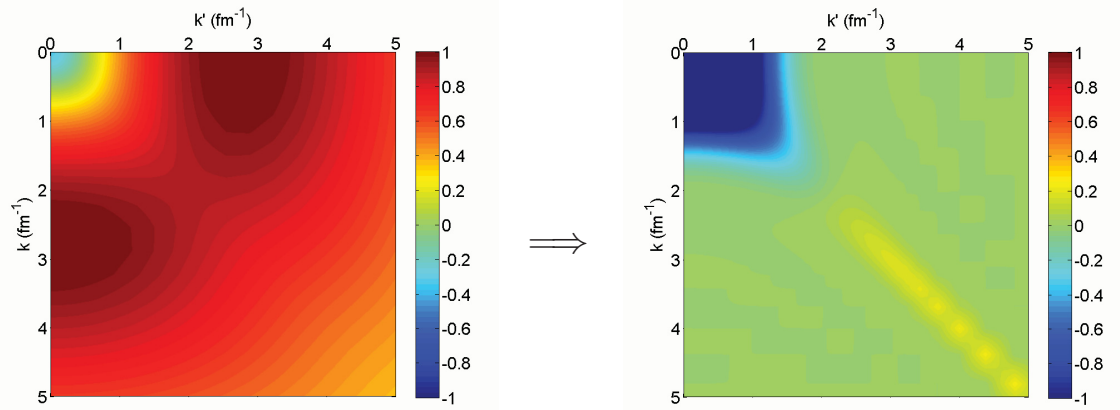


Figure 6.3: Recall the unevolved AV18 potential on the left compared to the same potential evolved to $\lambda = 1.5 \text{ fm}^{-1}$ on the right. The evolved potential lacks the coupling of high and low momenta need to produce SRCs.

of a photon-nucleon vertex and a NN interaction which is part of the ground state wave function and results in the SRC. For a correlated pair to be detected with large relative momentum in this picture, the nuclear interaction would need to couple matrix elements of nucleons with high and low relative momentum. This is exactly what we saw in the AV18 potential, for example, as shown again on the left side of Figure 6.3.

However, as we discussed in Chapter 1, the coupling between very high-energy components of the interaction and low-energy is inappropriate in the nuclear structure regime, as well as largely unphysical for point-like nucleons. Specifically, the high-energy components are in excess of what one would naively expect for the energy of bound-state nucleons, and at high enough energies, non-nucleon degrees of freedom must come into play. Indeed, for the interaction SRG evolved to a scale appropriate for low-energy nuclear states, as shown on the right side of Figure 6.3, the coupling at high and low momentum has been suppressed. As a result, so too have the apparent SRCs which were expected from experiment. So, what has happened here, and how can we interpret the vertex in Figure 6.2? Can the experimental results for these low-energy states be reproduced in the SRG approach to nuclear physics? Or, do we in fact need a detailed understanding of SRCs for a complete description of nuclear bound state problems and their reactions?

It might be thought naively that this physics is beyond the reach of low-momentum approaches, for which wave functions have drastically reduced short-range correlations. However, Eq. (1.17),

$$\langle \psi_\alpha(s) | \hat{O}_s | \psi_{\alpha'}(s) \rangle = \langle \psi_\alpha(0) | \hat{O}_{s=0} | \psi_{\alpha'}(0) \rangle ,$$

is unequivocal: The experimental cross section determined by this equation is unchanged with SRG evolution to low momentum if no approximations are made, even if the evolved wave function has almost no short-range correlations. This is simply a consequence of the unitarity of the transformation. The sources of high- and low-energy physics in the formalism have been rearranged and isolated though. In other words, at lower resolution the interaction in the vertex of Figure 6.2 is shifted into a more complicated vertex while making the wave function simpler, as we will see.

Theoretical analyses relate such experiments to nuclear momentum distributions if the impulse approximation is assumed to be valid for a high-cutoff interaction [101]. A simple way to understand this connection is as follows [102]. Let's assume we have just a scalar external scattering probe incident on a single nucleon that transfers momentum \mathbf{q} . The associated operator is then given by

$$\hat{\rho}(\mathbf{q}) = \sum_{\mathbf{p}, \mathbf{p}'} \langle \mathbf{p} | e^{-i \mathbf{p} \cdot \mathbf{r}} | \mathbf{p}' \rangle a_{\mathbf{p}}^\dagger a_{\mathbf{p}'} = \sum_{\mathbf{p}} a_{\mathbf{p}}^\dagger a_{\mathbf{p}-\mathbf{q}} \quad (6.1)$$

If we also assume that final-state interactions can be neglected, then an initial A-particle system in its ground state

$$|\Psi_i\rangle = |\Psi_0^A\rangle \quad (6.2)$$

will transition to a final A -particle state (actually an $(A - 1)$ -particle bound state and free particle with momentum \mathbf{p}) given by

$$|\Psi_f\rangle = a_{\mathbf{p}}^\dagger |\Psi_n^{A-1}\rangle . \quad (6.3)$$

The transition matrix element is thus given by (using $\{a_{\mathbf{p}}, a_{\mathbf{p}'}^\dagger\} = \delta_{\mathbf{p},\mathbf{p}'}$)

$$\begin{aligned}\langle \Psi_f | \hat{\rho}(\mathbf{q}) | \Psi_i \rangle &= \sum_{\mathbf{p}'} \langle \Psi_n^{A-1} | a_{\mathbf{p}} a_{\mathbf{p}'}^\dagger a_{\mathbf{p}'-\mathbf{q}} | \Psi_0^A \rangle \\ &= \sum_{\mathbf{p}'} \langle \Psi_n^{A-1} | \delta_{\mathbf{p},\mathbf{p}'} a_{\mathbf{p}'-\mathbf{q}} + a_{\mathbf{p}'}^\dagger a_{\mathbf{p}'-\mathbf{q}} a_{\mathbf{p}} | \Psi_0^A \rangle.\end{aligned}\quad (6.4)$$

Since we are assuming an ejected particle of sufficient momentum \mathbf{p} relative to the rest of the bound state particles that final state interactions can be neglected, the removal $a_{\mathbf{p}} |\Psi_0^A\rangle$ can be neglected, and so

$$\langle \Psi_f | \hat{\rho}(\mathbf{q}) | \Psi_i \rangle \approx \langle \Psi_n^{A-1} | a_{\mathbf{p}-\mathbf{q}} | \Psi_0^A \rangle \quad (6.5)$$

The cross section of the scattering process can then be expressed in proportion to

$$d\sigma \sim \sum_n \delta(\omega - E_i - E_f) |\langle \Psi_f | \hat{\rho}(\mathbf{q}) | \Psi_i \rangle|^2 \quad (6.6)$$

according to Fermi's golden rule. Since the missing momentum is given by $\mathbf{p}_m = \mathbf{p} - \mathbf{q}$ and the missing energy is $E_m = \mathbf{p}^2/(2m) - \omega = E_0^A - E_n^{A-1}$, we can rewrite this as

$$\begin{aligned}d\sigma &\sim \sum_n \delta(E_m - E_0^A + E_n^{A-1}) |\langle \Psi_n^{A-1} | a_{\mathbf{p}_m} | \Psi_0^A \rangle|^2 \\ &= S_h(\mathbf{p}_m, E_m)\end{aligned}\quad (6.7)$$

which is known as the spectral hole function. For a given system at energy E_m , this function relates to the probability density for removing a particle of momentum \mathbf{p}_m from the ground state and leaving an $(A-1)$ -particle system at energy E_n^{A-1} . For our purposes here, however, the scattering process is now related to the momentum distribution $n(\mathbf{p})$ via integration over the spectral function energies, as follows from the definition of the momentum distribution:

$$\begin{aligned}n(\mathbf{p}) &= \langle \Psi_0^A | a_{\mathbf{p}}^\dagger a_{\mathbf{p}} | \Psi_0^A \rangle = \sum_n |\langle \Psi_n^{A-1} | a_{\mathbf{p}} | \Psi_0^A \rangle|^2 \\ &= \int_{-\infty}^{(E_0^A - E_n^{A-1})} dE \sum_n \delta(E - E_0^A + E_n^{A-1}) |\langle \Psi_n^{A-1} | a_{\mathbf{p}} | \Psi_0^A \rangle|^2 \\ &= \int_{-\infty}^{(E_0^A - E_n^{A-1})} dE S_h(\mathbf{p}, E).\end{aligned}\quad (6.8)$$

We have seen in previous chapters how the number operator provides a rather simple,

yet non-trivial, test of our many-body operator methods. As such, and considering the connection between the issues outlined here, we will use calculations of the momentum distribution to explore the first applications of operator evolution and factorization in this chapter.

It should be pointed out that we have, in fact, already presented the first realistic calculation of an evolved operator in Chapter 4 for r^2 in the context long-range operator convergence. However, no truncations were made in the many-body space for that expectation value. Other *ab-initio* calculations can be carried out following procedures discussed in Chapter 3. Here we focus on the first application of operator evolution to perturbative methods. The ability to reproduce the so-called short-range correlations in the nucleus via perturbative methods will be a particularly strict test on the effectiveness of the SRG. As such, we will look at an application of SRG evolved potentials and operators to nuclear matter in Section 6.2.

A number of other issues arise about processes with large momentum transfers, such as $(e, e'p)$. Calculations find nearly universal scaling of the high-momentum tails of the momentum distributions, which is currently interpreted in terms of short-range correlations in the nuclear wave functions. A clear connection between this and the EMC effect has also recently been observed. Both of these issues have been longstanding problems in physics, and will be discussed in Sections 6.1 and 6.3 in the context of factorization of the SRG transformation. Specifically, we have shown in the previous chapter that under the relevant kinematic conditions there is factorization of the unitary transformation U_s . This leads to significant simplifications and an alternative interpretation of what we find to be universal high-momentum dependence and scaling. As a result, the effect of high energy probes can be fit naturally into the SRG low-momentum interaction framework. The calculations in Section 6.2 are also being performed in the context of these issues.

It should be noted that many of these calculations are still in progress and what is presented here is largely preliminary.

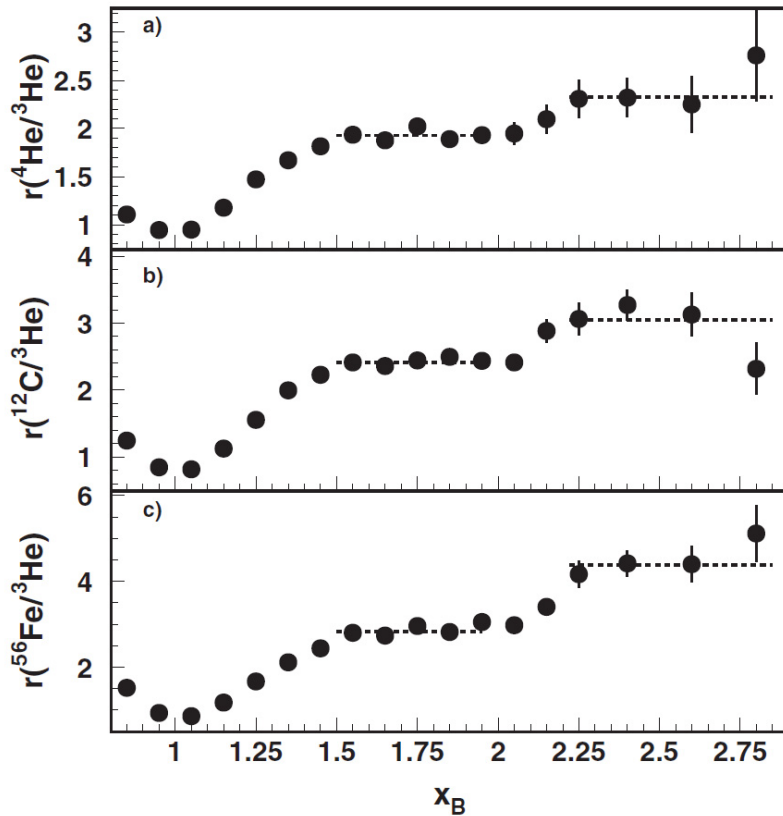


Figure 6.4: Inclusive electron scattering cross section ratios of various nuclei relative to ${}^3\text{He}$ as a function of x_B . For $1.5 < x_B < 2$ the plateaus indicate NN scaling, and for $x_B > 2.25$ shown here we have three-nucleon scaling [22].

6.1 Nuclear Scaling

Nuclear scaling is a phenomena which is observed in a number of circumstances both experimentally and in calculations with phenomenological potentials. For example, if one takes the ratio of inclusive electron scattering off various nuclei for large momentum transfer $Q^2 \geq 1.4 \text{ GeV}^2$, one sees plateaus emerge, as shown in Figure 6.4. Using $x_B = Q^2/(2m_N\nu)$ as our parameter (where ν is the energy transfer), plateaus which appear in the region $1.5 < x_B < 2$ are attributed to NN correlations and for $x_B > 2.25$ shown here the plateaus are related to three-nucleon correlations (this is simply a consequence of the fact that x_B , as defined, is the proportion of the momentum transfer on a single nucleon – so for $x_B > 2$ there are two or more nucleons involved, for $x_B > 3$ there are three or more, etc.). It is the

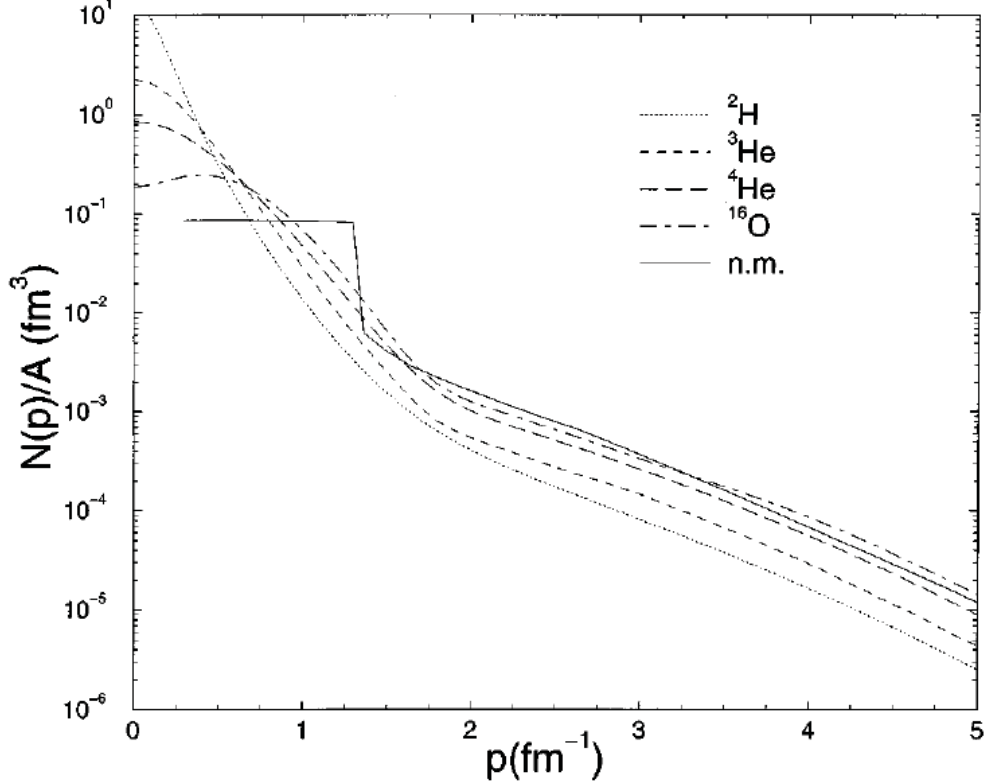


Figure 6.5: VMC calculation of the momentum distributions for various nuclei, as well as for nuclear matter [23]. Scaling of the distributions at high momenta is evident.

phenomena of this “scaling” at high momenta for the behavior of different nuclei that we are referring to.

As we have just seen, results from large-momentum-transfer experiments such as ($e, e'p$) can be related to the momentum distribution assuming a number of approximations hold true. The tails of momentum distributions calculated for nuclei and nuclear matter using phenomenological potentials exhibit a nuclear scaling behavior at high momentum too [23]. In particular, the momentum dependence of the distributions for nuclei ranging from the deuteron to oxygen, as well as nuclear matter, at high momentum is similar except for an overall nucleus-dependent scaling factor, as seen in Figure 6.5. Consequently, the nuclear scaling ratio is often parameterized by a_2 , as defined by the roughly constant ratio of the momentum distributions for a given nucleus at high momentum relative to that of the deuteron high momentum (where “high momentum” is taken as greater than the fermi

momentum, k_f), i.e.,

$$a_2(A, d) = \frac{n_A(k)}{n_d(k)} \quad \text{for } k > k_f. \quad (6.9)$$

One explanation for this behavior is based on the dominance of two-body forces in the interaction and SRCs in the wave functions because of the high-momentum scales involved [101]. We would like to know how we can explain this feature in an SRG-evolved calculation, however, for which high-momentum components and short-range correlations are suppressed. To do so, we can invoke the results of Chapter 5 regarding factorization of operator expectation values, and demonstrate scaling in a simple example.

6.1.1 Interpreting high-momentum scaling behavior of the momentum distribution: A 1D Many-body example

Factorization provides a compelling alternative explanation. Because the $a_q^\dagger a_q$ operator for large q has no coupling to low momentum, the entire q dependence comes through the function I_{QOQ} in Eqs. (5.28) and (5.29), which is independent of the low-momentum part. If induced many-body contributions to the operator are relatively small and we neglect for the moment effects from embedding two-body operators into an $A > 2$ space, we conclude that for $A \geq 2$ the momentum distribution should be approximately the same for every A , with a scaling factor given by an A -dependent low-momentum integral over the low-energy wave functions. Specifically, we can write

$$a_2(A, d) = \frac{n_A(k)}{n_d(k)} = \frac{\int_0^\lambda d\tilde{k}' \int_0^\lambda d\tilde{k} [\psi_A^\lambda(k')]^\dagger \left[\int_0^\lambda d\tilde{q}' \int_0^\lambda d\tilde{q} I_{QOQ} K_\lambda(k') K_\lambda(k) \right] \psi_A^\lambda(k)}{\int_0^\lambda d\tilde{k}' \int_0^\lambda d\tilde{k} [\psi_d^\lambda(k')]^\dagger \left[\int_0^\lambda d\tilde{q}' \int_0^\lambda d\tilde{q} I_{QOQ} K_\lambda(k') K_\lambda(k) \right] \psi_d^\lambda(k)},$$

and when the universal high-momentum dependence given by I_{QOQ} cancels, and we are left with

$$a_2(A, d) = \frac{\int_0^\lambda d\tilde{k}' \int_0^\lambda d\tilde{k} [\psi_A^\lambda(k')]^\dagger K_\lambda(k') K_\lambda(k) \psi_A^\lambda(k)}{\int_0^\lambda d\tilde{k}' \int_0^\lambda d\tilde{k} [\psi_d^\lambda(k')]^\dagger K_\lambda(k') K_\lambda(k) \psi_d^\lambda(k)}. \quad (6.10)$$

We have tested this proposal in a 1D model with an interaction that mimics features of the nuclear NN potential. This is the same model used and discussed at length in

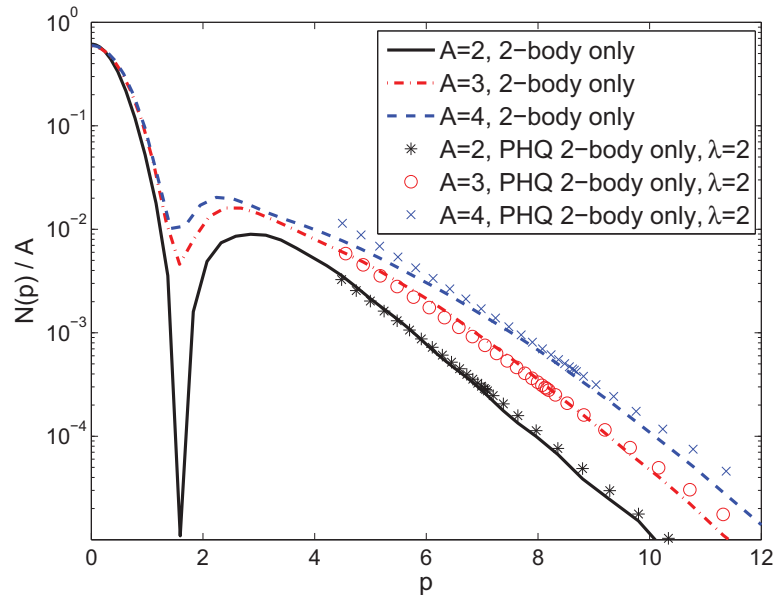


Figure 6.6: The scaling of momentum distributions at high momenta in a 1D model is tested by using the leading-order factorized approximation to the momentum occupation number operator to predict high-momentum scaling in $A = 2, 3, 4$ (symbols). The full momentum distributions for $A = 2, 3$, and 4 are shown with solid, dot-dashed, and dashed lines, respectively.

Chapter 3. The full momentum distributions for two, three, and four particle systems in this model are shown with solid, dot-dashed, and dashed lines, respectively, in Figure 6.6. The behavior at high momentum is analogous to the nuclear calculations [23]: The momentum dependence is similar for each system so that each curve differs only by a scaling factor. We then evolve the model interaction via the SRG to $\lambda = 2$ and extract the unitary transformation. Only the operator from $A = 2$ is used; that is, any induced three- or four-body component is neglected. By using the first term in the SVD expansion to factorize $U(k, q)$ in the region where $k < \lambda$ and $q \gg \lambda$, we are able to reproduce to a large extent the momentum distributions at high momenta (shown with symbols in Figure 6.6), and confirm our expectations regarding the scaling of the curves.

Since these calculations were initially presented [76], some doubt has been cast on the techniques used to approximately embed the high momentum factorized operators shown in this plot. Nevertheless, using the complete many-body operator extraction and embedding

procedures described in this work lead one to a similar, but more general insight regarding the nature of factorization. These curves were presented in Figures 3.8 and 3.9. In these figures it is clear that inclusion of induced three-body forces is to some extent important for recovering the scaling ratios at high momentum. However, the induced three-body components have the same high momentum I_{QOQ} dependence, to first order, as the two-body only curves. Thus, it would appear as though a more generalized three-body factorization exists which modifies the low-momentum structure, and hence the normalization of the curves, but is dominated by the two-body induced high-momentum dependence. Work is currently in progress on formalizing the nature of this factorization, along the lines presented for two-body factorization in Chapter 5. Overall, these results are very promising and so we continue this discussion in the context of operator calculations of the nuclear many-body system.

6.2 Nuclear Matter Calculations

We take symmetric nuclear matter (equal numbers of protons and neutrons) as our starting point for analysis of the SRG in perturbative calculations of nuclear many-body systems. For simplicity, we also start by calculating the pair momentum distribution to avoid any embedding issues associate with the single-particle number operator. It is clear that factorization and a scaling behavior at high momentum should be exhibited by this two-body operator too, based on the discussion of the previous section.

But first let's consider an *ab-initio* calculation of the pair density for various nuclei as a point of reference, as shown in Figure 6.7. These distributions were calculated in VMC using the high-resolution, hard-core interaction of AV18. The pair densities are given separately for neutron-proton (np) and proton-proton (pp) pairs at fixed total pair momentum $Q = 0$. In this plot, we clearly see the nuclear scaling effect at high momentum for the various nuclei. Another striking feature of the plot is the significantly larger distribution of np -pairs compared to pp -pairs. This is due to the strong correlations induced by tensor components present in the np interaction channel, as compared to the pp channel.

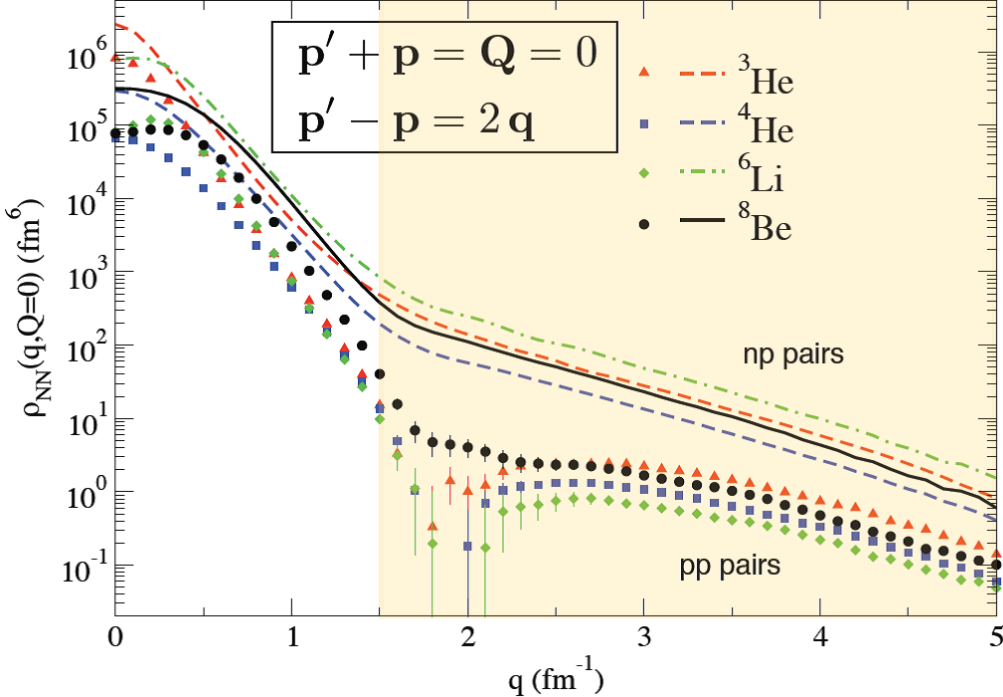


Figure 6.7: Relative *np*-pair (lines) and *pp*-pair momentum distributions (for total pair momentum $P = 0$) in various nuclei, as calculated in VMC [24]. Nuclear scaling for relative momentum distribution is evident, as well as the enhancement of *np* pairs versus *pp* pairs due to tensor forces in the interaction.

It has been claimed that the high momentum dependence observed here cannot be reproduced effectively in a low momentum framework [24]. However, in our alternative calculation using soft interactions and MBPT, we will see that both the enhancement due to tensor forces and the dependence of the distributions at high momentum can be reproduced.

6.2.1 Overview of Calculation

In general, to perform operator expectation value calculations one must initially make use of the technology developed in Section 3.5 to properly identify the evolved one-body, two-body, etc., operators in a second quantized formalism. The individual matrix elements of the associated coefficients can then be calculated in a numerically straightforward first-quantized basis. We also start with the high-resolution AV18 interaction for comparison to the features of the *ab-initio* calculations in Figure 6.7 (we do not include initial three-

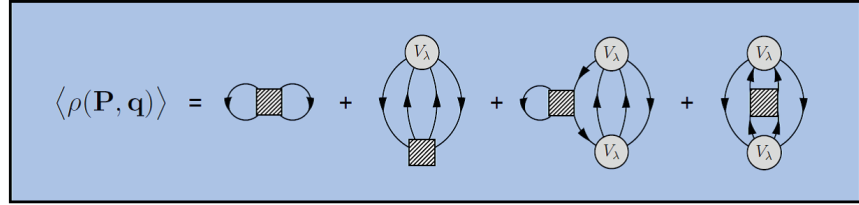


Figure 6.8: Perturbative expansion of evolved operator, as represented by a shaded box. Both the operator and the potential, V_λ , have been evolved to λ .

body interactions, however, for simplicity), and as a demonstration of the effectiveness of the SRG when applied to a high-resolution potential. After the evolution, the potential is significantly softer, and with consistent evolution of the operators MBPT will converge.

The standard techniques to perform the perturbative quantum many-body calculations of infinite, symmetric (in numbers of protons and neutrons) nuclear matter used here has been developed at length in the literature (see, for example, [59, 60]). To summarize, the diagrammatic expansion drawn schematically in Figure 6.8 has been implemented for the evolved two-body relative momentum number operators over a range of momenta q for fixed total individual pair momenta of $Q = 0$.

6.2.2 Results

The initial results of these calculations are presented in Figures 6.9 and 6.10 for evolved potentials and operators to small λ in the range of $1.8\text{--}3.0 \text{ fm}^{-1}$. They are very encouraging. The np -pair distribution is plotted in Figures 6.9. The interaction has been evolved for all of the curves, but operator evolution has been neglected for the dotted lines. Here, we see that without operator evolution, the calculation fails completely. At high momentum, it is clear that the distributions are dropping off as a function of the decreasing λ , much as we saw for the deuteron and the 1D model systems without operator evolution. With operator evolution, on the other hand, the momentum distributions converge to roughly resolution-independent (determined by the decoupling scale λ) curves. Also, as one would expect, with decreasing λ the curves begin to coincide at increasingly smaller values of q . The same approximate pattern holds true in a calculation of the ratio of relative np -pair to

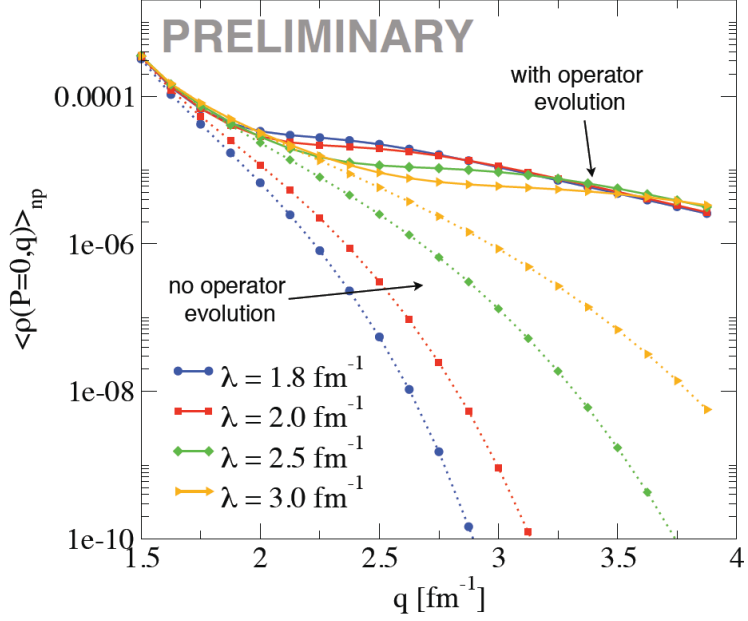


Figure 6.9: Relative np -pair momentum distribution (for total pair momentum $P = 0$) in nuclear matter at second order in perturbation theory for the AV18 potential evolved to various low-momentum values of λ [25]. The dotted lines show the result without evolving the operators. The solid lines show the result with operator evolution.

nn -pair momentum distributions, as shown on the left side of Figure 6.10. With evolution the curves all approximately coincide; but without evolution, there fails to be any obvious convergence to a ratio that does not depend on our SRG induced decoupling scale.

A careful comparison with an alternative *ab-initio* method, such as VMC, for determining the nuclear matter pair momentum distribution due to the AV18 interaction with consistent normalization factors, etc., has yet to be completed. However, we do have a number of significant initial checks on the validity of our perturbative calculations. First, there is the resolution independence of the curves with respect to the SRG decoupling scale, as just observed. Moreover, the approximately SRG converged curves presented in the plot on the right side of Figure 6.10 clearly show that a tensor force enhancement of the relative np -pair distribution to the nn -pair distribution can be reproduced at high momentum.

In addition, we can take advantage of our expectation of nuclear scaling here based on factorization, as well as the scaling exhibited for the single-particle momentum distribution calculation for nuclear matter in Figure 6.5, to provide a stricter check on the

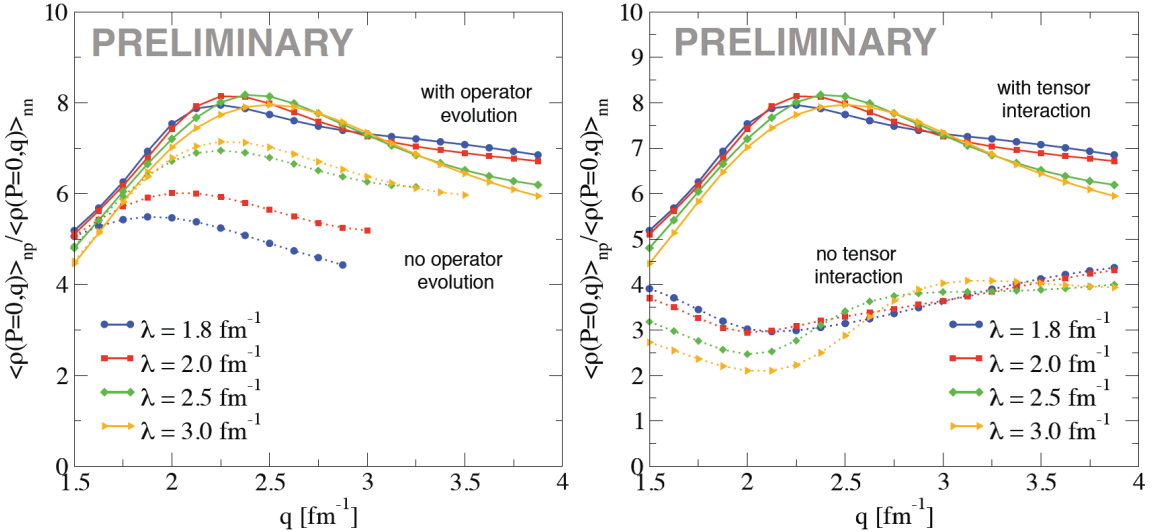


Figure 6.10: Ratio of relative np -pair to nn -pair momentum distributions (for total pair momentum $P = 0$) in nuclear matter at second order in perturbation theory for the AV18 potential evolved to various low-momentum values of λ [25]. On the left, the dotted lines show the result without evolving the operators; the solid lines show the result with operator evolution. On the right, the dotted lines show the result without including the tensor part of the interaction; the solid lines show the result with the tensor component. The operators have been evolved in both cases here.

high-momentum dependence of our MBPT distribution. Specifically, we can take the ratio of the the np -pair distributions to the deuteron momentum distribution (a single np -pair). If a plateau is observed at high momentum, then it should be clear that the MBPT calculations can reproduce the high-momentum dependence, other than a possible scaling factor, of the nuclear matter pair momentum distributions resulting from AV18. Indeed, this is the case, as seen in Figure 6.11. This ratio has been plotted for the lowest two values of λ , both at the nuclear saturation density, $k_f = 1.35 \text{ fm}^{-1}$, and at a density of $k_f = 1.05 \text{ fm}^{-1}$, more characteristic of atomic nuclei. In all cases a plateau is observed. Moreover, at both densities, the onset of the plateau occurs at lower momentum for lower values of λ , as one would expect.

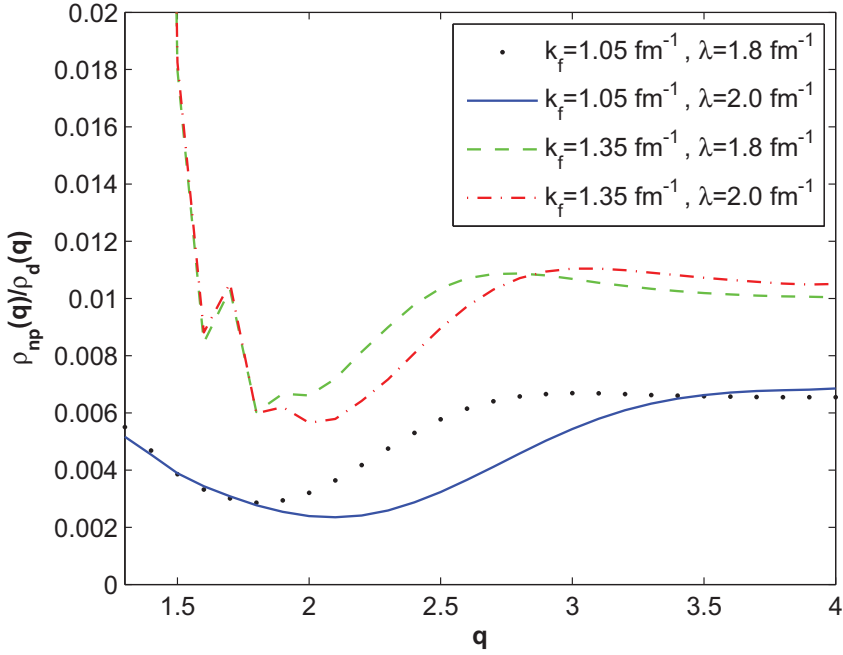


Figure 6.11: Ratios of perturbative nuclear matter momentum distributions at densities of $k_f = 1.05 \text{ fm}^{-1}$ and $k_f = 1.35 \text{ fm}^{-1}$ for $\lambda = 1.8 \text{ fm}^{-1}$ and $\lambda = 2.0 \text{ fm}^{-1}$, as specified, over *ab-initio* calculation of the deuteron. Assuming the presence of nuclear scaling, plateaus demonstrate the reproduction of high momentum behavior in perturbative calculation of nuclear matter momentum distribution.

6.2.3 Next Steps

Considering the very promising MBPT results we have thus far, the next stage of these calculations is to confirm the perturbative solution via alternative *ab-initio* solutions of the pair momentum distribution functions. Calculations of the single-particle momentum distributions in MBPT should also be performed at this stage. Considering the rather sizable three-body induced contributions to the 1D model momentum distributions, it may also be necessary to include three-body contributions to the nuclear matter calculations via density dependent two-body operators [13].

Clearly, we would like to next use these results to predict the a_2 of nuclear scaling for nuclear matter. Moreover, given the value of the nuclear matter expectation values as a function of density parameterized by the fermi momentum k_f , and given that an approxi-

mately mean field approach is successful with SRG evolved interactions, we can use these results to predict the approximate nuclear scaling ratios in a local density approximation (LDA) for a wide range of finite nuclei. This would involve calculating the momentum distribution expectation values by integrating over the density distribution of a nucleus convoluted with the nuclear matter operator function. Since low-momentum components of the wave will play a crucial role, a HF approximation to the density distributions should be sufficient.

To take this one step further, it should be straightforward to employ factorization of the operators here to avoid calculating the high-momentum dependence of the distributions all together, calculating the nuclear scaling ratio in a manner analogous to Eq. (6.10) for various nuclei. Although it may be difficult to confirm our results at this stage with explicit *ab-initio* calculations, we will at this point be able to confirm our predictions of nuclear scaling via comparison with experimental cross section ratios.

6.3 EMC Effect

The EMC effect was first observed in 1983 by the Electron-Muon Collaboration (EMC), hence the name. It was noticed in deep inelastic scattering experiments for momentum transfer $Q^2 \geq 2 \text{ GeV}^2$ and $0.35 \leq x_B \leq 0.7$ that the cross sections of deuterium differed from that of iron [103]. This was subsequently measured for a wide range of nuclei relative to deuterium. It was expected that the ratio of the cross sections, $R_{\text{EMC}}(x_B)$, should be roughly equal to one (i.e., independent of the nucleus), given the short-distance physics being probed. The physics leading to this effect has been a source of confusion ever since.

Very recently, however, it was noticed that a strong linear correlation exists between nuclear scaling and the EMC effect [26]. This is shown in Figure 6.12. Assuming the EMC effect can be parameterized by an effective high momentum operator, we can draw the same conclusion as found in this result based on SRG factorization. At leading order, SRG factorization tells us that the dependence of operator expectation values at high momentum is independent of the system size A . It also tells us that the system size dependence from

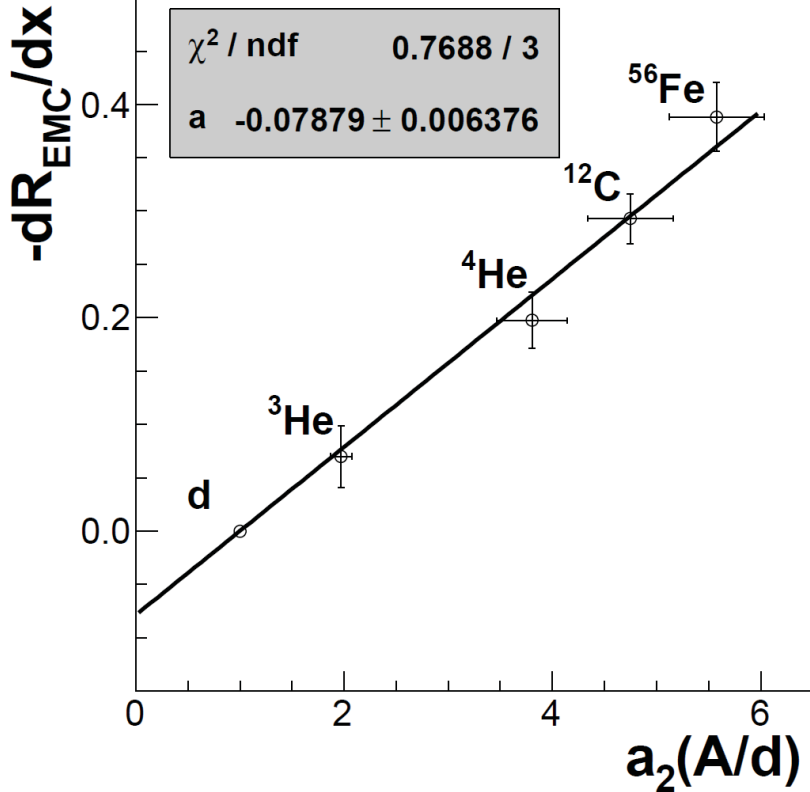


Figure 6.12: Linear correlation of the EMC effect related change in the ratio of cross sections with the nuclear scaling effect ratio given by a_2 [26].

low momentum matrix elements is independent of the operator. This would imply a linear correlation. It may be that both nuclear scaling and the EMC effect can be quantitatively explained via factorization of operators and the low momentum structure of the nuclei.

The issue of the EMC effect has also been recently addressed from an EFT perspective that aligns neatly with the operator factorization perspective presented here [104]. In fact, the EFT arguments lead directly to a factorization of the EMC effect (the modification of $R_{EMC}(x_B)$ relative to one) at leading order into a high momentum function of x_B and a low momentum function which depends on long-distance distance matrix elements depending on the structure of the nucleus. SRG evolution provides little insight on the unknown high-momentum physics; however, an important confirmation of the SRG/EFT factorization perspective will be to demonstrate that the long-distance EFT matrix elements coincide with the form of the low momentum integrals over the $K(k)$ function produced by SRG

evolution.

Moving forward, it seems clear from the correlation in Figure 6.12, that if good predictions of the nuclear scaling ratio can be achieved via SRG factorized operators, the EMC results can also be reproduced. Although an explicit operator may not be immediately constructed for the high momentum dependence, experimental data provides a means to parameterize that dependence when used in the context of factorization, so that predictions can be made for a host of different nuclei.

6.4 Chapter Summary

The topics introduced in this chapter are subjects of ongoing investigation. It should be clear, at this point however, that the issue of SRCs and high momentum scattering experiments on low-energy nuclear states can be addressed in the framework of the SRG. This is especially clear given that the SRG-soften interactions can be used effectively with the techniques of MBPT to reproduce the high-momentum dependence found in other solution techniques. Not covered here is work that is also in progress on fully *ab-initio*, realistic three-dimensional calculations for evolved operator expectation values.

Regarding the nature of SRCs, the effects of SRG evolution must alter our perception of the simple operators at high momentum for scattering and the momentum distribution introduced at the beginning of this chapter. Initially, these operators appear simple and rely on a mixture of high- and low-momentum effects tangled in the coupling of the interaction, and the resulting complicated correlations of the wave function. After evolution, while the wave functions become less correlated at high momentum, our original operators may appear more complicated. Factorization, however, provides us a means to clearly separate the high- and low- momentum contributions to the operators. The ability to cleanly reshuffle these contributions is a reflection of the physics involved with the nuclear interactions. A photon from an incoming electron may couple with non-nucleonic degrees of freedom such as pions involved in the nuclear force, for example. These different contributions are shown to be of relatively similar orders of magnitude in EFT formalism. Moreover,

this emphasizes the fact that one must in principle construct even the unevolved operators for high momentum probes in a manner which is consistent with the initial potential (a benefit of the EFT formalism), instead of making the simple assumptions for scattering discussed early in the chapter. This is unlike the case of atomic scattering where point-like interactions due to Coulomb forces dominate. However, thanks to the associated decoupling of high- and low-energy degrees of freedom, these effects can be treated separately so that the detailed high-momentum structure of the momentum distribution, for example, can be parameterized in some other way, while its overall normalization at high-momentum is given by low-momentum nuclear structure.

As mentioned in the EMC effect discussion, we can use this feature of factorization to provide a means to parameterize the unknown high-energy effects on external probes from non-nucleonic degrees of freedom. In this way, predictions of external probes incident on low energy bound states can be refined for a large set of nuclei, given experimental results on just a few.

Ultimately, we see that the role of explicit SRCs is a scale and scheme dependent phenomena. In the SRG, this dependence is parameterized by λ , and is seen in the reshuffling of contributions between our low-momentum function $K(k)$ and high-momentum function $Q(q)$ in our factorized form of the unitary transformation. As such, we see that different resolutions can lead to very different physical interpretations and intuition; the SRG has the great advantage of being able to connect these different pictures.

Chapter 7

SUMMARY AND OUTLOOK

In this thesis, we have seen that the SRG provides a means to lower the resolution needed in nuclear interactions, thereby reducing the computational difficulty of the nuclear many-body problem. In particular, we have demonstrated that nuclear operators can be effectively evolved and calculated in the framework of the SRG. The advantages afforded by SRG evolution of the Hamiltonian are not lost when attempting to calculate expectation values of other operators; quantum many-body calculation do not become intractable because the evolved operators make it too complicated (e.g., because of strong non-localities or too-large many-body components). Moreover, a careful analysis of the SRG transformation reveals new insights into the physics of the systems that are being studied. A more detailed summary of the major results presented in this thesis, and specific follow-up plans for the future can be found at the end of each chapter. The major results are also clearly outlined at the end of Chapter 1.

At this stage, we have a solid understanding of the properties of SRG operator evolution, as related to the associated flow in the Hamiltonian, as well as how operator strength flows in the many-particle space. In conjunction with this we have several strategies available to implement the many-body evolution of operators and extract the components necessary for use in nuclear structure calculations methods, whether they be *ab-initio* basis-expansion or stochastic methods, or perturbative in nature. Moreover, we understand how factorization results from the SRG evolution, and how it can be used in operator calculations.

We are just now beginning to apply this knowledge to calculations of the realistic nuclear many-body problem, such as to better understand the nature of so-called SRCs and the effectiveness of the SRG in perturbative calculations. It will be important to continue these calculations to see if issues such as nuclear scaling and the EMC effect can be sufficiently understood in the context of low-momentum nuclear structure. It is also necessary at this point to use the methods which have been developed here with a variety of nuclear quantum many-body solution techniques.

One should note that although we do understand how operators evolve in the many-body space, a formal understanding of the hierarchy of many-body induced components is still needed. In particular, we need to establish bounds on the growth of many-body operators. Until this is found, however, numerical analyses of convergence in the hierarchy, as shown here for binding energies and number operator expectation values, should suffice. A rich set of nuclear data is available to address this issue before one enters unknown territory. An important initial study using the methods and algorithms developed in this work will be to begin exploring the extent of the many-body induced operators needed for convergence in realistic, *ab-initio* nuclear calculations.

For genuine first-principles predictions of interactions between nuclei and external probes, work is needed to implement the operators associated with individual nuclear interactions independent of the SRG. Chiral EFT offers a solid framework for this work. The prediction of electromagnetic form factors for various nuclei would be a good first step, as a great deal of work has already been completed in constructing the initial chiral EFT operators. It is simply a matter of combining them with SRG assisted structure calculations. As mentioned in the previous chapter, the SRG even offers a way to refine these operators by parameterizing high-momentum effects through factorization. The effects of other interactions are also ready to be explored, such as more precise predictions of beta decay and the interaction of nuclei with neutrinos.

Methods that have traditionally been employed to calculate nuclear structure are now being modified to incorporate reactions, which involve dynamics of the nucleonic degrees of freedom. For instance, the NCSM is being united with the resonating-group method for

ab-initio calculations of reactions between nuclei [105, 106]. These will have applications to nuclear fusion and stellar evolution, among other things. As a first step in extending our operator evolution results to reactions which involve a change in the number of bound state nucleons, or groups of bound state nucleons, within a system, a study of deuteron electrodisintegration is planned. It is particularly natural to account for interactions induced by coupling to non-nucleonic degrees of freedom, with the formalism developed here.

BIBLIOGRAPHY

- [1] *DOE/NSF Nuclear Science Advisory Committee, The Frontiers of Nuclear Science: A Long-Range Plan (2007)*.
- [2] S. Aoki, T. Hatsuda, and N. Ishii. Nuclear Force from Monte Carlo Simulations of Lattice Quantum Chromodynamics. *Comput. Sci. Dis.*, 1:015009, 2008.
- [3] Walter Gloeckle, E. Epelbaum, U.G. Meissner, A. Nogga, H. Kamada, et al. Nuclear forces and few nucleon studies based on chiral perturbation theory. 2003.
- [4] G. F. Bertsch, D. J. Dean, and W. Nazarewicz. Computing atomic nuclei. *SciDAC Review*, 6:42, 2007.
- [5] P. Maris and J. P. Vary. *Private communication*.
- [6] John M. Brayer. Introduction to fourier transforms for image processing. June 2012.
URL: <http://www.cs.unm.edu/~brayer/vision/fourier.html>.
- [7] R.J. Furnstahl. The Renormalization Group in Nuclear Physics. 2012.
- [8] S. K. Bogner, R. J. Furnstahl, R. J. Perry, and A. Schwenk. Are low-energy nuclear observables sensitive to high- energy phase shifts? *Phys. Lett. B*, 649:488–493, 2007.
- [9] K. Wendt. *Private communication*.
- [10] S. K. Bogner et al. Convergence in the no-core shell model with low-momentum two-nucleon interactions. *Nucl. Phys. A*, 801:21–42, 2008.

- [11] E. D. Jurgenson, P. Navratil, and R. J. Furnstahl. Evolution of Nuclear Many-Body Forces with the Similarity Renormalization Group. *Phys. Rev. Lett.*, 103:082501, 2009.
- [12] E.D. Jurgenson, P. Navratil, and R.J. Furnstahl. Evolving Nuclear Many-Body Forces with the Similarity Renormalization Group. *Phys. Rev. C*, 83:034301, 2011.
- [13] K. Hebeler, S.K. Bogner, R.J. Furnstahl, A. Nogga, and A. Schwenk. Improved nuclear matter calculations from chiral low-momentum interactions. *Phys. Rev. C*, 83:031301, 2011.
- [14] Robert B. Wiringa, V. G. J. Stoks, and R. Schiavilla. An Accurate nucleon-nucleon potential with charge independence breaking. *Phys. Rev. C*, 51:38–51, 1995.
- [15] D. R. Entem and R. Machleidt. Accurate charge-dependent nucleon-nucleon potential at fourth order of chiral perturbation theory. *Phys. Rev. C*, 68:041001, 2003.
- [16] M. A. Belushkin, H. W. Hammer, and U. G. Meissner. Dispersion analysis of the nucleon form factors including meson continua. *Phys. Rev. C*, 75:035202, 2007.
- [17] E. Epelbaum, W. Glockle, and Ulf-G. Meissner. The two-nucleon system at next-to-next-to-next-to-leading order. *Nucl. Phys. A*, 747:362–424, 2005.
- [18] Eric D. Jurgenson. Applications of the Similarity Renormalization Group to the Nuclear Interaction. 2009.
- [19] E. Anderson, E. J. Jurgenson, R. J. Furnstahl, P. Navratil, and R. J. Perry. 2012. *In preparation*.
- [20] R. Subedi, R. Shneor, P. Monaghan, B.D. Anderson, K. Aniol, et al. Probing Cold Dense Nuclear Matter. *Science*, 320:1476–1478, 2008.
- [21] Douglas W. Higinbotham. Short-Range Nucleon-Nucleon Correlations. *AIP Conf. Proc.*, 1374:85–90, 2011.
- [22] K.S. Egiyan et al. Measurement of 2- and 3-nucleon short range correlation probabilities in nuclei. *Phys. Rev. Lett.*, 96:082501, 2006.

- [23] Steven C. Pieper, Robert B. Wiringa, and V. R. Pandharipande. Variational calculation of the ground state of ^{16}O . *Phys. Rev. C*, 46:1741–1756, 1992.
- [24] R. Schiavilla, Robert B. Wiringa, Steven C. Pieper, and J. Carlson. Tensor Forces and the Ground-State Structure of Nuclei. *Phys. Rev. Lett.*, 98:132501, 2007.
- [25] E. R. Anderson, R. J. Furnstahl, and K. Hebeler. 2012. *In preparation*.
- [26] L.B. Weinstein, E. Piasetzky, D.W. Higinbotham, J. Gomez, O. Hen, et al. Short Range Correlations and the EMC Effect. *Phys. Rev. Lett.*, 106:052301, 2011.
- [27] Jochen Erler, Noah Birge, Markus Kortelainen, Witold Nazarewicz, Erik Olsen, Alexander M. Perhac, and Mario Stoitsov. The limits of the nuclear landscape. *Nature*, 486:509–512, 2012.
- [28] Hideki Yukawa. On the interaction of elementary particles. *Proc. Phys. Math. Soc. Jap.*, 17:48–57, 1935.
- [29] R. Machleidt. The Meson theory of nuclear forces and nuclear structure. *Adv. Nucl. Phys.*, 19:189–376, 1989.
- [30] V.G.J. Stoks, R.A.M. Klomp, C.P.F. Terheggen, and J.J. de Swart. Construction of high quality $\text{N} \text{ N}$ potential models. *Phys. Rev. C*, 49:2950–2962, 1994.
- [31] Evgeny Epelbaum, Hans-Werner Hammer, and Ulf-G. Meissner. Modern Theory of Nuclear Forces. *Rev. Mod. Phys.*, 81:1773–1825, 2009.
- [32] A.M. Shirokov, J.P. Vary, A.I. Mazur, and T.A. Weber. Realistic Nuclear Hamiltonian: 'Ab exitu' approach. *Phys. Lett.*, B644:33–37, 2007.
- [33] Takumi Doi et al. Exploring Three-Nucleon Forces in Lattice QCD. 2011.
- [34] S.R. Beane, W. Detmold, K. Orginos, and M.J. Savage. Nuclear Physics from Lattice QCD. *Prog. Part. Nucl. Phys.*, 66:1–40, 2011.
- [35] Martin J. Savage. Nuclear Physics from QCD : The Anticipated Impact of Exa-Scale Computing. *AIP Conf. Proc.*, 1343:30–38, 2011.

- [36] J. Carlson, V.R. Pandharipande, and Robert B. Wiringa. Three-nucleon interaction in 3-body, 4-body, and infinite-body systems. *Nucl.Phys.*, A401:59–85, 1983.
- [37] B.S. Pudliner, V.R. Pandharipande, J. Carlson, and Robert B. Wiringa. Quantum Monte Carlo calculations of $A \leq 6$ nuclei. *Phys. Rev. Lett.*, 74:4396–4399, 1995.
- [38] Stanislaw D. Glazek and Kenneth G. Wilson. Renormalization of Hamiltonians. *Phys. Rev. D*, 48:5863–5872, 1993.
- [39] F. Wegner. *Ann. Phys. (Leipzig)*, 506:77, 1994.
- [40] Y. Suzuki and K. Varga. Stochastic variational approach to quantum-mechanical few body problems. *Lect. Notes Phys.*, M54:1–310, 1998.
- [41] Steven C. Pieper and Robert B. Wiringa. Quantum Monte Carlo Calculations of Light Nuclei. *Ann. Rev. Nucl. Part. Sci.*, 51:53–90, 2001.
- [42] Steven C. Pieper. Quantum monte carlo calculations of light nuclei. arXiv:0711.1500, 2007.
- [43] H. Kamada, A. Nogga, Walter Gloeckle, E. Hiyama, M. Kamimura, et al. Benchmark test calculation of a four nucleon bound state. *Phys. Rev. C*, 64:044001, 2001.
- [44] Y. Suzuki, W. Horiuchi, M. Orabi, and K. Arai. Global-Vector Representation of the Angular Motion of Few- Particle Systems II. *Few Body Syst.*, 42:33–72, 2008.
- [45] K.A. Wendt, R.J. Furnstahl, and S. Ramanan. Local Projections of Low-Momentum Potentials. 2012.
- [46] T. Abe, P. Maris, T. Otsuka, N. Shimizu, Y. Utsuno, et al. Benchmarks of the ab initio FCI, MCSM and NCFC methods. 2012.
- [47] Petr Navratil. Ab initio no-core shell model calculations for light nuclei. 2007.
- [48] E. Caurier, G. Martinez-Pinedo, F. Nowacki, A. Poves, and A.P. Zuker. The Shell model as unified view of nuclear structure. *Rev. Mod. Phys.*, 77:427–488, 2005.

- [49] S. Bacca, N. Barnea, and A. Schwenk. The Structure of 6He in the hyperspherical-harmonics approach. 2012.
- [50] W. Glöckle. *The Quantum Mechanical Few-Body Problem*. Springer-Verlag, Berlin, 1983.
- [51] A. Stadler, W. Glockle, and P.U. Sauer. Faddeev equations with three-nucleon force in momentum space. *Phys. Rev. C*, 44:2319–2327, 1991.
- [52] Kai Hebeler. Momentum space evolution of chiral three-nucleon forces. *Phys. Rev. C*, 85:021002, 2012.
- [53] D.J. Dean and M. Hjorth-Jensen. Coupled cluster approach to nuclear physics. *Phys. Rev. C*, 69:054320, 2004.
- [54] G. Hagen, T. Papenbrock, D.J. Dean, and M. Hjorth-Jensen. Ab initio coupled-cluster approach to nuclear structure with modern nucleon-nucleon interactions. *Phys. Rev. C*, 82:034330, 2010.
- [55] Dean Lee. Lattice simulations for few- and many-body systems. *Prog. Part. Nucl. Phys.*, 63:117–154, 2009.
- [56] Evgeny Epelbaum, Hermann Krebs, Dean Lee, and Ulf-G. Meissner. Lattice calculations for $A=3,4,6,12$ nuclei using chiral effective field theory. *Eur. Phys. J.*, A45:335–352, 2010.
- [57] N. Schunck, A. Baran, M. Kortelainen, J. McDonnell, J. More, et al. Computing Heavy Elements. 2011.
- [58] P. Hohenberg and W. Kohn. Inhomogeneous Electron Gas. *Phys. Rev.*, 136:B864–B871, 1964.
- [59] A. L. Fetter and J. D. Walecka. *Quantum Many-Particle Systems*. McGraw–Hill, New York, 1972.

- [60] J. W. Negele and H. Orland. *Quantum Many-Particle Systems*. Addison-Wesley, Redwood City, CA, 1988.
- [61] P Ring and P Schuck. *The nuclear many-body problem*, volume 103. Springer-Verlag, 1980.
- [62] Michael Bender, Paul-Henri Heenen, and Paul-Gerhard Reinhard. Self-consistent mean-field models for nuclear structure. *Rev. Mod. Phys.*, 75:121–180, 2003.
- [63] R. Roth et al. Hartree-fock and many-body perturbation theory with correlated realistic nn-interactions. *Phys. Rev. C*, 73:044312, 2006.
- [64] S. K. Bogner, T. T. S. Kuo, and A. Schwenk. Model-independent low momentum nucleon interaction from phase shift equivalence. *Phys. Rept.*, 386:1–27, 2003.
- [65] S. K. Bogner, R. J. Furnstahl, and A. Schwenk. From low-momentum interactions to nuclear structure. *Prog. Part. Nucl. Phys.*, 65:94–147, 2010.
- [66] Sergio Szpigel and Robert J. Perry. The Similarity renormalization group. 2000. Published in Quantum Field Theory, A 20th Century Profile.
- [67] Stanislaw D. Glazek and Tomasz Maslowski. Renormalized Poincare algebra for effective particles in quantum field theory. *Phys. Rev. D*, 65:065011, 2002.
- [68] S. Kehrein. *The Flow Equation Approach to Many-Particle Systems*. Springer, Berlin, 2006.
- [69] S. K. Bogner, R. J. Furnstahl, and R. J. Perry. Similarity renormalization group for nucleon-nucleon interactions. *Phys. Rev. C*, 75:061001, 2007.
- [70] E. D. Jurgenson, S. K. Bogner, R. J. Furnstahl, and R. J. Perry. Decoupling in the Similarity Renormalization Group for Nucleon-Nucleon Forces. *Phys. Rev. C*, 78:014003, 2008.
- [71] S. Ramanan, S. K. Bogner, and R. J. Furnstahl. Weinberg Eigenvalues and Pairing with Low-Momentum Potentials. *Nucl. Phys. A*, 797:81–93, 2007.

- [72] E. D. Jurgenson and R. J. Furnstahl. Similarity Renormalization Group Evolution of Many-Body Forces in a One-Dimensional Model. *Nucl. Phys. A*, 818:152–173, 2009.
- [73] Robert Roth. Importance Truncation for Large-Scale Configuration Interaction Approaches. *Phys. Rev. C*, 79:064324, 2009.
- [74] Robert Roth, Sven Binder, Klaus Vobig, Angelo Calci, Joachim Langhammer, et al. Ab Initio Calculations of Medium-Mass Nuclei with Normal-Ordered Chiral NN+3N Interactions. 2011.
- [75] K. Tsukiyama, S.K. Bogner, and A. Schwenk. In-Medium Similarity Renormalization Group for Nuclei. *Phys. Rev. Lett.*, 106:222502, 2011.
- [76] E. R. Anderson, S. K. Bogner, R. J. Furnstahl, and R. J. Perry. Operator Evolution via the Similarity Renormalization Group I: The Deuteron. *Phys. Rev. C*, 82:054001, 2010.
- [77] S. K. Bogner, R. J. Furnstahl, S. Ramanan, and A. Schwenk. Low-momentum interactions with smooth cutoffs. *Nucl. Phys. A*, 784:79–103, 2007.
- [78] I. Sick. Elastic Electron Scattering from Light Nuclei. *Prog. Part. Nucl. Phys.*, 47:245–318, 2001.
- [79] M. Garcon and J. W. Van Orden. The deuteron: Structure and form factors. *Adv. Nucl. Phys.*, 26:293, 2001.
- [80] Ronald A. Gilman and Franz Gross. Electromagnetic structure of the deuteron. *J. Phys.*, G28:R37–R116, 2002.
- [81] Daniel R. Phillips. Chiral effective theory predictions for deuteron form factor ratios at low Q^{**2} . *J. Phys.*, G34:365–388, 2007.
- [82] Manuel Pavon Valderrama, A. Nogga, Enrique Ruiz Arriola, and Daniel R. Phillips. Deuteron form factors in chiral effective theory: regulator-independent results and the role of two-pion exchange. *Eur. Phys. J. A*, 36:315–328, 2008.

- [83] S. K. Bogner and R. J. Furnstahl. Variational calculations of nuclei with low-momentum potentials. *Phys. Lett. B*, 632:501–506, 2006.
- [84] S. K. Bogner and R. J. Furnstahl. Variational calculations using low-momentum potentials with smooth cutoffs. *Phys. Lett. B*, 639:237–241, 2006.
- [85] B. Dainton and R. J. Perry. 2012. *In preparation.*
- [86] Steven Weinberg. Why the renormalization group is a good thing. In *Cambridge 1981, Proceedings, Asymptotic Realms Of Physics*, 1-19.
- [87] C. Alexandrou, J. Myczkowski, and John W. Negele. Comparison of mean-field and exact Monte Carlo solutions of a one-dimensional nuclear model. *Phys. Rev. C*, 39:1076–1087, 1989.
- [88] K. Varga and Y. Suzuki. Precise solution of few body problems with stochastic variational method on correlated Gaussian basis. *Phys. Rev. C*, 52:2885–2905, 1995.
- [89] E. Anderson et al. Block Diagonalization using SRG Flow Equations. *Phys. Rev. C*, 77:037001, 2008.
- [90] W. Li, E.R. Anderson, and R.J. Furnstahl. The Similarity Renormalization Group with Novel Generators. *Phys. Rev. C*, 84:054002, 2011. 10 pages, 12 figures.
- [91] Elena L. Gubankova, Hans-Christian Pauli, and Franz J. Wegner. Light cone Hamiltonian flow for positronium. 1998. 43 pages, LaTeX2e, 5 Figures, Submitted to Phys. Rev. D.
- [92] Elena Gubankova, Chueng-Ryong Ji, and Stephen R. Cotanch. Flow equations for gluodynamics in the Coulomb gauge. *Phys. Rev. D*, 62:074001, 2000.
- [93] S. K. Bogner, R. J. Furnstahl, and R. J. Perry. Three-Body Forces Produced by a Similarity Renormalization Group Transformation in a Simple Model. *Annals Phys.*, 323:1478–1501, 2008.

- [94] K. A. Wendt, R. J. Furnstahl, and R. J. Perry. Decoupling of Spurious Deep Bound States with the Similarity Renormalization Group. *Phys. Rev. C*, 83:034005, 2011.
- [95] Robert Roth, Joachim Langhammer, Angelo Calci, Sven Binder, and Petr Navratil. Similarity-Transformed Chiral NN+3N Interactions for the Ab Initio Description of 12-C and 16-O. *Phys. Rev. Lett.*, 107:072501, 2011.
- [96] Stanislaw D. Glazek and Robert J. Perry. The impact of bound states on similarity renormalization group transformations. *Phys. Rev. D*, 78:045011, 2008.
- [97] Petr Navratil. Local three-nucleon interaction from chiral effective field theory. *Few Body Syst.*, 41:117–140, 2007.
- [98] R.J. Furnstahl, G. Hagen, and T. Papenbrock. Corrections to nuclear energies and radii in finite oscillator spaces. 2012.
- [99] G.P. Lepage. How to renormalize the Schrodinger equation. pages 135–180, 1997. Lectures given at the VIII Jorge Andre Swieca Summer School (Brazil, 1997).
- [100] Eric Braaten and Lucas Platter. Exact Relations for a Strongly Interacting Fermi Gas from the Operator Product Expansion. *Phys. Rev. Lett.*, 100:205301, 2008.
- [101] Leonid Frankfurt, Misak Sargsian, and Mark Strikman. Recent observation of short range nucleon correlations in nuclei and their implications for the structure of nuclei and neutron stars. *Int. J. Mod. Phys. A*, 23:2991–3055, 2008.
- [102] W.H. Dickhoff and D. Van Neck. *Many-Body Theory Exposed!: Propagator Description of Quantum Mechanics in Many-Body Systems*. World Scientific, Singapore, 2nd edition, 2008.
- [103] J.J. Aubert et al. The ratio of the nucleon structure functions f_2^n for iron and deuterium. *Phys. Lett. B*, 123:275, 1983.
- [104] Jiunn-Wei Chen and William Detmold. Universality of the EMC effect. *Phys. Lett.*, B625:165–170, 2005.

- [105] Petr Navratil, Robert Roth, and Sofia Quaglioni. Ab initio many-body calculations of nucleon scattering on 4He , 7Li , 7Be , ^{12}C and ^{16}O . *Phys. Rev. C*, 82:034609, 2010.
- [106] Petr Navratil, Sofia Quaglioni, and Robert Roth. Ab Initio Theory of Light-ion Reactions. *Proceedings of the International Nuclear Physics Conference INPC 2010 (unpublished)*.

Appendix A

MANY-BODY EVOLUTION

Details are presented in the first section of this appendix regarding some of the results needed to define operators in a Jacobi coordinate basis which might otherwise appear to be non-trivial task. In the second section, the algebraic manipulations in a second-quantized formalism which provide the foundation for understanding of operator evolution and embedding are presented.

A.1 One-body operators in Jacobi coordinates

Our objective here is to demonstrate that one-body operators defined naturally in a single particle basis, can rather easily be written in the relative coordinate Jacobi basis, assuming the COM motion of the entire system can be neglected. To do this, we show that one of the single particle coordinates can be isolated, and shown to be equivalent to one of the Jacobi coordinates. Since we work in symmetrized bases, this is sufficient to define the one-body operator in specific A -particle bases.

Recall from the text that we have defined the Jacobi coordinates p_j in Eq. (3.6) via

$$p_j = \sqrt{\frac{j}{j+1}} \left[\left(\frac{1}{j} \sum_i^j k_i \right) - k_{j+1} \right],$$

for $j < A$ and

$$p_A = \frac{1}{A} \sum_i^A k_i$$

which is the COM coordinate of the system. Since k_A only appears in ρ_{A-1} , it would seem

to be the easiest to isolate. Rearranging terms then, we get

$$k_A = \frac{1}{A-1} \sum_{i=1}^{A-1} k_i - \sqrt{\frac{A}{A-1}} \rho_{A-1}. \quad (\text{A.1})$$

Adding $\frac{1}{A-1} k_A$ to both sides results in

$$\left(1 + \frac{1}{A-1}\right) k_A = \frac{1}{A-1} \sum_{i=1}^A k_i - \sqrt{\frac{A}{A-1}} \rho_{A-1}. \quad (\text{A.2})$$

Since the COM motion of the system can be neglected, we choose the rest frame (i.e., $\sum_{i=1}^A k_i = 0$) so that

$$\left(\frac{A}{A-1}\right) k_A = -\sqrt{\frac{A}{A-1}} \rho_{A-1} \quad (\text{A.3})$$

or simply

$$k_A = -\sqrt{\frac{A-1}{A}} \rho_{A-1} \quad (\text{A.4})$$

and thus we have recovered Eq. (3.8):

$$p_{A-1} = -\sqrt{\frac{A}{A-1}} k_A,$$

which gives a general relation between the last relative Jacobi coordinate and the last absolute coordinate in our coordinate system. It is important to point out that works for identical mass particles (which is most often the case in nuclear calculations thanks to approximate isospin symmetry). If we are not working in a system where this holds true, we need to be more careful, and account for the masses in the revised definition of the Jacobi coordinates.

In order to embed a one-body operator in an A -particle symmetric and identical particle space, it is sufficient to define an operator based on a this single coordinate and then to multiply by A after transforming to the symmetrized space, as discussed in the main text. This coordinate can be either the single-particle basis coordinate, or the appropriately scaled Jacobi basis coordinate. For instance, the single-particle momentum distribution momentum distribution used as an example throughout the text is defined by [101]:

$$n(q) = \sum_{i=1}^A \int \psi_A^2(k_1, k_2, k_i, \dots, k_A) \delta^3(k_i - q) \delta^3\left(\sum_{j=1}^A k_j\right) \prod_{l=1}^A d^3 k_l. \quad (\text{A.5})$$

In the Jacobi coordinates our calculations are explicitly independent of the COM motion, otherwise, we can project out the COM rest frame of the state. As such, we may ignore the delta function over the COM momentum in this expression, leaving us with the one-body number operator

$$\langle k_i | a_{\mathbf{q}}^\dagger a_{\mathbf{q}} | k'_i \rangle = \delta^3(k_i - q).$$

If we wish to express this in a symmetrized Jacobi basis, we can simply transform the matrix element for k_A so that

$$\langle k_A | a_{\mathbf{q}}^\dagger a_{\mathbf{q}} | k'_A \rangle \Leftrightarrow \sqrt{\frac{A}{A-1}} \delta^3 \left(p_{A-1} - \sqrt{\frac{A-1}{A}} q \right).$$

The kinetic energy is also, in principle, defined by the sum over one-body operators

$$KE = \sum_i^A \frac{k_i^2}{2m}, \quad (\text{A.6})$$

and so we could rewrite this as $(A-1) \frac{p_{A-1}^2}{2m}$ in a symmetrized Jacobi basis. However, thanks to the quadratic form of this expression, we can also rewrite this as a sum over the relative coordinates in the COM rest frame [40]:

$$KE = \sum_i^{A-1} \frac{p_i^2}{2m}. \quad (\text{A.7})$$

One can be convinced that this is true by adding back in the COM coordinate, transforming back to single particle coordinates, and expanding the expression for any given number of particles. Since we work in a symmetrized basis, this is effectively a two-body operator given by $C[A, 2] \frac{p_1^2}{2m}$. This is typically a much more convenient form to work with.

A.2 Separation of n -body components, 2nd quantized analysis

In this section we outline the details which lead us to conclude that any \hat{O}_s is completely determined up to its $\hat{O}^{(n)}$ contribution by its n -body matrix elements. This is a key result, as we have seen, for practical calculations involving many-body operator evolution. As

discussed in the main text, a general operator \hat{O} for an A -body system can be written as

$$\hat{O} = \hat{O}^{(1)} + \hat{O}^{(2)} + \hat{O}^{(3)} + \cdots + \hat{O}^{(A)}$$

where the $\hat{O}^{(n)}$ label the $n = 1, 2, 3, \dots, A$ -body components of the operator. The SRG evolved operator

$$\hat{O}_s = \hat{O}_s^{(1)} + \hat{O}_s^{(2)} + \cdots + \hat{O}_s^{(n)} + \cdots$$

will, in general, have additional contributions at all levels of n so that $\hat{O}^{(n)} \neq \hat{O}_s^{(n)}$.

Recall that we can write any single-particle state with the particle creation and annihilation operators as $|i\rangle = a_i^\dagger |0\rangle$ where $[a_i, a_j^\dagger] = \delta_{ij}$. Thus, many-particle basis states are given by

$$|i, j, k, \dots\rangle = a_i^\dagger a_j^\dagger a_k^\dagger \cdots |0\rangle$$

where i, j, k, \dots here label the quantum numbers of different single-particle states in any given basis. A one-body operator is given by

$$\sum_{ik} a_i^\dagger \langle i | \hat{O}^{(1)} | k \rangle a_k,$$

a two-body operator by

$$\left(\frac{1}{2!}\right) \sum_{ijkl} a_i^\dagger a_j^\dagger \langle ij | \hat{O}^{(2)} | kl \rangle a_k a_l,$$

etc., as can be easily determined by the number of a 's and a^\dagger 's.

The SRG equations can thus be written (e.g., using a 2-body interaction) as

$$\begin{aligned} \frac{d\hat{O}_s}{ds} &= [[T_{\text{rel}}, H_s], \hat{O}_s] = [[T - T_{CM}, H_s], \hat{O}_s] \\ &\Leftrightarrow \left[\left[\sum_{ij} T_{ij} a_i^\dagger a_j, \sum_{i'j'} T_{i'j'} a_{i'}^\dagger a_{j'} + \frac{1}{2} \sum_{pqkl} V_{pqkl,s} a_p^\dagger a_q^\dagger a_l a_k \right], \hat{O}_s \right] \end{aligned} \quad (\text{A.8})$$

where $V_{pqkl,s} = \langle pq | V_s^{(2)} | kl \rangle$ and $T_{ij} = \langle i | T^{(1)} | j \rangle$; the center of mass components commute with the relative Hamiltonian (we working in relative coordinates in general, but single particle coordinates are needed here) and so drop out. So, we can see that at each step in the solution of the SRG differential equation the commutators produce terms with additional creation and annihilation operators.

To clearly identify the many-body contributions produced at each step in the differential equations, we need to expand these commutators and normal order (i.e., write the equivalent expressions with all annihilation operators to the left and creation operators to the right) the resulting terms. This can be done by making use of Wicks theorem. It states that for general creation and annihilation operator A_i^\dagger and A_i states [18]:

$$\begin{aligned}
A_i A_j A_k \cdots A_m &= N(A_i A_j A_k A_l \cdots A_m) \\
&\quad + N \left((\overline{A_i} \overline{A_j} A_k A_l \cdots A_m) + \text{all single contractions} \right) \\
&\quad + N \left((\overline{A_i} \overline{A_j} \overline{A_k} A_l \cdots A_m) + \text{all double contractions} \right) \\
&\quad \vdots \\
&\quad + N(\text{all full contractions}) , \tag{A.9}
\end{aligned}$$

where $N(\cdots)$ refers to a normal ordered expression of creation and annihilation operators. This can be equivalently abbreviated by $N(\cdots) \Leftrightarrow \cdots$: Its corollary is given by (for 2 or more operators, but shown here for 2)

$$\begin{aligned}
N(A_i A_j) N(A_k A_l) &= N(A_i A_j A_k A_l) + N(\overline{A_i} \overline{A_j} A_k A_l) + N(\overline{A_i} \overline{A_j} \overline{A_k} A_l) \\
&\quad + N(A_i \overline{A_j} \overline{A_k} A_l) + N(A_i \overline{A_j} \overline{A_k} \overline{A_l}) + N(\overline{A_i} \overline{A_j} \overline{A_k} \overline{A_l}) \\
&\quad + N(\overline{A_i} \overline{A_j} \overline{A_k} \overline{A_l}) , \tag{A.10}
\end{aligned}$$

which simplifies contractions between products of normal ordered expressions. There is only one non-vanishing type of contraction in the vacuum

$$a_i \overline{a}_j^\dagger = \delta_{ij} \tag{A.11}$$

and the other three, $\overline{a}_i^\dagger \overline{a}_j$, $\overline{a}_i \overline{a}_j$, and $\overline{a}_i^\dagger \overline{a}_j^\dagger$, give zero.

With this technology, we can now begin to work out the commutators of

$$\frac{d\hat{O}_s}{ds} = \left[\left[\sum_{ij} T_{ij} a_i^\dagger a_j, \sum_{i'j'} T_{i'j'} a_{i'}^\dagger a_{j'} + \frac{1}{2} \sum_{pqkl} V_{pqkl,s} a_p^\dagger a_q^\dagger a_l a_k \right], \hat{O}_s \right]$$

to get (dropping the summation signs for clarity)

$$\frac{d\hat{O}_s}{ds} = \left[\left[T_{ij} a_i^\dagger a_j, \frac{1}{2} V_{pqkl,s} a_p^\dagger a_q^\dagger a_l a_k \right], \hat{O}_s \right] \quad (\text{A.12})$$

since

$$T_{ij} T_{i'j'} a_i^\dagger a_j a_{i'}^\dagger a_{j'} - T_{i'j'} T_{ij} a_{i'}^\dagger a_{j'} a_i^\dagger a_j = 0$$

thanks to the fact that we can redefine the dummy indices $i \leftrightarrow i'$ and $j \leftrightarrow j'$. To focus our attention on the relevant creation and annihilation operators, we will also drop the rest of the coefficients (other than for \hat{O}_s) so that we have

$$\frac{d\hat{O}_s}{ds} = \left[\left[a_i^\dagger a_j a_p^\dagger a_q^\dagger a_l a_k - a_p^\dagger a_q^\dagger a_l a_k a_i^\dagger a_j \right], \hat{O}_s \right]. \quad (\text{A.13})$$

Normal ordering this as much as possible first (with Wick's theorem and its corollary) we have

$$\begin{aligned} \frac{d\hat{O}_s}{ds} = & \left[\left[a_i^\dagger a_p^\dagger a_q^\dagger a_l a_k a_j + : (a_i^\dagger a_j)(a_p^\dagger a_q^\dagger a_l a_k) : + (\text{rest of single}) + (\text{double}) + (\text{triple}) \right. \right. \\ & \left. \left. - a_i^\dagger a_p^\dagger a_q^\dagger a_l a_k a_j - : (a_p^\dagger a_q^\dagger a_l a_k)(a_i^\dagger a_j) : - (\text{rest of single}) - (\text{double}) - (\text{triple}) \right], \hat{O}_s \right] \end{aligned}$$

where the long list of single, double, and triple contractions have been abbreviated. The abbreviated contractions to have vanishing contributions. As such,

$$\begin{aligned} \frac{d\hat{O}_s}{ds} = & \left[\left[a_i^\dagger a_p^\dagger a_q^\dagger a_l a_k a_j + \delta_{jp} a_i^\dagger a_q^\dagger a_l a_k + \delta_{jq} a_i^\dagger a_p^\dagger a_l a_k + 0' s \right. \right. \\ & \left. \left. - a_i^\dagger a_p^\dagger a_q^\dagger a_l a_k a_j - \delta_{li} a_p^\dagger a_q^\dagger a_k a_j - \delta_{ki} a_p^\dagger a_q^\dagger a_l a_j - 0' s \right], \hat{O}_s \right], \end{aligned}$$

and cancelling like terms, we have at this point that

$$\frac{d\hat{O}_s}{ds} = \left[\delta_{jp} a_i^\dagger a_q^\dagger a_l a_k + \delta_{jq} a_i^\dagger a_p^\dagger a_l a_k - \delta_{li} a_p^\dagger a_q^\dagger a_k a_j - \delta_{ki} a_p^\dagger a_q^\dagger a_l a_j, \hat{O}_s \right]. \quad (\text{A.14})$$

With this expression, we may now consider the contributions to individual n -body operators, starting with $\hat{O}_s^{(1)}$. For this operator,

$$\begin{aligned} \frac{d\hat{O}_s^{(1)}}{ds} = & O_{mn,s}^{(1)} \left[\delta_{jp} a_i^\dagger a_q^\dagger a_l a_k a_m^\dagger a_n + \delta_{jq} a_i^\dagger a_p^\dagger a_l a_k a_m^\dagger a_n - \delta_{li} a_p^\dagger a_q^\dagger a_k a_j a_m^\dagger a_n - \delta_{ki} a_p^\dagger a_q^\dagger a_l a_j a_m^\dagger a_n \right. \\ & \left. - \delta_{jp} a_m^\dagger a_n a_i^\dagger a_q^\dagger a_l a_k - \delta_{jq} a_m^\dagger a_n a_i^\dagger a_p^\dagger a_l a_k + \delta_{li} a_m^\dagger a_n a_p^\dagger a_q^\dagger a_k a_j + \delta_{ki} a_m^\dagger a_n a_p^\dagger a_q^\dagger a_l a_j \right]. \end{aligned}$$

Expanding, we get

$$\begin{aligned}
\frac{d\widehat{O}_s^{(1)}}{ds} = & O_{mn,s}^{(1)}[\delta_{jp} : (a_i^\dagger a_q^\dagger a_l a_k)(a_m^\dagger a_n) : + (\text{all contractions}) \\
& + \delta_{jq} : (a_i^\dagger a_p^\dagger a_l a_k)(a_m^\dagger a_n) : + \delta_{jq} \delta_{lm} (a_i^\dagger a_p^\dagger a_k)(a_n) + \delta_{jq} \delta_{km} (a_i^\dagger a_p^\dagger a_l)(a_n) \\
& - \delta_{li} : (a_p^\dagger a_q^\dagger a_k a_j)(a_m^\dagger a_n) : - \delta_{li} \delta_{km} : (a_p^\dagger a_q^\dagger a_j)(a_n) : - \delta_{li} \delta_{jm} : (a_p^\dagger a_q^\dagger a_k)(a_n) : \\
& - \delta_{ki} : (a_p^\dagger a_q^\dagger a_l a_j)(a_m^\dagger a_n) : - \dots \\
& - \delta_{jp} : (a_m^\dagger a_n)(a_i^\dagger a_q^\dagger a_l a_k) : - \delta_{jp} \delta_{ni} (a_m^\dagger)(a_q^\dagger a_l a_k) - \delta_{jp} \delta_{nq} (a_m^\dagger)(a_i^\dagger a_l a_k) \\
& - \delta_{jq} : (a_m^\dagger a_n)(a_i^\dagger a_p^\dagger a_l a_k) : - \delta_{jq} \delta_{ni} (a_m^\dagger)(a_p^\dagger a_l a_k) - \delta_{jq} \delta_{np} (a_m^\dagger)(a_i^\dagger a_l a_k) \dots \\
& + \delta_{li} : (a_m^\dagger a_n)(a_p^\dagger a_q^\dagger a_k a_j) : + \dots \\
& + \delta_{ki} : (a_m^\dagger a_n)(a_p^\dagger a_q^\dagger a_l a_j) : + \dots].
\end{aligned}$$

All two and three particle contractions necessarily vanish, so we have

$$\begin{aligned}
\frac{d\widehat{O}_s^{(1)}}{ds} = & O_{mn,s}^{(1)}[(\text{all contractions}) \\
& + \delta_{jq} \delta_{lm} (a_i^\dagger a_p^\dagger a_k)(a_n) + \delta_{jq} \delta_{km} (a_i^\dagger a_p^\dagger a_l)(a_n) \\
& - \delta_{li} \delta_{km} : (a_p^\dagger a_q^\dagger a_j)(a_n) : - \delta_{li} \delta_{jm} : (a_p^\dagger a_q^\dagger a_k)(a_n) : \\
& - \dots \\
& - \delta_{jp} \delta_{ni} (a_m^\dagger)(a_q^\dagger a_l a_k) - \delta_{jp} \delta_{nq} (a_m^\dagger)(a_i^\dagger a_l a_k) \\
& - \delta_{jq} \delta_{ni} (a_m^\dagger)(a_p^\dagger a_l a_k) - \delta_{jq} \delta_{np} (a_m^\dagger)(a_i^\dagger a_l a_k) \dots \\
& + \dots \\
& + \dots].
\end{aligned}$$

Thus, there are no one-body contributions (i.e., no $a^\dagger a$ terms) to the change in initial one-body operator with this generator. The same logic applies to the next step in the differential equation, and so is true for all s . Hence, we see that $\widehat{O}_s^{(1)} = \widehat{O}^{(1)}$ using the conventional choice of generator $G_s = T_{\text{rel}}$ as mentioned in the main text.

For the 2-body component of the operator

$$\begin{aligned} \frac{d\hat{O}_s^{(2)}}{ds} = O_{mn,s}^{(2)} & \left[\delta_{jp} a_i^\dagger a_q^\dagger a_l a_k a_m^\dagger a_x^\dagger a_y a_n + \delta_{jq} a_i^\dagger a_p^\dagger a_l a_k a_m^\dagger a_x^\dagger a_y a_n \right. \\ & - \delta_{li} a_p^\dagger a_q^\dagger a_k a_j a_m^\dagger a_x^\dagger a_y a_n - \delta_{ki} a_p^\dagger a_q^\dagger a_l a_j a_m^\dagger a_x^\dagger a_y a_n \\ & - \delta_{jp} a_m^\dagger a_x^\dagger a_y a_n a_i^\dagger a_q^\dagger a_l a_k - \delta_{jq} a_m^\dagger a_x^\dagger a_y a_n a_i^\dagger a_p^\dagger a_l a_k \\ & \left. + \delta_{li} a_m^\dagger a_x^\dagger a_y a_n a_p^\dagger a_q^\dagger a_k a_j + \delta_{ki} a_m^\dagger a_x^\dagger a_y a_n a_p^\dagger a_q^\dagger a_l a_j \right] \end{aligned}$$

Applying Wick's theorem,

$$\begin{aligned} \frac{d\hat{O}_s^{(2)}}{ds} = O_{mn,s}^{(2)} & [\delta_{jp} : (a_i^\dagger a_q^\dagger a_l a_k) (a_m^\dagger a_x^\dagger a_y a_n) : + (\text{all contractions}) \\ & + \delta_{jq} : (a_i^\dagger a_p^\dagger a_l a_k) (a_m^\dagger a_x^\dagger a_y a_n) : + (\text{4 singles}) + (\text{2 doubles}) + (\text{0 triples \& quads}) \dots \\ & - \delta_{li} : (a_p^\dagger a_q^\dagger a_k a_j) (a_m^\dagger a_x^\dagger a_y a_n) : - \dots \\ & - \delta_{ki} : (a_p^\dagger a_q^\dagger a_l a_j) (a_m^\dagger a_x^\dagger a_y a_n) : - \dots \\ & - \delta_{jp} : (a_m^\dagger a_x^\dagger a_y a_n) (a_i^\dagger a_q^\dagger a_l a_k) : - \dots \\ & - \delta_{jq} : (a_m^\dagger a_x^\dagger a_y a_n) (a_i^\dagger a_p^\dagger a_l a_k) : - (\text{4 singles}) - (\text{2 doubles}) - (\text{0 triples \& quads}) \dots \\ & + \delta_{li} : (a_m^\dagger a_x^\dagger a_y a_n) (a_p^\dagger a_q^\dagger a_k a_j) : + \dots \\ & + \delta_{ki} : (a_m^\dagger a_x^\dagger a_y a_n) (a_p^\dagger a_q^\dagger a_l a_j) : + \dots] \end{aligned}$$

Thus, there are no contributions at less than the 2-body level (i.e., no $a^\dagger a$ terms) to the change in the (initially) 2-body operator with this generator.

For the 3-body component of the operator we get

$$\begin{aligned} \frac{d\hat{O}_s^{(3)}}{ds} = O_{mn,s}^{(3)} & [\delta_{jp} : (a_i^\dagger a_q^\dagger a_l a_k) (a_m^\dagger a_x^\dagger a_b^\dagger a_c a_y a_n) : + (\text{all contractions}) \\ & + \delta_{jq} : (a_i^\dagger a_p^\dagger a_l a_k) (a_m^\dagger a_x^\dagger a_b^\dagger a_c a_y a_n) : + (\text{singles, doubles}) + (\text{0 otherwise}) \dots \\ & - \delta_{li} : (a_p^\dagger a_q^\dagger a_k a_j) (a_m^\dagger a_x^\dagger a_b^\dagger a_c a_y a_n) : - \dots \\ & - \delta_{ki} : (a_p^\dagger a_q^\dagger a_l a_j) (a_m^\dagger a_x^\dagger a_b^\dagger a_c a_y a_n) : - \dots \\ & - \delta_{jp} : (a_m^\dagger a_x^\dagger a_y a_n) (a_m^\dagger a_x^\dagger a_b^\dagger a_c a_y a_n) : - \dots \end{aligned}$$

$$\begin{aligned}
-\delta_{jq} : & (a_m^\dagger a_x^\dagger a_b^\dagger a_c a_y a_n) (a_i^\dagger a_p^\dagger a_l a_k) : -(\text{singles, doubles}) - (0 \text{ otherwise}) \cdots \\
+ \delta_{li} : & (a_m^\dagger a_x^\dagger a_b^\dagger a_c a_y a_n) (a_p^\dagger a_q^\dagger a_k a_j) : + \cdots \\
+ \delta_{ki} : & (a_m^\dagger a_x^\dagger a_b^\dagger a_c a_y a_n) (a_p^\dagger a_q^\dagger a_l a_j) : + \cdots].
\end{aligned}$$

Thus, there are no contributions at less than the three-body level (i.e., no $a^\dagger a$ or $a^\dagger a^\dagger aa$ terms) to the change in the (initially) three-body operator with this generator.

It is clear now that a pattern is emerging. We see that the only non-zero contractions which can take place between the normal ordered products are those on the “inner” parts of the products because of the order of the creation and annihilation operators. Specifically, these are between the double indexed operators below

$$(a_m^\dagger \cdots a_n^\dagger a_{mm} \cdots a_{nn}) (a_{xx}^\dagger \cdots a_{yy}^\dagger a_x \cdots a_y)$$

Thus the number of contractions is limited by the smallest set of $a_{mm} \cdots a_{nn}$ or $a_{xx}^\dagger \cdots a_{yy}^\dagger$ and so there are at least contributions at the n -body level given by the number, n , of operators in the largest set. Conversely, there are no contributions at less than the n -body level due to operators at the n -body level or above. Thus, we have our key result: any \hat{O}_s must be completely determined up to its $\hat{O}^{(n)}$ contribution by its n -body matrix elements.

Stated differently, the smallest space (in terms of “number of bodies” - n) in which there are contributions in the differential SRG equation is given by the largest (n -body) operator in the equation. Also notice that are also contributions at most in the (*largest + smallest*)-body operator in the equation) at each step in the equation. Thus, when integrated there are contributions induced in all spaces with a larger number of bodies.

It should be noted that the potential (in the generator) might also have three-body, four-body, etc. components. It is also clear by looking at the contractions, this will not be a problem, as these components will only have effects at the three-, four-, etc. body level or higher.

Based on the evolution equations, one will also note that it also appears as though T_{rel} does not evolve. This is simply the way we have chosen to define the potential. The two-body (induced) evolution of T_{rel} is actually “stuffed” into the matrix for $V^{(2)}$, and three-

body into $V^{(3)}$, etc. This definition was simply a matter of convenience for embedding the Hamiltonian into larger n -body spaces. It may be useful to notice that for matrix elements in the evolved wave functions, in general $\langle \psi_{s=0} | T_{\text{rel}} | \psi_{s=0} \rangle \neq \langle \psi_s | T_{\text{rel}} | \psi_s \rangle$ and $\langle \psi_{s=0} | V_{s=0} | \psi_{s=0} \rangle \neq \langle \psi_s | V_s | \psi_s \rangle$ because T_{rel} has no many-body components and V_s gains those components. Only $\langle \psi_{s=0} | H_{s=0} | \psi_{s=0} \rangle = \langle \psi_s | H_s | \psi_s \rangle = \langle \psi_s | U H_{s=0} U^\dagger | \psi_{s=0} \rangle$. So, it is important to distinguish between the matrix T_{rel} and the basis independent operator \widehat{T}_{rel} which does, in a sense, gain many-body components in the evolution.